Automated Rapid Thermal Imaging Systems Technology

By

Long N. Phan

B.S. Mechanical Engineering
Massachusetts Institute of Technology, 1999

M.S. Mechanical Engineering
Massachusetts Institute of Technology, 1999

SUBMITTED TO THE DEPARTMENT OF MECHNICAL ENGINEERING IN PARTIAL FULFILLMENT OF THE REQUIREMENTS FOR THE DEGREE OF

DOCTOR OF PHILOSOPHY IN MECHANICAL ENGINEERING
AT THE
MASSACHUSETTS INSTITUTE OF TECHNOLOGY

June 2012

Signature of Author: _____
Department of Mechanical Engineering
June 2012

Certified by: _____
Alexander H. Slocum
Professor of Mechanical Engineering
Thesis Supervisor

Accepted by: _____
David E. Hardt
Professor of Mechanical Engineering
Chairman, Committee for Graduate Students

Automated Rapid Thermal Imaging Systems Technology

By

Long N. Phan

Submitted to the Department of Mechanical Engineering on May 22nd, 2012 in Partial Fulfillment of the Requirements for the Degree of

Doctor of Philosophy in Mechanical Engineering

ABSTRACT

A major source of energy savings occurs on the thermal envelop of buildings, which amounts to approximately 10% of annual energy usage in the United States. To pursue these savings, energy auditors use closed loop energy auditing processes that include infrared thermography inspection as an important tool to assess deficiencies and identify hot thermal gradients. This process is prohibitively expensive and time consuming. I propose fundamentally changing this approach by designing, developing, and deploying an Automated Rapid Thermal Imaging Systems Technology (ARTIST) which is capable of street level drive-by scanning in real-time. I am doing for thermal imaging what Google Earth did for visual imaging. I am mapping the world's temperature, window by window, house by house, street by street, city by city, and country by country. In doing so, I will be able to provide detailed information on where and how we are wasting energy, providing the information needed for sound economic and environmental energy policies and identifying what corrective measures can and should be taken.

The fundamental contributions of this thesis relates to the ARTIST. This thesis will focus on the following topics:

- Multi-camera synthetic aperture imaging system
- 3D Radiometry
- Non-radiometric infrared camera calibration techniques
- Image enhancement algorithms
    - Hyper Resolution
    - Kinetic Super Resolution
    - Thermal Signature Identification
    - Low-Light Signal-to-Noise Enhancement using KSR

Thesis Supervisor: Alexander H. Slocum
Tile: Professor of Mechanical Engineering

Foreword & Acknowledgement

As I sit here on two days away from my thesis defense, I am reminded of what I am doing here and my reasons for being at MIT. It has definitely been a long journey for me, dating back to 1994 when I first arrived at MIT as a freshman. It is indeed, long ago, almost 18 years to be exact, just about the age of an incoming freshman next year. It does make me put things in perspective and I would like to share some of my stories, experiences, and begin to thank the many people who made this journey possible for me.

First and foremost, I would like to thank my parents, who, through their sacrifices and efforts have made it possible for me exist and have the opportunities in front of me today. My parents, when I was 2.5 years old, decided to make the ultimate sacrifice at the time, leaving their home country and place of birth, Vietnam, to take me and my uncle (my mother's younger brother) to leave Vietnam as boat refugees. It was a perilous time in the late 1970's and they had to leave everything behind; their home, their valuables and belongings, only to carry what they could on their backs literally. I will save the details for a later time but would summarize their actions brave, courageous, and risky. For them to have left the way they did and I'm not sure if I would have the determination to do the same. I am grateful and thankful to my mother and father for finding the will and way to survive and get everyone safely to our destination, the United States. We arrived here as immigrants in December of 1979. Both my parents were relatively common people – neither of them with any significant amount of schooling, my mother left high school so work at a textile factory so she can take care of her family and my father dropping out of grade school. This made life difficult for them the first few years in a new land, working relatively laborious jobs as a janitor and doing whatever it took to survive and adjust to life in a new land. There are countless examples of their sacrifices throughout the first 18 years of life; my father delivering my daily newspaper route so I can earn money to take computer classes and my mother working late into the night as a stay-at-home sewer (making aloha shirts and shorts). I will leave the stories and details for a later time. The reason why I share this is to make it clear who I am dedicating my degrees too. I wish I dedicate all my success and 3 MIT degrees to my parents, who, through me, have achieved the peaks of education and who through me, will soon possess my third MIT degree, a PhD in Mechanical Engineering.

Next, I will thank individual people(s) who have made a difference in my life in chronological order. My apologies for not prioritizing this list as it is fairly long and I want to make sure I am complete in acknowledging those who have made a lasting difference in my life.

To begin, I would like to acknowledge my siblings, Napoleon and Elizebeth Phan, who are both some of most loyal and loving siblings an older brother can have. To this date, my siblings still acknowledges me in the old fashioned way in Vietnamese traditions, calling me "Anh hai", which literally means brother number two or eldest brother (in Vietnamese traditions, we start with the number two to mean the oldest). They have been good to me over the years. I am proud of the both of them; my sister for her hard work, considerate and caring nature and to my brother, for his courage to face challenges and new experiences. Both in my eyes, are some of the best siblings one can ask for.

In Elementary school, one teacher stands out, or, to be more specific, one Librarian- Ms Muronaga from Lincoln Elementary. Ms Muronaga who pushes to encourage students to be leaders and provides them with the opportunities to shine and be recognized in early in life. Ms Muronaga ran a 'library aide' program where she selects hard working students to aid her in running the library, giving them privileges to leave class early to perform their duties. My particular duty was to take care of the computer lab; to setup and take-down the computers every day at school. This is how I got exposed to working with computers early on – that and taking extra computer programming night classes.

In middle school, two teachers stood out in my eyes, Ms. Oda and Mr. Larson, both from the Science Department at Stevenson Intermediate School. Both of them gave me the opportunity to lead the school's toothpick bridge building team as captain, designing competitions and challenges (Louvee air car), and then recognizing and awarding me the Outstanding Science student award. I am very grateful of their early recognition of my science skills, which only served to encourage me to study the sciences. I am particularly grateful to Mr. Larson for doing two things; 1) he would hold regular games in the class whenever we had spare time to do multiplication challenges where he would ask, what is XX times YY, and the first person to raise their hands would win a point for their side of the class (luckily, I was always the first and then after a while, he would disallow my participation for lack of fairness to the other students) and 2) he showed me a video of the MIT 2.70

challenge in 7th grade where I saw Thomas Massey and Professor Woodie Flowers from MIT, which became my sole obsession and inspiration for getting into MIT (just so I can do the competition). This video became the driving force for the next 6 years of my life, as I competed in competition after competition, year after year, to prepare myself for MIT. Little did I know how difficult it was to get into MIT at the time.

In high school, I had many teachers who supported and natured my education. Three of them stand out in particular; Mr. Lau, Mr. Ching, and Ms. Kadooka. Mr. Lau was my electronics teacher, who came into teaching when I was a junior- he became an advisor for several solar car competitions that I competed in, spending countless hours with the students, helping us design and build our competition machines. Mr. Ching who pushed me to become a better person, who had compassion for a student who physically sub-par, and who trained me to become a decent volleyball athlete. Mr. Ching would make me do push ups and sit ups during recess to build my strength. Over a period of three years, he trained me from a volleyball nobody into an important member of the team where we won the division championship. Mr. Ching spent countless summers training and teaching us how to think competitively on the court. On top of that, he was also a friend and life mentor who taught us to be good people off the court as well. Finally, Ms. Kadooka, who has always been like a second mother to me and taught me Physics. She was always pushing me to think, understand, and learn science in a more intuitive manner. Over the years, she has been one of my biggest believers and supporter. The most memorable event for me from Ms. Kadooka was her gracious letter to MIT on my behalf, where she praised me for being one of her best students- I never forgot this as she has had many students over her career and to be considered one of the best, I was honored and grateful. For all the help through my schooling, I am thankful to my teachers. There are many who have been instrumental in my development in elementary, middle, and high-school. If I have forgotten to mention you specifically, I would like to say "thank you".

I would like to take this brief moment to mention a very old friend of mine, who when I was 17, called him up for a last minute MIT interview, explaining that I was applying early, the deadline was 2 weeks away, and that I needed an interview to complete the early action application. This interviewer and life long friend, is Mr. Richard Lowe, whom over the years have kept in touch with me, supported, and truly believed in me in so many ways. Richard interviewed me, wrote 5 pages of

of gracious comments and somehow influenced MIT admissions enough to get me in early. I am grateful for this life changing event.

I remember leaving for college shortly after I turned 18- arriving at MIT in the Fall of 1994. One of the very first thing I did was join a fraternity, Chi Phi, where I met many brothers and close friends till today. I want to thank the brothers of the Beta Chapter of the Chi Phi fraternity for providing me with a home and environment of friendship and brotherhood, which has helped me grow as an individual and a man.

One particular organization that I would like to thank is the Charles Stark Draper Laboratory, who, throughout my entire undergraduate and half of my graduate years, provided me with both opportunity and funding. In my first year at MIT, I had joined Draper Lab as an intern, working on developing autonomous helicopters- a field where there was no success at the time. Draper has funded and supported the development of an autonomous helicopter, in conjunction with MIT, to compete in the annual International Aerial Robotics Competition. As a freshman, I was fortunate enough to join the team when it was just forming, lead by Bill Hall and Paul DeBitetto. During our first year, we got crushed at Georgia Tech. Our tireless work over the next year resulted in our development of the very first fully autonomous helicopter in 1996, which competed at Disney World. For the first time, we demonstrated a fully autonomous flying helicopter that took off, flew, and landed completely autonomously. These were exciting times and I remember how many countless hours we had to put in to make it work. On one evening, I even realized almost near midnight that I had forgotten that day was my birthday- because we had worked so hard. Paul DeBitetto became my supervisor over the next few years until 1999, when I graduated with an M.S. Draper Laboratory had provided me with a home and environment to learn for 5 years. Even for my second year of my doctoral program, Draper offered me a Draper Fellowship for which I am grateful. Of all my experience and time spent at company, I have spent my most time at Draper Laboratory. I am grateful to all those who have mentored and participated in helping a young kid there.

Next, I would like to thank a number of Professors at MIT. Professor Rohan Abeyaratne, Professor Ernesto Blanco, Professor Leon Glicksman (committee member), Professor Doug Hart (committee member), Professor Timothy Gutowski, Professor David Wallace, ProFessor Borivoje Mikic,

Professor Woodie Flower, Professor Alex Slocum (chairman of the committee), and Professor Sanjay Sarma (committee member); all professors in the Mechanical Engineering Department who have taught me in their classes, given me a grade, and had to endure my questions and "best answer" responses on exams. In particular, I would like to take Professor Alex Slocum, who is the chairman of my doctoral committee and Professor Sanjay Sarma my former thesis advisor (BS/MS) and committee member. Both of these gentlemen, I have known for almost my entire time at MIT. Professor Slocum who taught 2.007 (aka 2.70) when I took his class and won 3rd place, has been an inspirational instructor and good person in life, who works tirelessly to better his students and prepare them for the challenges of life. To Professor Sarma, who have been an academic mentor throughout my entire collegiate career, who have supported my crazy ideas (from miniature LIDAR to drive-by scanning), and has always pushed me to be the best person that I can be. It is rare to have a relationship with one advisor for one's entire academic career spanning over such a long period of time. I would like to personally thank Professor Sarma for all his support, encouragement, and dedication to me and his students through the years. I would like to also thank Professor Douglas Hart and Professor Leon Glicksman, also members of my thesis committee. A special thank you to Professor Glicksman who was especially encouraging and helpful in the topic of heat transfer. His class, 2.52 Modeling and Approximation of Thermal Processes, was particularly helpful in developing an understanding of some of the theory behind my thesis.

Next, I would like to thank the members of the MIT Field Intelligence Laboratory, who have been my friends and academic family over the past 3 years. I would like to particularly thank two members, Dr. Jonathan Jesneck and Dr. Sriram Krishnan. Dr. Jesneck and I worked together to for many of the manual data collection part of the research where we braved the freezing snow and rain to take infrared images and then spent long nights over the summer trying to create a successful multi-frame super resolution algorithm (KSR). We have definitely come a long way since we started working together. Dr. Krishnan, my friend and thesis reader, have been working tirelessly over the last few months, reviewing my work, checking for accuracies, and mentoring me on how to be more academic. He is an "intellectual maven" and a man of many talents. I am thankful for his presence in helping me prepare for my thesis defense.

I would also like to thank my professional colleagues, former and current co-workers, whom I have had a professional relationship with. Many of you have believed and trusted in my leadership and friendship. For that, I am thankful of your support.

I save this for last, because it is the one person I would like to recognize the most; to my wife Laurie Q., who, through the years have continued to support me through all my journeys and challenges, in good times and in bad. She has been pillar of strength and support for which I draw my courage and desire to push forward with the challenges that lay in front of me. She was the person, who encouraged me after being away from MIT for 10 years, to leave Wall Street and return to the Institute to use my skills for good and do something more meaningful in life. I know life with me has been challenging on my wife, but I hope that now that I will be done soon, that she and I will focus on the good times ahead.

If I have missed anyone, please accept my apologies in advance. I know there are many people with whom I have interacted with through the years, worked with, and perhaps even cried with at times. This final thank you that goes out to all those who have helped me along the way, been a part of my life, and have contributed to making me who I am today.

With many thanks,

Long N. Phan

Table of Contents

Table of Figures

Table of tables

LIST OF SYMBOLS

$M_b(\lambda, T)$ = Spectral Radiance of a black body [W/m^2·sr·μm]
M_b = Radiance [W/m^2·sr]
T = Absolute Temperature [K]
k = Bolztmann constant is 1.3806488·10^{-23} J/K
λ = wavelength [m]
h = Planck constant [6.62606957·10^{-34} J·s]
c = speed of light [2.998·10^8 m/s]
c_1 = first radiation constant ($2\pi hc^2 = 3.7418 \times 10^8 W \cdot \mu m \cdot m^{-2}$)
c_2 = second radiation constant ($\frac{hc}{k} = 14{,}388\ \mu m \cdot K$)
σ = Stefan-Boltzmann constant [5.67x10^{-12} W/cm^{2}K^4]
ε = emissivity
ε_N = normal emissivity
r = reflectance
α = absorptance
Q = energy [J]
Φ = radiant flux [W=J/s]
Φ_A = absorbed flux [W]
Φ_R= reflected flux [W]
Φ_{TT}= transmitted flux [W]
A = absorbance coefficient
R = reflectance coefficient
TT = transmission coefficient
$d\Phi$ = radiant power
dA = projected area
$M(\lambda,T)$ = radiant emittance [W/m^2]
$\varepsilon(\lambda, T)$ = total emissivity
ε_λ= grey body emissivity
Ω = solid angle
I_v = intensity of radiation
δv = frequency band
A = area [m^2]
W = energy per second [W]
$E = A\Omega = \bar{A}\bar{\Omega}$ = etendue
$\bar{A}$ = focal plane area
$\bar{\Omega}$ = aperture solid angle
S_{ob}= observed radiance
$R(\lambda)$ = spectral responsivity
C_{th} = thermal capacitance
G_{th} = thermal conductance
ΔT = temperature difference
Φ_o = amplitude of the sinusoidal radiation emittance

$R_{th} = 1/G_{th}$ = thermal resistance
τ_{th} = characteristic thermal response time
NETD = noise equivalent temperature difference [K]
U_n = voltage
ΔU_s = voltage increment
T_{ob} = black body temperature
T_o = background temperature
$NETD_{\frac{1}{f}}$ = 1/f-noise of the bolometer
$NETD_{Johnson}$ = Johnson noise of the bolometer
$NETD_{thermal}$ = thermal fluctuation noise of the bolometer
$NETD_{ROIC}$ = readout integrated circuit (ROIC) related noise
F = F-number of the infrared optics
$\phi_{\lambda 1-\lambda 2}$ = transmission of the infrared optics in the wavelength interval from λ_1 to λ_2,
TCR = temperature coefficient of resistance of the thermistor material
K = 1/f noise constant of the thermistor material
υ = volume of the thermistor material
R_{bol} = resistance of the bolometer thermistor
β = bolometer fill factor
$\varepsilon_{\lambda 1-\lambda 2}$ = infrared absorption rate of the bolometer membrane in the wavelength internal from λ_1- λ_2
f_s = shutter uniformity correction frequency for the bolometer array
f_r = read-out frequency of the bolometer
x_1 = amount of bolometer pixels per column
f_i = the image readout frequency
f_{eff} = effective integration frequency of the bolometer
f_{bol} = thermal integration frequency of the bolometer
τ = thermal time constant of the bolometer pixel
U_{bias} = bolometer bias voltage
R_{ROIC} = input impedance of the ROIC
V_{ROIC} = total noise voltage of the ROIC
V_{amp} = input reference noise voltage of the ROIC
V_Q = input reference analog to digital quantization interval
I_{ROIC} = current noise from the ROIC input including the bolometer bias current source
$\left(\frac{\Delta P}{\Delta T}\right)_{\lambda 1-\lambda 2}$ = temperature contrast in the wavelength interval from λ_1 to λ_2
ω = modulation frequency of the infrared signal
absPixel = value of the pixel post-compensation
LFunc = value of processing characteristic of a linearized function for the raw value *imgPixe*
globalGain and *globalOffset* = constants representing the parameters of the camera's amplifiers in the signal processing path
Obas = base offset used in a nonlinear conversion
L = calibration constant linearizing the raw pixel values
p = raw pixel value
φ_{ob} = flux emitted by the target object
φ_{refl} = flux emitted by the ambient background and reflected from the target object

φ_{atm} = flux emitted by the atmosphere
ε_{ob} = band emissivity of the target surface
M_{atm} = radiant emittance of the atmosphere,
M_{ob} = radiant emittance of the target object,
M_o = radiant emittance of the ambient background
TT_{atm} = band transmittance of the atmosphere
T_{atm}, T_{ob}, T_o = temperature of the atmosphere, object, and ambient background [K].
C = parameter that accounts for the atmospheric damping, the camera's optical system, and the detector's properties
s = observed radiance arriving at the detector
s_{ob} = detector signals that corresponds to the total observed radiance from target object's heat radiation intensity
s_o = total observed radiance of an ideal black body heat radiation intensity at ambient temperature
A, B, and C = constants associated with the camera calibration characteristics
TT_{atm} = coefficient representing the absorption of the infrared radiation by a layer in the atmosphere
d = distance
ω = relative humidity
σ_{RT}^2 = real-time position error variance
σ_{GPS}^2 = GPS position error variance
σ_{IMU}^2 = IMU prediction error variance as a function of time
$\dot{Q}_A$ = heat flux [W/m^2]
s_{image} = signal output from the detector
s_{bgd}= signal contributed by the background environment
ε_{source} = emissivity from the source
s_{source} = signal from an ideal black body source
S_o = radiance detected by the infrared camera
$\tilde{S}$ = total radiance of the black body
T_o = the surface temperature of the object
T_b= the background temperature
T_a = the ambient temperature
τ = the transmission coefficient of the atmosphere
ε_o = the emissivity of the object
ε_r = the emissivity of the reference emitter object
$\frac{\varepsilon}{\varepsilon_N}$ = normalized directional emissivity
Q = maximum bandwidth
Y(k) = observed sequence of K low-resolution images from a camera
D(k) = down-sampling operator, which is also known as the "decimation operator"
H(k) = blurring kernel
$F(k)$ = encodes the motion information of the kth frame, represents the camera movement
X = unknown high-resolution image
$V(k)$ = additive system noise
x_k = row offset

y_k = the column offset
θ_k= angle offset
Y_0 =reference image
I = a two-dimensional impulse function
PSF_{camera} = motion point spread function
I_{super}= super positioned image
s_{total} = total standard deviation
U_{total} = total uncertainty in the system
ψ_E = angular error
v = velocity in displace per time unit in units of pixel/frame
$\vec{v}_c$ = correct velocity vectors in 3D
$\vec{v}_e$ = estimated velocity vector in 3D
v_n = normal velocity
U_ε = total emissivity uncertainty
$U_{\varepsilon,mat}$ = uncertainty in estimating an object's normal emissivity without a priori knowledge
$U_{\varepsilon,\alpha}$ = uncertainty in emissivity related to angular dependencies
U_{T_w} = net effect of uncertainty on the background temperature

Q_e= Radiant energy [J]
Φ_e= Radiant flux [W]
$\Phi_{e\lambda}$ = Spectral power [W/m]
I_e = Radiant intensity [W/sr]
$I_{e\lambda}$= Spectral intensity [W/m·sr]
L_e = Radiance [W/m^2·sr]
$L_{e\lambda}$ = Spectral radiance [W/m^3·sr]
E_e = Irradiance [W/m^2]
$E_{e\lambda}$ = Spectral irradiance [W/m^3]
M_e = Radiant exitance or radiant emittance [W/m^2]
$M_{e\lambda}$ = Spectral radiant exitance or spectral radiant emittance [W/m^3]
J_e = Radiosity [W/m^2]
H_e = Radiant exposure [J/m^2]
ω_e = Radiant energy density [J/m^3]

Chapter 1: Introduction

1.1 Thesis Motivation

This thesis originated from a vision to merge two scientifically rich topics, medical imaging and energy diagnostics. I present a way to image buildings by scanning them from a vehicle on the street, and assigning temperatures to points on surfaces. We refer to this as drive-by thermography. We believe that this approach will be an important first step in analyzing the thermal performance of buildings. The surface temperature maps will enable researchers in the future to perform heat-transfer analysis and definitively determine the inefficiencies in the envelopes of buildings in a scalable and inexpensive way. We do not perform heat transfer analysis in this thesis.

Specifically, we have designed, developed, and deployed an Automated Rapid Thermal Imaging System Technology (ARTIST) based on commercial off-the-shelf technology. In my thesis, I provide a scientific understanding of the technology, present challenges pertaining to both the physics and the engineering of thermography, and describe a way to perform thermography at lower costs and higher speeds.

1.2 Contributions of this Thesis

This thesis focuses on the following topics:

- Multi-camera synthetic aperture imaging system
- 3D Radiometry
- Non-radiometric infrared camera calibration techniques
- Image enhancement algorithms
    - Hyper Resolution
    - Kinetic Super Resolution
    - Thermal Signature Identification
    - Low-Light Signal-to-Noise Enhancement using KSR

The thesis builds on a large body of previous work in thermography. However, drive-by scanning of the type we present here has seldom been tried before. The physics of radiometry and radiation need to be understood and combined to ensure that drive-by scanning is feasible. I present these topics as well. The components are summarized below.

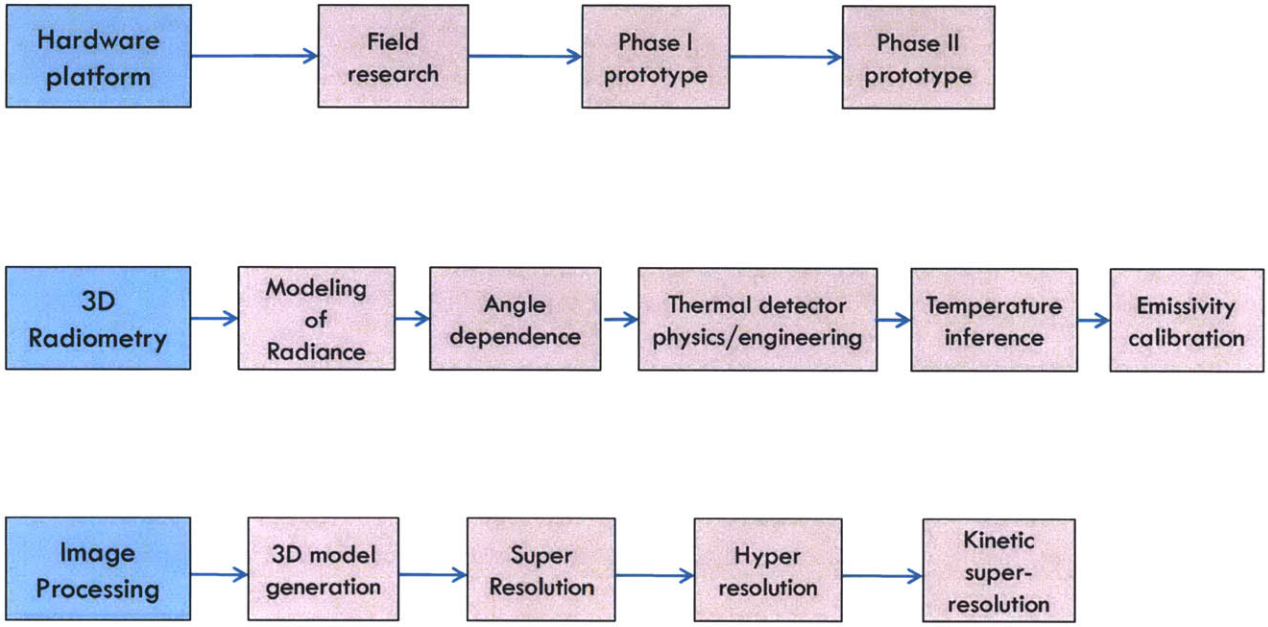

Figure 1: Automated Rapid Thermal Imaging Systems Technology

This research was conducted in the context of a larger team effort. The mechanical conception and design, the camera hardware, the instrumentation, research of the physics and engineering or thermography, and the error budgeting were principally my work. The data collection and software were developed jointly with my colleagues, mainly Dr. Jonathan Jesneck, and at some points with Dr. Liang Chen, Dr. Hui Kong and Professor Sanjay Sarma. In the thesis I acknowledge their invaluable contributions where appropriate. I present the entire body of work here for completeness.

1.3 Approaches to the Problem

There are tools and well-practiced methods to generating a good energy audit report such as LEED Certification [1], but it is costly and time consuming. One very successful tool that has been used by

energy saving practitioners is thermal imaging [2, 3]. Thermal cameras allow one to "see" the energy leaks in the specific wavelength that heat emits thermal radiation. This is accomplished by visually looking for hot spots or areas of large thermal gradients in the image and relating those areas to the physical locations on the structures to identify energy leakage. The problem is that thermal cameras are very expensive and time consuming to operate.

To approach this, I proposed to designed, developed, and deployed an Automated Rapid Thermal Imaging System Technology (ARTIST). In my thesis, I provide the fundamental scientific understanding behind the technology, present challenges and solutions, and show novel approaches, methods, and applications in imaging and synthetic aperture camera design.

1.4 The Energy Problem

An increasing global population will need to fuel that growth with an increased demand for energy – for the production of goods and services, transportation, food and fresh water production, and a host of other energy demanding tasks that ultimately ends at the individual consumption level. From 2004-2020, the projected annual growth rate for energy consumption will be 30% greater than the realized annual growth rate observed between 1986 and 2004 according to the EPA.

Critical analysis has pointed towards 2 generalized solutions to the problem of energy production: Find new sources of energy (finding megawatts) or finding new sources of efficiencies (finding negawatts[1]). This thesis is a step towards finding negawatts.

Building energy consumption comprises 41% of the total annual US primary energy supply according to EIA (2010) [4]. A TIAX [5] report suggests that the majority of buildings stand to improve their energy efficiency by 20 - 30% [6-9]. With buildings responsible for wasting roughly 10% of our national energy supply, residential energy use has enormous savings potential of approximately 6 quadrillion British Thermal Units (BTUs) by 2020 [10]. The reclaimable component of residential energy use remains one of our greatest untapped domestic energy resources which can

[1] The term "Negawatt" is theoretical unit of power representing an amount of energy (measured in watts) saved. The term was coined by Amory Lovins in 1989.

be used to offset our declining oil & gas reserves globally. This unclaimed "Negawatt" reservoir can be viewed as an untapped oil or gas field and represents a substantial source of natural energy supply.

It is estimated that the average home in the US loses up to 35% of the input energy through inefficiencies on the thermal envelope of the building. The aggregate potential energy of all those leaks occurring on the envelope totals approximately 10% of our total annual national energy usage or $100B+ annually in financial terms [11]. The magnitude of this problem serves as further inspiration to this thesis.

1.4 The Energy Audit

Theoretically and practically, it would be cost effective to search and generate negawatts through energy efficiency initiatives. By reducing the need to use energy at the end-user (the home), all the production, generation, and transportation of the same energy to the end-user would be removed. One watt of power at the end-user may require three watts generated at the power plant, additionally reducing environmental pollution and fuel requirements. "Negawatt mining" refers to the methodical and systematic process of identifying the sources of negawatts and extracting them through retrofit remedies, the negawatts that are most cost- and return on investment efficient.

The path to extracting negawatts begins with identifying the potential negawatt energy lost, through energy evaluation processes such as 'energy audits'. Energy audits can come in many forms and varying levels of details, analysis, and recommendations. The more detailed the analysis, the costlier the energy audit becomes both from a financial and time investment point of view. A typical home energy audit is part of a professional service that undertakers use to understand the energy efficiency of house [12]. The audit evaluation process is completed by a professional using tools such as a blower door test or a thermal infrared camera. The goal of an energy audit is to determine and recommend the most efficient methods to improve the energy efficiency of home for heating and cooling.

An energy audit of a home will involve analyzing the different areas of the building envelope, which includes walls, ceilings, floors, doors, windows, vents, and chimneys [13]. Each of these

components will have an effective area and thermal resistance to heat flow (R-value) [14]. Additionally, the leakage rate or air infiltration will be estimated through the blower door test [14]. An energy audit attempts to characterize a building's energy performance so that it's efficiency, physical property and condition, and improvement performance can be reported.

1.4.1 Blower Door Test

A blower door machine is a device used to measure the air tightness of small to medium sized buildings [15]. Blower door tests are typically used by energy auditors to determine the effective air leakage of a home. A blower door is a powerful fan that mounts into the frame of an exterior door [16]. The fan pulls air out of the house, lowering the effective air pressure inside while external air at a higher pressure flows in through all unsealed cracks and openings. The tests determine the air infiltration rate of a building. The pressure differences are tested in the range anywhere between 10 to 60 Pa, although the results are standardized to a difference of 50 Pa (using the standard of cfm50 - cubic feet per minute at a 50 Pascal pressure difference). The ranges of cfm50 are shown in the table below.

House Leakiness Category	cfm50
Tight House	<1,200
Moderately Leaky House	1,200-3,000
Very Leaky House	>3,000

Table 1: Relationship between cfm50 and leakiness of a house (Van der Meer) [17]

Equipped with a house's cfm50, one can approximate the equivalent leakage area (ELA) [18]. The correlation between cfm50 and the ELA in inches squared is about 0.1 [19], meaning that a house with a cfm50 of 1200 would have an ELA of about 120 squared inches. Every air leak on the building envelope contributes to total leakage area of a building. The ELA merges all the smaller leaks into a combined or effect single opening. This value is presented in a way that assumes that the opening is kept open 24/7, 365 days a year. A blower door test can take a few hours for setup and additional for testing.

1.4.2 Infrared Thermography Audit

The advent of high resolution thermography has enabled inspectors to identify potential issues within the building envelope by taking a thermal image of the various surfaces of a building. For purposes of an energy audit, the thermographer will analyze the patterns within the surface temperatures to identify heat transfer through convection, radiation, or conduction. It is important to note that the thermography only identifies surface temperatures, and analysis must be applied to determine the reasons for the patterns within the surface temperatures.

For those who cannot afford a thermal inspection, it is possible to get a general feel for the heat loss with a non-contact infrared thermometer and several sheets of reflective insulation. The method involves measuring the temperatures on the inside surfaces of several exterior walls to establish baseline temperatures. The best manner in which to do this is when the temperature differential (ΔT) between the inside and outside of the structure is at least 20 degrees F [2]. During the condition where the internal temperature of the house is greater than the external ambient temperature, the building will experience various modes of heat transfer, mainly, conduction, convection, and radiation. Dominant modes will become more visually apparent in the thermal images while less dominant modes will exhibit lower surface temperatures. The act of understanding and interpreting the thermal images is still an art. To better understand the problem and develop effective solutions, more emphasis should be placed on a more scientific approach to the problem as a whole.

Figure 2: Sample infrared thermal image of home taken with a FLIR LWIR Camera

1.4.3 Aerial Thermography

The concept of using aerial thermography has previously been proposed as a tool to help find sources of energy leaks in buildings during wide area scans. From above, an infrared camera system would scan the surface of the Earth below and record the coordinates of the scan to create a temperature map of the surface as shown in [20]. Hot areas would be identified as "hot spots" triggering potential further investigations. It has also been proposed that unmanned aerial vehicles be utilized for these tasks as to minimize the operational costs of gathering data. The use of UAV is current impractical and brings up issues such as safety when operating in residential areas. In theory, aerial thermography may sound like a good idea initially because of the wide area potential of the system. However, upon closer examination, aerial thermography is limited by several reasons:

a. Spatial resolution of aerial thermography limited to ~ 3-4 meter/pixel (at 35,000 ft) down to 0.5 meter/pixel at closer distances, making it difficult to identify location of cause of leak.
b. Vertical viewing angle to the target object is limited to normal angle to the roof making it difficult to see energy leaks located on the side of buildings, unless the airplane was very far away from the object with the camera pointed towards the side. This would cause a decrease in spatial resolution due to the longer distance.

c. Long distances from camera to object surface makes atmospheric noise more prevalent.
d. Induced camera shake and image blurring effects from aerial thermography requires fast thermal imaging systems, which requires cooled infrared camera system for high speed imaging. This is both cost and operationally prohibitive.

Although aerial thermography does allow one to capture thermography data quickly and over a wide area, issues such as poor spatial resolution, camera shaking and image blurring, and no direct view of the building envelope on the side makes aerial thermography a very limiting method. Poor spatial resolution ranging from several meters to several feet per pixel makes aerial thermography impractical for detailed thermal inspections.

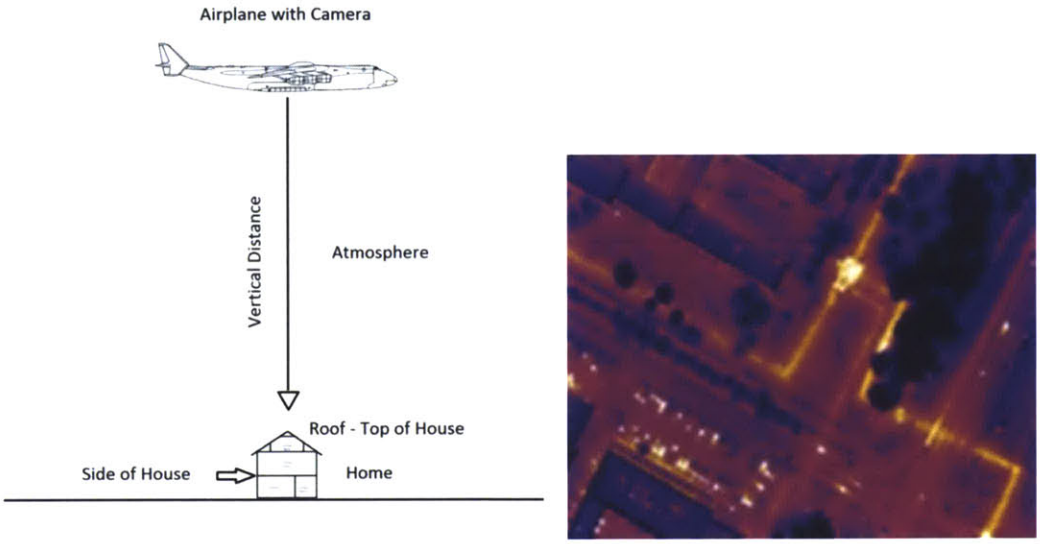

Figure 3: Aerial Thermography Diagram (Left) and Example of Aerial LWIR Image (Right)

1.5 A Case for 3D Radiometry

Thermographic imaging, the science of estimating the surface temperature from an infrared image is poorly understood. At the core of a thermal imager are sensors that model the physical world into photons and electrons that are used to interpret the thermal radiation effects of the environment into a digital signal. LWIR imaging is a well modeled and well understood science from a two dimensional (2D) imagery point of view. It is driven by Planck's law and approximated by the Sakuma-Hattori equations [21] for band limited applications. Thermography is commonly

understood to follow the Lambertian surface approximation, which relates to *Lambert's cosine law*, and the conservation of radiance and etendue. However, some of these assumptions are overly simplified and does not relate well to a real world environment. Emissivity, distance, viewing angle, and surface area of interest are poorly quantified and can either over-magnify or under-estimate the thermal related issues at hand resulting in poor scientific modeling of the actual problems.

Each camera manufacturer utilizes a diverse and specific combination of hardware, electronics, and algorithms to interpret and display the long wave signals as a signal output from the camera. The unique and proprietary nature of each component makes it difficult to understand infrared technology from model to model and maker to maker. Because of the potential uses of the technology, the US State Department has very tight ITAR [22] export controls on the equipment. Due to this and the competitiveness in LWIR technology from different manufacturers, it is extremely difficult to have intimate knowledge of the inner operations of common LWIR cameras.

Not all LWIR cameras are radiometric, meaning they lack the thermography capability of interpreting the digitally measured observed radiance representation of each pixel into an estimated temperature profile. FLIR, a dominant maker and distributor of thermal infrared camera equipment globally, sells both radiometric and non-radiometric cameras according to their website. FLIR's *radiometric* cameras have thermography features and price them differently by a factor of two or more versus the non-radiometric cameras of the similar image quality.

Although there are many types of LWIR imaging technologies, the most cost-effective LWIR technology is based on uncooled microbolometers [23-29]. Due to the high quality and low production cost, uncooled microbolometer technology usage has become explosive in recent years and can be found on most commercial off the shelf thermal cameras. For this thesis, we will focus on microbolometer based LWIR imaging.

The focus of this thesis is primarily around thermography and thermal imaging for the purpose of mapping surface temperature. Energy losses at the surface depend both on the local surface temperature and on the heat transfer processes. Other research groups at MIT and elsewhere are focused on studying heat transfer. I believe having accurate automated temperature mapping would help contribute to future research on urban scale heat transfer studies.

1.6 Layout of Thesis

The ARTIST system consists of 3 core components:

1. Hardware Platform
2. 3D Radiometry
3. Image Processing

In Chapter 2, I will give an overview of infrared theory and discuss both the physics and engineering behind thermal detectors. In this Chapter, I will start with Planck's equation for spectral radiance and show how the Stefan-Boltzmann law is not applicable for band limited (8000 nm-14000nm) applications like infrared thermography. I will show how the Sakuma-Hattori equations, a Planckian form approximation, represented by three variables is used in infrared imaging systems. Additionally, I will discuss the conservation of radiance with distance, how surfaces are non-Lambertian, and show the dependence of viewing angle on emissivity and discuss why 3D radiometry is important.

In Chapter 3, I will give a walk-through of a three step process for how I developed the hardware system behind ARTIST. On the hardware platform, I will discuss my initial field research in infrared imaging and show how I used insights gather to develop a Phase 1 prototype. For Phase 2, I sought to maximize spatial, spectral, and temporal resolution by designing, developing, and deploying a multi-camera synthetic aperture imaging system. I concluded that it was critical for ARTIST to maximize resolution and showed how I developed a multi-camera synthetic aperture imaging system to maximize resolution through spatial, spectral, and temporal domains. I show that the ARTIST hardware platform is a plug-n-play system that can easily integrate with new components, software, and techniques, that over time, will continually evolve depending on the needs of the constraints of the future.

In Chapter 4, I will discuss the concept of 3D radiometry and show how ARTIST implements 3D radiometry using drive-by-imaging data capture. In this Chapter, I show how we use motion information to reconstruct a wireframe model using off-the-shelf optical flow algorithms. Through the 3D models, we can extract distance and viewing angle information to help correct for directional

emissivity. Additionally, I show a method for calibrating for material emissivity using a reference emitter and steps for calibrating a non-radiometric infrared camera for interpreting temperature from grey-scale camera output.

In Chapter 5, with the help of my colleagues, we have implemented several super resolution algorithms (Hyper Resolution and Kinetic Super Resolution) and concepts useful for combining motion-based multi-frame images to super-resolve for a high resolution image. Additionally, I show two additional concepts, Thermal Signature Identification and Low-Light Signal to Noise-Enhancement using KSR for improving imaging quality in low lighting situations.

In Chapter 6, I discuss uncertainty in the ARTIST system based on the following areas- scene uncertainty covering emissivity, background reflections, sensor uncertainty in hardware, and motion uncertainty during drive-by imaging. I will summarize which area of uncertainty is most critical to focus on and discuss methods of mitigation for issues related to each uncertainty.

Chapter 7 concludes this thesis with a summary of contributions, topics of future work, and gaps in the thesis.

Chapter 2: An Overview of Infrared Theory

2.0 Introduction

During a typical operation of drive-by imaging using ARTIST, an IR camera is pointed at buildings and records a video consisting of individual thermal image frames. The radiation emitted from a source – buildings in the case of ARTIST – gets converted by the thermal detector inside an IR camera into a corresponding temperature signal and subsequently displayed as a thermal image to the user. The field of radiation thermometry has grown over the last few decades as a niche research area and as an industry. Many manufacturers have developed radiation thermometers and infrared cameras targeted at a growing range of applications. Manufacturers however provide little detail behind how different IR cameras operate or how the temperature measurements in a particular camera may be affected by properties such as emissivity. I will discuss the physics of IR thermography and the engineering of IR detectors in this chapter. Next, I will show how users can infer the temperature from thermal image output from IR cameras. I will clarify a few misconceptions along the way and argue why emissivity estimation is important and why we must pay close attention to the viewing angle. These insights will help us build a case for 3D Radiometry that is implemented in ARTIST and discussed in Chapter 4. Finally, I will present a brief summary of today's IR camera hardware.

2.1 Why are emissivity and viewing angle important?

Despite being around as an industry for a few decades, there are a few misconceptions about the physics of IR detectors. One might assume that the radiance observed by the IR camera follows Stefan-Boltzmann law. If it were true, then the radiance received would be proportional to the emissivity and to the fourth power of temperature. Alternately, the estimated temperature would depend inversely on the fourth-root of emissivity. Small variations in emissivity would then have a reduced effect on the temperature measurement. However, if emissivity variation is large, as we will show later in this thesis, the effect on temperature measurement would be significant. Hence, emissivity measurement is important.

In practice, Stefan-Boltzmann law only applies when all wavelengths are considered. For the IR band, or any band-limited radiation detector, the original Planck's integral must be evaluated within the wavelength band to estimate the radiance. This cannot be done in closed form, and "fitting" functions have been proposed to relate the radiance received to the source temperature. The radiance incident on the camera aperture is collected by the detector is converted into a voltage signal. The voltage signal is correspondingly counted on an A/D converter. The camera calibration charts specific to each manufacturer would relate the blackbody radiance to the signal count from the A/D converter. Manufacturers deem the calibration parameters and the signal processing within IR cameras proprietary and in such a 'black-box' model of operation, emissivity estimation becomes important.

Next, we clarify some misconceptions about radiation physics. In particular we review the assumption of a Lambertian surface. A Lambertian surface is an ideal diffuse emitter and the radiance of a Lambertian surface is directionally constant. As a result, the emissivity of a Lambertian surface would be directionally constant and under a Lambertian assumption, emitter angle would not matter. Experimental evidence however shows that emissivity has a strong dependence on angle and the angle of the emitter surface impacts the radiance. As a consequence, the **Lambertian surface approximation is not valid and we need to consider the 3D orientation** of the various emitter surfaces when we perform drive-by imaging using ARTIST.

In the initial sections of Chapter 2, we discuss the physics of IR detectors, point out some misconceptions and show how the correct analytical model can only be implemented through calibration. Later in this chapter, we will present an overview of IR detector hardware.

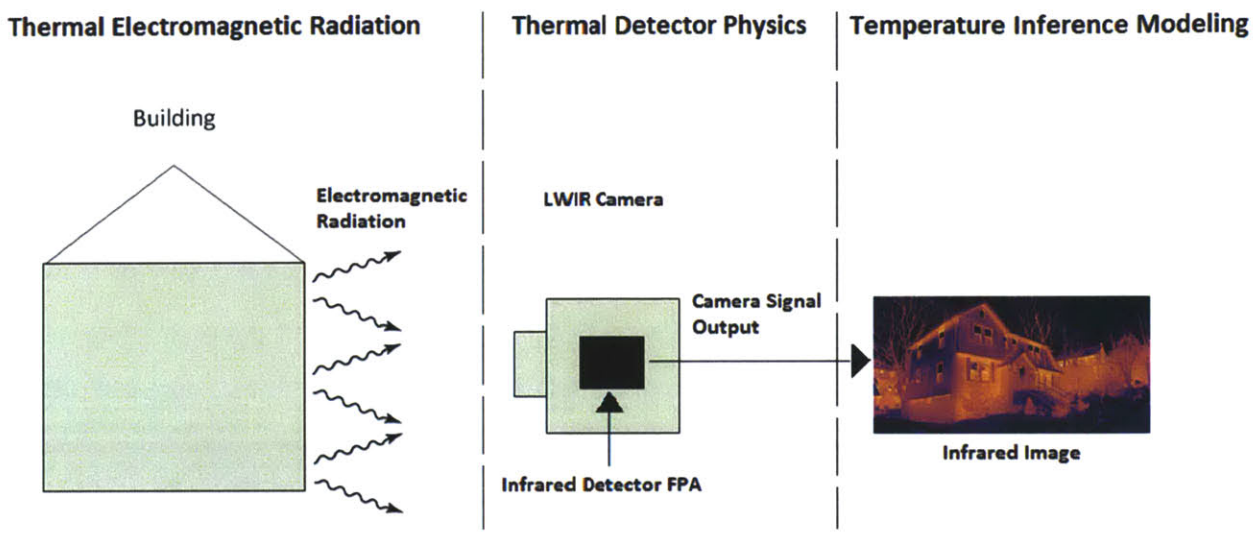

Figure 4: An Abstract view of Infrared Radiation to Imaging

Thermography refers to the science of measuring infrared radiation. The process of thermography is abstracted into three steps: (1) thermal electromagnetic radiation is emitted from a target source, (2) the emitted radiation is detected by a camera sensitive to LWIR wavelengths, (3) output from camera that can be interpreted to infer temperature. This is shown in Figure 4.

2.1.1 An Outline of the Theoretical Background

Planck's law of thermal radiation governs the radiation emitted by any surface. Planck's law relates the spectral radiance of an ideal black-body to its wavelength and temperature. Spectral radiance is the radiance emitted per unit wavelength per unit area of the surface. Planck's equation is given by

$$M_b(\lambda, T) = \frac{2\pi hc^2}{\lambda^5}\left[\frac{1}{e^{\frac{hc}{\lambda kT}} - 1}\right] \quad (1)$$

where $M_b(\lambda, T)$ is the spectral radiance of the black body [W/m^2·μm], T is the absolute temperature [K], k is the Bolztmann constant is $1.3806488 \cdot 10^{-23}$ J/K, λ is the wavelength [m], h is Planck constant is $6.62606957 \cdot 10^{-34}$ J·s, and c is the speed of light is $2.998 \cdot 10^{8}$ m/s [30-33].

Planck's law can be written concisely as:

$$M_b(\lambda, T) = \frac{c_1}{\lambda^5}\left[\frac{1}{e^{\frac{c_2}{\lambda T}} - 1}\right] \quad (2)$$

Where c_1 is the first radiation constant ($c_1 = 2\pi hc^2 = 3.7418 \times 10^8 W \cdot \mu m \cdot m^{-2}$) and c_2 is the second radiation constant ($c_2 = \frac{hc}{k} = 14{,}388\ \mu m \cdot K$).

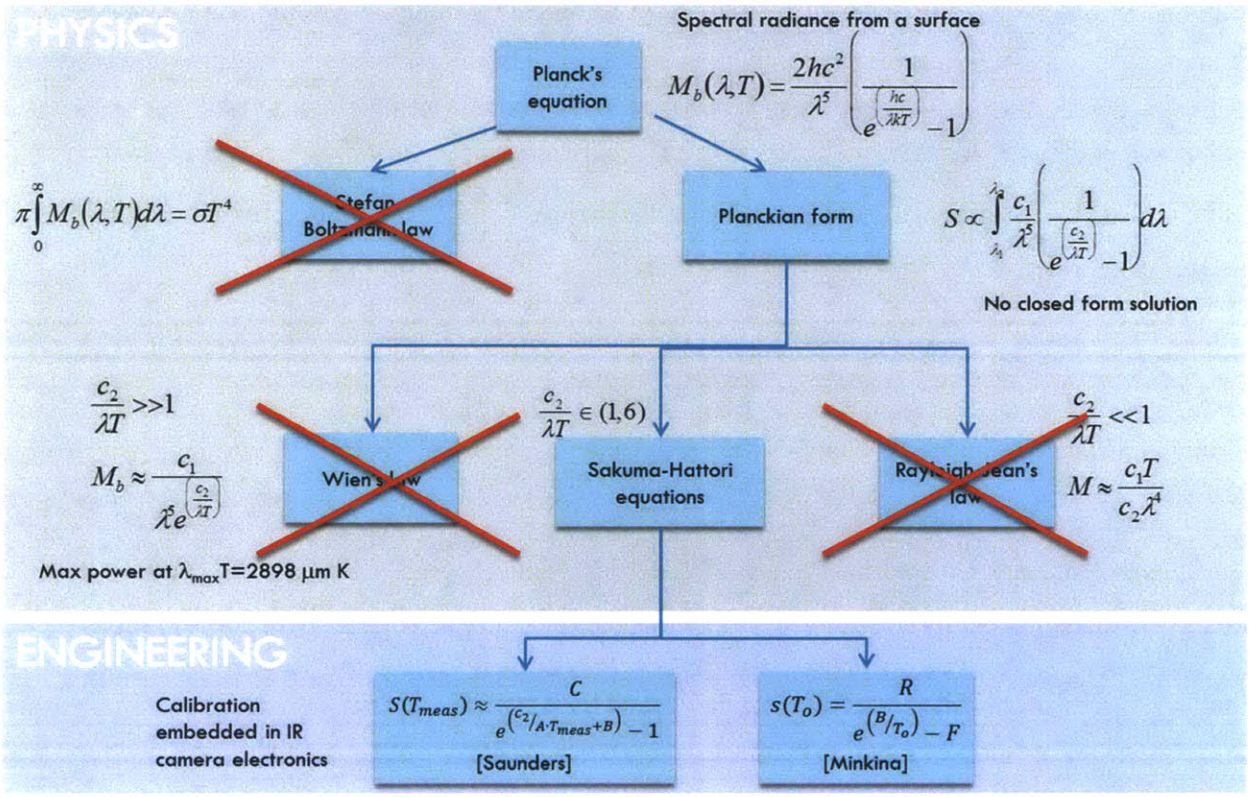

Figure 5: A conceptual walk of the theory behind IR imaging

For a black body, the radiance is independent of angle. Integrating over all solid angles yields the monochromatic emission power which is π times the spectral radiance. To determine the radiance over all wavelengths and all solid angles, we integrate Planck's equation over all wavelengths from 0 to ∞ and obtain Stefan-Boltzmann's law.

$$e_b(T) = \int_0^\infty \pi M(\lambda, T)d\lambda = \int_0^\infty \frac{2\pi hc^2}{\lambda^5}\left[\frac{1}{e^{\frac{hc}{\lambda kT}} - 1}\right]d\lambda = \frac{2\pi^5 {k_B}^4}{15c^2h^3}T^4 = \sigma T^4 \quad (3)$$

$$e_b(T) = \sigma T^4$$, for a black body

$$e(T) = \varepsilon\sigma T^4$$, for a grey body with emissivity ε (as well as non-grey bodies)

Where $e_b(T)$ is the emissive power of the black body [W/m^2], $\sigma = 2\pi^5 k_b^4/15c^2h^3$ is the Stefan-Boltzmann constant and have a value of 5.67×10^{-12} W/cm^2K^4, ε is the emissivity of the object.

However, LWIR detectors are only sensitive to radiation in the wavelength range of 8000 to 14000 nm. Stefan-Boltzmann's law is thus not applicable to IR thermography and one would have to evaluate Planck's integral in a band-limited wavelength range. In IR thermography we have to use the Planckian form,

$$S \propto \int_{\lambda_1}^{\lambda_2} \frac{c_1}{\lambda^5}\left(\frac{1}{e^{\left(\frac{c_2}{\lambda T}\right)}-1}\right)d\lambda \qquad (4)$$

The above expression shows how the received radiance signal is proportional to the Planck's law integral (rewritten using the first and second radiation constants by convention), and the wavelength range of a detector determines the integral limits [21]. The Planckian form in a band-pass setting such as IR thermography does not allow for a closed form analytical solution. Approximation or numerical integration is required.

Within the Planckian form, we analyze further the effect of the term $\frac{c_2}{\lambda T}$ which is found in the denominator. From the basics of heat transfer, we are familiar with approximations to M_b at extreme values of $\frac{c_2}{\lambda T}$.

When $\frac{c_2}{\lambda T} >> 1$,

we obtain the Wien's law approximation. Under a Wien's approximation, the spectral radiance function achieves a maximum at a wavelength λ_{max} such that T = 2898 μm.K. Wien's law is used to estimate the temperature of distant stars based on the radiance observed by narrow-band detectors.

When $\frac{c_2}{\lambda T} << 1$,

we obtain the Rayleigh-Jean's law where the spectral radiance depends linearly with temperature and inverse fourth-power with wavelength. To date, there are no known applications of Rayleigh-Jean's law.

For the range of temperatures that are common for street-level imaging and for LWIR band, $\frac{c_2}{\lambda T}$ would evaluate to be approximately in the range of 1 to 6. As a result, neither Wien's law nor Rayleigh-Jean's law approximations are vaid and we have to work with the Planckian form integral.

Sakuma-Hattori equations are numerical approximations to the Planckian form integral where the integral is curve-fitted to the temperature using three calibration constants. The Sakuma-Hattori equations were first proposed in 1982 as numerical approximation equations for Planck's integral in IR regime [21]. In 1996, Sakuma and Kobayashi evaluated the accuracy of 10 different formulations of such curve-fit equation expressions and found the Planckian form expression,

$$S(T) = \frac{C}{e^{\left(\frac{c_2}{AT+B}\right)} - 1} \qquad (5)$$

to be most accurate [5] . The international standards organization for measurement, BIPM, has used the above format in the uncertainty budget evaluation for its radiation thermometry temperature standard ITS-90.

The calibration constants A, B and C are specific to each detector. A and B are shown to be related to a detector' spectral responsivity function, i.e., the extent to which the detector is sensitive to individual wavelength and C could be related to the emissivity of the detector material. Saunders has

shown that the calibration constants in Sakuma-Hattori equations are related to mean wavelength of the detector and the standard deviation of the spectral responsivity function [34].

Different camera manufacturers utilize different versions of the Sakuma-Hattori equations. Camera manufacturers do not publish the calibration constant values for their particular detectors either. There have been reviews of commercially available camera hardware indicating that nearly 16 camera manufacturers have implemented a calibration similar to the Sakuma-Hattori equation shown above. Minkina has also reported a similar, yet different calibration equation that could be used to calibrate thermal detectors [35-37].

In practice, just like any digital camera, the calibration and the detector physics are built within the electronics of the IR camera and its firmware. What the user sees as an output is a thermal image of the scene (for an IR camera) or a temperature read-out (for an IR thermometer).

The output of a thermal infrared camera could have two possible formats:

1. An output file of the measured radiance signal(s) received by the detector
2. An output file depicting a false color map representative of the temperature profile of the scene.

In the first case, if the output of a detector is purely a measure of radiance, a thermal model is applied to interpret the measured radiance signal into an estimate of the remote object's surface temperature. It is computed based on a number of variables that include the object's emissivity, environment conditions, and factory calibrated parameters that are applied to the thermal model to interpret the temperature. In the second case, a false color image will be produced depicting a color map that is representative of the surface temperature profile, typically shown in linearized form. In our experience, we find that camera manufacturers are very private about the type of radiance model used and the associated calibration parameters. In the literature, we find references that show different calibration models that are implemented currently in thermal detectors: (a) Minkina model [35] and (b) Saunders model [34].

The above detailed discussion of the detector physics is necessary to better appreciate the importance of emissivity measurement in ARTIST. In a later section, I will correct another common misassumption relating to Lambertian surfaces and show why viewing angle is important in ARTIST. Combining these two arguments, I build a case for 3D Radiometry which is implemented within ARTIST. Details of 3D Radiometry are in Chapter 4.

2.2 A Primer on Radiance

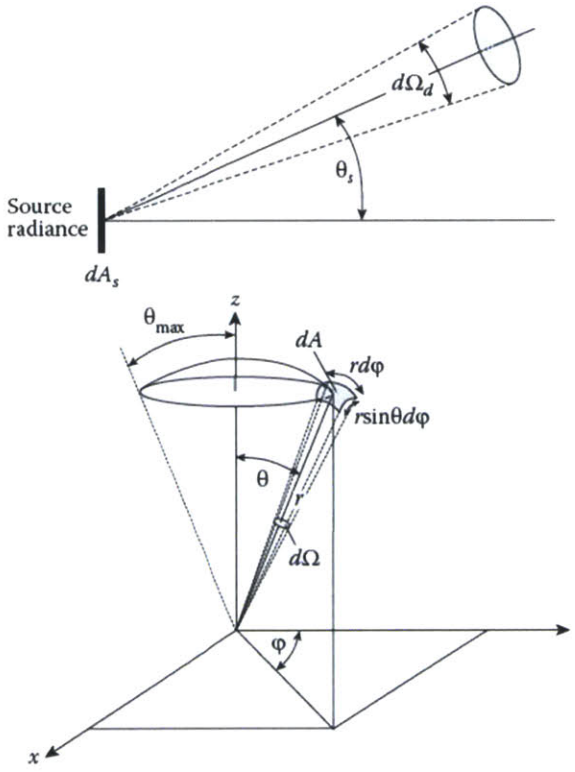

Figure 6: Coordinate system for radiance and irradiance (From Rogalski [37], with permission)

2.2.2 Basic Definitions

Heat flux Φ or radiant flux is the energy Q (J) radiated by a source per unit time in all directions above the source:

$$\Phi = \frac{dQ}{dt} \quad (6)$$

The unit of radiant flux is in Watt. If this radiant flux falls onto a surface of body, that flux will be absorbed (Φ_A), reflected (Φ_R), and transmitted (Φ_{TT}) across the body of the surface. They are defined as absorbance coefficient A, reflectance coefficient R, and transmission coefficient TT:

$$A = \frac{\Phi_A}{\Phi}, \quad R = \frac{\Phi_R}{\Phi}, \quad TT = \frac{\Phi_{TT}}{\Phi} \tag{7}$$

When radiant energy is incident on a surface, energy is conserved in the form of:

$$A + R + TT = 1 \tag{8}$$

The ratio of radiant power $d\Phi$ to a projected area dA (from the source), is called the radiant emittance (the term radiant emittance is used synonymously with radiant exitance when discussing emitted radiation) $M(\lambda,T)$:

$$M(\lambda, T) = \frac{d\Phi(\lambda, T)}{dA} \tag{9}$$

Where the radiant emittance $M(\lambda,T)$ is expressed in W/m^2.

2.2.2 Black body vs Grey body Assumptions

In dealing with Planck's law, we have assumed that the surface of the objects we are discussing are black bodies where the emissivity is unity ($\varepsilon_b = 1$). In practice, the surface of real objects have emissivity values < 1 which affects the amount of energy radiating from the object. For Planck's law and black body assumptions, the radiant emittance for a fixed temperature and wavelength can be calculated from the law's governing equations. However, under real conditions where $\varepsilon < 1$, Planck's law serves only to as an upper bound estimate of radiant emittance. Unfortunately, most physical bodies have limited absorbing capacity and therefore, would not satisfy Planck's postulate for a "perfect black body". In these cases, many are called 'grey bodies'. A grey body is surface that emits radiation at the same spectrum as a black body at the same temperature but with less intensity and emissivity ε does not vary with wavelength λ. For a surface, the ratio of diffuse grey body emittance and black body emittance at the same temperature is defined as the monochromatic

emissivity, which is dependent on λ and T. When evaluated at a particular viewing angle, we get monochromatic directional emissivity:

$$\varepsilon\,(\lambda, T, \theta) = \frac{M(\lambda, T, \theta)_{grey}}{M(\lambda, T)_{black}} \quad (10)$$

I summarize the key differences for a black vs grey body:

1. A black body is a body who's emissivity value = 1. A black body's emissivity is unity and is invariant to wavelength and angle.
2. A grey body is a body who's emissivity value $\varepsilon_{grey-body} < 1$. A grey body's emissivity is constant and is invariant to wavelength.

Black and grey body assumptions are based on ideal property assumptions just described. In practice, materials do not exhibit black or grey body properties as described.

According to Kirchhoff's law of thermal radiation, directional emissivity and spectral directional absorptance are equal for a grey body emitter.

$$\varepsilon(\theta, \varphi) = \alpha(\theta, \varphi) \quad (11)$$

Where θ and φ are the angular coordinates. Energy conservation and the assumption of zero transmissivity means that the sum of absorptance and reflectivity is 1. Therefore, the sum of the emissivity of a material, at a given temperature and the directional hemispherical reflectivity equals one. In the general form of Kirchhoff's law :

$$\varepsilon_\lambda(\lambda, \theta, \varphi) + r_\lambda(\lambda, \theta, \varphi) = 1 \quad (12)$$

Where λ is the wavelength. As an engineering approximation for LWIR, we write:

$$\varepsilon + r = 1 \quad (13)$$

Where the respective terms are likely averaged over the wavelength band of the camera. This approximation does not hold in general, if we consider the effects of transmissivity.

2.2.3 Conservation of Radiance

Long wave infrared cameras measure radiance. Radiance is defined as the radiant power per unit source area, per unit solid angle that the detector subtends at the source (the term radiance is synonymously used as 'intensity' in heat transfer). Radiance is also defined as the radiant power entering the detector, per unit detector area, per unit solid angle subtended by the source at the detector. Radiance can be written as:

$$\text{Radiance} = \frac{\text{Radiant Flux}_{detector}[W]}{Area_{dectector}[m^2] \cdot \Omega_{source}[sr]}$$

Where radiance is the what the camera measures [W/m^2·sr], radiant flux is in [W], $\text{Area}_{\text{detector}}$ is the foreshortened or projected area of the detector [m^2], and Ω_{source} is the solid angle subtended from the source to the detector [sr]. The foreshortened area is related to the actual area by the cosine of the viewing angle θ. It is well-known in radiation physics that radiance is conserved. In Chapter 4, I will present data from our experiments where we find evidence that radiance is conserved in Figure 96. We discuss the conservation of radiance below.

As the source moves further away from the detector, the radiant flux from the source arriving at the detector decreases by inverse square law. At the same time, the solid angle that the source subtends at the detector also decreases with the inverse square of distance (by definition). As a result, the effects of the inverse square law on radiant flux and solid angles between the source and detector, cancels out, making observed radiance distance invariant and is unaffected by distance. Hence, we say that radiance is conserved.

Conservation of radiance implies that, barring losses from transmission, there is no distance dependency for the radiance signal that an IR camera receives from an object.

Next, I will describe the concept of etendue [38] which is a property of the optic system, also called the AΩ product or the collecting power of the optic system

2.2.4 Etendue

Etendue equals the foreshortened or projected area of the source times the solid angle subtended by the detector. Etendue is also equal to the foreshortened or projected area of the detector times the solid angle subtended by the source. The foreshortened area is related to the actual area by the cosine of the viewing angle θ. This is often referred to as the conservation of etendue. Although the terminology may be unfamiliar to many, the conservation of etendue shows up as the law of reciprocity of view factors in heat transfer theory.

Let us consider a source of light from a focal plane, whose area $\bar{A}$ uniformly emits radiations of intensity I_v (W/sr), the flux at a given wavelength per solid angle, with a frequency band of δv. The total amount of energy per second W reaching the entrance of pupil of foreshortened area A [m^2], positioned at a distance d [m] from the source, which is represented by the inverse square law is:

$$W = \frac{A \cdot \bar{A}}{d^2} I_v \delta v \tag{14}$$

The solid angle Ω represents the field of view:

$$\Omega = \frac{\bar{A}}{d^2} \tag{15}$$

Therefore, total energy W becomes:

$$W = A\Omega I_v \delta v \tag{16}$$

The product of $A\Omega$ is called optical Etendue which is an invariant quantity through a perfectly transmissive optical system. The etendue, E is invariant:

$$E = A\Omega = \bar{A}\bar{\Omega} \tag{17}$$

Where $\bar{A}$ is the focal plane area, $\bar{\Omega}$ is the aperture solid angle, A is the pupil area, and Ω is the field solid angle.

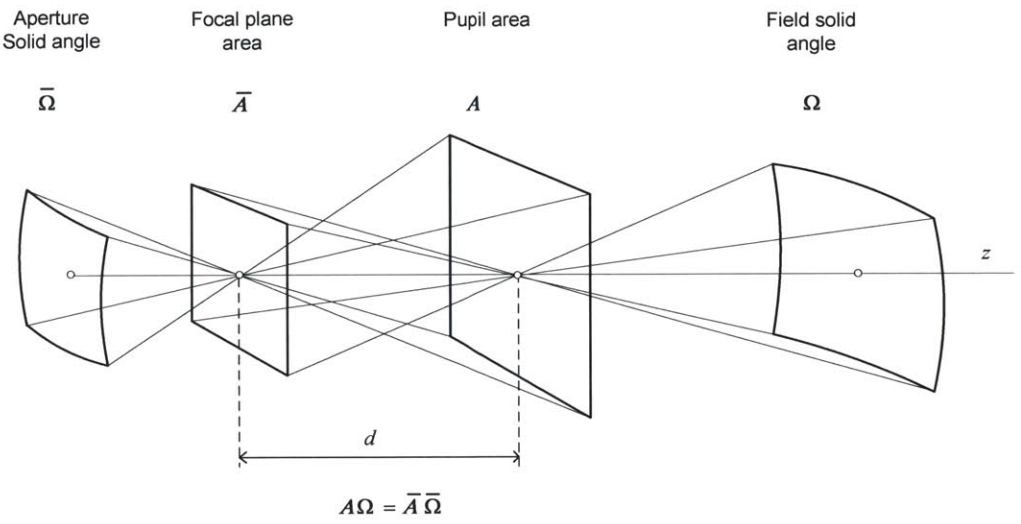

Figure 7: The optical Etendue invariant through a perfect system

2.3 Angle Dependence and Emissivity Modeling

2.3.1 Specular vs Diffuse Surfaces

All electromagnetic waves follow the law of reflection. For specular reflection, an electromagnetic wave will reflect in a manner that the angle of incidence is equal to the angle of reflection. This behavior exhibits a mirror-like reflection of waves from a surface and produces similar effects for light rays as well as electromagnetic waves and non-electromagnetic waves.

Another mode of reflection is 'diffuse reflection' where the incoming light or electromagnetic wave is reflected in a broad range of directions. The most direct way to think about the difference between specular versus diffuse reflection would be to compare the difference between glossy and matt paints. Glossy paints exhibit both specular and diffuse reflection while matte paints exhibit primarily diffuse reflection.

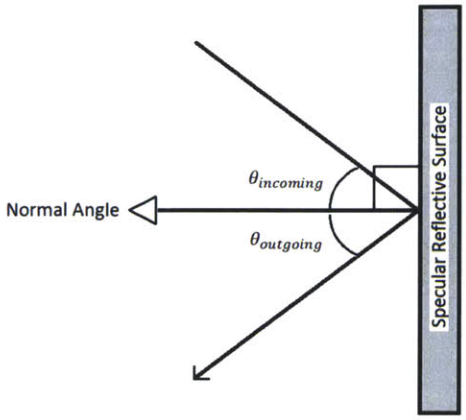

$$\theta_{incoming} = \theta_{outgoing}$$

Figure 8: Radiant flux for a specular reflective surface

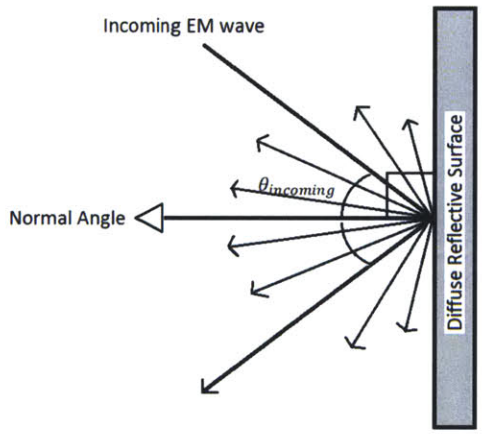

Figure 9: Radiant flux for a diffuse reflective surface

In reality, most objects and surfaces exhibit a mix of specular and diffuse reflective properties.

2.3.2 Lambert's Cosine Law & Lambertian Surfaces

In many cases, the term "Lambertian surface" and "Lambert's cosine law" is often used to inadvertently and perhaps incorrectly, describe long wave infrared imaging and its underlying principles. Lambert's law states that when viewed from any angle, a Lambertian surface will exhibit the same radiance. The corollary of a Lambertian surface assumption is Lambert's cosine law, which

states that radiant flux [W] depends on $\cos\theta$, where θ is the observed emission angle. Lambert's law assumes an ideally diffuse surface, which is the case for both black and grey bodies by definition. In this section, we will clear up some confusion regarding these assumptions.

A Lambertian surface has constant radiance, which is independent of viewing angle and follows Lambert's cosine law for radiant flux (W). Lambert's cosine law is not universal; it is only applicable to Lambertian surfaces. As described earlier in Section 2.2.2, a black body is an ideal surface where the emissivity $\varepsilon = 1$, is Lambertian, and has constant radiance which is independent of viewing angle. A Lambertian grey body is follows a black body assumption, except its emissivity $\varepsilon < 1$, is Lambertian, and has constant radiance independent of viewing angle. The only difference between a black body and a grey body is that a black body's emissivity is unity while a Lambertian grey body's emissivity is less than 1. All black bodies are Lambertian, but a Lambertian surface need not be a black body.

In practice, most surfaces exhibit a radiance that has angle dependence; hence, the Lambertian surface assumption is not valid. The angle dependence of radiance does not violate the law of conservation of radiance as the conservation law primarily deals with the effect of distance. In order to capture the deviation of radiance with angle as compared to an ideal black body's radiance, the parameter called emissivity (normal or directional, as appropriate) is introduced. Directional emissivity is a parameter that captures the variations in radiance of common surfaces with respect to the equivalent black body radiance at specific angles. Normal emissivity alone can be regarded as a material property as it has been shown with experiments to be repeatable with a finite error band. Directional emissivity shows considerable variance in the angle from 60 to 90 degrees, as we will discuss in the following section in the Chapter.

Lambert's assumption and its limitations have been reported in textbooks [39-41]. However, instead of providing more discussions on the angle dependence of emissivity, many authors instead talk about Lambertian surfaces and the analysis of Lambertian surfaces. This might be because the math for Lambert's cosine law allows for a more simplified modeling.

I would also like to clarify the difference between emissions, which refers to radiant flux (W) vs radiance ($W/m^2 \cdot sr$). Emissions for Lambertian surfaces alone, follows Lambert's cosine law while radiance is constant. The signal measured by infrared detectors is radiance, not radiant flux.

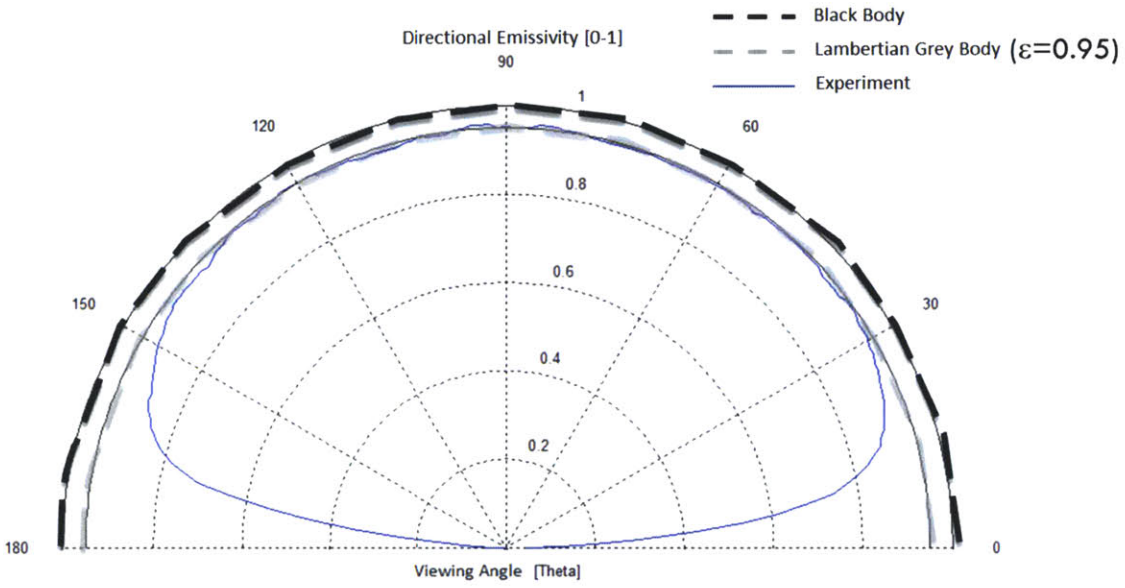

Figure 10: Black Body, Lambertian Grey Body, and Observed Non-Metal Direction Emissivity vs Viewing Angle

The Figure 10 above describes three situations: black body ($\varepsilon = 1$), a Lambertian grey body ($\varepsilon = 0.95$), and observed emissivity for a non-metal material ($\varepsilon_{normal} = 0.95$) vs viewing angle. The important insight from this is that the material does not behave uniformly for all viewing angle as expected for a grey body assumption. It can be considered reasonably uniform for viewing angle $\theta < 60°$ and non-uniform for viewing angle $\theta > 90°$.

2.3.3 Directional Variation in Emissivity

According to research done by Schmidt and Eckert 1935 [42], Fehlman and Hinders 2009 [43], and Cardone & Ianiro 2011 [44], there is an element of directional emissivity, shown in their data. In Figure 11, Schmidt and Eckert showed directional emissivity as a function of angle θ for different materials and thus, $\varepsilon(\theta)$ = varies. As shown in the Figure, at angles $\theta < 60°$, non-metal materials have an almost constant emissivity. At $\theta > 60°$, emissivity drops significantly, with respect to angle. Most infrared camera calibration experiments are done where $\theta \sim 0°$ or normal to the surface, thus, this can be defined as normal emissivity. However, others including Fronapfel & Stolz 2006 [45], have conducted and written experiments where $\theta = 0$, 45, 60, and 75° viewing angles and have confirmed the presence of angular emissivity variations. Commercial off-the-shelf infrared cameras have optical field of view between 10° to 40°.

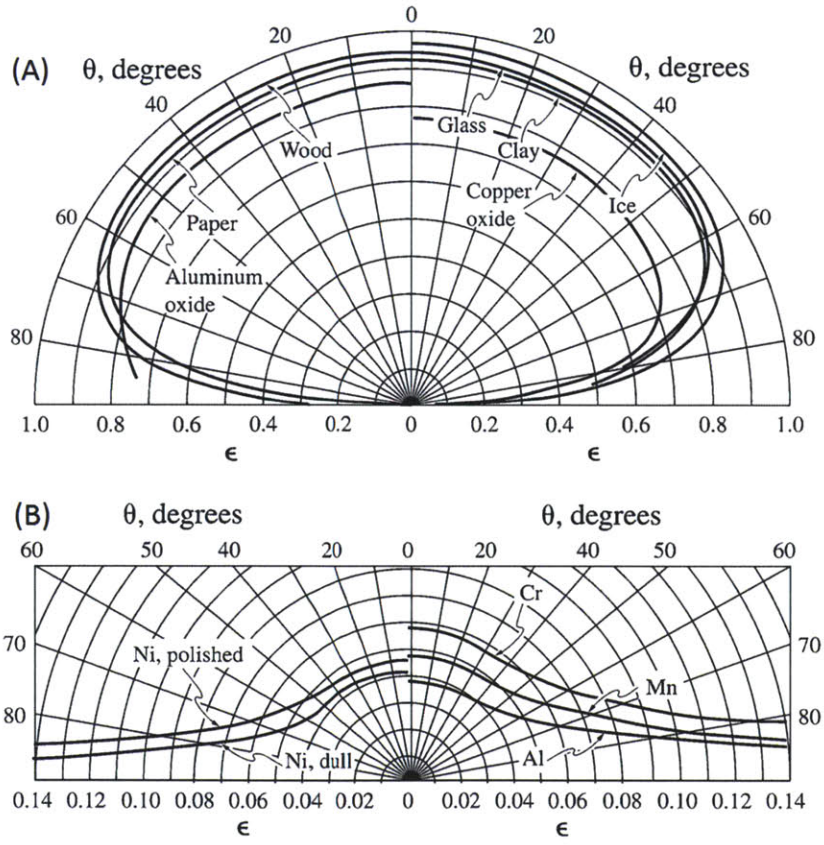

Figure 11: Directional emissivity variation with angle θ for (A) non-metal surfaces (B) metal surfaces. (From Schmidt & Eckert 1935 [6], with permission from Publisher)

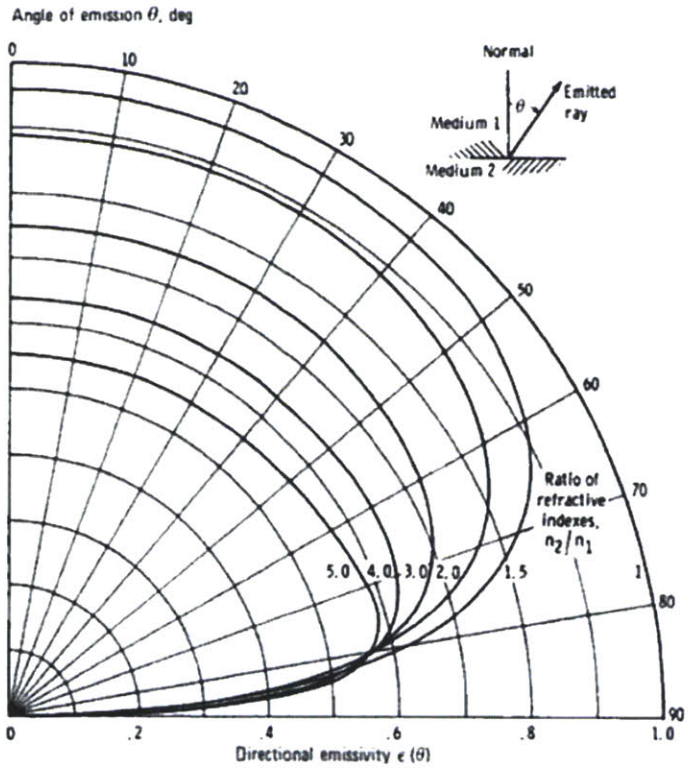

Figure 12: Directional emissivity predicted from electromagnetic theory from Siegel & Howell [46]

Figure 11 shows the importance of understanding how ε(θ) varies. This is necessary in situations when working at high angle θ's where the understanding between ε and θ must be accurately known. We will take a closer look at the topic of directional emissivity in Chapter 4: 3D Radiometry.

From Figure 11, the important insight is that from an emissivity perspective, materials behave differently for metals versus non-metals. From Figure 11(A), a chart of non-metals, which includes materials such as paper, aluminum oxide, wood, glass, clay, copper oxide, and ice, directional emissivity decreases from the normal emissivity value ($\theta = 0°$). However, for metals in Figure 11 (B), such as polished nickel(Ni), dull nickel(Ni), aluminum(Al), manganese(Mn), and chromium(Cr), directional emissivity seems to increase with angle ($\theta > 40°$) vs the normal emissivity.

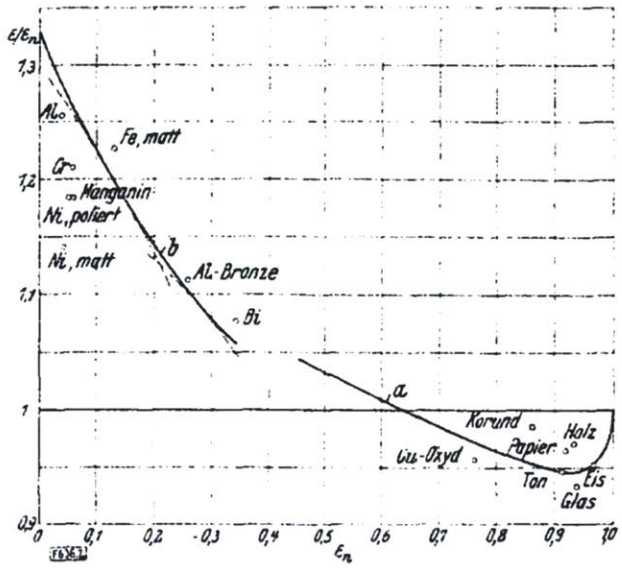

Figure 13: Normalized emissivity $\frac{\varepsilon}{\varepsilon_N}$ y for non-metal and metal materials.
(From Schmidt & Eckert 1935 [42], with permission from Publisher)

One important insight in the Schmidt & Eckert paper [42] that is commonly overlooked is a second chart (Figure 13) that shows the normalized emissivity $\frac{\varepsilon}{\varepsilon_N}$ which is consistently uniform for non-metals (within 6%) and varies widely for metals (> 30%):

$$\frac{\int_0^{\pi} \varepsilon_\theta \cos\theta \, d\theta}{\int_0^{\pi} \varepsilon_N d\theta} \approx 0.94 - 1.00, \text{ Non-Metals} \quad (18)$$

$$\frac{\int_0^{\pi} \varepsilon_\theta \cos\theta \, d\theta}{\int_0^{\pi} \varepsilon_N d\theta} \approx 1.10 - 1.30, \text{ Metals} \quad (19)$$

For non-metals, there seems to be a geometric consistency in the impact of for directional emission variation. In Figure 12, we show a chart from Siegel & Howell [46] for predicted directional emissivity from electromagnetic theory. Here, directional emissivity is shown as a function of the ratio of refractive indices at an interface. Schmidt & Eckert's [42] results were based on experimental data while Siegel & Howell [46] showed theoretically derived predictions. The results of between observed and predicted seems to confirm one another and suggests that directional emissivity can be predicted for ideal surfaces.

A table of normalized emissivity values for common building surface materials is attached in Appendix A for 126 common building materials. From an initial analysis, a histogram chart was created to show the distribution of normalized emissivity values in Figure 14. The insight from this analysis shows that a majority, over 80%, of common building materials have relatively high emissivity values above $\varepsilon_{high} > 0.70$. Only about 10% of the materials listed have emissivity values below $\varepsilon_{low} > 0.50$.

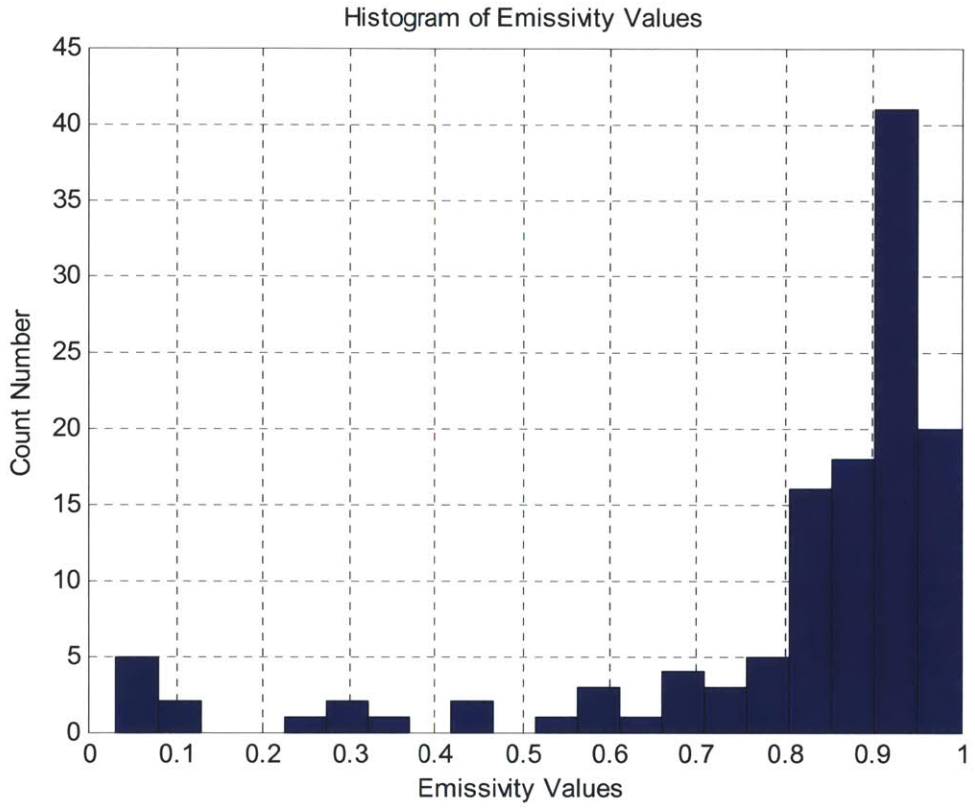

Figure 14: Histogram of normalized emissivity values based on 126 common building materials listed in Appendix A

2.3.4 A Case for 3D Radiometry

We find in many instances in recent literature and industry practices that thermography is based on 2D radiometry principles- which can be simplified into two core assumptions: (a) the use of a constant emissivity value for all points on a long wave infrared image and (b) a fixed distance to all points on an image, regardless of geometry. Although we have discussed the conservation of

radiance, making radiance distance invariant, the surface area of the target surface must be normalized using viewing angle and distance information. 2D radiometry assumptions can fail in situations where the scene is complex and view is not normal to the surface. We will discuss this in detail and show examples in Chapter 4: 3D Radiometry.

From the discussion thus far, we summarize the following:

1. Angular dependency of emissivity has been reported in the literature. The most often cited reference dates back to 1935, based on the experiments by Schmidt and Eckert.
2. The Lambertian surface approximation is not valid for all situations.
3. Drive-by imaging of an urban environment involves 3D scenery both in the buildings, the ambience and their orientation.

Therefore, to properly model the three dimensional environment, I develop the concept of 3D radiometry and how it is implemented within the ARTIST in Chapter 4. 3D radiometry refers to the process of modeling the 3D environment using sources like drive-by imaging to extract viewing angle and distances from the model. In doing so, we can correct for the effects of directional emissivity and normalizing surface areas.

2.4 Thermal Detector Physics

Thermal detector physics refers to the physical modeling of the electromagnetic waves from the source to target detector. For thermography applications, the sensors and sensor components are specifically chosen to operate at wavelengths sensitive in the 8000-14000 nm range. LWIR has higher sensitivity to radiance from objects at or near the ambient temperature and much better transmission through mist and smoke. From Figure 15, we show the emittance ratio $M_{[8\text{-}12\ \mu m]}/M_{[3\text{-}5\mu m]}$ against temperature for ranges from 270°K to 400°K. One can see that at ambient temperatures near 300°K, LWIR [8 – 12 μm] has a higher emittance vs MWIR [3-5 μm] emittance by a ratio of over 20 to 1.

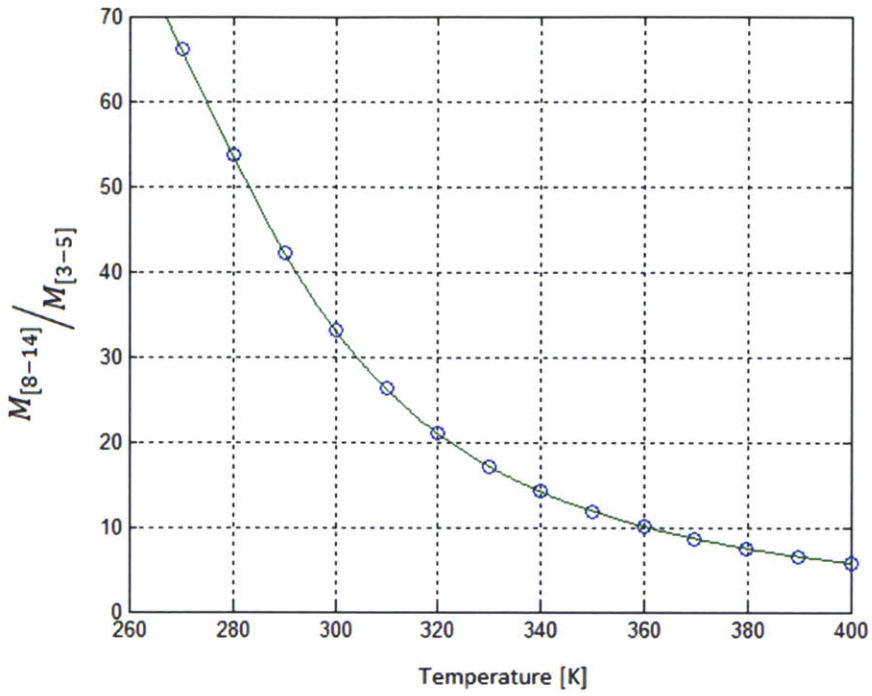

Figure 15: Emittance Ratio $M_{[8\text{-}12\ \mu m]}/M_{[3\text{-}5\mu m]}$ against temperature based on Planckian form integral.

2.4.1 Planckian Form is necessary to model IR thermography

In IR thermography, we use the generalized form of Planck's equation for band limited applications (typically operating in wavelengths of 8000-14000 nm) based the Sakuma-Hattori equations [21]:

$$M_b(T,\lambda) = \frac{c_1}{\lambda^5 \cdot \left[e^{\frac{c_2}{\lambda \cdot T}} - 1\right]} \quad (20)$$

$$S_{ob} = \int_{\lambda_1}^{\lambda_2} R(\lambda) \cdot M_b(T,\lambda) d\lambda \quad (21)$$

Where $M_b(T,\lambda)$ is expressed in [W/m^2·sr·μm], the first radiant constant $c_1 = 2\pi hc^2 = 3.741 \cdot 10^{-16}$ Wm^2, and the second radiant constant $c_2 = hc/k = 1.438 \cdot 10^{-2}$ mK, and $R(\lambda)$ is the spectral responsivity of the detector.

As a recap from earlier in this chapter, I show below the two well-known approximations based on the limits of the value for $\frac{c_2}{\lambda \cdot T}$, and how they are not applicable. The IR detector sums up the emitted

irradiance of the source for the wavelength range of LWIR (8000—14000 nm). For thermal imaging, the temperature range varies for buildings, T ≈ 300°K (ambient) – 1000°K (industrial applications).

The wavelength range for LWIR is 8000 nm to 14000 nm. At this range:

$$\frac{c_2}{\lambda \cdot T_{max}} = \frac{0.01438\ \mathrm{m \cdot K}}{8 \cdot 10^{-6}\ m \cdot 300K} \sim 6.0$$

$$\frac{c_2}{\lambda \cdot T_{min}} = \frac{0.01438\ \mathrm{m \cdot K}}{14 \cdot 10^{-6}\ m \cdot 1000K} \sim 1.0$$

For thermal imaging applications, the resulting values $\frac{c_2}{\lambda \cdot T} \in (1,6)$ are outside of those required for Wien's law or Rayleigh-Jeans law approximation.

Case 1) $\frac{c_2}{\lambda \cdot T} >> 1$: Wien's displacement law

$$M_b(\lambda, T) \approx \frac{c_1}{\lambda^5 \cdot e^{\frac{c_2}{\lambda \cdot T}}}, \text{ with a peak at } \lambda_{max} \text{ such that}$$
$$\lambda_{max} T = 2898\ \mu m K \qquad (22)$$

Case 2) $\frac{c_2}{\lambda \cdot T} << 1$: Rayleigh-Jean's law

$$M_b(\lambda, T) \approx \frac{c_1}{\lambda^5 \cdot \left[\frac{c_2}{\lambda T} + \frac{1}{2!}\left(\frac{c_2}{\lambda T}\right)^2 + \cdots\right]} = \frac{c_1}{c_2} \cdot \frac{T}{\lambda^4} \qquad (23)$$

For Case 1, Wien's law and deals with the wavelength at which the function $M_b(\lambda, T)$ law approximated from Planck's law (when $c_2/\lambda T \gg 1$), is at a maximum:

$$\frac{dM_b(\lambda, T)}{d\lambda} = \frac{d}{d\lambda}\left[\frac{c_1}{\lambda^5 \cdot \left[e^{\frac{c_2}{\lambda \cdot T}}\right]}\right] = 0 \qquad (24)$$

This will determine the wavelength λ_{max} for the radiant emittance of a black body at a given temperature T reaches a maximum. The equation can be solved to obtain:

$$\lambda_{max}T = 2898\ \mu mK \tag{25}$$

Where λ_{max} is the peak wavelength, T is the absolute temperature of the black body, and $b = 2898\ \mu mK$ is a constant of proportionality, also called Wien's displacement constant. Wien's law is commonly used to estimate the temperature of a distant star using it's spectral radiance.

For Case 2, The Rayleigh-Jeans law is a further approximation of Planck's law for conditions where $\lambda T \gg c_2$. In this situation, $M_b(\lambda, T)$ is expanded into a series:

$$e^{\frac{c_2}{\lambda T}} - 1 \approx \frac{c_2}{\lambda T} + \frac{1}{2!}\left(\frac{c_2}{\lambda T}\right)^2 + \cdots \tag{26}$$

When the higher order terms are neglected, the following Rayleigh-Jeans formula expresses the radiant emittance of a black body when $\lambda T \gg c_2$:

$$M_b(\lambda, T) \approx \frac{c_1}{c_2} \cdot \frac{T}{\lambda^4} \tag{27}$$

Although Rayleigh-Jeans law allows for a simplified equation for $M_b(\lambda, T)$, there are not many direct applications for Rayleigh-Jeans law.

As a result, we have to use Planck's equation or its alternate Planckian form in IR thermography. The observed radiance detector signal is:

$$S(\lambda_1, \lambda_2) \propto \int_{\lambda_1}^{\lambda_2} \frac{R(\lambda)c_1 d\lambda}{\lambda^5 \cdot \left[e^{\frac{c_2}{\lambda \cdot T}} - 1\right]} \tag{28}$$

Where $S(\lambda_1, \lambda_2)$ is the observed radiance detector signal received from the infrared camera. The integral on the right can only be numerically evaluated.

According to Dewitt and Nutter [47] and Saunders 2008 [34], one can show the approximate dependence of spectral radiance on temperature, as proportional to an exponent x of the temperature:

$$M_b(\lambda, T) \propto T^x$$

Where the exponent x is given by the following expression:

$$x = \frac{c_2}{\lambda T\left[1 - e^{\left[\frac{-c_2}{\lambda T}\right]}\right]}$$

We evaluated this expression for x to show the following relationship between $\frac{c_2}{\lambda T}$ and the exponent. In this chart, we also show, the typical LWIR regime and the two approximations at the extremes.

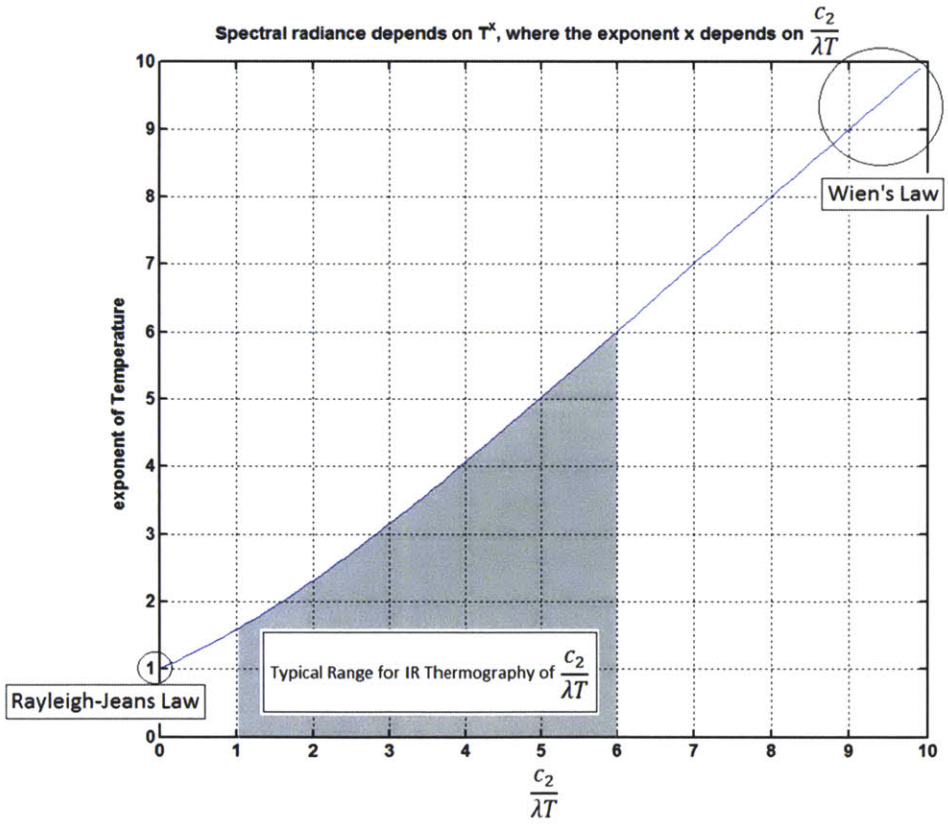

Figure 16: Temperature (x) relationship vs $\frac{c_2}{\lambda T}$

2.4.2 Sakuma-Hattori Equations Approximation

The Sakuma-Hattori equations are commonly used as a numerical approximation to the Planckian form and is commonly used in many LWIR cameras today [21, 34]:

$$S(T_{meas}) = \frac{S_{meas}}{\varepsilon_{inst}} + S(T_d) \approx \frac{C}{e^{\left(c_2/A \cdot T_{meas} + B\right)} - 1} \qquad (29)$$

(The details of this expression is fully explained in Chapter 4: 3d Radiometry) This form, presented by Saunders 2008 [34] has been reported to be implemented for 16 different IR camera makes and models. We find that the Sakuma-Hattori equations [21] is indeed commonly used for IR thermography according to Saunders [34], Vellvehi [48], and Liebmann [49].

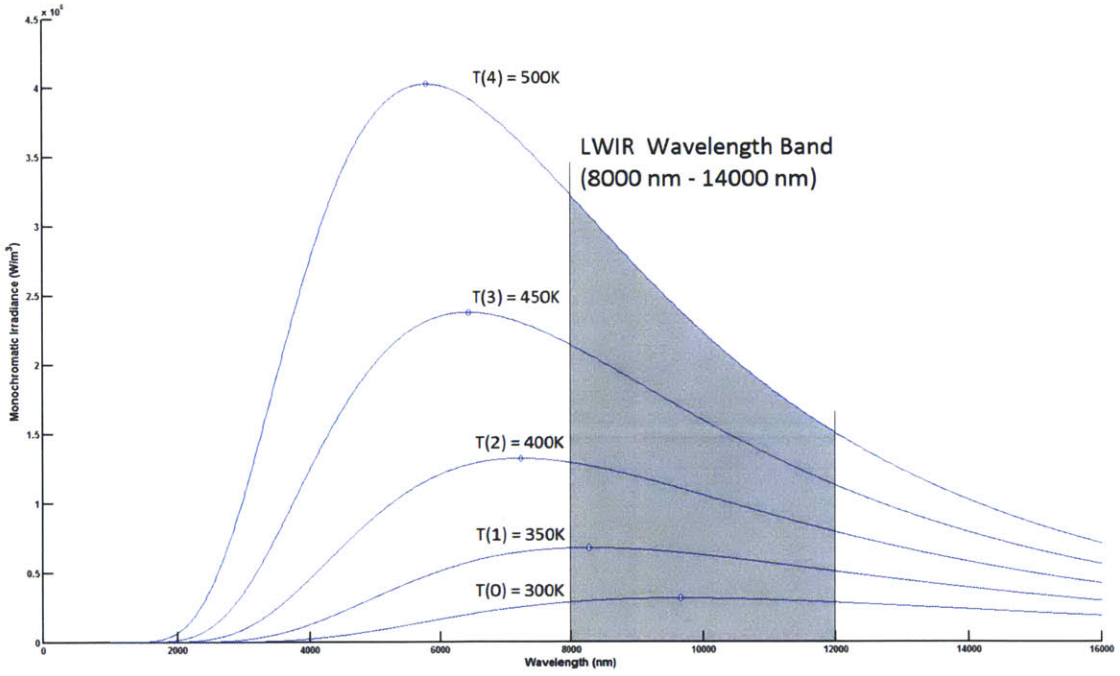

Figure 17: Planckian form of Sakuma-Hattomi equation [21] for temperature 300K to 500K

2.4.3 Minkina Approximation

Another approximation to the Planckian form is:

$$S_o = \frac{R}{e^{\left(B/T_o\right)} - F} \qquad (30)$$

presented by Minkina 2009 [35], Fehlman & Hinders [43], Rogalski [37] as another commonly used approximation model for monochromatic infrared detectors. In this thesis, we will focus our discussion on the Planckian form and the related Saunders model [34]. Although we know the general curve fitting models for interpreting observed radiance signal into temperature estimates, very little specific details of the calibration parameters have been published by any manufacturers.

For illustrative purposes, we plot below the numerical integration of the Planckian form using Mathematica. We note that the Sakuma-Hatori equations are numerical approximations to the curve shown in Figure 18 using three calibration constants.

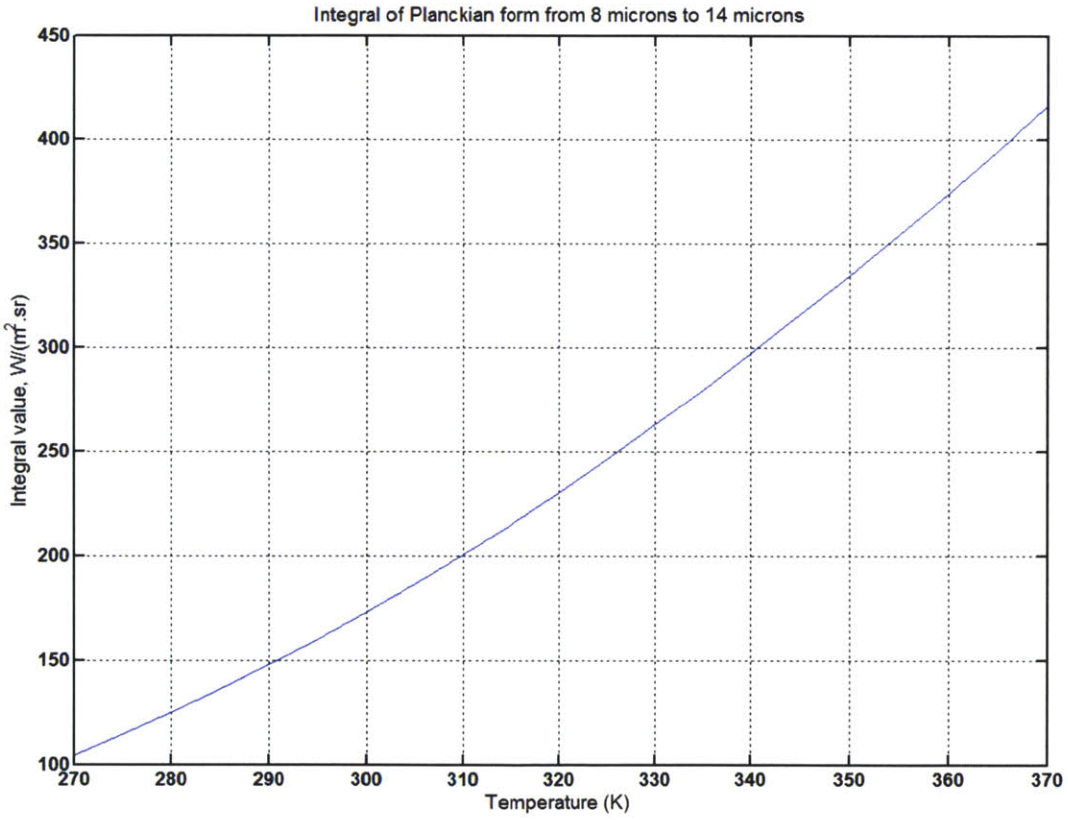

Figure 18: Integral of the Planckian form from 8 μm to 14 μm (Courtesy of Isaac Ehrenberg)

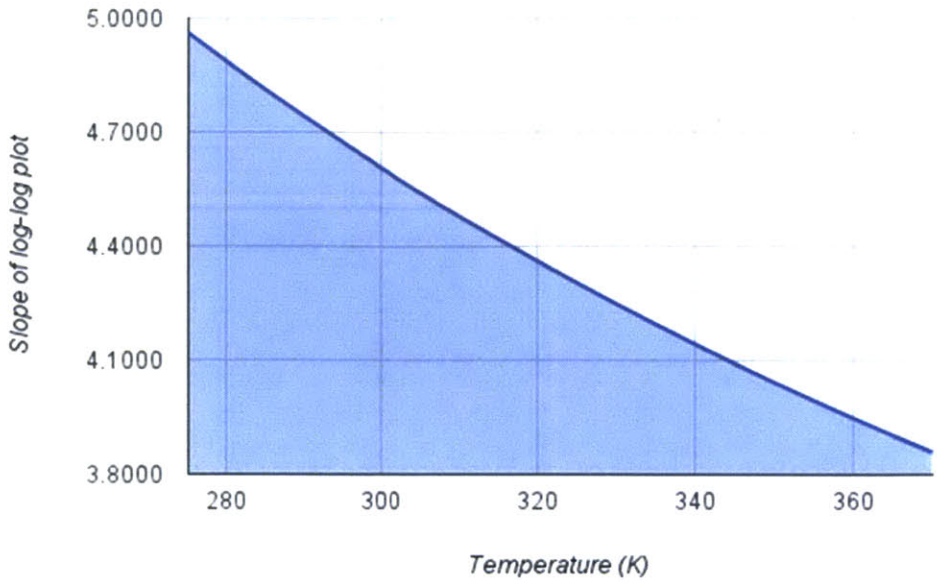

Figure 19: Slope of log-log plot of Sakuma-Hattori Integral (8-14 microns) vs Temperature

As pointed earlier, the observed radiance would depend as an exponent (x) of temperature as shown above in Figure 19. The exponent itself depends inversely with temperature.

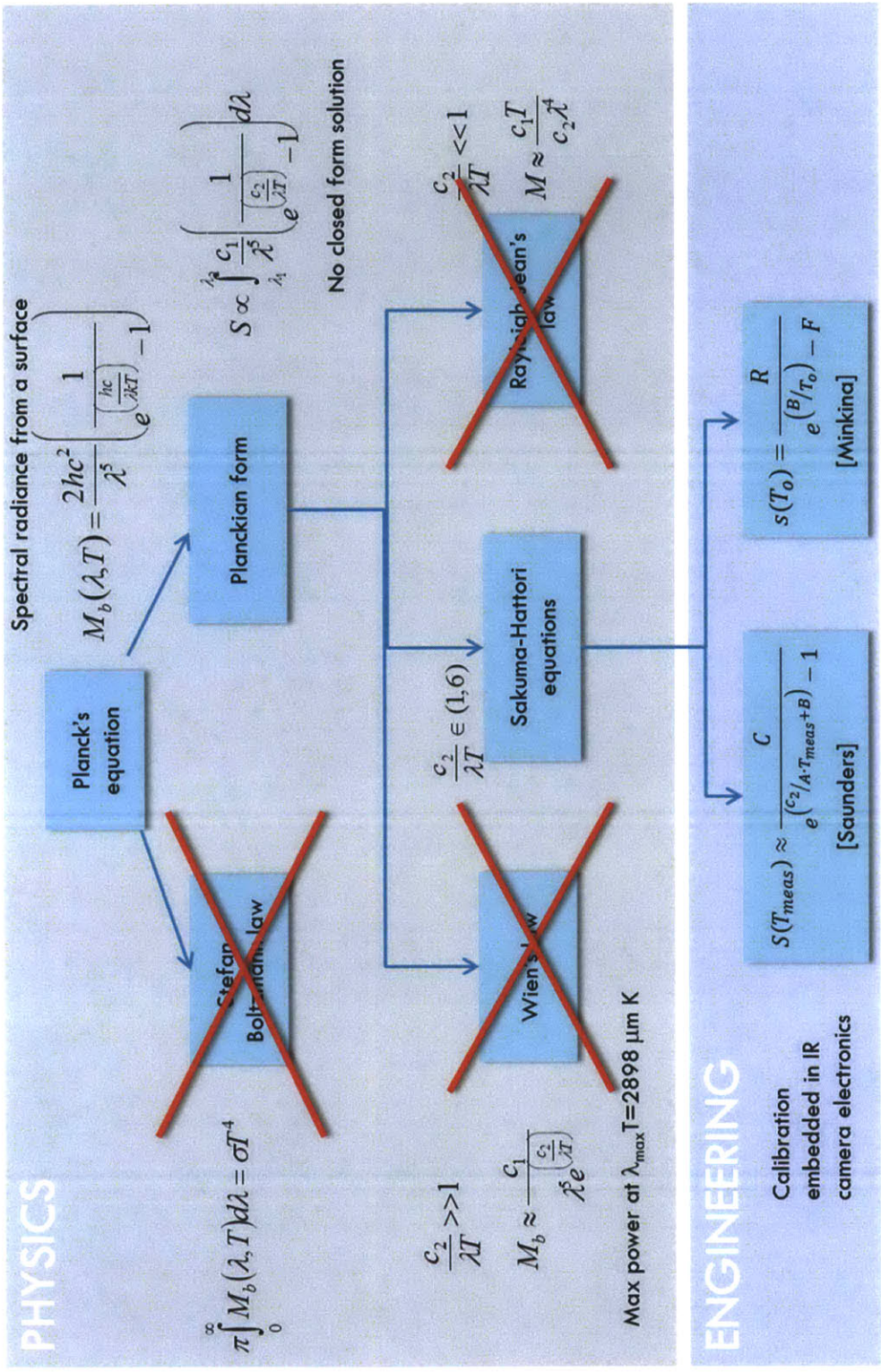

Figure 20: Theoretical modeling of Infrared Applications

2.5 Thermal Detectors vs Thermal Cameras

In this section, we will contrast thermal detectors vs thermal cameras based on the information content. The total amount of radiation received from any object is the sum of the emitted, reflected, and transmitted radiation. Objects where the $\varepsilon < 1$ emit only a fraction $\varepsilon(\lambda)$ of the equivalent black body radiation. The remaining fraction of $1- \varepsilon(\lambda) = r$ is reflected. A thermal image is created when there are temperature variations or differences in emissivity (for the same temperature) in the scene. Thermal contrast is an important parameter in characterizing IR imaging devices. It represents the ratio of the derivative of the spectral radiant emittance to the spectral radiant emittance.

$$C = \frac{\partial M(\lambda, T)/\partial T}{M(\lambda, T)} \quad (31)$$

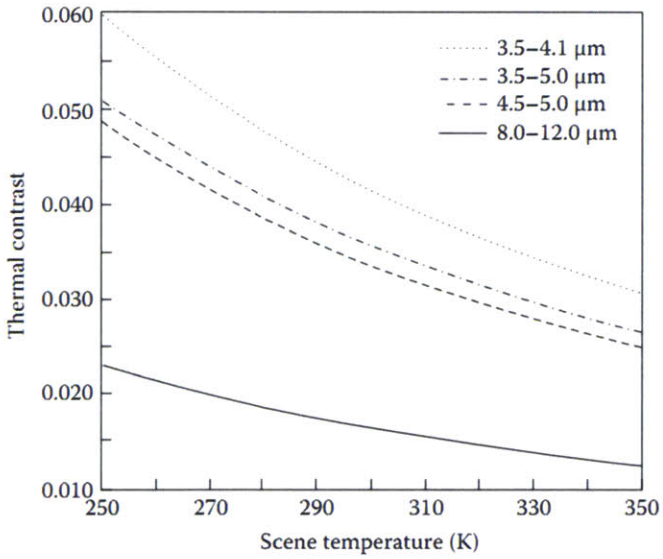

Figure 21: Spectral photon contract in MWIR and LWIR [50]

From Figure 21 above, we see that the smaller the wavelength, the greater the thermal contrast at a particular temperature. The greater the temperature, the lower the thermal contrast for a particular wavelength which will affect the marginal performance of the infrared camera system at high temperatures.

2.5.1 Thermal Detectors – History

I begin with a brief history of thermal detectors.

Although we focus on long wave infrared, there are many other types of infrared cameras: short wave infrared (between 2 and 5 μm), longwave infrared (between 8 and 14 μm), and even mid-wave infrared for wavelengths in between. Additionally, there are also detectors which work in the near IR (0.8 – 1.5 μm) which are based on quantum and photoemissive detectors and detectors that work in the far IR (8 – 14 μm) which are considered thermal detectors. The 8-14 μm band is appropriate for high performance thermal imaging. It has higher sensitivity to ambient temperature objects [36] and much better transmission through mist and smoke environments [35].

Another way to classify the detectors is based on detector cooling: cooled detectors containing cryocoolers and uncooled detectors, which operate using ambient air temperature. The cooler allows the camera to reduce locally induced radiant noise to a level that is below the target signal being imaged. Cooled cameras exhibit the most sensitivity to small differences in scene temperature. Prior to 1997, virtually all thermal detectors built where equipped with cooling units which typically operated between -70° to -200° C. Cooled detectors are much more expensive due to the cryocooling hardware, electronics, and sensitive components [37].

For thermography, manufacturers of thermal detectors offer measurement IR cameras which are calibrated at the manufacturer and used for temperature measurements. For non-thermography based applications, a basic IR imaging camera typically show only a false color map of the approximate temperature gradient. They do not include the software package required to interpret the signals into corresponding temperature estimates. Basic imaging IR cameras are much cheaper as they are produced in higher quantities and offered to a broader non-scientific environment. Thermographic cameras are sometimes referred to as 'radiometric' whereas basic cameras can be referred to as 'non-radiometric'.

Thermal IR detectors are generally divided into two types: (a) single point detector or (b) a linear and array detector (based on Focal Plane Array) which are built on matrices of single point detectors, for example a 320x240 array consisting of 320x240 individual detectors.

Single point detectors are often based on scanners, which are optomechanical scanning systems consisting of rotating, oscillating mirrors, or scanning prisms. The typical scanning rates of these systems are 25-60 Hz. In a single detector design, the image of the observed area is built, point by point at sequential time instants. The radiation arriving at the detector is based on the observed radiance of the individual points in the image and transduced by the detector into electrical signals. These type of systems were utilized for a better part of the last 20 years or so after they were originally invented and were limited by the thermal and spatial resolution of the type of scanner. One distinguishing feature of a single point detector is the uniformity of the thermogram, as all points in the image are derived by a single point on the same detector. Beyond single point, ruler or linear scanners utilized the same concept and that the scanner was either correspondingly vertical or horizontal oriented, depending on the mounting configuration [23, 26, 35-37, 50].

Since 1993, focal plane array detectors were introduced and became more common. A typical array may consist of 640x480 detectors which is 307,200 individual pixels. With these systems, there were no mechanical or moving parts.

In 1997, further development in IR technology introduced the first IR camera with a microbolometer array with an un-cooled detector. The elimination of moving systems and cooling needs in microbolometer technology made the operational parameters much more diverse, allowing for more reliable and faster operations. In this thesis, we will focus exclusively on microbolometer technology. It is based on a tiny vanadium oxide resistor that has a large temperature coefficient on the silicon element of large surface area exhibiting low heat capability and good thermal isolation [26]. The changes in the scene's temperature will cause a change in the bolometer temperature, which is converted directly into electrical signals and processed into an image. Uncooled cameras are typically less expensive than their cooled counterparts because the manufacturing economics of scale and the exclusion of the cryocooler, which is costly to produce and operate. They also have a longer service life based on the reduced wearing of parts. Therefore, the inherent advantage of lower cost, longer life, and less operational overhead makes uncooled thermal imaging cameras a prime choice for use in the ARTIST system.

2.5.2 Engineering of Thermal Detectors

We will model a single detector which could be projected into a line array or focal array. At the core of every infrared sensor array is a single detector that can be modeled according to the following Figure.

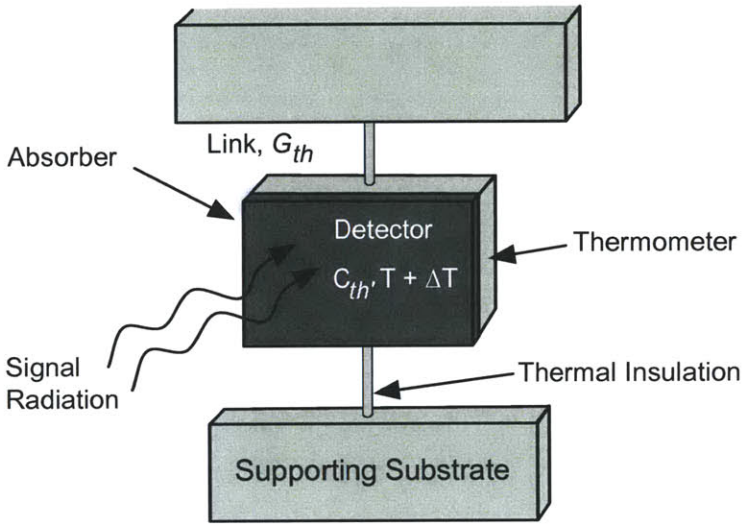

Figure 22: Thermal detector mounted via lags to heat sink

According to Rogalski [2009] [37] , the simplest representation of a thermal detector is shown in Figure 22 and is represented by the following differential equations:

$$C_{th}\frac{d\Delta T}{dt} + G_{th}\Delta T = \varepsilon\Phi \qquad (32)$$

Where C_{th} is the thermal capacitance, G_{th} is the thermal conductance, ΔT is the temperature difference due to radiant emittance signal Φ between the detector and its surrounding physical environment within the enclosure, and ε is the emissivity of the detector.

Since radiant power is modeled as a periodic function,

$$\Phi = \Phi_o e^{i\omega t} \qquad (33)$$

Where Φ_o represents the amplitude of the sinusoidal radiation emittance. The solution to the differential heat radiation is:

$$\Delta T = \Delta T_o e^{-\left(G_{th}/C_{th}\right)t} + \frac{\varepsilon \Phi_o e^{i\omega t}}{G_{th} + i\omega C_{th}} \quad (34)$$

The first part of the solution is the transient response and can be removed when analyzing the steady-state response due to the incident radiant flux. This can be summarized into the following:

$$\Delta T = \frac{\varepsilon \Phi_o}{\sqrt{(G_{th}^2 + \omega^2 C_{th}^2)}} \quad (35)$$

Thus, in infrared detection and sensing, it is advantageous to make ΔT as large. To accomplish this, one must minimize the thermal capacity of the detector C_{th} and G_{th}. To maximize ΔT, the incident radiation received on the thermal detector is maximized, due to source and geometry, when the thermal contacts with other parts of the system is minimized. This is why individual thermal detectors have small mass and very fine wires connecting to the heat sink.

A characteristic thermal response time for the detector can be generalized and defined as the following:

$$\tau_{th} = \frac{C_{th}}{G_{th}} = C_{th} R_{th} \quad (36)$$

Where $R_{th} = 1/G_{th}$ is the thermal resistance. The typical thermal time constant for infrared detectors is on the order of milliseconds. This is much slower than the response time of a typical photon detector.

Summary of insights to improve performance:

1. Design for low thermal capacity C and thermal conduction G.
2. Increase thermal integration frequency f_{bol}, by reducing τ, the thermal time constant of the bolometer.

3. Minimize R_{bol} , the resistance of the bolometer thermistor.

2.5.3 Cost versus Resolution Trade-Off

Infrared technology is inherently costly due to several main factors:

1. The raw material costs in the optical lens and detector (e.g. thermopiles) is relatively high compared to other components in the system.
2. The economies of scale in manufacturing and production is relatively low compared to the scale of production for modern day digital SLR.
3. Market competition is relatively low, there is only a limited number of LWIR camera manufacturers in the world.

Many of the high performance systems are solely developed for military and scientific usage. Mainstream usage of high performance LWIR systems is typically very limited to small scale application specific needs. To boost performance in resolution, the focal plane array (FPA) must be compressed and reduced in size. However, there are limited factors preventing such actions, mainly, the wavelength of the electromagnetic radiation. Since long wave infrared operate in the 8000-14000 nm, this equates to the wavelength being of the order of 8 – 14 microns. LWIR FPA technology is manufactured of the order of 17 microns per pixel, operating near the wavelength of the long wave infrared electromagnetic wave. As a result of these physical limits to the pixel size, we may not be able to shrink the pixels further in order to enhance resolution. Operationally, you can not make a detector size smaller than the wavelength of the electromagnetic wave you are attempting to detect [51].

To increase the resolution of LWIR cameras, we must employ a larger FPA array and increase the size of the optical lens system. Both of these actions are prohibitively costly due to material cost and low volume manufacturing.

2.6 Temperature Inference

As previously discussed, the output of a LWIR camera comes in two forms:

1. An output file of the measured radiance signal(s) received by the detector
2. An output file depicting a false color map representative of the temperature profile of the scene.

The term 'radiometric cameras' in the IR camera industry refers to infrared cameras that include a software or algorithm that interprets the output radiance reading into a temperature estimate of the target. Not all LWIR cameras are calibrated and sold with the radiometric feature. In fact, many off-the-shelf infrared cameras do not come with radiometry features. In this section, we will discuss how one can interpret the camera signal output (pixel intensity) to estimate temperature.

2.6.1 Infrared Camera Signal Processing

An infrared detector array contains a number of individual pixel detectors. Each of these detectors have slightly different characteristics and thus, different processing applied by the manufacturer. It can be modeled as:

$$s_j = f(M_j) \tag{37}$$

Where s_j is the output signal output (pixel intensity) and M_j is the observed radiance intensity.

Initially, at power on, an internal calibration procedure is performed automatically and after that power on, additional algorithms are utilized to compensate for detector signal non-uniformity. According to Minkina [35] who utilized the TOOLKIT IC2 (described in his book), compensation is performed using the following formula:

$$absPixel = globalGain \cdot LFunc\,(imgPixel) + globalOffset \tag{38}$$

Where *absPixel* is the value of the pixel post-compensation, *LFunc* is the value of processing characteristic of a linearized function for the raw value of *imgPixel*, and *globalGain* and *globalOffset* are constants representing the parameters of the camera's amplifiers in the signal processing path. *LFunc* is a linearization function based on two coefficients, *Obas*, which is the base offset used in a nonlinear conversion, and *L*, the calibration constant linearizing the raw pixel values. According to Minkina [35], *LFunc* is defined as:

$$LFunc = \frac{p - Obas}{1 - L \cdot (p - Obas)} \quad (39)$$

where p is the raw pixel value.

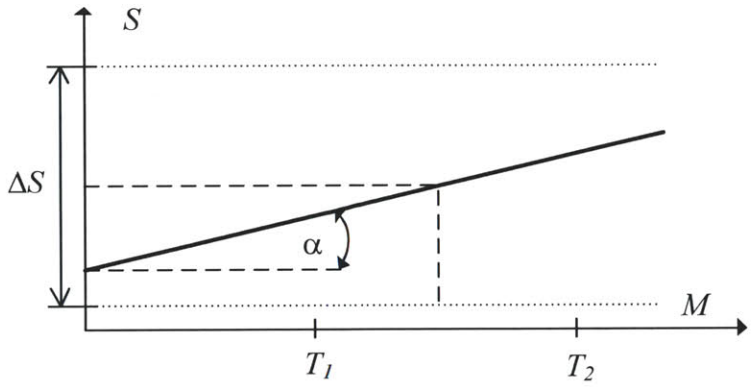

Figure 23: Calibration process of pixel detector's static processing characteristics $s_j = f(M_j)$ [35]

2.6.2 Output Color Mapping

After the initial signal processing, the next task of a camera system is to display the recorded data as a false color map of the thermogram. For this, the camera applies an imaging procedure which maps the temperature readout to values defined by the color map based on a color palette. The histogram matching algorithm is applied, the number of colors per internal is calculated, and then each pixel is mapped to a corresponding index in the defined color map table. The color palate is typically carefully chosen based on the specific application and visual needs of the application. At times, the color mapping of the camera signal output (pixel intensity) may not be linear to temperature for all applications.

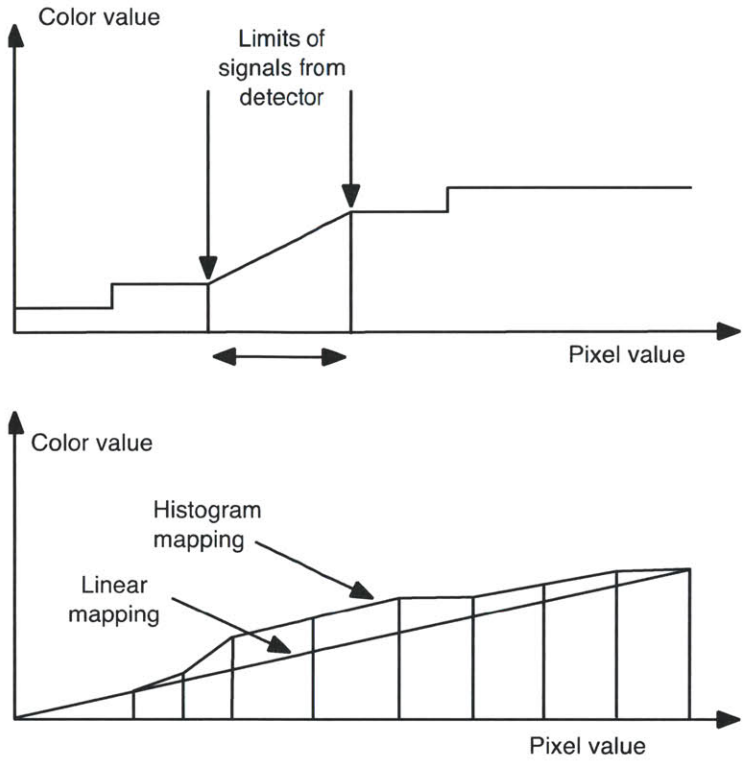

Figure 24: Isothermal colorizing algorithm for FLIR Cameras (top) Histogram colorizing algorithm

2.6.3 Modeling of Measurement with Infrared Cameras

In this section, I will discuss the temperature inference modeling behind infrared imaging hardware. As a recap, the two generalized temperature calibration models in IR detectors are reviewed by Minkina [35] and Saunders [34].

At the detector, the following heat fluxes are considered:

$$\varphi_{ob} = \varepsilon_{ob}(T_{ob})TT_{atm}(T_{atm})M_{ob}(T_{ob}) \quad (40)$$

$$\varphi_{refl} = [1 - \varepsilon_{ob}(T_o)]\varepsilon_o(T_o)TT_{atm}(T_{atm})M_o(T_o) \quad (41)$$

$$\varphi_{atm} = [1 - P_{atm}(T_{atm})]M_{atm}(T_{atm}) \quad (42)$$

Where $\varphi_{ob}$is the flux emitted by the target object, φ_{refl} is the flux emitted by the ambient background and reflected from the target object, and φ_{atm} is the flux emitted by the atmosphere, ε_{ob} is the band emissivity of the target surface, M_{atm}, M_{ob}, M_o are the radiant emittance of the

atmosphere, target object, and ambient background, TT_{atm} is the band transmittance of the atmosphere, T_{atm}, T_{ob}, T_o are the temperature of the atmosphere, object, and ambient background [K]. Other fluxes emitted by the optical components of the imaging system and its relative influences are negligible.

When accounting for all the heat fluxes into the detector, the following output signal of the camera s is observed:

$$s \approx C(\varphi_{ob} + \varphi_{refl} + \varphi_{atm}) \quad (43)$$

Where C is a parameter that accounts for the atmospheric damping, the camera's optical system, and the detector's properties.

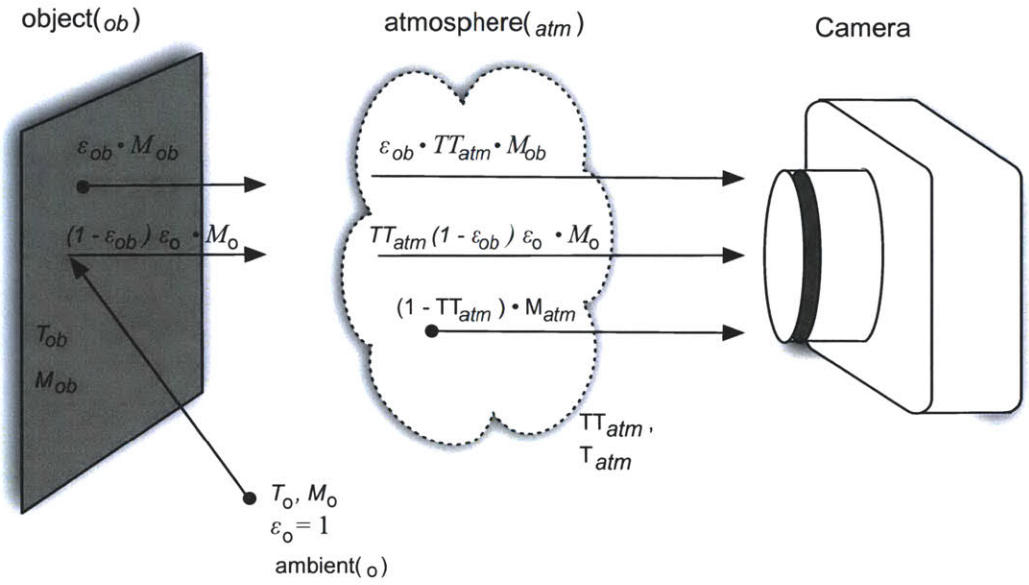

Figure 25: Radiation flux model with an infrared camera

Therefore, the signal output of the camera can be expressed as the following:

$$s = \varepsilon_{ob} \cdot TT_{atm} s_{ob} + TT_{atm} \cdot (1 - \varepsilon_{ob}) s_o + (1 - TT_{atm}) s_o \quad (44)$$

Where s is the observed radiance corresponding to the total camera signal output (pixel intensity) arriving at the detector, s_{ob} and s_o are observed radiance signals that corresponds to the target

object's heat radiation intensity and an ideal black body heat radiation intensity at ambient temperature(assumption: background radiation is black).

The Planckian form of signal s_o based on the Sakuma-Hattori equations [21] can be summarized as:

$$s_o(T_{meas}) \approx \frac{C}{e^{\left(c_2/A \cdot T_{meas}+B\right)} - 1} \quad (45)$$

Where A, B, and C are constants associated with the camera calibration characteristics. These parameters are stored in the camera's microcontroller and used to account for emissivity of the target object, atmospheric temperature, ambient temperature, camera to object distance, and atmospheric relative humidity. Modern day infrared cameras have built-in hardware to measure and approximate these values, and then automatically choose the correct parameters to apply in real-time. However, more advance cameras will give users the option to manually change the parameters on demand. Considering all these variables, we can summarize and model the radiant flux density at the detector signal level as:

$$s_{ob} = s\frac{1}{\varepsilon_{ob} TT_{atm}} - \left[\frac{1-\varepsilon_{ob}}{\varepsilon_{ob}} \cdot \frac{C}{e^{\left(c_2/A \cdot T_{meas}+B\right)} - 1} + \frac{1-TT_{atm}}{\varepsilon_{ob} \cdot TT_{atm}} \cdot \frac{C}{e^{\left(c_2/A \cdot T_{meas}+B\right)} - 1}\right] \quad (46)$$

The coefficient TT_{atm} is represents the absorption of the infrared radiation by a layer in the atmosphere. It is important and is caused by the water molecules (H_2O), carbon dioxide (CO_2), and ozone (O_3). These atmospheric components are functions of the weather, climate, season, and geographic location.

The simplified expression for atmospheric transmission TT_{atm} considers relative humidity $\omega_{\%}$, camera-to-object distance d, and atmospheric temperature T_{atm} :

$$TT_{atm} = f(\omega_{\%}, d, T_{atm}) \quad (47)$$

In practice, TT_{atm} is very complex to model fully as it has considerations for more than nine other coefficients according to Minkina.

The final model to represent the object's temperature based on the Saunders model [34] is expressed as:

$$T_{ob} = \frac{c_2}{A \cdot ln\left(\frac{C}{s_{ob}} + 1\right)} - \frac{B}{A} \quad (48)$$

It can be further expressed as function of the following major variables:

$$T_{ob} = f(\varepsilon_{ob}, T_{atm}, T_o, \omega, d) \text{ [K]} \quad (49)$$

It must be emphasized that this model is a simplified way of looking at how to interpret infrared signals into temperature maps. In practice, the detector receives radiation from different sources including radiation from the clouds, buildings, ground sources, and from the atmosphere. All these radiation sources have influence that is relative to one another and will depend on the exact nature and situation of the scenario. To account for these external influences, we need to develop a more analytical and systematic approach to determine the correct assumptions to apply to the model and correct for errors that may otherwise propagate in our estimation. In Chapter 4, I will present 3D Radiometry and ARTIST based methods for reconstructing the 3D environments of a scene. In doing so, we start to consider the influences of the surrounding environments and its effects on the target surface.

2.7 Conclusion

In this Chapter, we have presented a broad overview of radiation theory and how it relates to infrared imaging systems and thermography. The major insights in this Chapter include the following:

1. Planck's law is the most common analytical form representing radiation.
2. Stefan-Boltzmann law is valid only for full spectral applications and not for band limited applications like long wave infrared.
3. In Planckian form, the Sakama-Hattori equation approximation has been shown to be the most applicable fit for long wave infrared applications.

4. Most material surfaces are not Lambertian. Lambert's law states that when viewed from any angle, a Lambertian surface will exhibit the same radiance. Lambert's law is based on a black body assumption, whose emissivity is wavelength invariant and angle invariant, and is an ideal diffuser.
5. Commonly published emissivity values are based on normalized emissivity and often overlook angle dependency. Angular emissivity is assumed to be constant from incidence angle $\theta < 60^{\circ}$ and varies for angle $\theta > 60^{\circ}$ based on observations as far back as 1935 based by Schmidt and Eckert [42]. Emissivity is variant depending on the material, surface, and incidence angle.
6. In thermal imaging, the conservation of radiance dictates no dependence on distance. Radiance is equal to radiant flux over etendue. Radiance is invariant for a perfectly transmissive optical system.

These fundamental insights will be useful for the later Chapters when we discuss concepts related to 3D radiometry.

Chapter 3: Multi-Spectral Synthetic Aperture Imaging System

3.0 Introduction

In Chapter 2, I presented the physics behind thermal imaging. In this Chapter, I will summarize a field study on the use of a FLIR thermal infrared camera for manual street-level thermography. I will discuss the challenges of this approach and based on lessons learnt, will show a two phase design approach for the ARTIST hardware system. In Phase 1, we develop a prototype rapid thermal imaging data collection system using the FRDPARRC design methodology, Slocum [52, 53], and then in Phase 2, introduce refinements to the idea to show the development of a multi-camera synthetic imaging system. This entire process will walk us through the how the ARTIST hardware system was designed, developed, and deployed.

ARTIST was originally designed to be a wide area thermal mapping system. Towards achieving this capability, I developed three specific modular system components:

a. Hardware module - Developing an approach to collecting large scale, high through thermal imagery. This will require the combination of hardware, software, and system product design.
b. Image Processing module – Contributions to methods that can increase thermal imaging resolution and capabilities.
c. 3D Radiometry module - A generalized approach examining 3D thermal imagery and its importance and significance to leading the way to a more quantitative and accurate approach to modeling heat transfer, energy diagnosis, and potential applications in non-energy related fields.

For the remainder of this Chapter, we will focus on the (a) Hardware component of ARTIST. The end-product is a portable multi-camera synthetic aperture camera system.

3.1 Initial Field Study

In the Introduction in Chapter 1, we discussed that energy auditors use thermal imaging as a tool to help assess thermal deficiencies through visual inspections. By inspecting areas of high thermal gradients in the images, auditors use these images to show evidence of thermal leakage and make expert interpretations of the images from their own user based experiences. The handheld thermal imagers are typically battery-operated handheld devices that allow the user to capture images of radiant leaks at wavelengths of 8000-14000 nm, the long wave infrared (LWIR) band. Thermal imagers are based on uncooled microbolometer technology, which is cost effective when mass manufactured. Energy auditors use these devices, which can be as small and portable as a digital multimeter to something that can be as large and heavy as a large camcorder video recording system.

In a typical use case, an operator carries these handheld infrared systems in the two potential settings:

a. Internal operation – the user carries the device internally into the building to areas like a basement, attic, HVAC system, or any internal area where there can be significant energy leak which can be identified by the thermal imager. This can be done during the day or night.
b. External operation – the user carries the device externally to the building, focusing on examining for energy loss on the thermal envelop of the building. This is typically done only at night, to avoid the effects of solar radiation in the images.

This part of the field research study was conducted in the Winter of 2009-2010 by me along with MIT researchers Dr. Jonathan Jesneck, and Thomas Piper.

3.1.1 FLIR Camera Rental

With support from Professor Sanjay Sarma and the MIT Field Intelligence Laboratory, I performed an initial feasibility and proof-of-concept study utilizing an off-the-shelf FLIR camera. The camera was used to image and subsequently analyze energy leakage snapshot images of the thermal envelope. The goal of the field study was to mimic an energy auditor's thermography work to

provide insight into how data is collected, processed, and analyzed for determining heat flow out of a home. A broader goal was also to estimate feasibility of performing manual thermal imaging over an entire neighborhood and at city-scale.

The most prohibitive component of an infrared imaging field study is the cost of the camera system itself. At the time of the field study, the most commonly used off-the-shelf infrared camera system was the FLIR model P-660 camera. The system has a retail price of $40,000 with additional costs for accessories. The main specification of the camera is the imaging capability of 640x480 pixel images using a 38mm lens, 24° field of view. In order to operate under limited budget, I decided on a lease/rental unit that was available from FLIR at a cost of $1500/8 nights.

Figure 26: FLIR Model P-660 Thermal Infrared Camera

3.1.2 Data Collection

Upon receiving the FLIR P-660 camera, we conducted 8 nights of data collecting to perform. Over the course of the following 7 nights, imaging data the following cities were collected:

Description	Date	Images	MeanT	MaxT	MinT	Conditions
1. Night 1: Somerville, MA	1/13/2010	1115	22	30	14	Scattered Clouds
2. Night 2: Somerville, MA	1/14/2010	526	27	33	21	Scattered Clouds
3. Night 3: Somerville, MA	1/15/2010	843	39	46	31	Overcast
4. Night 4: Belmont, MA	1/16/2010	831	40	48	32	Partly Cloudy
5. Night 5: Lexington, MA	1/17/2010	771	36	41	31	Light Rain

6.	Night 6: Lexington, MA	1/18/2010	813	33	34	31	Light Snow/Freezing Rain
7.	Night 7: Cambridge, MA/MIT	1/19/2010	345	34	36	31	Light Rain

Table 2 Field Study Summary for 7 Nights of manual data gathering using a FLIR P-660 LWIR camera

Every evening, the team would gather at around 6 pm and collected data until about 2 am in the morning. The first night was spent learning how to use the camera system, how to make adjustments to for better image quality, and learning the capabilities and limits of the system in general. Even on the first night, it became clear that one can indeed "see" the thermal leakage visually. The images were powerful visually in that common issues such as air leakage, thermal bridges, and poor insulation were all visually evident on the thermal envelop of the building. It was the first time that anyone on the team has utilized or experienced how to use a thermal infrared camera system. The operation of an infrared camera system is intuitive and similar to how one operates consumer digital cameras:

a. Point at scene
b. Press auto-focus button
c. Press auto-gain lock to adjust for image brightness
d. Click on button to capture image
e. Repeat

Figure 27: Example 640x480 Pixel Image of a Home in Cambridge taken with a FLIR P-660 Camera.

Each night, thousands of infrared images were captured of homes, building, and various parts of a city. The average time to capture each was approximately 30 seconds and every home required multiple images taken from a single point of view and subsequent manual tiling process to image the entire surface of house. The average home required 10-15 minutes of operation to capture one full frame using the tiling method. The FLIR P-660 was a fairly heavy camera weighing approximately 4.5 pounds and required operations without glove because of the small size of the control buttons. Operator training and a good amount of dexterity is required to successfully operate the infrared handheld camera on a repeatable, consistent basis.

To estimate the time it would take to capture one full image per home for a small city like Cambridge, with 22,000 homes.

$$Total\ time = Time\ per\ home \times Number\ of\ Homes$$

$$Total\ time = 15\ \frac{min}{home} \times 22{,}000\ homes$$

$$Total\ time = 330{,}000\ minutes = 5{,}500\ person\ hours = 229\ person\ days$$

I estimate that it would take a total of approximately 5,500 person hours or 229 person days to gather all the data for each of every residential home in Cambridge, MA.

3.1.3 Image Tiling & Digital Stitching

Image tiling is an on-site manual camera operational process used to move the camera stepwise in a Cartesian grid of the scene. Using a tiling process can virtually extend a camera's field of view and resolution but can be a very time consuming and tedious process to complete. In our case, we used on-site image tiling because of the limited field of view and limited resolution of a single camera system. The tiling process begins with an overall selection of a scene, starting from one end of a corner, and methodically moving the camera frame by frame to create a virtual mosaic of the scene. An outline of the steps to capture images of home:

1. Find desired home to image
2. Find reasonable distance to stand from the home
3. Align camera to take an image
4. Focus and lock the thermal setting onto the scene
5. Capture the image in the selected area
6. Move the camera slightly to the next scene with partial overlap over the original scene
7. Repeat steps 5-6 until entire scene of home is captured
8. This entire process will take about 10-15 minutes per home.

Example of tiling of images to create a stitched mosaic of a single home is shown in Figure 28.

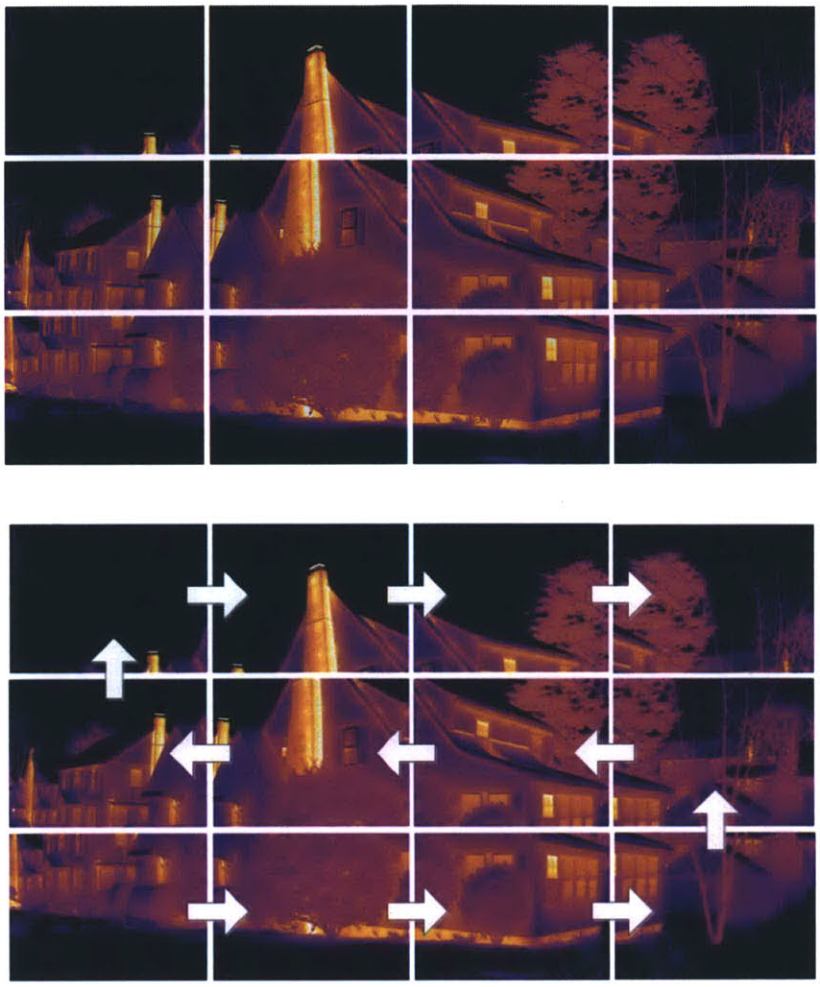

Figure 28: On-site image tiling process to increase field of view and resolution of the camera. 12 Raw Images (Top) Manual tiling process (Bottom)

After the infrared imaging data is collected, the next step is to process the images of each house by using a commercial panorama software program like PTGui. PTGui allows for manual stitching using accurate cross photo markers and positions. Although not perfect, the software is suitable for digital image stitching with the manual help of the operator. The most unique challenge of computerized mosaic is the placement of unique markers used to identify locations matches between two images. Infrared images contain less color density and unique features compared high resolution electro-optical (EO) cameras. Therefore, mosaicking from tiled images is more difficult and challenging to accomplish.

Figure 29: Post-processed fully mosaicked example of Home A in Belmont, MA

Figure 30: IR image showing high gradient regions that are easy to identify in Home A

Figure 31: Another example of a post-processed infrared image of Home B in Belmont, MA

Figure 32: Post-processed image of a commercial building. Building 35 at MIT, Cambridge, MA

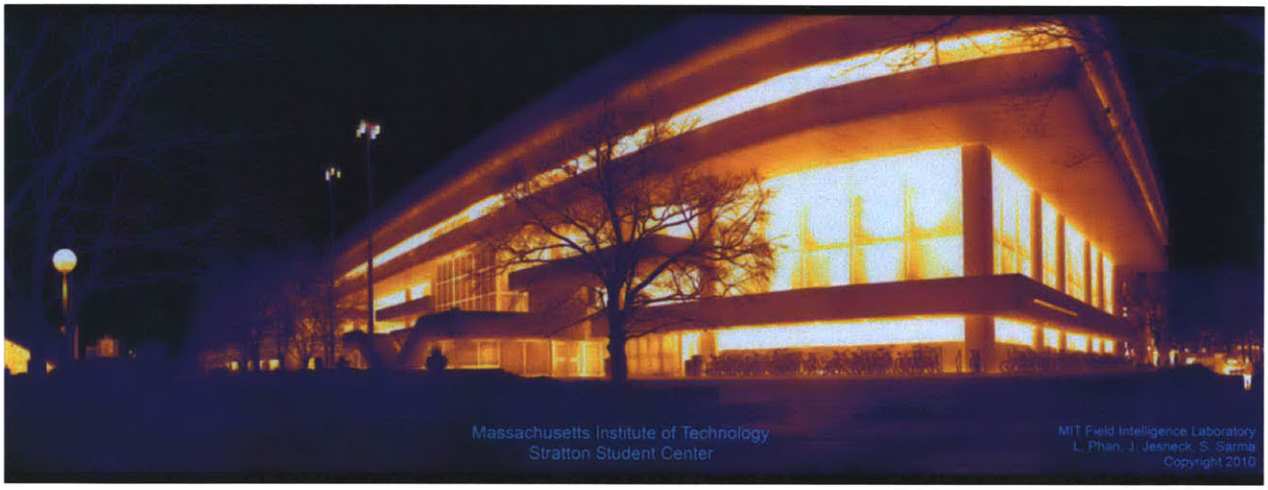

Figure 33: Post-processed image of a commercial building. MIT Student Center, Cambridge, MA

Figure 34: A unique 360° view of the Massachusetts Institute of Technology in LWIR

This image was taken with a FLIR P-660 LWIR Camera using 4x360° rotations through manual on-site tiling method and manual digital stitching and image correction.

3.1.4 Insights & Summary of Initial Field Study

Upon careful examination of the FLIR formatted digital thermal imagery .jpg files, the following is observed:

1. The FLIR file size is unusually large and contains about three times the amount of data for an equivalent image of that pixel size and color depth.
2. My hypothesis was that a FLIR file contained multi-layers of data, which I later confirmed. The first layer is a jpeg formatted color mapped thermogram representing a post processed s_j signal.
3. From the information that was gathered, the layered data is encrypted and is likely to contain the raw signal s of the camera system along with localized variables $\varepsilon_{ob}, T_{atm}, T_o, \omega, d$ along with the internal calibration settings of the camera related to the R, B, and F constants used to determine the precise conditions of the camera at the time the thermal image was taken. My attempts to understand this process in more detail were rejected by FLIR, citing proprietary nature of their technology. I supposed that the data is encrypted with proprietary and complex radiometric data.
4. The only method to extract a temperature interpretation of the image required utilizing a FLIR originated software where it could unencrypt the data beneath the jpeg data which allow porting a temperature table to an external program such as Microsoft Excel. FLIR does provide a free version of this software called Quick Report, but it is limited in features and will only allow one image at a time to be converted.

The result of the field study over 8 nights of operating the FLIR P-660 camera in varying weather conditions yielded many observations, an illustrative sample of which include:

- Over 100 homes were imaged, many times, multiple times per night and at different locations and field of view to the building.
- It was extremely time consuming to manually gather the images. Each image took an average of 30 seconds to acquire and each home required anywhere from 4 – 16 images per

mosaic. Manual mosaicking each home was not efficient. The average home required at least 5 minutes or more to completely image.

- The task was both tedious and physically painful – both from dealing with the cold weather and physical and emotional duress of working in such extreme weather conditions.
- The images were insightful in allowing one to "see" the energy leaks from the building allowing one to visualize problems with air leaks, poor insulation on the doors, windows, roofs, sills, and many other problems on the thermal envelope of the building.
- The manual process of gathering data by walking from home to home would NOT be scalable and was subject to high degree of inconsistency from home to home, from neighborhood to neighborhood.
- Weather variations such as rain and snow affected the quality and operation of the camera and images.
- The average number of homes per night would be approximately 20-30 homes.
- Post data mosaicking was slow and time-intensive.
- Commercially available FLIR Thermal Camera Systems are can only be modeled as a blackbox that must use FLIR's proprietary software to operate the thermal radiometry feature of the camera.
- $\varepsilon_{ob}, T_{atm}, T_o, \omega, d$ data is encrypted as a layer on FLIR jpeg images along with R, B, and F constants used for mapping temperature information for the P-660 model.
- The feedback and conclusions drawn by the researchers will be utilized as part of the system design process to in developing a more methodical, systematic, and scalable way to collect thermal imagery data.

These insights will be utilized in the next section as we develop a formal system design methodology.

3.2 Design Framework for ARTIST

ARTIST stands for Automated Rapid Thermal Imaging Systems Technology – it was conceived to help overcome the challenges of manual infrared imaging data collection process, which we have shown in the last section to be a challenging task. We used the field study in the previous section to

help us better understand the challenges of image data collection. Now, we will use the remainder of this Chapter to help us design a better thermal image data collection system. The central concept behind ARTIST is to do for thermal mapping what Google Street View did for visual imagery. Today, Google Street View has the technology to deploy fleets of vehicles to quickly and efficiently map an entire city, state, or even country. Their technology is capable of being deployed on a global scale. There is no such system for thermal imagery. Therefore, we propose to build such an automated system. We begin by focusing on the hardware design of the ARTIST system and will develop the same in two phases:

Phase 1: Initial proof-of-concept device to explore the concept of wide area thermal mapping

Phase 2: Develop and refine hardware for an advanced multi-camera synthetic aperture system

The goal of this section is to give the reader a conceptual and technical understanding of how hardware product development is progressed for an idea such as ARTIST.

3.2.1 Phase 1: Proof of Concept Device

Based on the challenges we faced during the field test of a manual infrared data collection process, we go to straight to the drawing board to think of how to address some of those key challenges using a proof of concept device system. In Phase 1, we apply a FRDPARRC design approach to develop a proof-of-concept device. I proposed the use of a hardware mounted conventional vehicle system to capture thermal imagery. The sequenced thermal images can be mosaicked into a single panoramic frame allowing one to take a single stitched panorama of an entire street. Such an image would be powerful and would demonstrate the ability to map entire neighborhoods quickly and efficiently. This process would provide an initial framework to thermally map large areas in a short period of time. The "drive-by" approach is highly desirable as it confirms to existing road networks, is non-conspicuous, and is an acceptable form of imagery data capture based on Google Streetview's precedence in the space. According to court records, it is legal to capture imagery data from any publicly accessible road [54].

3.2.1.1 FRDPARRC Design Approach

FRDPARRC is an acronym for Functional Requirements, Design Parameters, Analysis & References, and Risks & Countermeasures. Each part will be detailed in the following sections as we work through the exercise for the design. This process was chosen because it is a well–known approach in design pedagogy.

3.2.1.1.1 Functional Requirements

We initiate the design process with a vision of the product – a multispectral system that can record data in 3 wavelength bands, EO, NIR, and LWIR bands – this is also referenced as multi-band imager. This system would be vehicle mounted and driven at normal speeds on the road.

1. Multispectral imaging system:
    a. Capable of Electro Optical or EO imaging(350-700 nm)
    b. Capable of Near infrared or NIR imaging(700nm-1200nm)
    c. Capable of Long wave infrared or LWIR or FarIR imaging(8000-14000nm)
    d. Capable of using forward lateral motion to target object (a house), through forward motion of vehicle, so that a scan be completed at different locations along a building.
    e. Capable of application of ±2 pixel motion for demonstrating the application of Kinetic Super Resolution[2] (to be discussed in a later Chapter)
    f. Operable in near-infrared, low-lighting conditions, in areas of limited or zero natural or street lighting conditions.
2. Ability to operate in both day and night conditions
3. Imaging system must be mounted atop a vehicle, with sufficient stability and fixturing. Minimize motion of imaging system during transport and road use.
4. Relatively lightweight for ease of installation and removal
5. System must have low power consumption, capable of drawing power directly from existing car battery system.

---

[2] MIT ID#14538: Kinetic Super Resolution Imaging (J. Jesneck, L. Phan, S. Sarma)

6. Imaging system must meet 10 feet vertical elevation from the ground to avoid viewing other obstructive objects, such as other vehicles, directly.
7. Geo-location logging capable with GPS logging capability for pro-processing GPS tagging.

3.2.1.1.2 Design Parameters

Towards addressing the functional requirements for the relevant design parameters and alternate component choices are:

1. Imaging System
    a. Modified Sony HDR-XR550 HD Capable 330nm-1200nm functional camcorder with recording capabilities
    b. FLIR Photon 320 Camera + Accessories (320x240 pixel) IR Imager 8000-14000 nm with local PC storage capabilities
    c. Reliable enclosure and mount for both cameras
2. Structural Mounting on Vehicle
    a. Bike rack mount, snowboard mount or professional suction cup design and must be able to withstand significant shake & movement from moving vehicle
    b. Centralized cabling system from inside the vehicle to the imager/equipment
    c. IR illumination in the ~800nm range through the use of infrared LED flood lighting
3. Power Requirements
    a. 12v DC > 120v AC power conversion in vehicle for powering the equipment
4. Data Logging
    a. Real time GPS logging capabilities for imagery geotagging

These are the sequence of actions while operating the device:

1. Drive-by imaging of buildings on the street-side to create a street mosaic
    a. Utilizing daylight to capture EO Video (300-700nm) with HD Sony Camcorder
    b. Utilizing IR floodlamps to capture Near IR Videos ~800nm with HD Sony Camcorder

c. Utilizing FarIR/NearIR coupled mode to simultaneously record NearIR and FarIR videos

2. Application of sufficient motion to image to attain ±2 Pixels Movement for Kinetic Super Resolution

3.2.1.1.3 Analysis & References

We need to consider the motion of the vehicle parallel to the homes and buildings. We will estimate the upper bound on the vehicle speed based on the field of the view of the components of imaging system is and the sampling rate of the imaging system in frames per second (FPS) that will minimize motion blurring from in the imagery from vehicle motion. While a wide angle camera will encapsulate a larger area of coverage in the image, a smaller field of view will limit the speed of vehicle and cause significant motion blurring due to relative motion of the imaging system.

In this section, we will focus on the system design of the prototype of a low cost multi-spectral imaging system and forgo the discussion concerning motion blur in particular. Imaging motion will be discussed in a later chapter and a method will be presented to take advantage of camera motion for post imaging processing for producing resolution enhancement through super resolution methodologies. For now, we will focus on the constraints of minimizing motion blur through design and maximizing imagery capture of a scene.

The vehicle motion limits is based on 3 possible conditions:

1. Overlap of successive image frame (minimum percentage overlap)
2. Pixel Velocity limits based on optical flow algorithms (pixel/frame)
3. Camera integration time to avoid blur (~ integration time)

Of the 3, we have observed (2) to be the most important and we will discuss it in more detail in Chapter 6. LWIR camera integration times were found to be approximately ~ 8 ms. Next, we will analyze and discuss (1) Overlap of successive image frame.

Vehicle Motion Imaging Considerations:

FLIR Photon 320 Camera with 14.25° Lens: 46° Horizontal x 36° Vertical, 320x240 (H x V) Pixels, 30 fps

Assuming the distance to the object is typically between 5 – 10 m and the camera is placed on a landscape mode during imaging. We want to estimate the upper limit of the motion we can we apply to the imaging system given the hardware constraints.

$$\textit{Maximum Lateral Motion Distance} = 2 \times \textit{Distance to Object} \cdot \sin(FOV/2)$$

$$\textit{Maximum Lateral Motion Distance} = 2 \times 5\ m \cdot \sin(46°/2) = 3.9m \textit{ between frames @ 5m distance}$$

$$\textit{Maximum Frame Rate} = 1/30\ sec$$

$$\textit{Maximum Lateral Motion Speed} = 3.9m/(1/30\ sec) = 117\ m/s \sim 262\ mph$$

What this means is that if a car moves 262 mph, it can traverse laterally/parallel to the house at a rate of 3.9 m in between full frames of 1/30 of second between each frame. However, in reality, we want to create a virtual panoramic image of the neighborhood and require each frame to have *some* information from the last frame. If we say, we want each corresponding imaging frame to have 90% of the information from the last frame, we limit the lateral speed of the camera by $9/10^{th}$ of the maximum speed. Thus, the vehicle must move at speeds of 26.2 mph or less if we wish to create a virtual stitch of the entire neighborhood. This is an upper limit constraint for motion estimate.

In reality, a vehicle moving at 26.2 mph will introduce motion blur to the captured thermal images. Thermal imagery has limited pixel integration times unlike the conventional visual band during daylight conditions, and therefore, is inherently frame rate limited. Uncooled microbolometers are particularly vulnerable to these limits. The solution therefore is (a) faster frame rate and pixel integration time by utilizing a cooled infrared system or (b) slow the vehicle down.

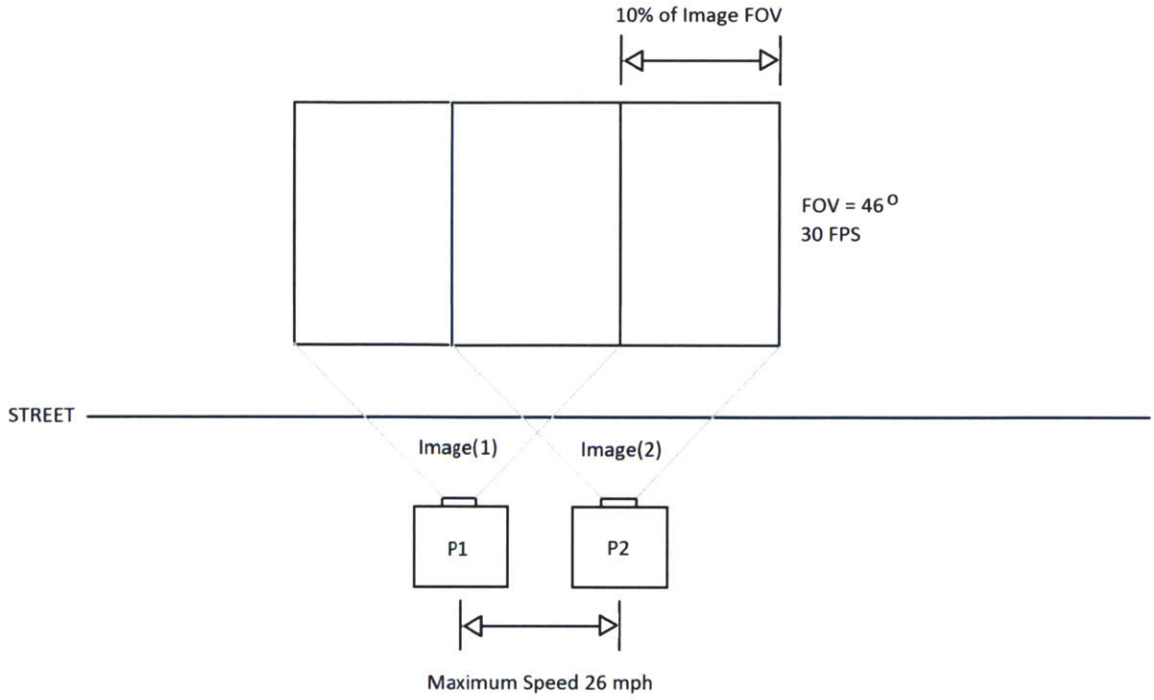

Figure 35: Operational diagram depicting displacement of imaging system and projected image.

Vehicle Vibration modeling:

We are primarily concerned with vehicle vibration due to vehicular motion and road obstacles that will ultimately translate into unstable vibrations for the imaging system, causing damage or unstable operations. The effect of vehicle motion on the ARTIST system can be analyzed in two main categories:

1. Steady vehicle motion and its effect on the optical flow algorithm and on motion blur
2. Vibration induced uncertainty on the imaging system overall.

Vehicle motion and vibrations are a well understood topic. I refer to literature for quarter-car modeling [55-57]. For this purpose of this project, we are not principally concerned with motion inside the vehicle, but more concerned with residual harmonic vibrations that can damage the sensitive imaging equipment at the top of the vehicle. Fortunately, for this project, we have access to a brand new Acura RDX light SUV vehicle, with good suspension systems. The design of the vehicle has incorporated vibration minimization design during its development, testing, and

construction process. Additionally, we will assume that the device is fully coupled to the top of the vehicle through a secured mounting device with a low center of balance. Therefore, we believe that with a well rated new vehicle, uncontrolled harmonic vibration will not be an issue

Small Camera Motion required for Kinetic Super Resolution Process

Without getting into the specific of the motion induced resolution enhancement algorithm, lets lightly discuss another use for this device. I, and other colleagues at the MIT Field Intelligence Laboratory have developed an algorithm called Kinetic Super Resolution, which can enhance the resolution of an imaging system by an order of magnitude or more. This is done through a method called Multi-Frame Super Resolution. The general idea is that by imaging multiple low resolution frames together, we have the ability of infer a high resolution image. It is one the goal of this prototype to develop a demonstration of how KSR can be applied to a vehicle motion for resolution enhancement, particularly in the far infrared range (8000-14000nm) where LWIR technology is financial costly and resolution limited.

To achieve KSR, the imaging system requires multi-frame images with shifts on the order of ± 2 pixels, stochastically derived through random motion. Thus, motion is critical to the success of this project. The key question is: how much source translational motion would be required to achieve ± 2 pixels stochastic random motion in the imaging system, we attempt to model the magnitude of physical lateral and angular displacement to achieve this.

The FLIR Photon 320 Camera with 14.25° Lens: 46° horizontal x 36° vertical field of view, 320x240 (H x V) pixels, 30 fps

320 pixel, 46 degree Field of View = 6.9 pixels/degree Horizontal

240 pixel, 36 degree Field of View = 6.6 pixels/degree Vertical

Thus, for ± 2 Pixels, we are looking to achieve 0.3 degree FOV angular displacement in both the horizontal and vertical directions.

For objects that are 10 m away from the imaging system, that equates to ~ 10m x sin (0.3°) ~ 0.05 m ~ 2 inches. Given this constraint, the requirement for KSR to achieve success is the application of motion so the imager sees 2 inches of imaging displacement on the scene at distances to target object of 10m or 0.3° angular displacement at the base of the camera imaging system.

3.2.1.1.4 Risks & Countermeasures

Risks:

1. Movement of vehicle/imaging system which can cause destructive motion of camera/mounts.
2. The loosening of mounting structure, nuts, bolts, and clamps holding the system together.
3. Cable disconnection issues due to shake
4. Weather corrosion and damage.

Countermeasures:

1. Ensure all joints and mounts are securely fastened. Consider permanent or extreme locking procedures. Reduce all slack within system. Use rigid material selection process.
2. Design using proven mounting systems that have been well tested in actual operating conditions. Consider reliable off the shelf solutions.
3. Manage cable system properly through proper cable management system. Reduce the ability of the cables to get jammed or locked during setup and operation. Considering tubing and cable tie locking in critical areas.
4. Build durable hardware enclosure. Ensure that enclosure can withstand significant physical usage and shock resistance to small damage.

3.2.1.2 Total Cost Estimate, System Parts, & Other Design Considerations

The proposed budget for the imaging system was approximately $18,500. The most expensive components of the system were the camera systems, which accounted for over 70% of the total prototype budget.

System Components & Parts:

Num	Item	Description
1	Sony HDR-XR550V	EO/Near IR HD Camcorder
2	Flir Photon 320	Far IR Camera Far IR Camera
3	Flir Photon 320	Far IR Accessories
4	Car Bike Rack/Mount System	
5	Mid-High End Laptop	Data Capture Machine
6	Near IR Flood Light	800-1000nm LED Floodlights
7	Misc Accessories/Cables/Mounts/Hardware	

Additional Design Considerations:

The design requirements lead to the purchase of modified Sony HD-550V (NIR capable) camcorder with 240gb of local disk storage. The goal was to minimize the data transfer requirements for extended imaging times. This camera was specifically modified to extend the imaging capability of the original manufacturer specification with capabilities to capture images which extend between 300-1200nm. Most conventional camcorders are sold with 350-700nm, which is the visible wavelengths. Beyond this wavelength is infrared, which is considered noise to imaging systems. Conventional CCDs have a thin layer of IR filter film to remove signals beyond 700nm. For our specific need, we wanted to be able to do drive-by imaging at night. Thus, we needed night imaging capabilities. For this to be possible two things needed to be accomplished:

1. Remove IR filter from camera
2. Provide an additional source of IR illumination.

Thus, our intention is to provide IR illumination by use of an IR illuminator thereby allowing us to "see in the dark". This makes night imaging much less intrusive and totally passive and invisible to the naked eye. Hardware power requirement was provided by a 12V DC/AC power inverter using the car's existing power plug to power the entire system which includes imaging, illuminator, and portable computer

3.2.1.3 Design Review

A key design parameter to consider is the primary method for which the device can be mounted to the vehicle for easy installation and removal; yet maintain a high standard of stability and rigidity so that the imaging equipment is protected from being damaged while the vehicle is in motion. The total value of the equipment to be protected through the mounting device is substantial so it is critical that the mounting interface performs to specifications to protect the imaging equipment from physical damage. To achieve this, the following approaches were considered:

Approach 1: Use of existing vehicle mounted "jib" devices that's used in Hollywood movie production and car photography projects

Approach 2: Use of suction devices (single or multiple) that can fasten to the car

Approach 3: Off-The-Shelf ski/snowboard rack mounting devices that you can purchase for vehicles

Approach 4: Build your own mount from scratch

	Quality	Secure	Ease of Mounting	Ease of Removal	Cost	Development Time	Adapting Angle of Camera	Total
Jib	0	0	0	0	0	0	0	0
Suction	0	-	+	+	+	0	-	+1
Rack	+	+	+	+	-	0	+	+4
Build	-	-	0	0	-	-	+	-3

Table 3: Pugh chart selection process for imaging system vehicle mount.

A pugh chart design selection process was utilized to determine which approach is most appropriate for proposed needs of the system. It was determined through this selection process that utilizing an off-the-shelf ski/snowboard rack mount presented the most benefit given the operating constraints. Off-the-shelf racks are a proven technology that many recreational sports enthusiast use to mount their equipment while traveling at high speeds on the highway. Thus, using such a device would help ensure the imaging system's stability requirements would be met.

3.2.1.4 Construction of the System

For the vehicle selection, a 2011 Acura RDX was selected as the default choice mainly because it was my personal vehicle. The RDX came with factory installed roof rack rails integrated on the top of the vehicle. The roof rack rail is rigidly mounted and bolted onto the frame. The rails were designed to mount skis or snowboards mounts directly onto the top of the vehicle via clamps with rubber cushions. The goal then is to design a snowboard-like platform for the device that can be easily mounted and removed with minimal effort, yet provides a stable and secure platform for the imaging system while vehicle is operational.

Figure 36: Acura RDX Roof Rack Mount for winter sport gear [58]

When closed, the compression force of the rubber pads will provide sufficient cushioning and rigidity to hold the snowboard aluminum panel in place. The imaging system will then be securely mounted onto the snowboard plate. This simplistic design easily removable and will be easy to operate for mounting and removing the imaging system on/off the vehicle. After considerable searching at various mountain sports stores, the following were concluded:

1. A majority of skis and snowboard did not provide the stiffness requirement for the needs of the systems.
2. Adult Snowboards are large, much bigger in size and length than is required for mounting the imaging hardware.

Fortunately for the project prototype, the youth section of Sports Authority provided a selection environment that was sufficient and the selection of a small snowboard made of 100% plastic demonstration a very stiff platform for the system. The top of the board is curved while the bottom of the board is flat. A modified version of the board would fit our needs of the systems. The solution to increasing stiffness is to sandwich the plastic board along with a plate of aluminum together (combined weight is less than a comparable aluminum the size of the snowboard and make it easier to transport).

The next part of the phase is to design a method for the imaging cameras to be mounted and removed quickly. An adapted concept from photography was considered and utilized where one can quickly mount and remove a camera from a tripod securely. The chosen method was to use a Manfrotto Quick Connect adapter. It has a dual locking mechanism for a quick release and a smaller gold lock provide double security to ensure the equipment does not get released prematurely. This is all bolted with a ¼" screw. Multiple core base units are used so the imaging equipment is interchangeable and configurable. Additionally, the Manfrotto adapter was utilized allow the change in orientation of the imaging system into portrait mode, thus, allowing the cameras to orient the imaging system vertically as to capture a wider field of view. This crucial design component was important because many homes are multi-story height requirements. Using the cameras in conventional landscape mode will reduce the vertical field of view and would limit the full view of a home. THIS MOUNT DESIGN IS A CRITICAL COMPONENT. With this new mount; one can

adjust, configure, and remove the camera easily. All imaging data from the camcorder needs to be retrieved at the end of a run.

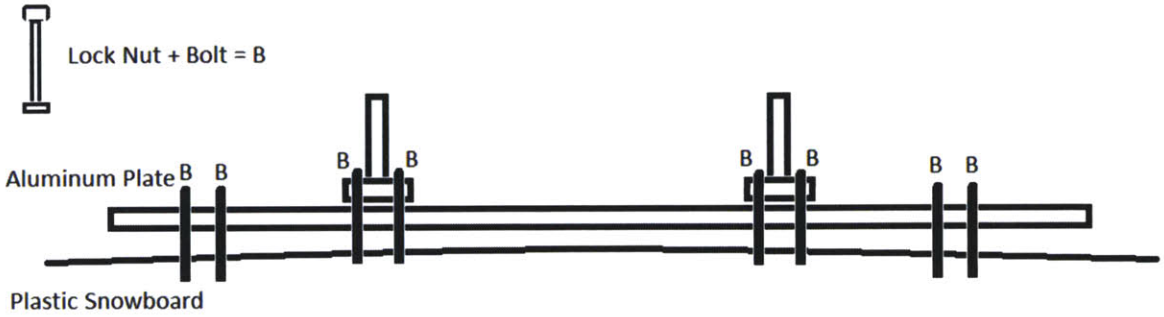

Figure 37: Snowboard & Aluminum Plate Mount Design

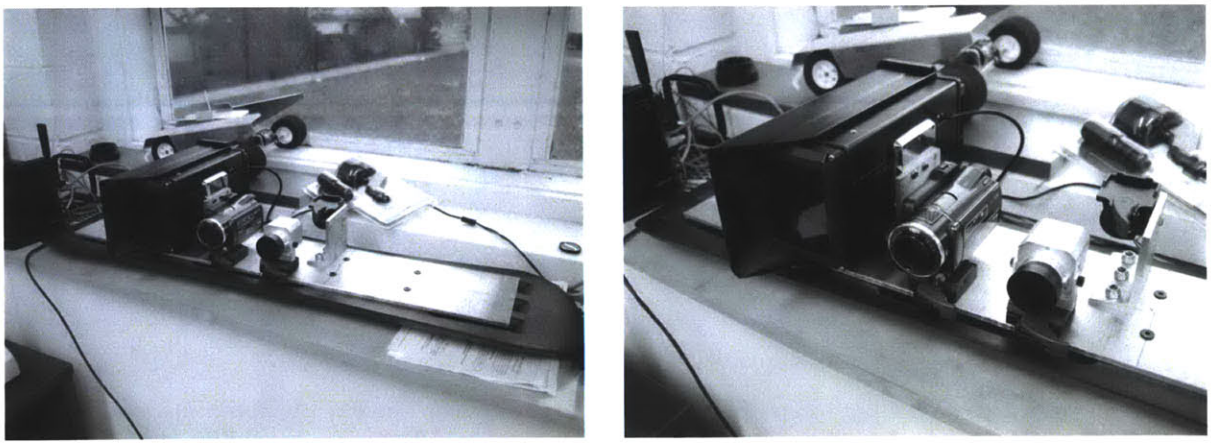

Figure 38: Finished Phase 1 Prototype of Multi-Spectral Imager.

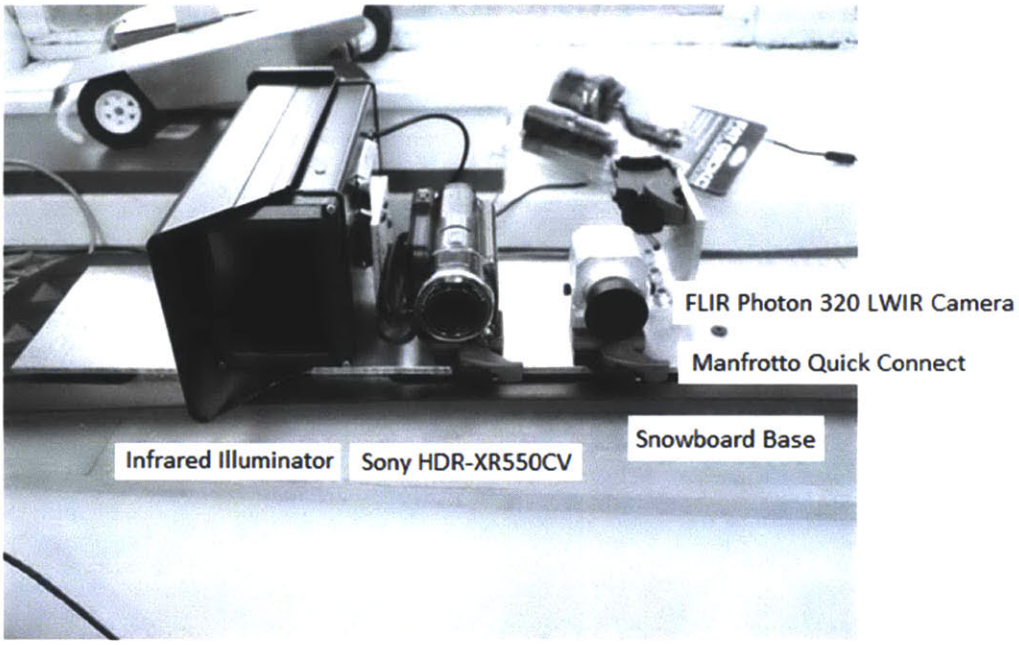

Figure 39: Finished Phase 1 Prototype of Multi-Spectral Imager with details.

3.2.1.5 Operating the System

Once the device was prototyped, it was able to demonstrate full operation by driving through Cambridge and Somerville, MA. The neighborhood chosen to complete the imaging is one that was familiar with because the previous field research using a handheld infrared camera was conducted in the same area. The goal of the Phase 1 proof-of-concept prototype was to demonstrate the ability to conduct high throughput wide area multi-spectral (mainly LWIR) scans. This was successfully demonstrated using the prototype system. The vehicle was able to use drive-by imaging to gather infrared, near-infrared, and EO images. The imager showed stability both in extreme weather and through normal street driving conditions. Even with the potholes and excitations, the system did not fall apart or break down at any point during the field test and actual use of the device.

Furthermore, upon completion of the prototype, the system was utilized to fully map the City of Cambridge, MA where MIT and Harvard reside. Additionally, at the request of the Army Corps of Engineers, the system was successfully demonstrated on an Army Installation.

Figure 40: Finished Phase 1 Prototype Demonstrated with Mount on Vehicle

Figure 41: Tri-Band multi-spectral sample images of a single home in Somerville, MA

The data is captured and stored in real time on a portable laptop PC. Each frame is saved separately as an individual bitmap image and time synced to the laptop's system clock. The laptop system clock is regularly synced to the atomic clock to maintain accuracy. Separately, the laptop is also storing real time GPS coordinate data through a USB enabled device at 10 hertz. In a post processing procedure, each individual frame is synced and geotagged with the GPS data. The data can thus be post processed using a GIS framework to map the infrared images into a visual database and overlaid onto mapping systems like Google Map. In Figure 41, we show that the prototype

system can be used to gather EO, NIR, and LWIR images and relocated on a map. Each wavelength details different visual information that can be used later in a multi-spectral image processing framework.

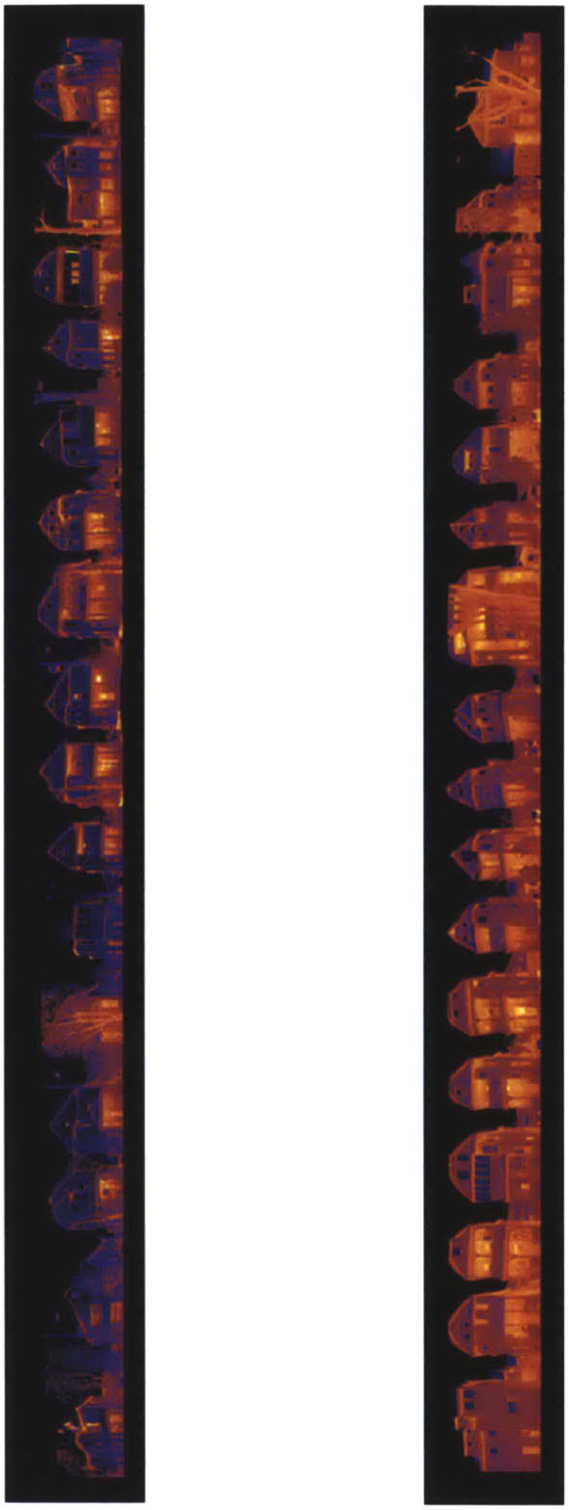

Figure 42: Full Street Thermal Scan of both sides of a street (constructed from thousands of images) in Somerville, MA

The images above were created by mosaicking thousands of individual images together to create the world's first full thermal street scan. This image is of Burnside Avenue, Somerville, MA.

3.2.1.6 Demonstrating the Results

The prototype was successfully demonstrated for the purpose of Phase 1. The key measure of success was that the system was able to acquire several types of imagery using vehicle motion; EO, NIR, and LWIR images at 30 fps on all bands with the ability to geotag reference the location of all the images. This will allow post processing of all the information to be explained in the later Chapters.

An early demonstration of the results is in Figure 42. Utilizing a multi-frame image stitching algorithm through translational image registration developed at the Field Intelligence Laboratory, the research team was able to demonstrate a wide area 2D reconstruction of an entire street. The algorithm is similar to that presented by Levin, Zomet, and Weiss. It will be explored further in the following Chapters.

The image processing required to demonstrate this is extremely complex and will explained later with the introduction of 2D to 3D object reconstruction and how it relates to infrared imaging. For now, the focus will be in examining the results of the multi-spectral imagery collection process. We will note that there are significant observed challenges when dealing with drive-by imaging. These include but not limited to the following:

1. Translational and rotational effects of the vehicle relative to the objects (buildings)
2. Relative motion of varying distance of objects, closer objects move faster, further objects move slower.
3. Optical warping of lens through non-uniformity, particularly the LWIR lens
4. Motion blur introduced from moving vehicle/imager
5. Objects such as trees and cars blocking the view to the target object.

3.2.1.6.1 Image Analysis

An initial first order image processing analysis was performed on the Cambridge, MA data. The following sequences of post processing steps were taken to analyze the thermal images:

1. Aggregate all thermal images onto one source
2. Geotag each image with the GPS coordinate of the location of the vehicle
3. Place all data onto a GIS map database to organize the data into a spatially accessible map of all the images.
4. Individually apply object detection algorithm to automatically segment thermal leaks based on gradient and camera signal output (pixel intensity) information on the images.
5. Apply a generic scoring system to qualify an energy score

This initial analysis was only utilized to obtain very preliminary results for a spatially variant energy map for the City of Cambridge, MA. As one can see in the following example, the leaks are not distance and viewing angle normalized, which means the score is based on an absolute scale and has significant limitations and value in interpretation. This early preliminary finding inspired further research into 3D modeling and image reconstruction in the following Chapters. However, the preliminary results were very encouraging and served to show that it is possible and valuable to be able to map and find energy leaks, albeit at a very crude first pass at quantifying energy losses through analysis wide area thermal imagery.

$$energy\ score_{building} = \sum_{n=0}^{n=N} f(Area, Luminosity\ Intensity, Radial\ Location\ on\ Map) \quad (50)$$

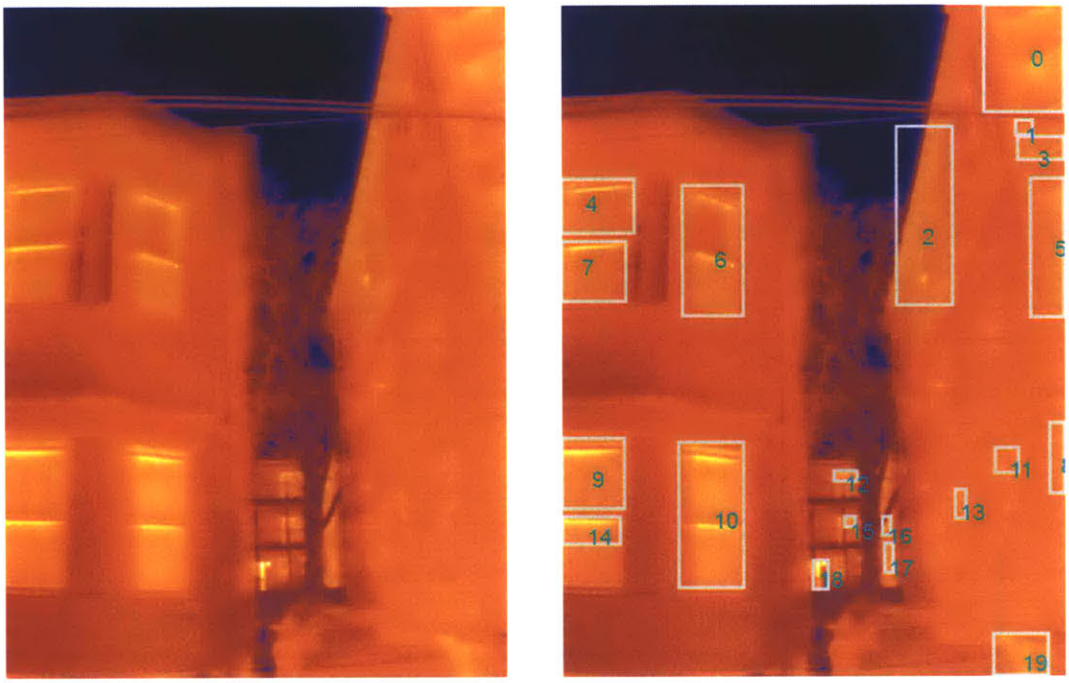

Figure 43: LWIR image of Home A (left) and post-segmented for thermal gradients (right). Courtesy of Dr. Jonathan Jesneck, Research Scientist, MIT.

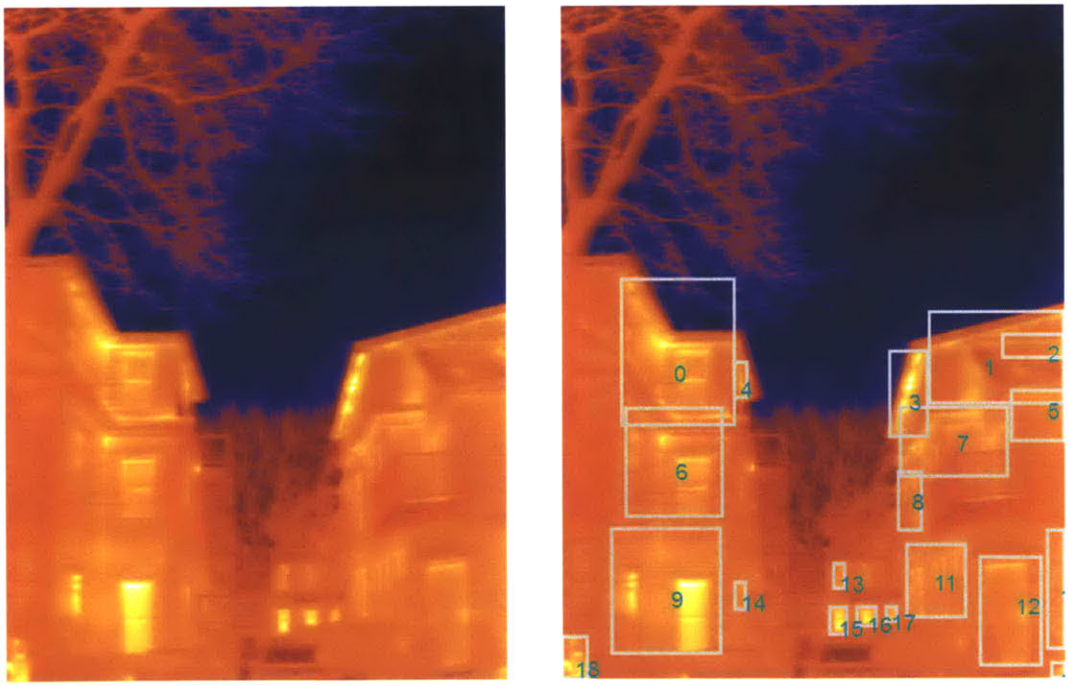

Figure 44: LWIR image of Home B (left) and post-segmented for thermal gradients (right). Courtesy of Dr. Jonathan Jesneck, Research Scientist, MIT

3.2.1.6.2 Leak Size Analysis

In this analysis, we will quantify the size of each of the segmented pixel area identified as having a high thermal gradient, as identified by the segmentation algorithm. Although an area may be identified as a high thermal gradient, it need not be thermal leak, e.g. it may be a warm street lamp or a hot vehicle. The thermal gradients of interest refer to 'energy leakage', which may fall into one of two categories: (a) conduction losses due to poor insulation, such as a poorly insulted wall or (b) convection losses due to air leaks, such as a small gap under the door.

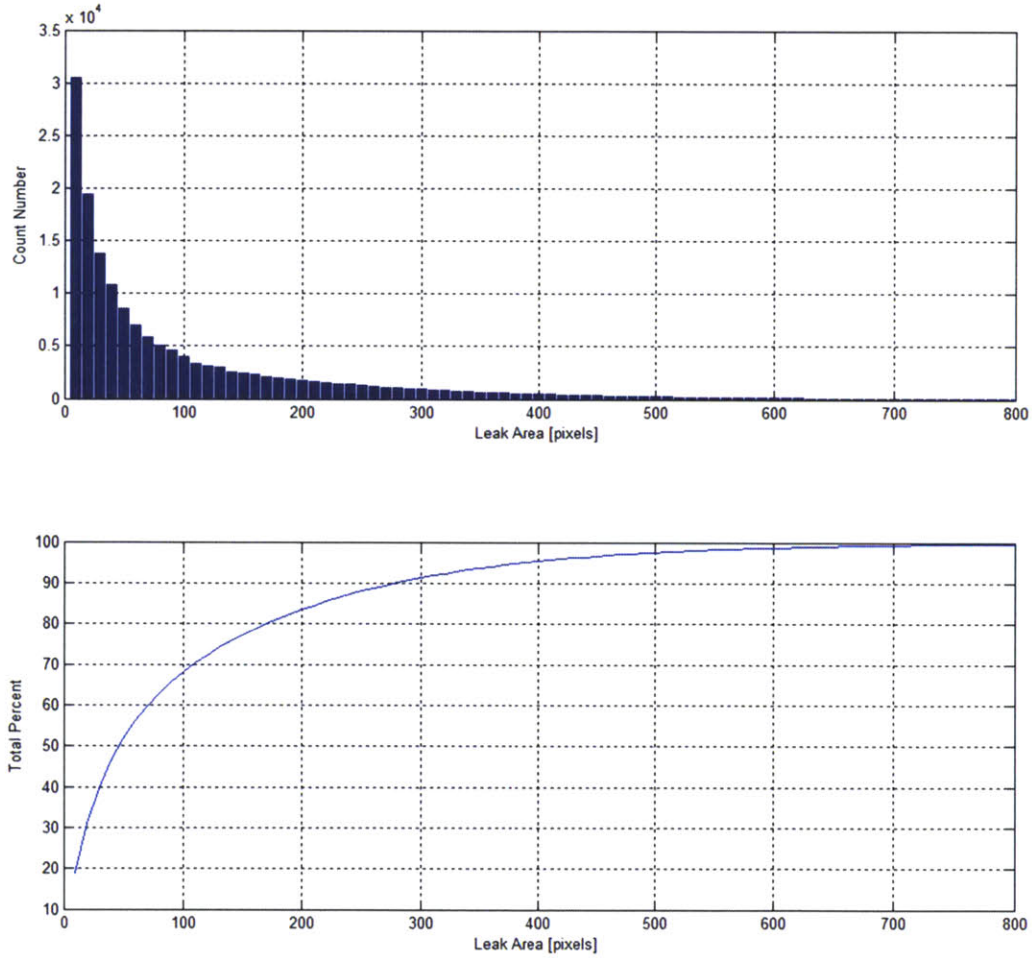

Figure 45: Histogram of synthetic energy leak size (based on gradient analysis) vs quantity for City of Cambridge, MA

From analyzing all the images from Cambridge, MA, we were able to segment and quantify the size of each hot thermal gradient (pixels) based on high thermal gradients. We have not identified the

nature of the thermal gradient, such as conduction due to poor insulation or convection due to air leakage. Size quantification of the hot thermal gradient is seen as a crude but effective way of quantifying the relative number and size of the problems from a macro urban scale. In Figure 45, we show a histogram of this analysis. What this histogram signifies is that there are a significantly greater number of small thermal gradients identified in Cambridge than large ones. The results resemble a Pareto 80/20 diagram, where 80 percent of the problems occur in 20% of the solutions. Therefore, if we take a similar view of the problem, 80% of the problems occur in the smallest 20% of the leaks. However, to be more precise, this number looks to be about 70/20, where 70% of the problems occur at the smallest 20% of leaks. At least from a preliminary point of view at this point, size does matter, specifically "small" leaks. This brings up more questions than answers:

- Why are there so many small leaks (by thermal gradient) ? Is it leaks on the envelope of buildings or foreign objects?
- What about distance to the object, does it matter?
- What about viewing angle to the object, does that matter? How to account for this?
- What are the limits of detecting small leaks? Does improving resolution help? Why?

These are some of the common questions that came up at the end of this initial research study. The conclusion points to the fact that it is important to be able to perform detailed analysis on small leaks, mainly due to the fact that there are so many small leaks compared to large ones. Imaging resolution does matter and thinking of higher resolution infrared imaging will be critical to detecting small leaks.

3.2.1.6.3 How to Increase Resolution

Understanding that maximizing imaging resolution will be critical to understanding and detecting small leaks, there are three areas of resolution enhancement in the system: spatial, spectral, and temporal resolution. In the ARTIST system, we are targeting to maximize resolution in all 3 domains using the following methods.

	Hardware	Software
Spatial	Multi-Camera Synthetic Aperture	Hyper Resolution/KSR
Spectral	EO-NIR-LWIR Bands	none
Temporal	30 FPS Real-time	none

3.2.1.6.4 Energy Score Mapping

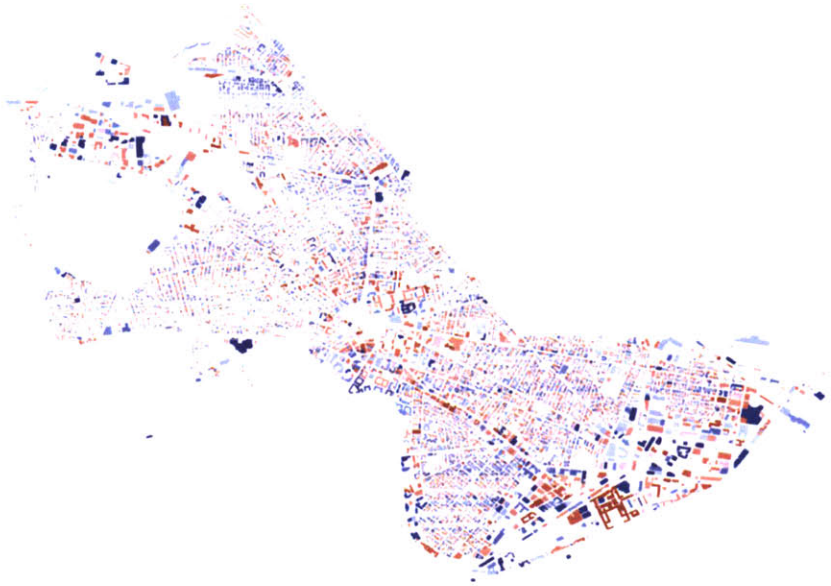

Figure 46: GIS mapping of synthetic energy score for City of Cambridge, MA[3]

[3] Courtesy of Dr. Jonathan Jesneck, Research Scientist, MIT

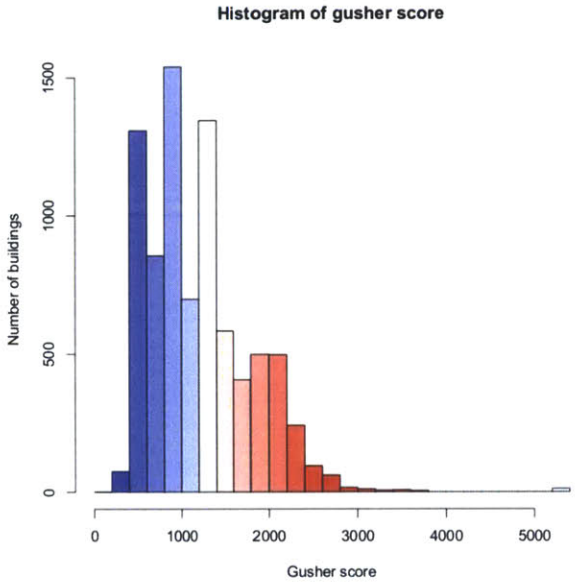

Figure 47: Histogram of synthetic energy scores for City of Cambridge, MA[4]

The result from analyzing the City of Cambridge infrared imagery data plotted onto a GIS map showing the raw score (not normalized) for individual buildings on the map. Red signifies "energy gushers", high scores, and blue signifies "non-gushers", low scores. This is presented as a simple way to allow one to visualize "negawatt" potential within a city based on first order analysis of thermal imagery. Additionally, an online demo was created to show the ability to zoom into a particular building in the city to display the infrared imagery of that building via the web.

3.2.2 Phase 2: A Synthetic Aperture Multi-Spectral Imaging System

A synthetic aperture imaging system is a virtual camera system that extends the total capability of system beyond the native capability of the single camera. It is "synthetically" creating a camera system beyond the native capabilities of a single camera. Through digital manipulation and image processing, it is now possible to create a virtual camera system by combining two or more cameras together in a configuration that mimics camera tiling, like we demonstrated in the previous sections. By tiling the cameras in a synthetic configuration, the system overcomes the need to manually move

[4] Courtesy of Dr. Jonathan Jesneck, Research Scientist, MIT

the camera after each successive frame to increase the total field of view. The new synthetic effective field of view (FOV) is the sum of the field of view of each in individual camera minus the overlapping pixel areas. In essence, the total field of view of the system can be extended through this virtual tiling method. Additionally, but mounting the system onto a platform like a vehicle, we can additionally use the vehicle's forward motion for further enhance the total field of view or "aperture" of the system. Together, these two concepts make the synthetic aperture idea appealing.

$$Effective\ FOV\ (H,V) = \sum_{c=1}^{c=N} FOV\ of\ Single\ Camera\ (H,V) - \sum_{c=1}^{c=N} FOV\ of\ Overlap\ (H,V) \quad (51)$$

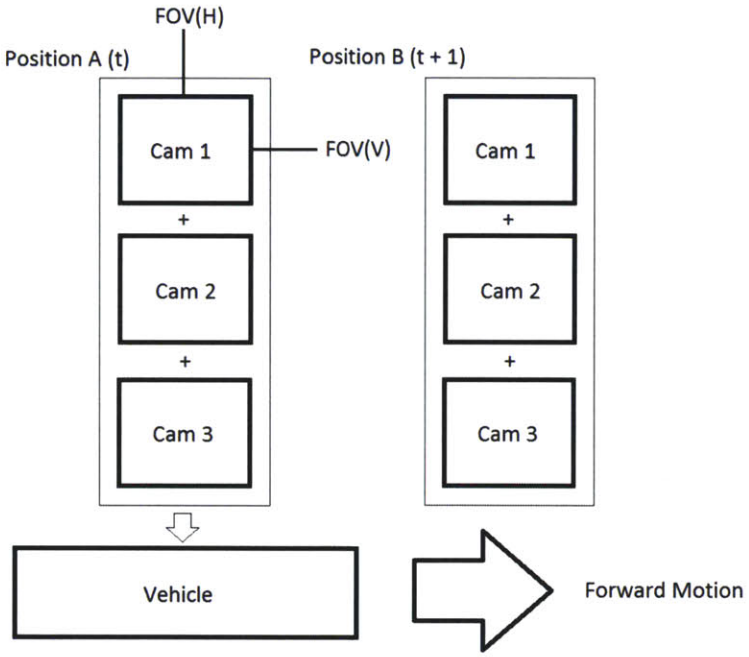

Figure 48: Vehicle & camera system displacement showing motion of single sided synthetic aperture system (3 camera design).

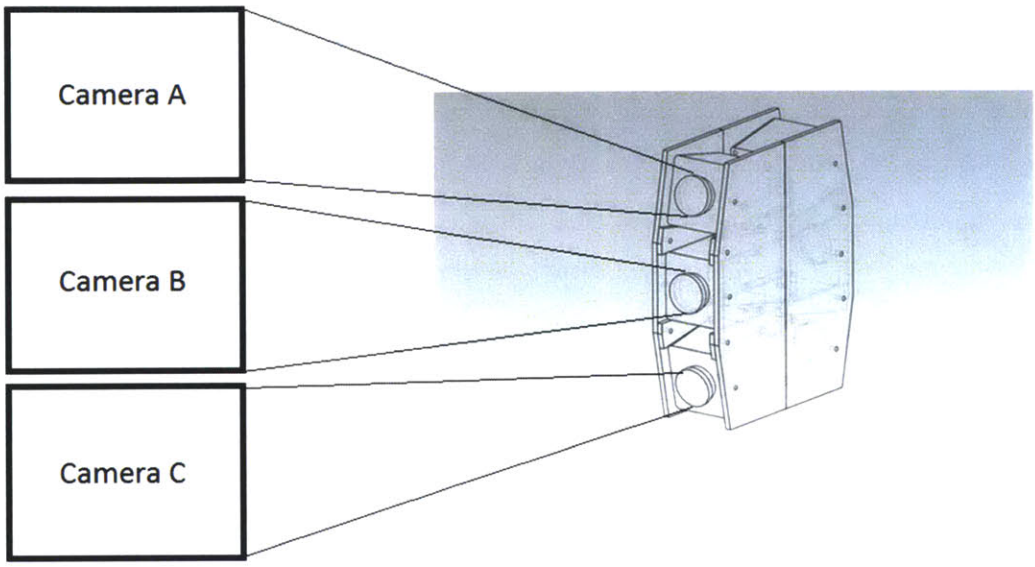

Figure 49: An initial prototype of the multi-camera synthetic aperture mount design with corresponding projected image.

Additionally, we should also consider the benefit of extending this capability into multiple wavelength imaging bands to create a multi-spectral system. From Phase 1, we demonstrated that the system can take images in EO, NIR, and LWIR wavelengths. By doing so, we can see information at surface that may include color, texture, reflections, and temperature. By fusing this information together, we can consider the possibility that artificial intelligence or learning algorithms can be used to predict the nature, type, and morphology of each energy problem.

3.2.2.1 Lessons Learned from Phase 1

In Phase 1, the prototype was able to provide a significant amount of insight and lessons learned. However, there were inherent limitations on the system because it was only meant to be a proof-of-concept prototype. Some of the limitations of the prototype system were:

1. Limited Resolution on LWIR (320x240)
2. Limited vertical field of view
3. One side of vehicle only
4. Not cost effective (LWIR imager ~ $10,000 with accessories)
5. Required continuous portable computing support for imagery and GPS recording
6. No thermography capability, Non-radiometric LWIR camera

7. Auto-gain control and gain-locking features very difficult, control requires portable PC

These limitations allow us to refactor these variables into the design of a new system. The biggest limitation on the system was (a) resolution and (b) field of view. The limited resolution of the prototype system made it difficult to classify the nature of many of the leaks. The low resolution made difficult to determine what exactly was the type of problem, what type of heat transfer is happening at the area of interest, and makes it difficult to track and re-identify the problem in a follow up scan.

Therefore, we determined ultimately the system's performance was driven primarily by resolution. There are three types of resolution:

1. Spatial resolution
2. Spectral resolution
3. Temporal resolution

For our new system, we are interested in maximizing all three. Increasing spatial resolution will allow us to see more details in a particular area of interest. Increasing spectral resolution, through multi-spectral imaging, will allow us to see more details in different spectral wavelengths. Increasing temporal resolution will reduce motion blur and provide more frames to analyze at any particular spatial mapping area.

3.2.2.2 New Design Parameters

The limiting factors of the original prototype made the design of the next prototype significantly more challenging. Immediately following the winter of 2011, a complete redesign was initiated to solve some of these challenges. In the Phase 2 design, the following functional requirements and considerations are taken into account:

1. Increase total imagery spatial resolution of the system
2. Increase the total field of view, FOV
3. Be able to see both sides of the streets
4. Must be cost-effective to develop and manufacture

5. Requires no support from portable computing systems
6. Easy camera control for controlling gain settings
7. Thermography capability a MUST

Most importantly, of all these design parameters, the system must have a wide field of view and be able to see an entire view of a home or building of 4 stories or higher at a reasonable distance from the vehicle. Assuming each level of home is approximately 4 stories, or 40 ft. The problem with the Phase 1 prototype imager is that it was based on one thermal camera with a specific lens, which provided a field of view of 40° by 30°, the widest angle available for commercial thermal lens. Based on a single thermal imager alone, it was not possible to meet the wide field of view objective unless one wanted to reconsider mechanical mirror systems based on single line scanners. Therefore, an entirely new approach had to be considered for the next and final prototype of Phase 2.

3.2.2.3 Spatial Resolution Analysis

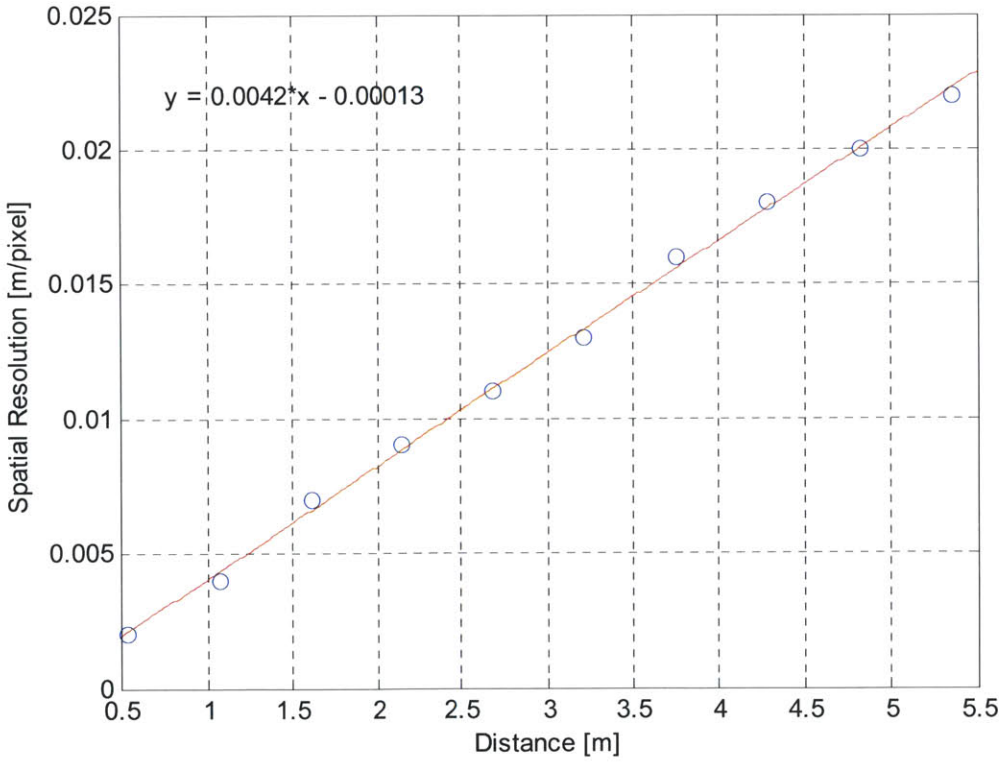

Figure 50: Spatial Resolution vs Distance for FLIR Photon 320 camera

Figure 50 above illustrates the spatial resolution transformation table that shows the spatial resolution per pixel at various distances to the camera. At 10 meters, which is about 32 feet, a typical distance to a residential building, the spatial resolution is ~2.2 cm/pixel. This is relatively poor spatial resolution since a majority of air infiltration leaks on buildings are much smaller than 2.2 cm, making it very difficult to detect in post-processing.

One way to improve the spatial resolution is to increase the camera's resolution. Commercial off-the-shelf LWIR systems are inherently limited by costs, resolution, and frame rate. The FLIR Photon 320 is a 320x240, 30 FPS, and costs about $10,000 (accessories included). It is an uncooled LWIR camera, which means it does not have to be cryocooled and thus, suffers from the inherent limitations of detector sensitivity due to local radiant noise.

3.2.2.4 System Goals & Solutions

Based on the goals outlined at the beginning, the proposed design parameters and solutions is the following:

Problem	**Solution**
• Increase total imagery spatial resolution of the system	• Use higher resolution 640x480 uncooled microbolometer LWIR cameras
• Increase the total FOV	• Array multiple cameras into a configuration that will cover a wider FOV
• See both sides of the streets	• Place camera system on BOTH sides of the vehicle
• Design for manufacturing	• Apply design for manufacturing techniques, be able to outsource future production
• Requires no support from portable computing systems	• Develop non-portable computing storage mechanisms
• Easy camera control for controlling gain settings	• Develop independent camera control system
• Thermography capability a MUST	• Develop new calibration techniques for thermal use for non-radiometric cameras (No thermal features).

At the end of winter 2011, the project managed to recruit several students and volunteers to help build the next version of the prototype. Joshua Siegel (MIT SB, '11), Mark Nuykens (High School Summer Intern), and Napoleon Phan. Together, the team helped to redesign and build of a new alpha prototype of the multi-spectral imaging system.

3.2.2.5 System Components

We start to design the new layout of the multi-camera synthetic aperture system. To accomplish this, we designed a multi-camera array comprising of 3 LWIR cameras each side of the video and 2 EO/NIR cameras facing the front and 2 facing the rear, on each side of the vehicle. In total, the system contains 6 LWIR Cameras, 8 EO/NIR Cameras, and has a much more sophisticated controller/vehicle position recording system.

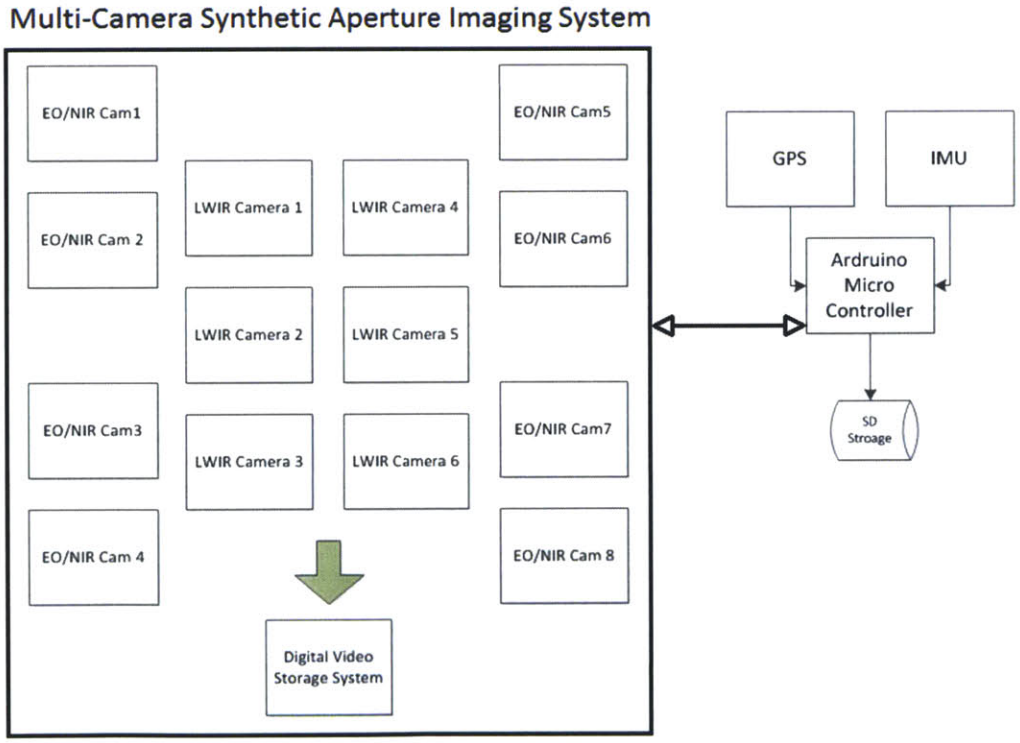

Figure 51: The ARTIST Hardware Design Layout of the Multi-Camera Multi-Spectral Imaging System

3.2.2.5.1 LWIR Camera: DRS UC640-17

For the infrared camera, we considered a number of different camera models from a group of different manufacturers. At the conclusion of the LWIR selection process, the DRS UC640-17 camera was chosen. It had excellent price performance profiles and was highly recommended by many of the LWIR distributors [59]. The introduction of the DRS 640 camera brings and immediate spatial resolution improvement from 2.2 cm/pixel to 1.1 cm/pixel at a distance of 10 m. The DRS UC640-17 is a long-wavelength (8 – 14 microns) uncooled VOx Microbolometer camera designed for infrared imaging applications, is built for high resolution, small size, light weight, and low power consumption. The UC640-17 is available in two configuration formats: a ruggedized, environmentally sealed OEM (housed) and SC (open frame split electronics) configuration. It comes with a variety of lens focal length options. The UC640-17 camera is designed for "volts-in, video-out" capability. The introduction of the DRS 640 camera into the new design brings an immediate spatial resolution improvement from 2.2 cm/pixel (Photon 320) to 1.1 cm/pixel at a distance of 10 m. Some additional specifications for the DRS UC640-17 camera:

- Local Area Processing (LAP™) image enhancement technology
- Resistance to solar damage
- Configurable SMPTE-170/PAL Analog Video Format
- Commercial digital frame grabbing (Camera Link)
- 14-bit front end resolution
- Frame synchronization capability

Figure 52: DRS UC640-17 Microbolometer LWIR Imager

3.2.2.5.1 EO/NIR Camera: TPS-QLBAZ1

Next, we made a selection process for the EO/NIR based, which came from a security camera apparatus. The EO/NIR camera was chosen to we replaced the modified Sony Digital camcorder with an off-the-shelf solution using a night vision camera Model # TPS-QLBAZ1. This is a high performance camera meant for security related applications with the following specifications.

The main specifications for the camera Model # TPS-QLBAZ1 is:

- 1/3 inch Sony High Resolution Superhad CCD
- 650 TV Lines, Super High Resolution
- Minimum Illumination 0 Lux
- 12V DC/24V AC
- Current Consumption 80mA
- Dimensions 3.5 inch(w) x 8.5 inch(l)
- Operation Temperature -4° ~ 140°F
- Weight 3.5 lbs

Figure 53: Model TPS-QLBAZ1 EO/NIR Night Vision Security Camera

3.2.2.6 Design Notes

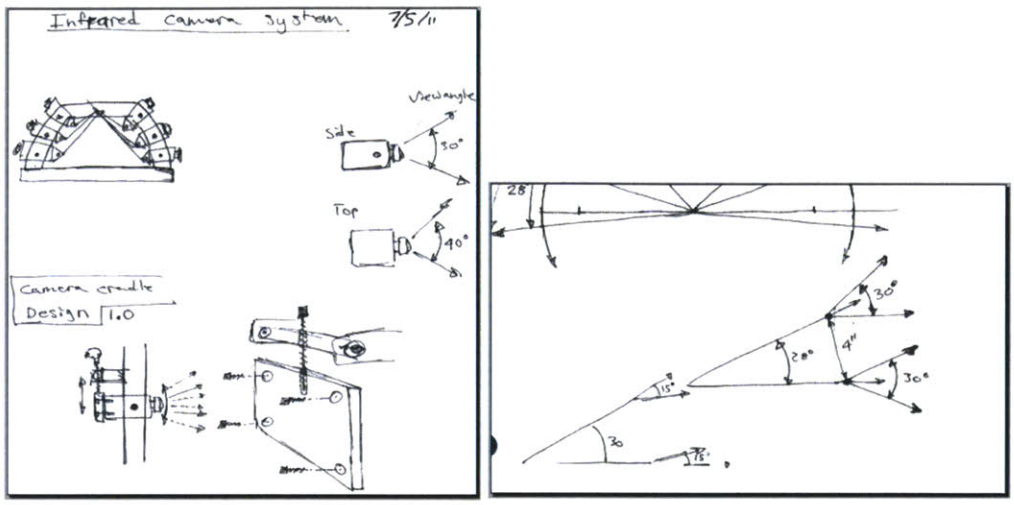

Figure 54: Notes from initial design of new camera layout (Courtesy of **Mark Nuykens, Summer 2011)**

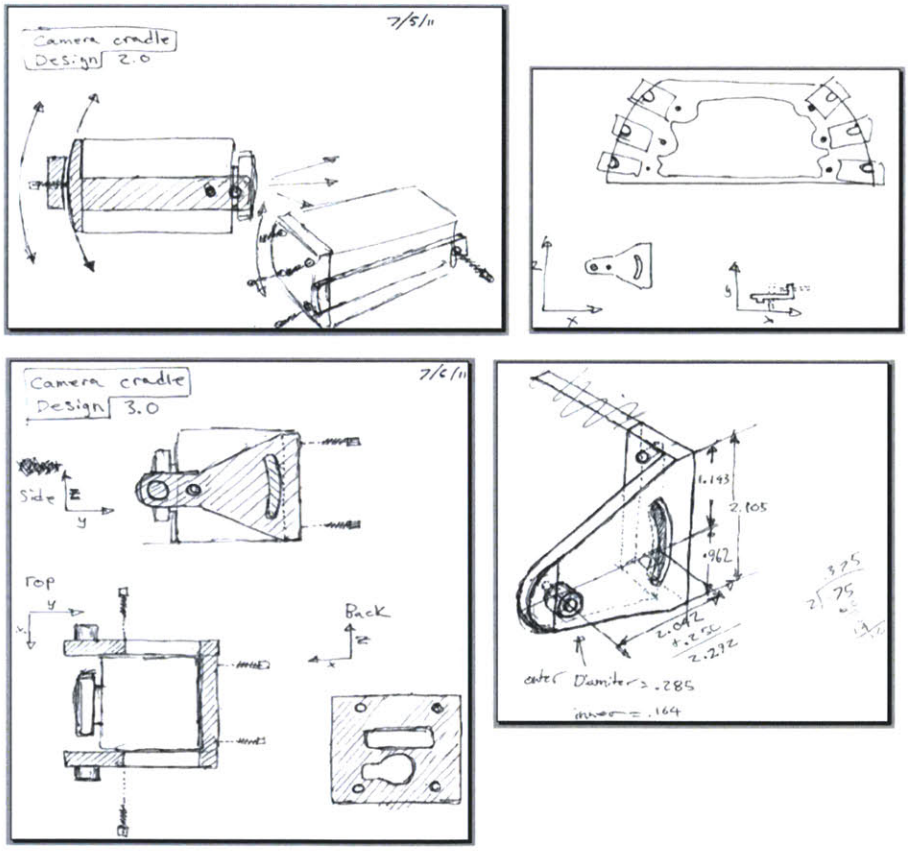

Figure 55: Notes from initial camera mounting system (Courtesy of **Mark Nuykens, Summer 2011)**

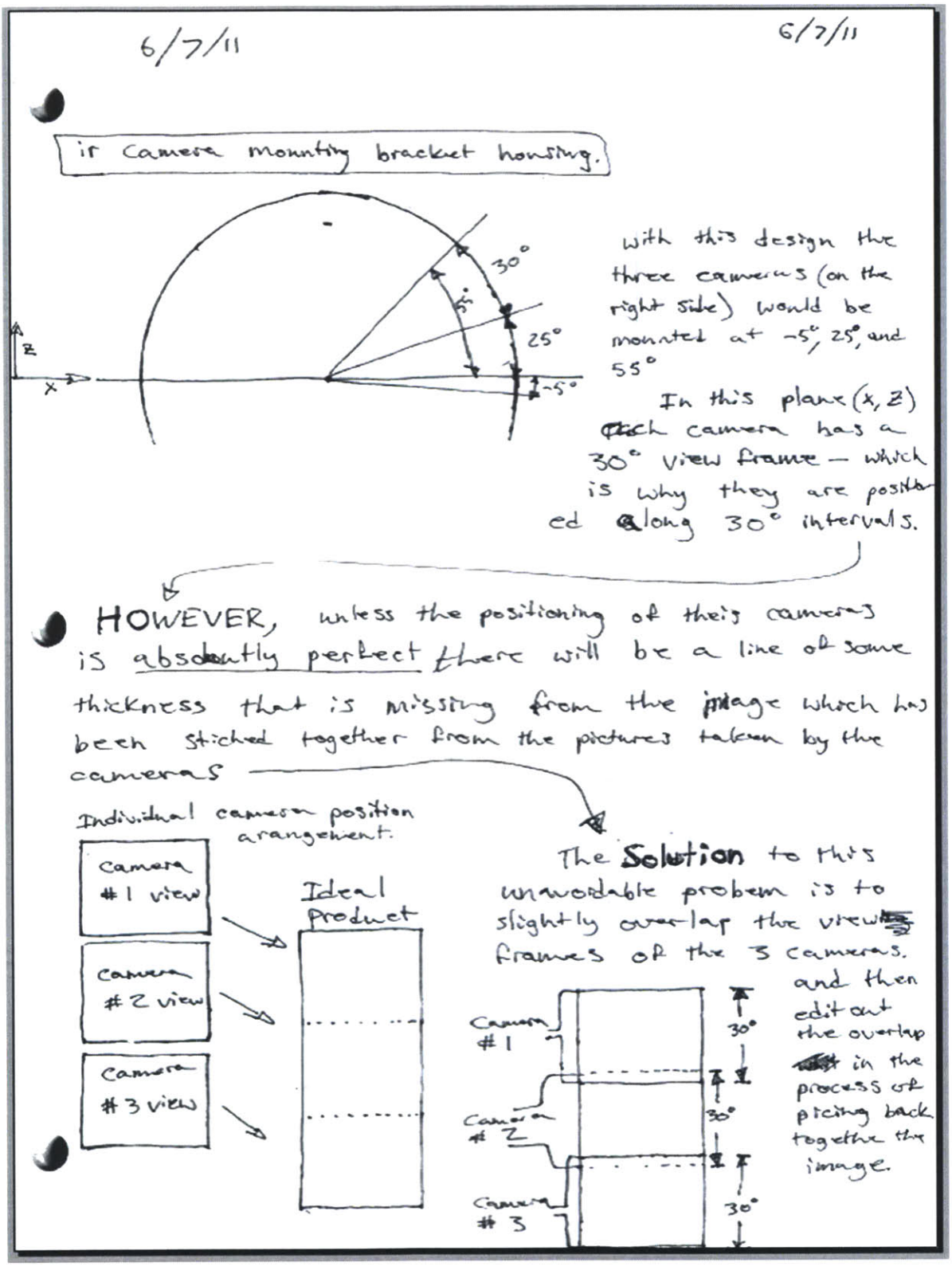

Figure 56: Camera arraying design consideration (Courtesy of Mark Nuykens, Summer 2011)

3.2.2.7 Constructing the System

With the combined efforts of the research team, the team was able to design and construct the entire Phase 2 system over the course of 6 weeks in the summer of 2011. Together, the individual members worked on the following components:

- Designed layout of new system
- Purchased and gather parts
- Waterjet cut major parts
- Assembled components into the imager
- Designed wiring system
- Designed and developed navigational electronics and LWIR control system
- Made cabling components for each individual camera and designed tubing system and enclosure for the entire system.
- Individually test each sub-system
- Integrated all systems together to create a working prototype.
- Mounted on a 2011 Ford Explorer vehicle
- Implemented Increased Spectral & Temporal Resolution:
    - 6 x Long Wave IR Cameras, 640x480
    - 8 x EO/NIR Cameras, 640x480
    - 30 FPS Real-Time Recording

Upon completion of the system, it was rigorously tested in the field during the summer of 2011. In total, the system operated successfully for hundreds of hours of field test and thousands of miles of driving while successfully surviving the rigors of road usage. Among the most complex part of the system was the cabling. Each individual camera required its only set of power, video signal, and camera control signal. In the case of long wiring, attenuation of noise through the wiring system require correct grounding of and proper shielding. In certain cases, the wiring became loose over time and required the cabling system to be redone for that specific camera. Additionally, the DRS-640 cameras required a specific type of connector that was both costly and very challenging to work with due to the extremely small size and double coloring system.

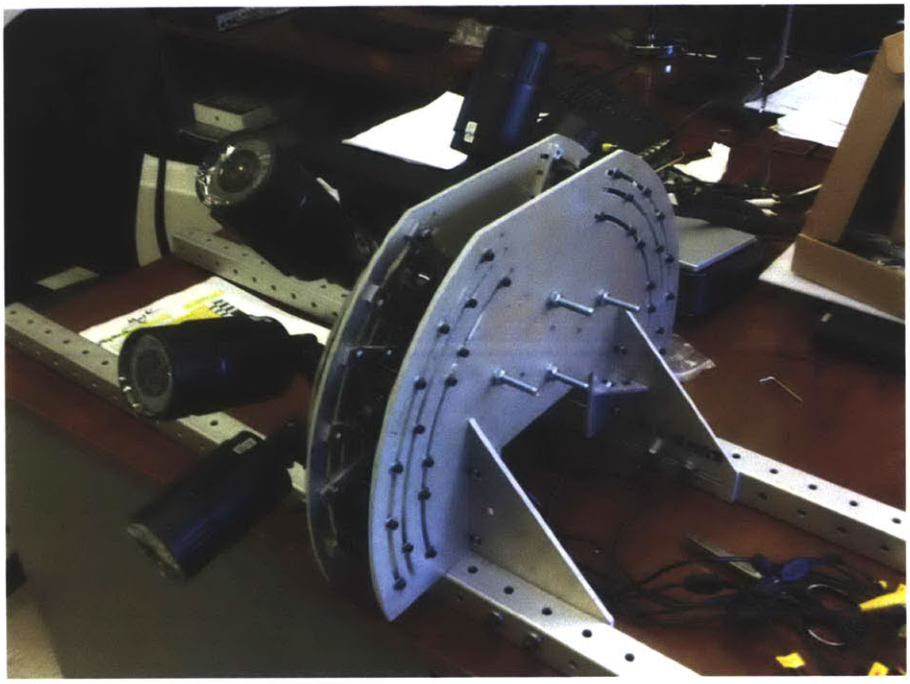

Figure 57: Partially assembled ARTIST Phase 2 prototype of hardware imaging system

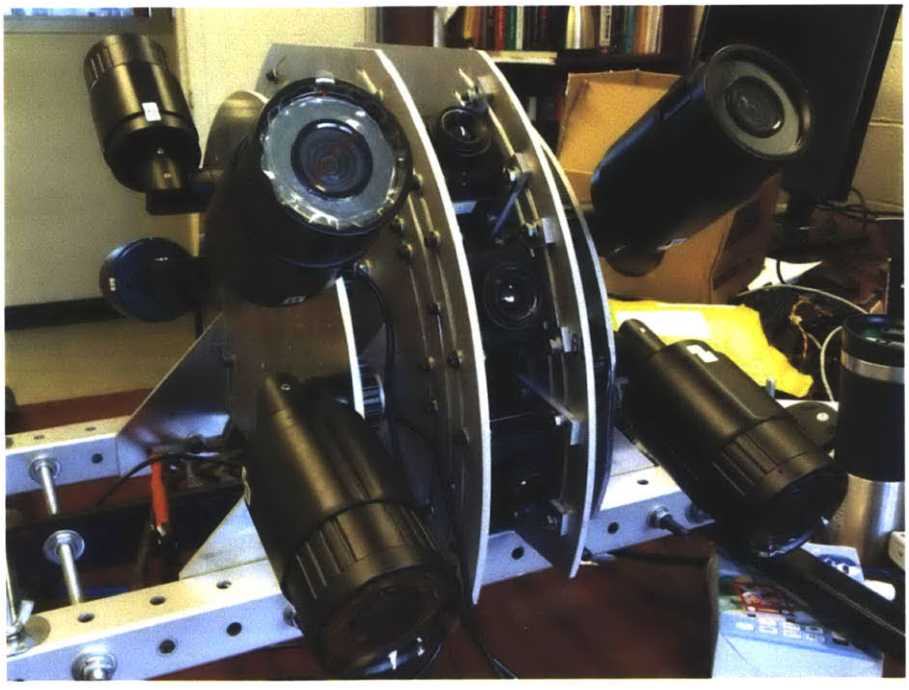

Figure 58: Fully assembled ARTIST Phase 2 prototype of hardware imaging system

Figure 59: Research team mounting of ARTIST Phase 2 prototype on 2011 Ford Explorer

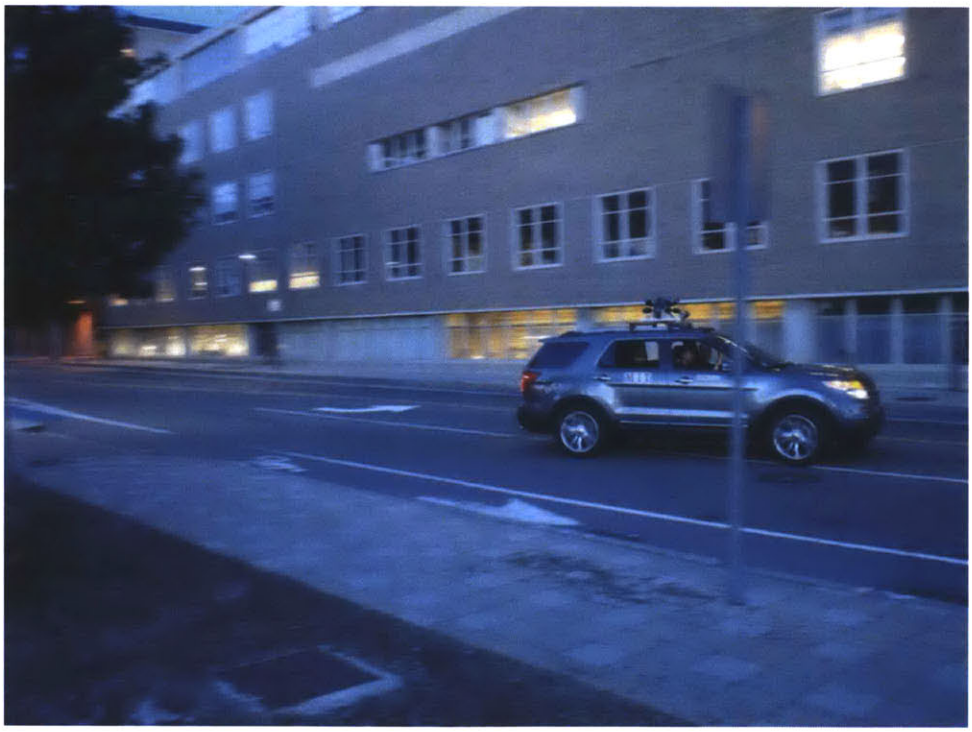

Figure 60: Road test ARTIST Phase 2 prototype in front of MIT Building 35

3.2.2.8 Vehicle Data Recorder

In the Phase 1 prototype system, we used USB based GPS data logger that required a PC to operate. During the alpha prototype design, it was critical that the GPS and IMU logger be capable of operating without a PC. For that purpose, a designed was chosen to have a completely independent data recorder, similar to blackbox flight recorder, except this is a vehicle data recorder used to log vehicle data. The focus was to build a highly accurate GPS recorder with high sampling rate. This is necessary because the imagery data being recorded is captured at 30 fps. 10 hz GPS recording is the highest speed commercially available cost effective solution. Combined with the Razor IMU, the system is capability of very high resolution positioning of ± 3 ft. The primary components for a vehicle blackbox recorder are:

1. Arduino Mega 2560 R3 microcontroller
2. MediaTek MT3329 GPS 10Hz
3. 9 Degrees of Freedom - Razor IMU
4. Arduino Ethernet Shield

The components were assembled into single integrated vehicle blackbox recording system.

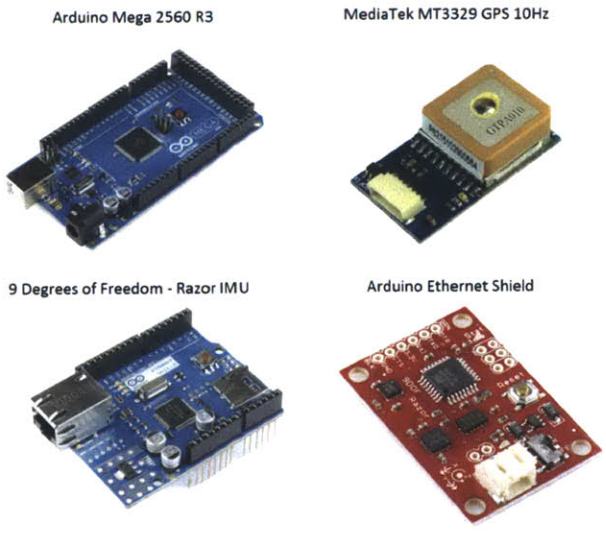

Figure 61: Individual hardware components of vehicle blackbox recording system

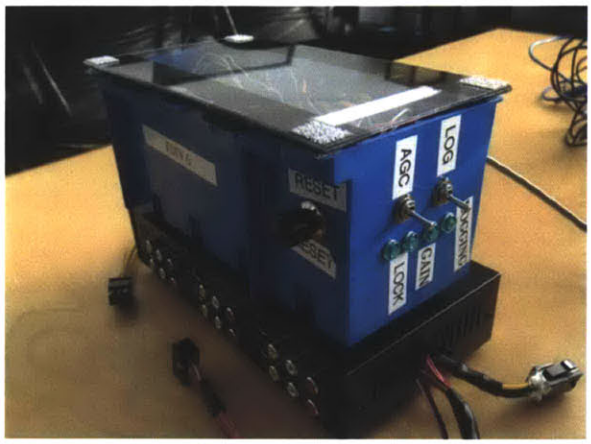

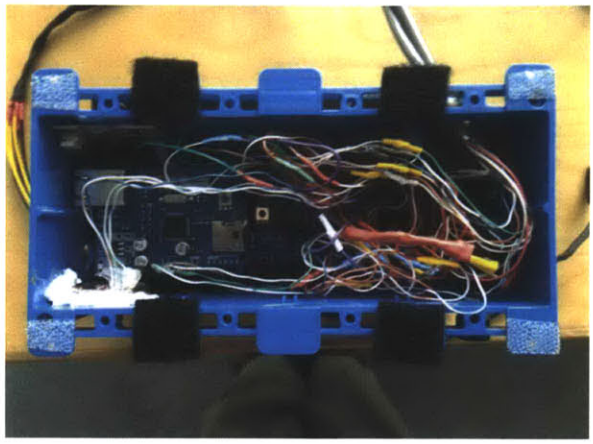

Figure 62: Fully assembled vehicle blackbox recording system- allows operation of imaging system without the need for a portable computer for recording GPS/IMU data and camera calibration.

Specifications of components:

- Arduino Mega 2560 R3 microcontroller [60]
- ATmega2560 microcontroller
- Input voltage - 7-12V
- 54 Digital I/O Pins (14 PWM outputs)
- 16 Analog Inputs
- 256k Flash Memory
- 16Mhz Clock Speed

MediaTek MT3329 GPS 10Hz Specifications [61]

- L1 Frequency, C/A code, 66 channels
- High Sensitivity:Up to -165dBm tracking, superior urban performances
- Position Accuracy:< 3m CEP (50%) without SA (horizontal)
- Cold Start is under 35 seconds (Typical)
- Warm Start is under 34 seconds (Typical)
- Hot Start is under 1 second (Typical)

- Low Power Consumption:48mA @ acquisition, 37mA @ tracking
- Low shut-down current consumption:15uA, typical
- DGPS(WAAS, EGNOS, MSAS) support (optional by firmware)
- USB/UART Interface

9 Degrees of Freedom - Razor IMU Specifications [62]

- ITG-3200 - triple-axis digital-output gyroscope
- ADXL345 - 13-bit resolution, ±16g, triple-axis accelerometer
- HMC5883L - triple-axis, digital magnetometer

Arduino Ethernet Shield [63]

The Arduino Ethernet Shield allows an Arduino board to connect to the internet. It is based on the Wiznet W5100 ethernet chip providing a network (IP) stack capable of both TCP and UDP. The latest revision of the shield adds a micro-SD card slot, which can be used to store files for serving over the network.

3.2.2.8.1 Extended Kalman Filtering for Navigation Analysis

The GPS sensor and IMU were built fully integrated enclosure, fully coupled into a rigidly mounted enclosure. The GPS is a low frequency sensor, providing state information at relatively low update rates [10 hz]. The errors in GPS positioning occurs when the GPS carrier signal undergo multipath errors in an urban environment. Hence, the term "urban canon" used to describe such situations. Specifically, these errors occur when the GPS signal is reflected off of one or more surfaces before it reaches the GPS receiver antenna. The slight increase in time delay for the signal to reach the antenna will affect the GPS fix and as it alters the phase of the signal being used to calculate position. Another possible can error, although much less often, is when the GPS changes satellite configuration due to geometry of the observed satellite signal fix. Thus, errors in positioning in a GPS is predominantly environment dependent. Open environments, no trees, buildings, mountains, or clouds are more ideal operating environments for GPS devices. Even with improved performance on the hardware design and components, multipath errors will always remain.

The primary advantage of using an IMU is the high update rates for acceleration, angular rotation, and attitude information. Therefore, velocity and position of the vehicle can evaluated using pre-defined filters. The disadvantages of an IMU are errors caused by bias in the sensors which accumulate over time. The IMU utilized in the blackbox design is based on three accelerometers, three gyros, and three magnetometers. These sensors provide acceleration, rotation rate, and tilt of the blackbox.

The GPS and IMU systems are fused to form an integrated navigation system utilizing an extended Kalman filter. Mathematically, the real-time positioning error can be expressed as:

$$\sigma_{RT}^2 = \sigma_{GPS}^2 + \sigma_{IMU}^2 \quad (52)$$

where σ_{RT}^2 is the real-time position error variance, σ_{GPS}^2 is the GPS position error variance, and σ_{IMU}^2 is the IMU prediction error variance as a function of time.

The navigational blackbox data recorder is used to record GPS and IMU data in real time. It is not critical for this project to predict real-time positioning. Therefore, it is important to state that the logged data will be utilized in in post-processing framework to infer accurate position for geotagging purposes. An extended Kalman filter was applied to the GPS/IMU data for fairly accurate positioning calculation that resulted in accurate positioning over 99% of the time. References for extended Kalman filter for GPS/IMU integrated referenced. The following reading is suggested: Caron, F. Duflos, Pomorski, D, Vanheeghe, P. *GPS/IMU data fusion using multisensor Kalman filtering* [64] and P. Zhang, J. Gu, E.E. Milios, P. Huynh. *Navigation with IMU/GPS/digital compass with unscented Kalman filter [65]*, Lin [66], and Clipp [67].

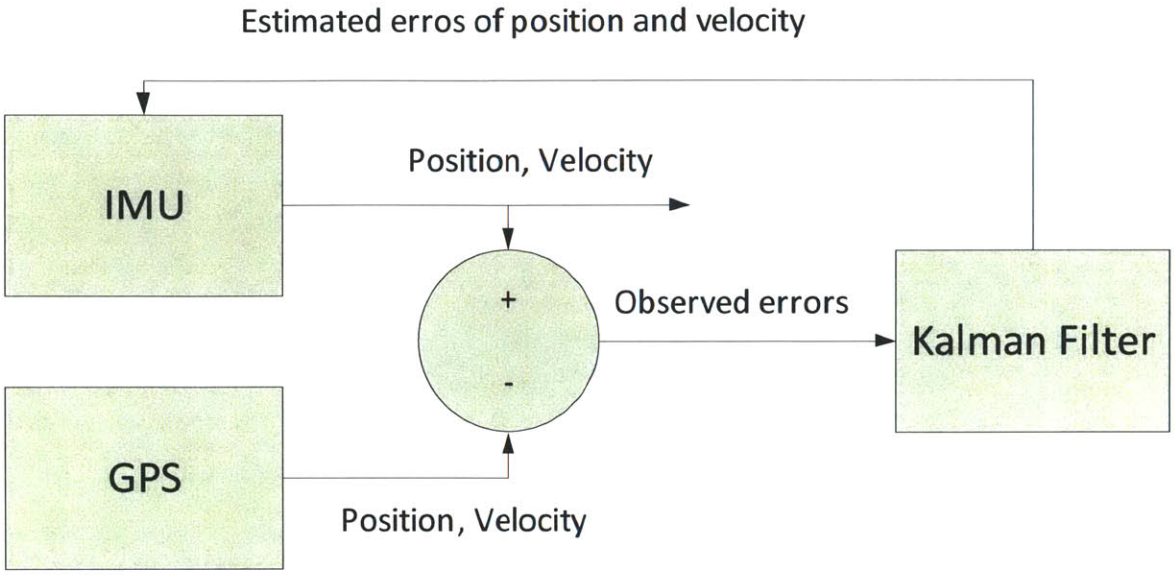

Figure 63: GPS/IMU integration using a direct feedback Kalman filter method.

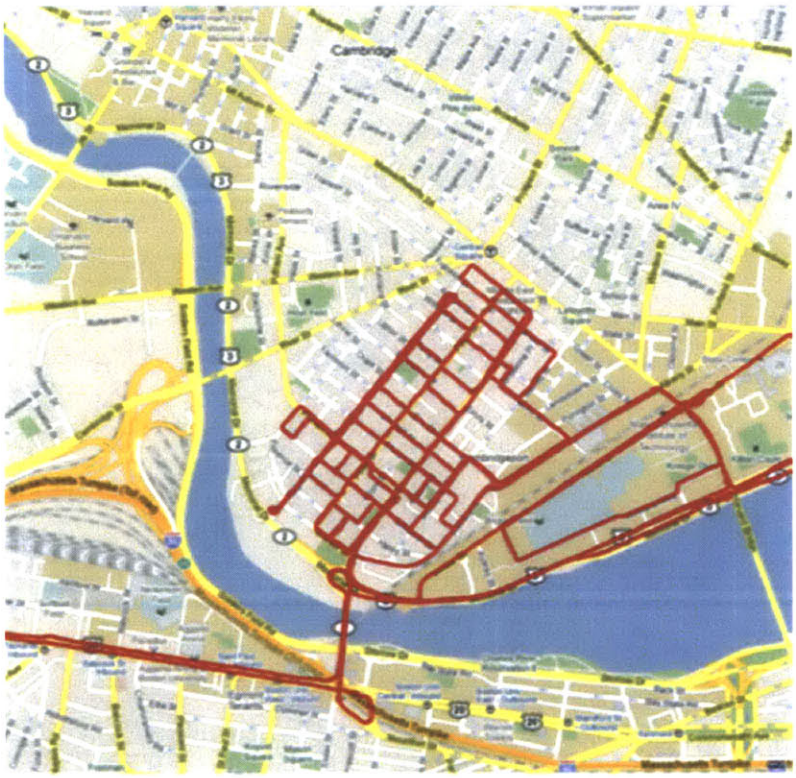

Figure 64: Demonstration of the GIS mapping capabilities of the new vehicle logging system.

Further research into image based navigation can be investigated using methods proposed by P. Debitetto [68]. Debitetto proposes that in urban environments where GPS and IMU accuracies are limited, image processing can be used to find target features from local landmarks and used to triangulate local positioning information. ARTIST can be used to gather data for this purpose.

3.2.2.9 Post Data Collection Process

On the road, the system does not process all the data imagery in real-time. It does not have that need or requirement. Thus, most of the data processing is done back at the lab where imagery data is fused with location data for geotagging each individual image frame from the video data. All imagery data is recorded separately using an independent digital video recording system capable of storage real time video data on 16 channels at full data rate (640x480, 30 fps). In summary, the Phase 2 multi-camera synthetic aperture imaging system is capable of the following:

- 6 x DRS 640 model cameras, 640 x 480 (LWIR), 30 fps
- 4 EO/NIR cameras, 640x480 (EO/NIR), 30 fps
- Real-time 10 hz GPS logger with IMU
- No PC required operate
- 80° Vertical FOV, 40° Horizontal FOV

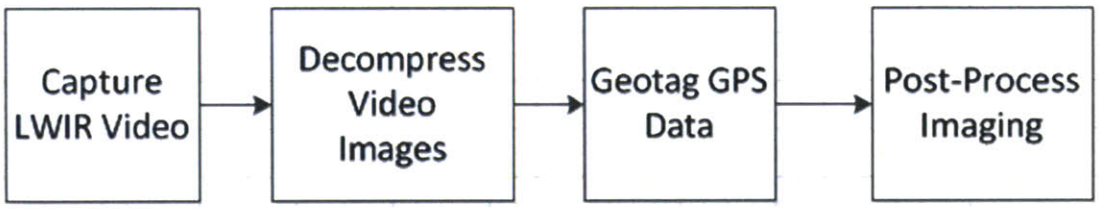

Figure 65: ARTIST procedure for processing recorded video sequences.

Data storage rate: 10 GB/hr

Target operational velocity: 10 mph

3.2.2.10 Demonstrating ARTIST's Synthetic Aperture Imaging System

Tested in an Industrial Environments

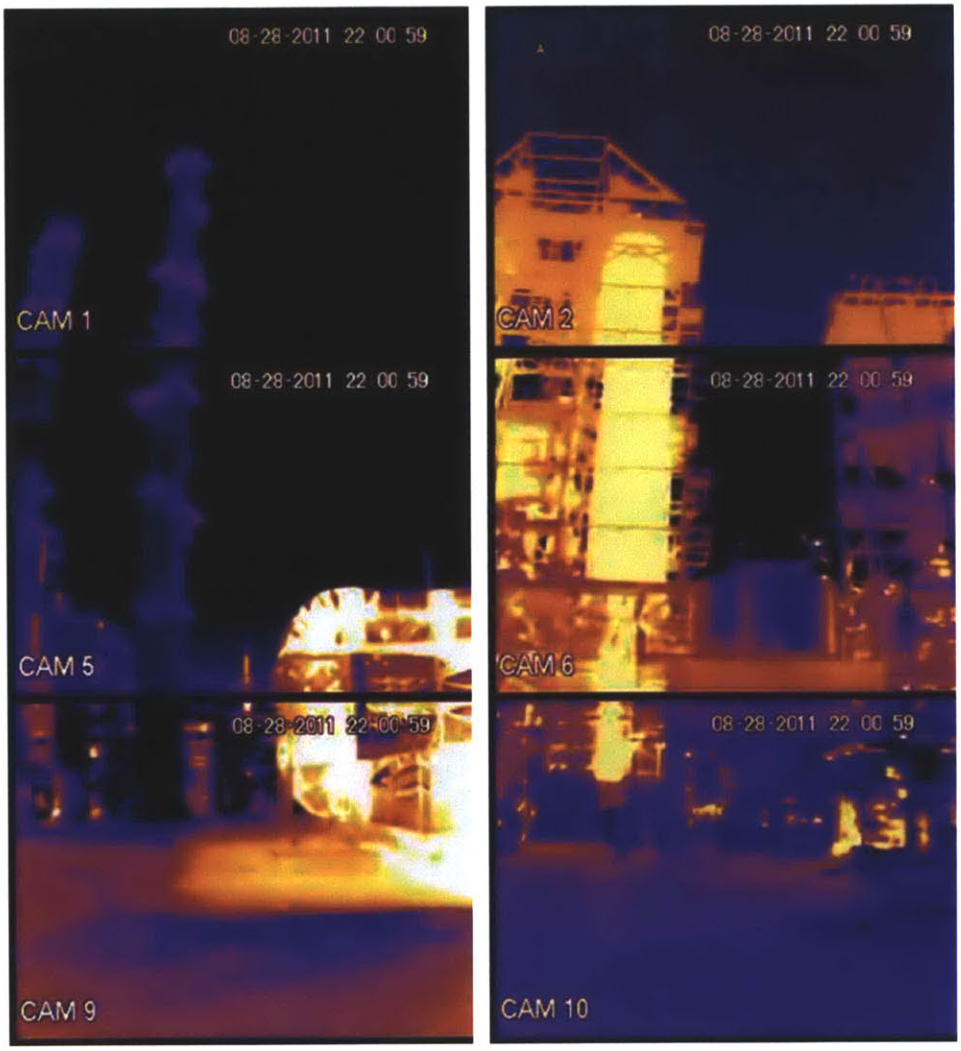

Figure 66: Demonstration of the WAMS in an industrial environment

Description: a research partner had inquired about the possibility of applying the wide angle multi-spectral imaging system (WAMS) system for non-urban environments, specifically, in an industrial setting where one can use the equipment to monitor and examine thermal related problems such as pipe thinning, pressure buildup, and overheated equipment. The system was tested in such an environment, showing a feasibility study. The WAMS demonstrated a very wide angle field of the view in the LWIR band. NAME AND LOCATION WITHHELD FOR CONFIDENTIALITY PURPOSES.

Tested in an Urban Environment

Figure 67: Demonstration of the WAMS in an urban neighborhood. (Implemented and tested by Dr. Liang Chen)

Description: These images show the result of (3) 640x480 frames fused into a single frame using an affine stitching method. The equivalent resolution of the camera system is 1400x640 pixels with a vertical field of view of 90 degrees allowing a full view of buildings beyond 3 stories. Notice the cars, trees, and objects that may obstruct the view of the building or structure.

3.3 Summary & Conclusion

We presenting a multi-phase process to understanding how thermal imaging works from a single user point of view. Next, we introduced a 2 Phase design process to show how to solve some of the challenges of manual data collection by introducing automation. The system was successfully developed, assembled, and fully tested. It was shown to be fully operational according to specifications and design parameters. In the final system, all video data was recorded in real-time while the imaging system is operational contained an independent GPS/IMU logging system, and no portable computing system required. In summary, the following processes were observed:

1. Field Research – Research infrared imaging by utilizing a handheld infrared camera system in real life operating conditions. Apply knowledge and experience to develop a better method or system.
2. Phase 1 – Develop a prototype large scale multi-spectral imaging system
3. Phase 2 – Develop a full scale multi-spectral imaging system with a wide angle field of view, dual side, real time recording system.

This design process demonstrates the methodology employed to understand and improve thermal imagery data collection through an automated. It is meant to be used as a guide to understanding the principals and tradeoff considered when taking a hardware design approach. First, understand the problems or need, then develop a prototype or demonstration of the key problems you are trying to solve through an alpha prototype, and then finally, how would you incorporate feedback and changes necessary to show a pre-production version of what you trying to developing through a beta prototype. This product and system design is critical part of understanding that these steps are also fundamentally important parts of the theoretical components as well. In the next few Chapters, we will focus on a) image processing and b) wide area thermal mapping.

Chapter 4: 3D Radiometry

4.0 Introduction

In Chapter 2, we discussed a theoretical framework behind the thermography in the ARTIST system. In Chapter 3, we discussed the design and prototype of the hardware system behind ARTIST, with the ability to produce urban scale scanning in multiple modalities including optical, long wave infrared, and near infrared. In this chapter, we will discuss the concept of 3D radiometry and show how the ARTIST system is used to:

a. Model the world in 3D using drive-by imaging
b. Account for the effects of directional emissivity

In practice, a majority of images taken by the ARTIST system consists of complex shapes, materials, and viewing angles to the surface. When lateral vehicle motion is applied, the scenes are continuously changing and thus, the viewing and distance to the object is in flux. In Chapter 2, we discussed the idea of a Lambertian surface, in which the emissivity and radiance remains constant for changes in viewing angle θ. However, we also noted that for typical engineering surfaces, Lambert's cosine law does not hold as ε is a function of viewing angle θ for viewing angles $\theta > 60°$. Since ε is now dependent on viewing angle θ, it becomes more critical to understand the nature of infrared surface scenery when estimating surface temperature. The simplifying assumptions of fixed emissivity and fixed distances to object prevent accurate modeling of the thermal environment. Although many references including Minkina [35], Rogalski [36],Saunders [34], Avdelidis [69], Cuenca [70], Labed [71], Schott [71], and Sobrino [72]; discuss the use of emissivity values to estimate target temperature or the acknowledgement of variations in emissivity in their error estimates, they do not investigate the use of 3D information to form their models on an urban scale. More recently, temperature mapping of 3D surfaces for a wind tunnel experiment have been presented by Cardone [44]. Next, we will investigate the concept of 3D Radiometry and how it can be applied for wide area temperature mapping of an urban environment.

In traditional thermography, inferring temperature from an image is based on two dimensional surface assumptions [50, 58, 73, 74]. Here, we introduce the analysis of radiometry in three dimensional space and consider how it affects the science of interpreting temperature readings. We propose to present thermal imaging in a 3D framework which is critical to understanding how distance and viewing angle to the object plays a critical role in how one can precisely target and estimate energy losses.

4.1 A Case for 3D Radiometry

Modern day thermography is based on 2D principles- which can be simplified into two core assumptions: (a) the use of a constant emissivity value for all points in a long wave infrared image and (b) a fixed distance to all points on an image, regardless of geometry [50, 58, 73, 74]. 2D radiometry assumptions can fail in situations where the scene is complex and view is not normal to the surface. Such is the case of drive-by imaging in ARTIST. The constant motion of the vehicle relative to the scene naturally forces the ARTIST system to capture images where the viewing angle is oblique to the target object. In these situations, the relative distance and viewing angle needs to be considered.

Observed radiance is invariant to distance. This is known as the conservation of radiance. Both the radiant flux [W] received at the detector and the solid angle [sr] from the source to the detector drops with the inverse square law, thereby cancelling each other out. This works to our advantage for ARTIST since many of our scenes will have varying distances and radiance is invariant to distance.

In Chapter 2, we discussed how Lambertian surface approximations are sometimes used in thermography. If it were true, as is the case with a black body, a Lambertian surface emits radiance (which is radiant flux (W) per unit projected area (m^2) per unit solid angle (sr)) that is constant with angle. A blackbody has an emissivity value of 1 and is invariant to wavelength and angle. The same is true for a Lambertian grey body, except a Lambertian grey body has emissivity values less than one. This would mean that for a black body and Lambertian grey body, there is no wavelength or angle dependency. Unfortunately, most materials are non-Lambertian and in Chapter 2, we show our experimental results and the literature which discuss this topic further. The Lambertian

surface approximation is not valid. Most materials are non-Lambertian. For non-metals, radiance, hence, emissivity is observed to be uniform from 0° to 60°. Beyond 60°, observed radiance and hence, emissivity, starts to drop off significantly. For metals, radiance, emissivity is observed to be uniform from 0° to 45°. Beyond 45°, observed radiance and hence, emissivity, starts to increase. Angular dependency of emissivity has been reported in the literature. The most often cited reference dates back to 1935, based on the experiments by Schmidt & Eckert 1935 [42]. Siegel & Howell [46] showed theoretically derived predictions from electromagnetic theory. This shows that angular dependence is observed and can be theoretically modeled for certain materials. The observed radiance is dependent on emissivity, temperature, angle, and independent of distance. From the previous Chapters I will summarize the following insights that will be relevant to our case for 3D radiometry:

1. Observed radiance is invariant to distance.
2. Directional emissivity is dependent on viewing angle and exhibits different behavior for metals (low ε) and non-metals (high ε).
3. The Lambertian surface approximation is not valid as most engineering materials are non-Lambertian, therefore, radiance is dependent on viewing angle.
4. Drive-by imaging of an urban environment involves capturing images from a 3D environment with changing viewing angles, in many cases oblique angles. These effects should be considered, modeled, and corrected.

Therefore, to properly model the three dimensional environment, I develop the concept of 3D radiometry and show how it is implemented within the ARTIST. 3D Radiometry refers to the process of collecting imaging information, developing a wire-frame 3D model from the drive-by scenes, and then using scene information including viewing angle and distance to correct for temperature and normalized surface areas.

4.1.1 A Recap of Thermography

The following temperature inference model is based on Saunders model [34] presented in Chapter 2. It captures how infrared manufacturers use calibrated tables (variables A,B,C) to help infer temperature:

$$T_{ob} = \frac{c_2}{A \cdot ln\left(\frac{C}{s_{ob}} + 1\right)} - \frac{B}{A} \quad (53)$$

$$T_{ob} = f(\varepsilon_{ob}, T_{atm}, T_o, \omega, d) \text{ [K]} \quad (54)$$

Where A,B, and C are camera specific calibration parameters, c_2 is the second radiant constant, the emissivity ε_{ob} of the surface is a constant variable that is set by the user (typically ε_{ob} is set at 0.95 but can be adjusted), T_{atm}, T_o, ω are variables measured or estimated by the camera system, and d, the distance is estimated by the auto-focus setting of the camera. Combined with variables A, B, and C, which is based on the calibration tables provided by the manufacturer at the factory, the thermal camera solves for the expected value of T_{ob} to estimate the object's surface temperature.

4.1.2 Recap of Concepts from Radiation Heat Transfer

The view factor of two differential areas dA_1 and dA_2 at a distance S is:

$$F_{1\to2} = \frac{\cos\theta_1 \cos\theta_2}{\pi S^2} dA_2 \quad (55)$$

Where θ_1 and θ_2 are the viewing angles between the surface normal and ray between the two differential areas.

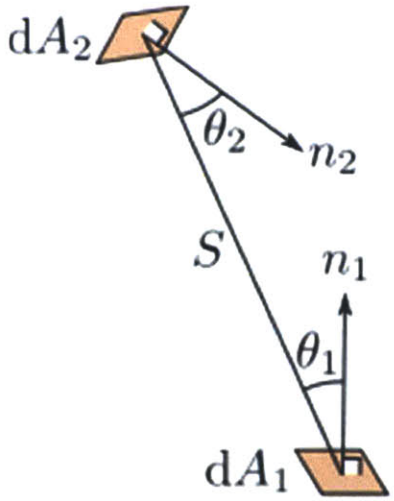

Figure 68: Two body view-factor diagram

Since radiation leaving a surface is conserved, the sum of all view factors from a given surface, S_i sums to unity:

$$\sum_{j=1}^{n} F_{S_i \to S_j} = 1 \qquad (56)$$

From Figure 68, we see that the view factor between the two objects have a dependencies on θ_1 and θ_2 which relates to the viewing angle of both objects relative to one another. If either θ_1 or θ_2 becomes overly large, where $\theta > 60°$, the product of the component becomes very small and $F_{1\to 2}$ approaches zero. Additionally, as θ_1 and θ_2 becomes larger, the effects from a decreasing ε_1 and ε_2 will further cause variations in the observed radiance for the same surface temperature. Therefore, it becomes more important to quantify the viewing angle and distance to the object. The development of a 3D depth map and the wireframe model of a building will help us estimate camera viewing angle for surface features.

4.2 3D Radiometry Implementation

I implement 3D Radiometry in this thesis using a 3 step approach:

1. Construct 3D model of environment using the ARTIST hardware
    a. Depth map using optical flow model
    b. Object size estimation
    c. Surface area normalization
2. Calibrate non-radiometric infrared camera: camera signal output (pixel intensity) vs observed radiance for blackbody temperature
3. Calculate emissivity based on radiance

4.2.1 3D Reconstruction based on Motion Estimation, Depth Map, and Solid Model Generation

To construct a 3D model of the environment, I applied the following process:

1. A multi-frame motion estimation algorithm is used based on an optical flow model
2. The optical flow model is used to reconstruct a depth map of the scene
3. A solid model is overlaid onto the scene from the depth map.

The science of optical flow modeling has been well-documented and presented through the years. Well known optical flow models include the methods of Horn and Schunck [75], Lucas and Kande [76], Uras[77], Nagel [78], Anandan [79], Singh [80], Heeger [81], Waxman [82], Fleet and Jepson [83], Prazdny [84],and Farneback [85]. The performance of many of these algorithms have been tested against varying datasets representing different scenarios in [86], *Performance of optical flow techniques.*

Utilizing the imaging system's forward motion, which is parallel to the scene of interest, we will compute the motion based on successive imaging. At this stage, we assume knowledge of the positional state of the vehicle and corresponding positional displacement based on the computed output of the GPS/IMU sensors processed through an extended Kalman filter [64] and other methods presented in Chapter 3.

There are many optical flow based methodologies that one can use to estimate optical flow based on image pixel displacement. I have used a polynomial based method similar to Farneback [85] . The polynomial optical flow method is shown to have good performance in minimizing angular error and standard deviation [85]. My colleague, Dr. Liang Chen, implemented the optical flow algorithm in the ARTIST system and I present some of the details here for completeness.

4.2.2 Polynomial Optical Flow using Farneback Method [34]

The Farneback [85] polynomial based motion estimation algorithm estimates motion flow using data from two successive imaging frames. The main idea behind the method is to apply a polynomial expansion function to define an approximate neighborhood of each pixel. By doing so, the algorithm can uniquely define each neighborhood in a projected search area. Within such a neighborhood, the search algorithm minimizes the difference in displacement between the projection of the first frame and the second frame.

I summarize the polynomial optical flow method below:

Step 1:

The first step of method is develop a local signal model based on a quadratic polynomial:

$$f(x) \sim x^T A x + b^T x + c \quad (57)$$

Where $f(x)$ is the polynomial function defined by a symmetric matrix A, the vector b, and a scalar c, in a local coordinate system. The coefficients in A, b, and c, can be determined from the weighted least squares fit of the signal values in the neighborhood of each pixel.

Step 2:

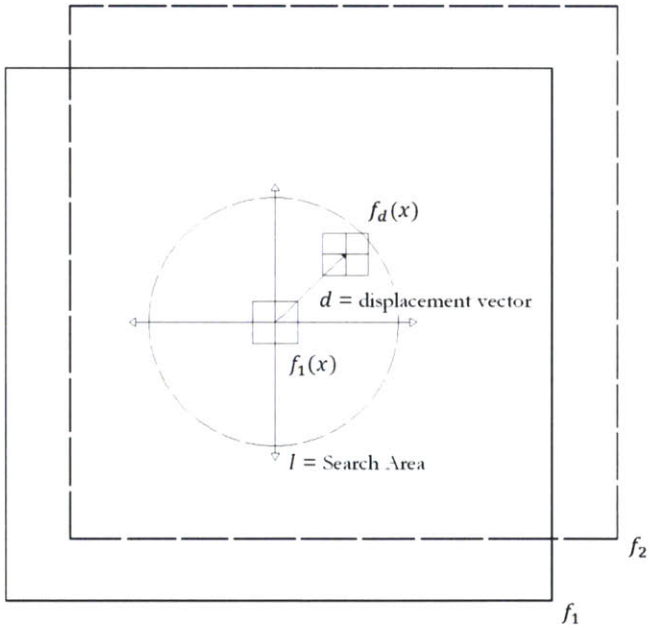

Figure 69: Farneback [85] polynomial optical flow search algorithm over neighborhood of I for d

In the second step, the polynomial expansion function is applied to the first frame f_1 and second frame f_2, using the predefined polynomial model $f(x)$ to yield:

$$f_1(x) = x^T A_1 x + b_1^T x + c_1 \quad (58)$$

$$f_2(x) = x^T A_2 x + b_2^T x + c_2 \quad (59)$$

Where f_1 is the first frame, A_1, b_1, c_1 are the symmetric matrix, vector, and scalar of the frame f_1, f_2 is the second frame, A_2, b_2, c_2 are the symmetric matrix, vector, and scalar of the frame f_2.

Next, the method constructs a new frame $f_d(x)$ based on the global displacement variable d relative to frame f_1:

$$f_d(x) = f_d(x - d) = (x - d)^T A_1 (x - d) + b_1^T (x - d) + c_1 \quad (60)$$

Where $f_d(x)$ is the projected displacement of global displacement vector d, in the search displacement field $d(x)$, in the neighborhood of I which defines the search area, for which we would like to search for pixel optimal pixel displacement p between frames f_1 and f_2.

Step 3:

Finally, the algorithm searches for the optical pixel displacement to find the optimal pixel displacement approximation, the minimum of the expectation value is given by:

$$e(x)_{min} = \sum w \, \Delta b^T \Delta b - d(x)^T \sum w A^T \Delta b \quad (61)$$

Where , w is the weighted least squares of the points in the neighborhood, $A(x)$, Δb, and $d(x)$ are represented by the following:

$$A(x) = \frac{A_1(x) + A_2(x)}{2} \quad (62)$$

$$\Delta b(x) = -\frac{1}{2}(b_2(x) - b_1(x)) \quad (63)$$

$$d(x) = \left(\sum w A^T A\right)^{-1} \cdot \sum w A^T \Delta b \quad (64)$$

We find d(x) by minimizing over a neighborhood of I of x to find the optimum pixel displacement value where $e(x)$ is minimized. We show an example of the implementation in the following figure

prepared with help from a collaborator Dr. Liang Chen. I refer to Farnbeback [85] for further references, additional details, approximations, and further insights into his methodology.

Figure 70: Example of 6 successive frames captured during vehicle lateral motion in urban neighborhood

In this section, we show that we can compute for the optical flow displacement of the vehicle by extracting and using successive imaging frames to derive motion flow information. From the motion flow model, we translate the relative pixel motion into a depth map. The depth map is used to create a overlaying solid mesh map. The solid mesh map can then be used to infer the viewing angle and distance to the surface. We demonstrate this procedure using LWIR scene taken from 3 cameras with the ARTIST hardware system. In the scene, the 3 cameras are fused to form a synthetic aperture. Digitally, the scenes were mosaicked together. In this scene, the imaging system is conducting a drive-by test between two 3 story buildings. At the center of the image is a car very close to the imager. In the distant background is the sky, which is dark and represents very low camera signal output (pixel intensity) reading. In Figure 71, we show the (a) Optical Flow Diagram, (b) Depth Map, and (c) Mesh Map examples. In Figure 72, we outline the steps for creating the 3D model.

The optical flow method here is developed by Farneback [85] is meant to demonstrate the feasibility of applying off-the-shelf algorithms onto the ARTIST system. ARTIST is developed to be plug-n-play for other motion based optical flow and 3D reconstruction algorithms.

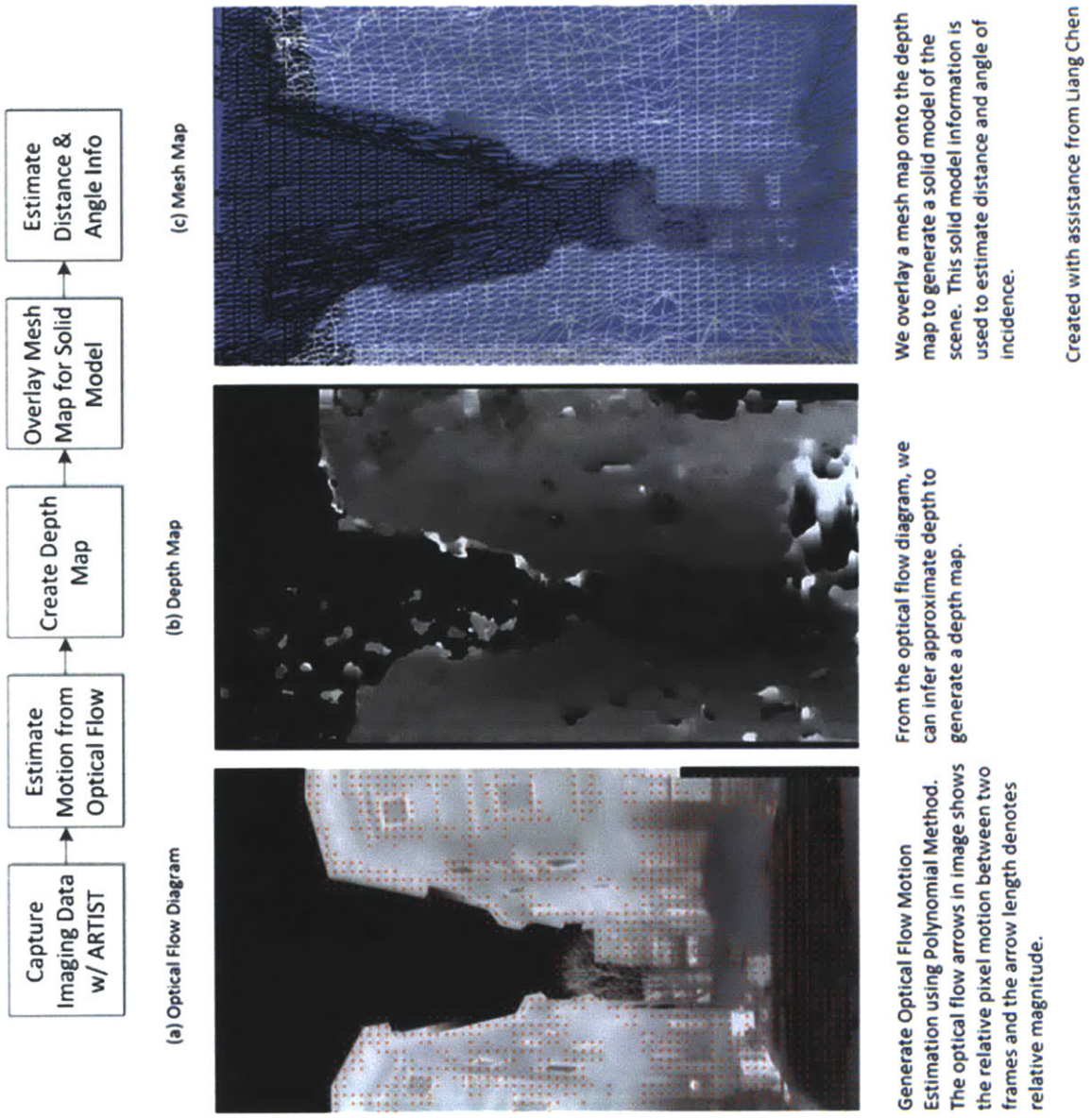

Figure 71: ARTIST method for 3D reconstruction in LWIR with examples (a) Optical Flow Diagram, (b) Depth Map, and (c) Mesh Map of the scene

Figure 72: Urban based drive-by imaging generated point cloud map displayed in Meshlab.

Implemented and Tested by Dr. Jonathan Jesneck

Using the ARTIST hardware platform, one can create an urban scale depth map using information integrated over many successive frames during a drive-by scan. In this model, we show a neighborhood scan using Meshlab, an opensource 3d modeling software. The point cloud model shown integrates all the depth information from many frames during a single drive-by scan. Image created with assistance from Jonathan Jesneck.

4.2.3 Calculate Remote Object Size

To correctly represent a target object's normalized size in width and height, based on the actual distance to the target object, we must calculate the focal length and height as observed on the focal plane array (FPA). The focal length width and height is represented by the number of projected pixels seen as the output of the imaging camera. To calculate the normalized size, we must first determine the thermal detector's physical size based the width and height of the sensor. In our case, we are utilizing a DRS 640 model which is based on 17 μm technology. The FPA's physical size in width and height is:

FPA width = 640 pixels x 17 μm/pixel = 10.88 mm

FPA height = 480 pixels x 17 μm/pixel = 8.16 mm

Where FPA sensor's physical size ix 10.88 mm x 8.16 mm. With this information about the detector's size, we can solve for the object's normalized width and height based on the observed size of the projected image on the FPA sensor, focal length width and height, based on the following formula:

$$Focal\ length\ height = \frac{Working\ Distance\ \times FPA\ height}{Object\ height + FPA\ height} \quad (65)$$

$$Focal\ length\ width = \frac{Working\ Distance\ \times FPA\ width}{Object\ width + FPA\ height} \quad (66)$$

Focal length height is based on the observed area's height in pixels x 17 μm, focal length width is based on the observed area's width in pixels x 17 μm. Working distance is the actual distance from the LWIR camera to the target object. Therefore we can solve for the object's width and height by rearranging the previous equations:

$$Object\ height = \left[\frac{Working\ Distance\ \times FPA\ height}{Focal\ length\ height}\right] - FPA\ height \quad (67)$$

$$Object\ width = \left[\frac{Working\ Distance\ \times FPA\ width}{Focal\ length\ width}\right] - FPA\ width \quad (68)$$

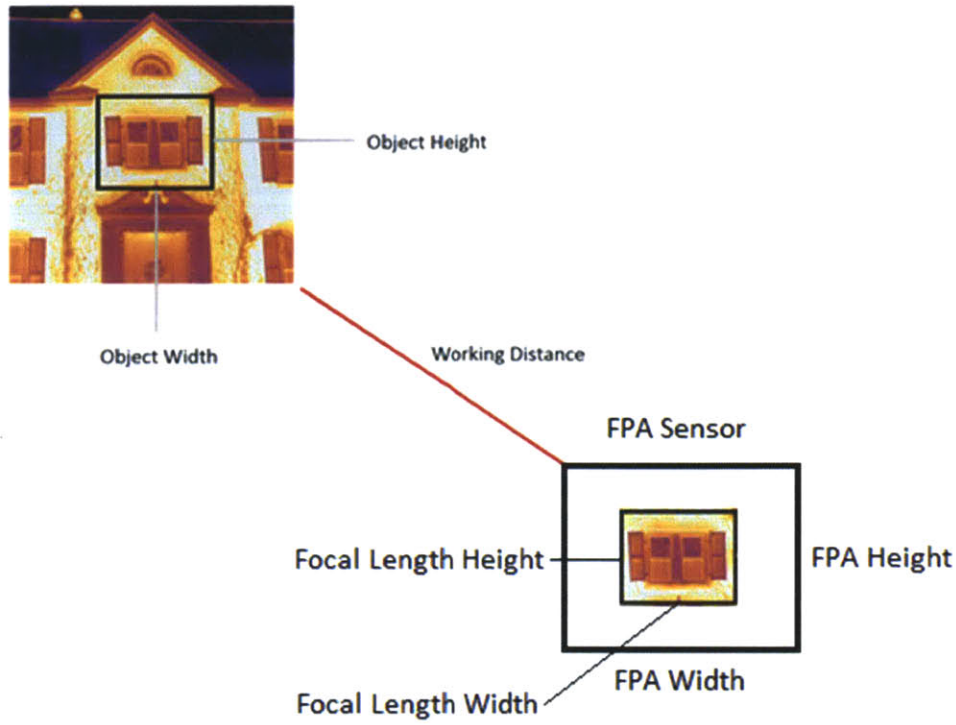

Figure 73: Diagram showing method for calculating observed object's height and width

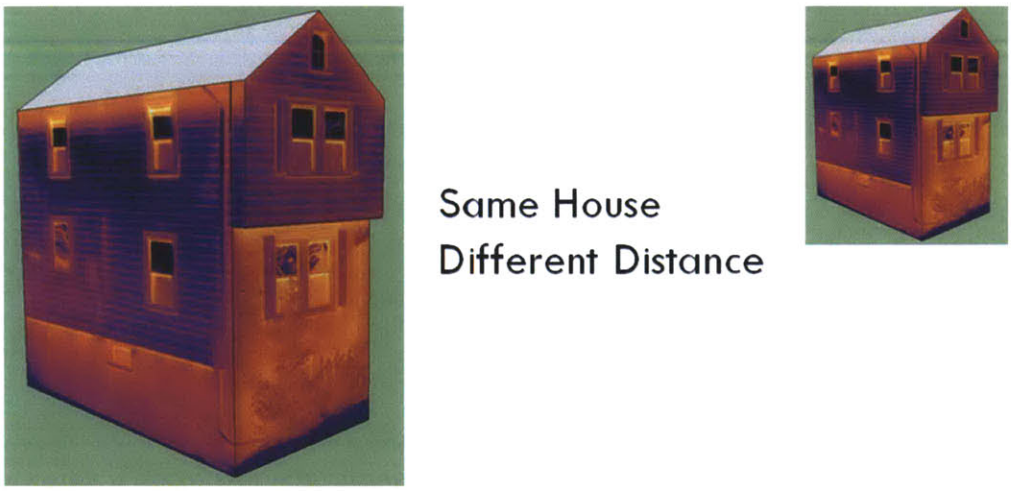

Figure 74: The effects of varying distances on an object. Left (distance = d_1) and Right (distance = $2 \cdot d_1$)

4.2.4 Normalizing Surface Area

When viewing a surface area remotely from an angle, the viewing angle plays a critical factor in determining the normalized surface area of the object. Therefore, we need to consider the normal surface and viewing angle to properly determine the correct surface area. For this, we introduce the concept of projected area as:

$$A_{projected} = \int_A cos\alpha dA \quad (69)$$

Where A is the original area, α is the angle between the normal to and the surface A and the normal to the camera plane, in our case, the viewing angle. From this, one can see that projected area decrease as a function of cosine θ. The greater the viewing angle θ, the lower the projected area. Below is an example of this, where on the left, θ ~ 90°, and the left side of the building is not visible. As θ decreases, the projected area of the left side of the building increases.

From the projected area, normalized surface area of an object can be estimated from images at different view angles. The normalized surface area is the area of the object's surface in an orthographic projection, i.e. when view from infinity along a particular viewing direction.

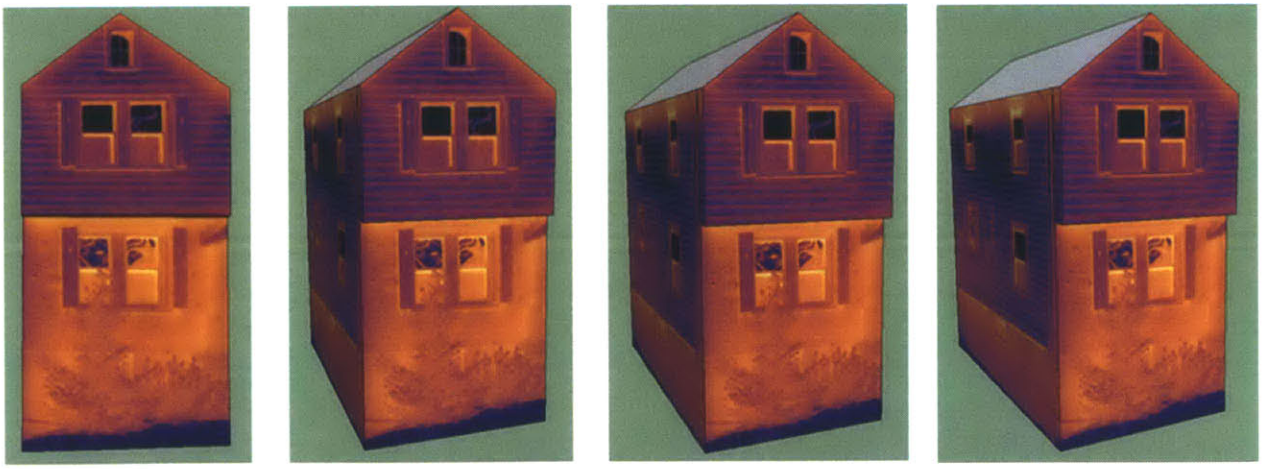

Figure 75: Viewing angle rotation of the front of a building at different viewing angles.

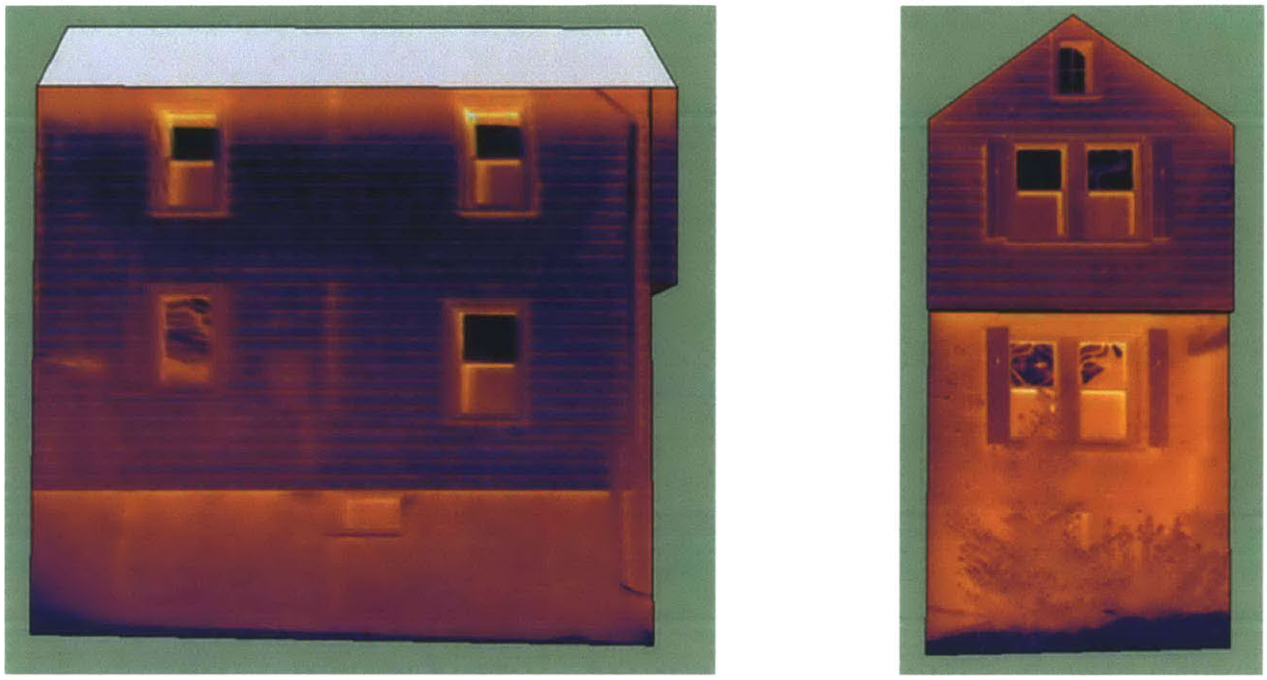

Figure 76: Demonstration of a normalized surface area viewing of the side and front of the building from Figure 75

4.3 Non-Radiometric LWIR Camera Calibration

I describe below a process for calibrating any LWIR camera system and related non-radiometric infrared camera. Typically, thermal calibration for infrared cameras are completed at the manufacturer's factory and the calibration tables are saved directly into the camera's internal system, which allows an effective and fast lookup to infer distance temperatures in the form of camera calibration parameters R,B, F according to Minkina (2009) [35] and similar parameters A,B,C according to Saunders[34]. An alternate infrared calibration technique is presented Liebmann [87]. In our setup, we use a reference material with known emissivity and acquire accurate temperature measurements using a thermistor device. We present a repeatable methodical process for the calibration of an infrared camera system and outline the steps below:

1. Scene Selection:
    a. Find a steady state environment, such as a temperature controlled room. Minimize air flow or anything that may affect the local temperature significantly. Look to

minimize convection air flow of any sort or next to a window where the sun is shining.

2. Instruments:
    a. Use an thermal infrared camera connected to a video frame grabber, 8 bit b/w
    b. Find a precision thermocouple device with accurate temperature sensor
    c. Find a handheld infrared thermometer with laser sighting
    d. Gather 2 dark 8 ounce ceramic cups, black electric tape, and a bag of ice cubes
3. Calibration Steps
    a. Turn infrared camera on, wait till steady state with room ~ 30 mins.
    b. Setup camera to look at 2 cups at a fixed distance d from cup. Ensure that both cups are clearly visible.
    c. Place ice cubes with water into cup, stir ice water well. Measure cup temperature externally. It should remain at steady state temperature until ice completely melts. Cup temperature is expected to be 35-40°F.
    d. Wrap black electric tape on second cup. Leave about half of the cup exposed and half covered with black tape.
    e. Place water in second cup, place in microwave till boiling. Take out immediately and place next to ice water cup.
    f. Allow the hot water to go through natural convective cooling.
    g. Record infrared frame at regular intervals. Measure hot water temperature at every frame grab and make recording.
    h. Make necessary preparation for approximately 2 hours of experimental time.
    i. Repeat for varying distances $d_1, d_2, d_3, \ldots, d_n$ in multiples of d.

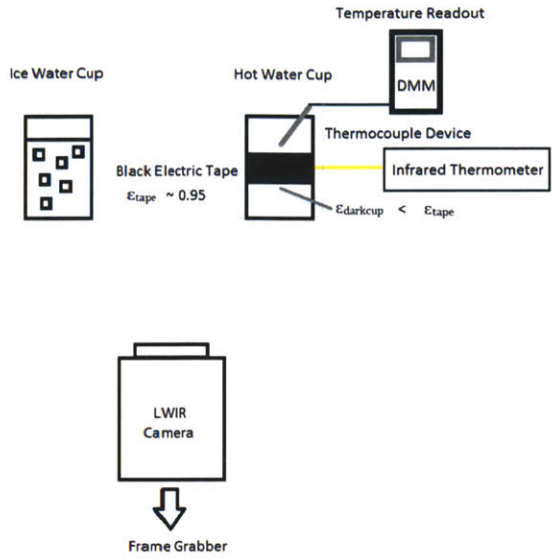

Figure 77: An experimental setup for non-radiometric infrared camera calibration

4.3.1 Camera Signal Output (Pixel Intensity) vs Observed Radiance Temperature Calibration

The LWIR imagers are recorded in real time at 30 fps through a PC framegrabber. The ice water-filled cup, as measured by the thermistor digital multimeter, is at 6.8° C and maintains a consistent temperature as long as there is sufficient unmelted ice in the cup. Dark black electric tape ($\varepsilon_{tape} \sim 0.95$) is wrapped around the hot water cup as to maximize the surface emissivity of the cup. The entire ceramic cup is dark brown, but we assume that $\varepsilon_{tape} > \varepsilon_{darkcup}$. The first experiment estimated the emissivity of the ceramic cup based on the knowledge that $\varepsilon_{tape} \sim 0.95$, $T_{ice} = 6.8°$ C, $T_{amb} = 23°$ C, and T_{cup} as measured by a thermistor connected to a digital multimeter with ± 0.1 C accuracy. LumT, LumM, and LumB are top, middle, and bottom are camera signal output (pixel intensity) readings based on 8 bit digitized readings.

LumT	Tstdev	LumM	Mstdev	LumB	Bstdev	Infrared[°C]	Thermistor [°C]
191.9	2.7	208.7	0.9	197.8	0.7	83.4	85.9
165.7	2.5	178.6	0.5	170.5	0.7	74.6	77.5
146.4	2.6	157	0	151.3	1.1	67.6	70.1
136	1.4	144.3	0.5	140.4	0.6	62.8	65
127.4	1.5	135.6	0.5	131	0.4	58.6	61
121.6	1.3	128.9	0.6	125.8	0.4	55.6	58.1
113.5	1.6	120.9	0.5	117	0.8	51.2	53.1
106.7	1.4	112.9	0.4	110.3	0.8	48.2	50.2
102.7	1.3	108.9	0.7	106.6	0.6	46.4	48
98.7	1.3	104.9	0.5	102	0.7	44.2	45.9
93.8	1.4	99.2	0.4	97.5	0.5	42.4	43.7
89.6	1.5	95.1	0.3	93.2	0.5	40.4	42.1
75.9	1.4	85.9	0.4	83.8	0.4	39.6	41.5
35.1	0.5	32.3	0.8	31	0.5	21	21
33.9	0.4	31.2	0.6	30.6	0.5	21	21.2

Table 4: Results from camera calibration test. The table here shows the varying experimental data observed. Lumt, LumM, and LumB are the camera signal output (pixel intensity) in top, mid, and lower part of the cup. Tstdev, Mstdev, and Bstdev are the standard deviation of the camera signal output. Infrared is the measured reading from the infrared thermometer pointed at the cup [°C]. Thermistor is the observed reading from the thermistor [°C].

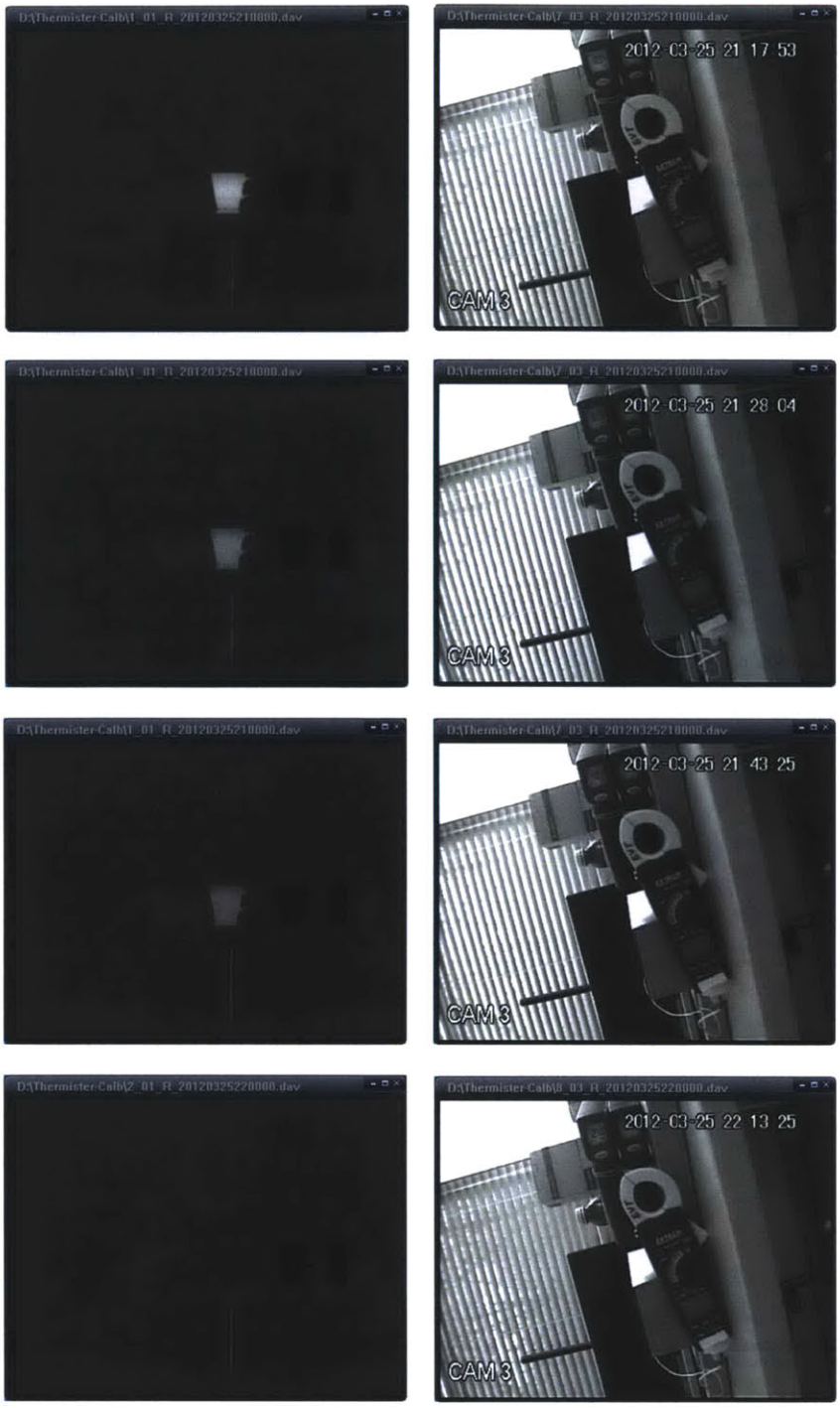

t_o

t_1

t_2

t_3

c

Figure 78: (4) Different screenshots of varying time sequences of experiment. The cup is filled with hot water and allowed to cooled through natural convection at room temperature. t_0, t_1, t_2, t_3 are discrete observations made at different stages of the experiment. A timestamp is provided on the upper right hand corner of the right images.

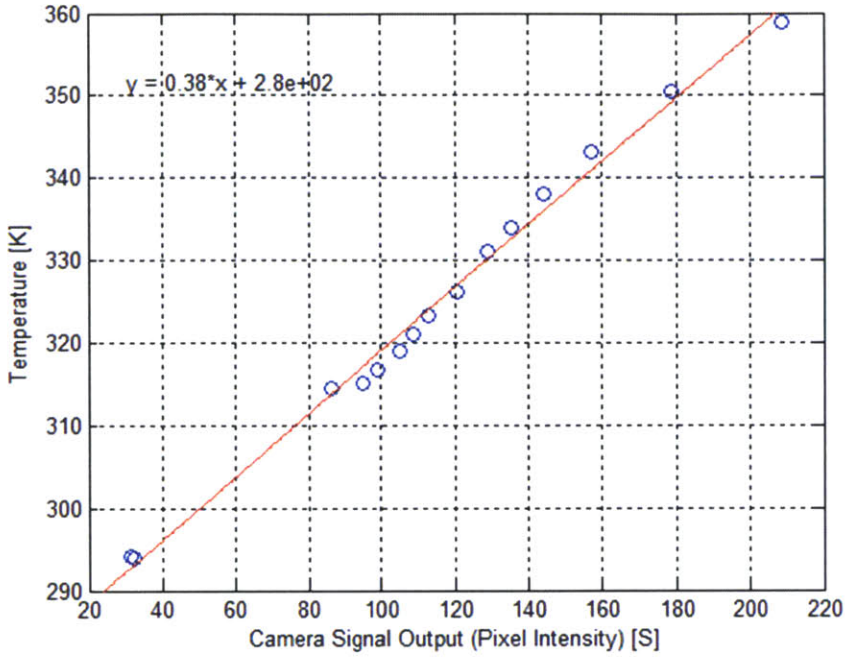

Figure 79: IR Camera Signal Output (Pixel Intensity) [S] vs. Absolute Temperature [d = 48 in] by Thermistor

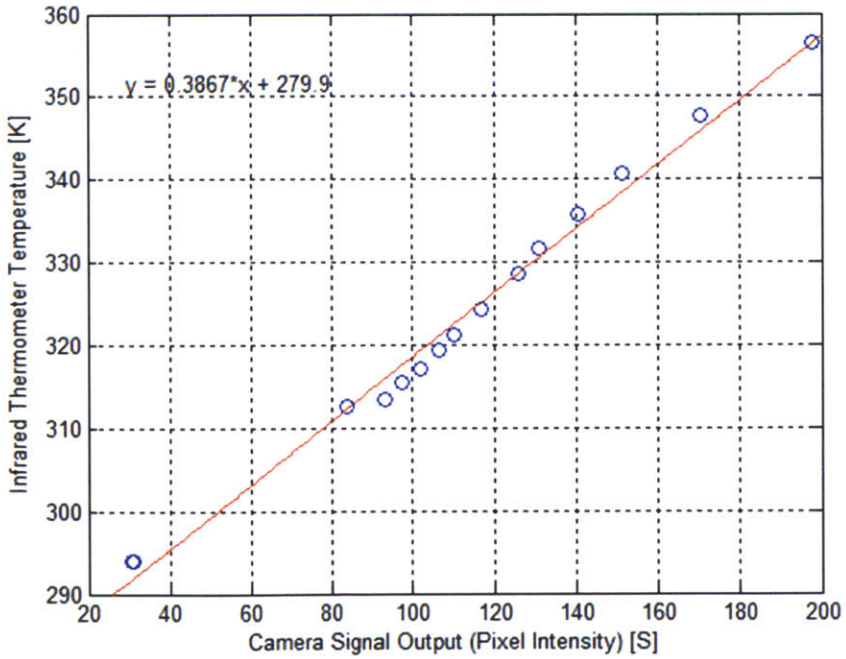

Figure 80: IR Camera Signal Output (Pixel Intensity) [S] vs. Infrared Thermometer Temperature [d = 48 in]

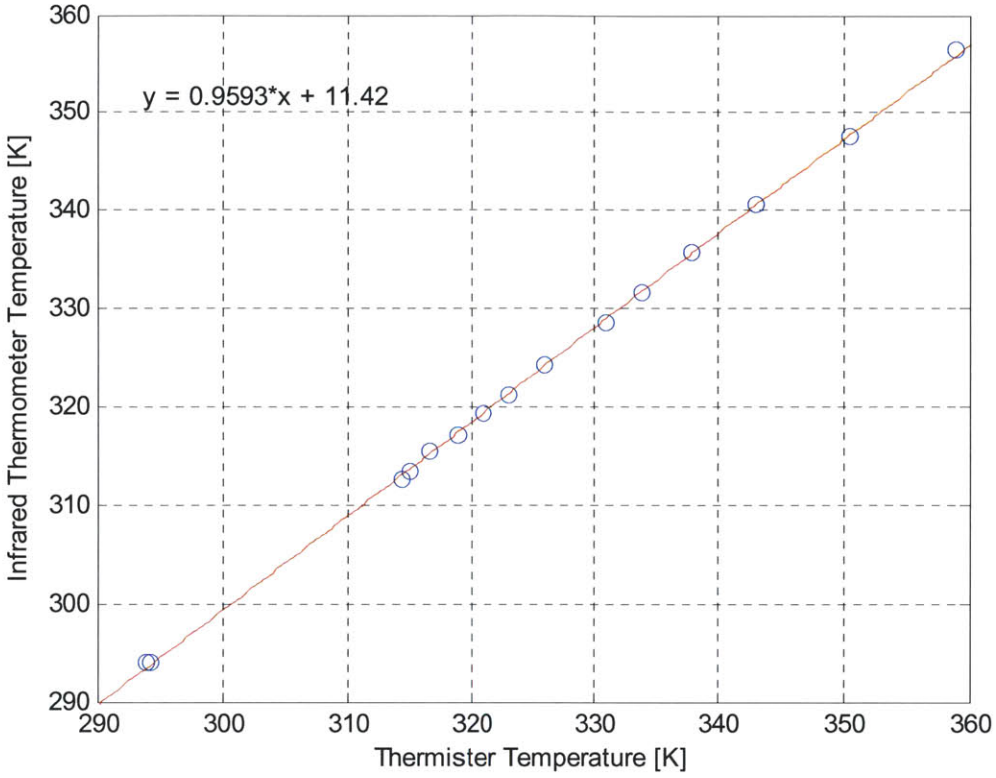

Figure 81: Comparison of Temperature Measurements for Infrared Thermometer vs Thermistor

In Figure 81, we show a good fit between the measured temperature based on the infrared thermometer and a thermistor. What this means is that the infrared thermometer is fairly accurate when it comes to estimating the surface temperature of the reference surface.

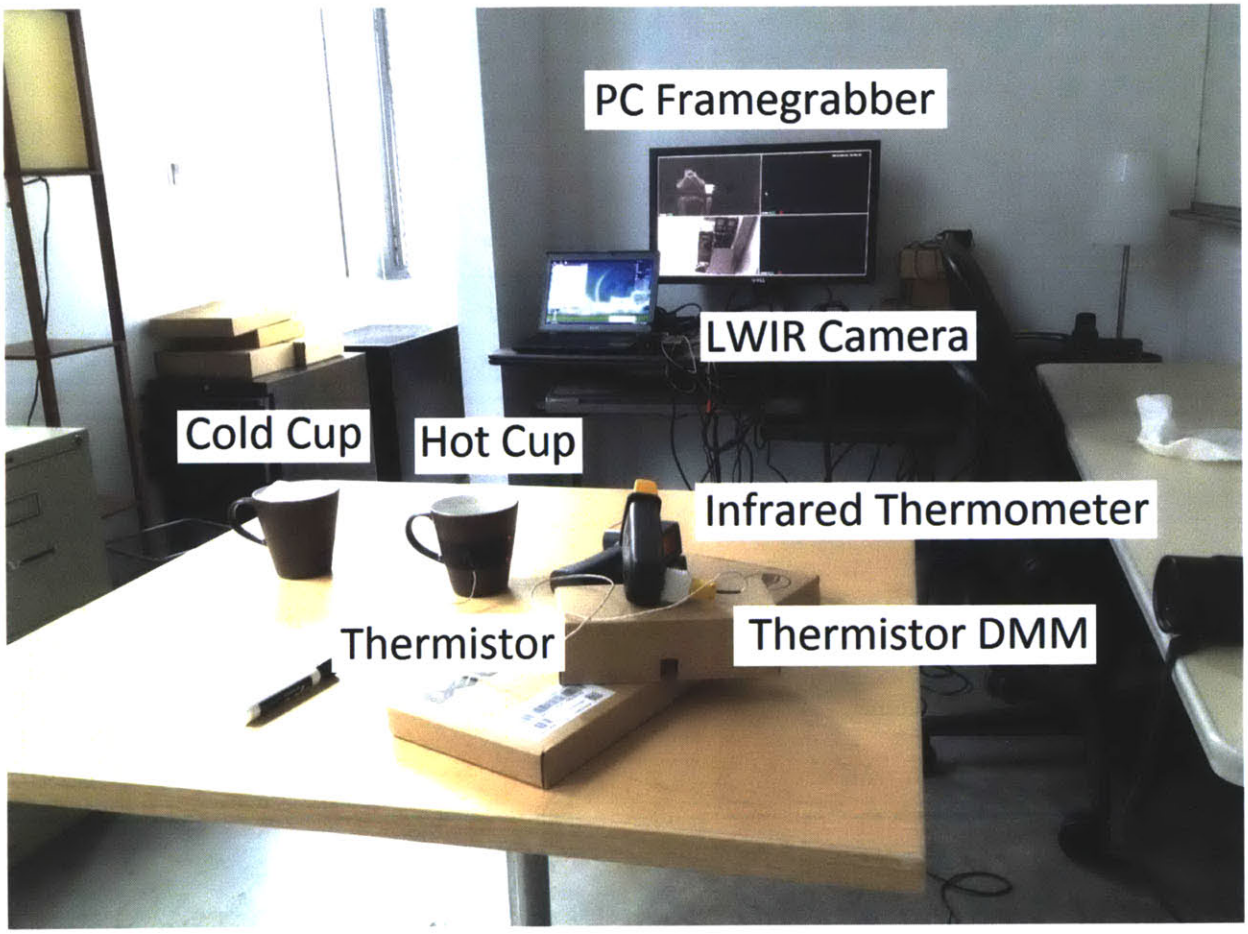

Figure 82: Complete view of experimental setup for calibration experiment

The LWIR camera is connected to a PC framegrabber and is aimed at the experimental setup with a hot cup filled with hot water and a cold cup filled with ice water. This experimental setup is consistent with the outlined procedure in Section 4.3.

4.4 Reference Surface Emissivity Calibration

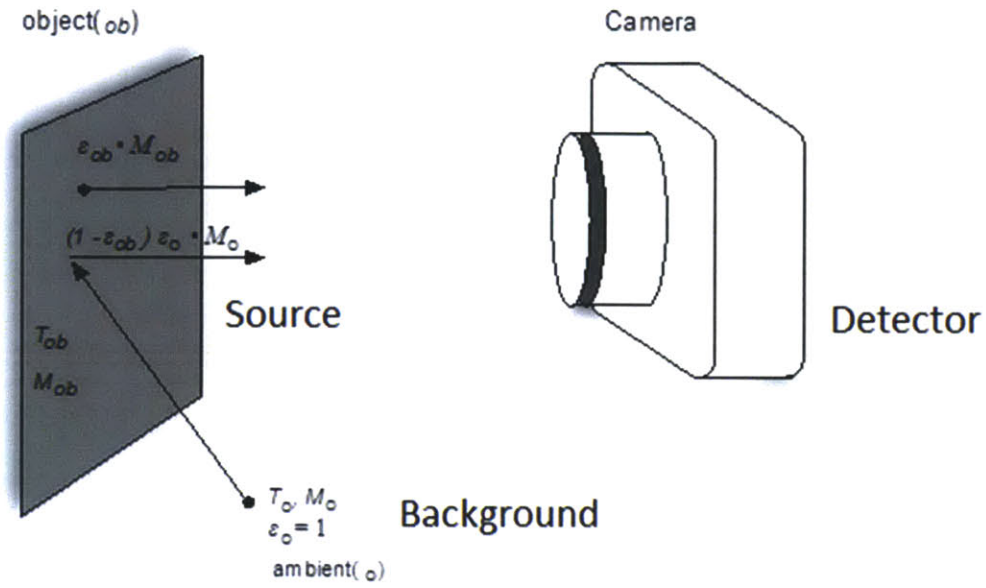

Figure 83: Simple Source, Background, Detector Model for LWIR imaging

The initial calibration result is mapped in a linearized form y = Ax + B in Figure 79:

$$y_{48\ in-black\ tape} = 0.383x + 7.8\,,\ R^2 = 0.9922 \qquad (70)$$

Where y is the remote surface temperature of the cup as measured by the thermistor, A = 0.383 °C/lum, B = 7.80° C, and the R^2 = 0.9919, which represents a very linear fit in Figure 80.

$$y_{48\ in-infrared\ thermometer} = 0.367x + 7.78\,,\ R^2 = 0.9919 \qquad (71)$$

Where y is the remote surface temperature of the cup as measured by the infrared thermometer pointed the black electric tape, where $\varepsilon_{\text{black-tape}} = 0.95$, A = 0.367 °C/lum, B = 7.78° C, and the R^2 = 0.9919, which represents a very linear fit.

Most conventional off-the-shelf infrared thermometers are sold with fixed emissivity settings where ε is set to 0.95. In our experiment, we confirm ε = 0.95 in the thermometer's documentation and use this information to compare the absolute temperature as measured by the thermistor with the output temperature read by the infrared thermometer to verify the accuracy of the thermometer.

$$y_{infrared\ thermometer} = \varepsilon_{IRT} \cdot 0.383x + 7.80 \quad (72)$$

$$\varepsilon_{IRT} \cdot A_{black-tape} = A_{IRT} \quad (73)$$

$$\varepsilon_{IRT} \cdot 0.383x = 0.367x \quad (74)$$

$$\varepsilon_{IRT} = 0.958 \quad (75)$$

From our experimental observation of $\varepsilon_{IRT} = 0.958$ vs our expected $\varepsilon_{IRT-documented} = 0.95$, we can confirm that the result accurate to within 1% of the expected value from the infrared thermometer's internal settings. The actual emissivity of the reference object will directly affect the accuracy of the surface temperature estimates.

4.4.1 Surface Emissivity Estimation

In our calibration experiment, we measure two values:

1. Output Camera Signal (Pixel Intensity) in the thermal image
2. Temperature of the unknown surface using a thermistor

Our hypothesis is that the camera grey-scale pixel output is calibrated linearly to the radiance entering the detector. Therefore, pixel intensity at each temperature would be linear to the corresponding Planckian form integral at that temperature. In the following three figures, we show how we take the measurement datapoints of pixel intensity and temperature to develop our calibration charts of pixel intensity vs radiance. In the section below, I show how such charts for a known reference material is used to estimate emissivity of an unknown material at the same temperature.

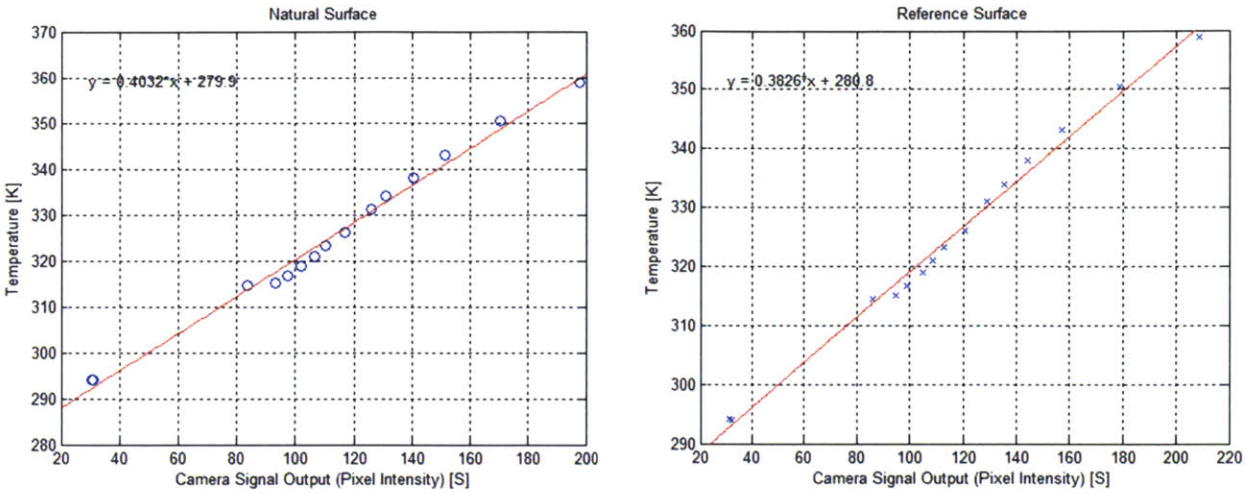

Figure 84: Calibration results for Temperature of Natural Object Surface [S_o] (left) & Reference Emitter Surface [S_r] (right) vs camera signal output (pixel intensity) output from LWIR camera

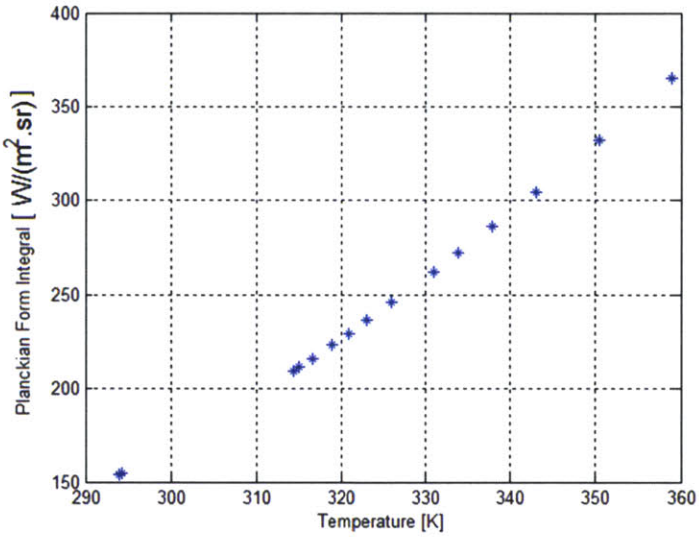

Figure 85: Planckian Form Integral Results vs Observed Temperature of Experiment

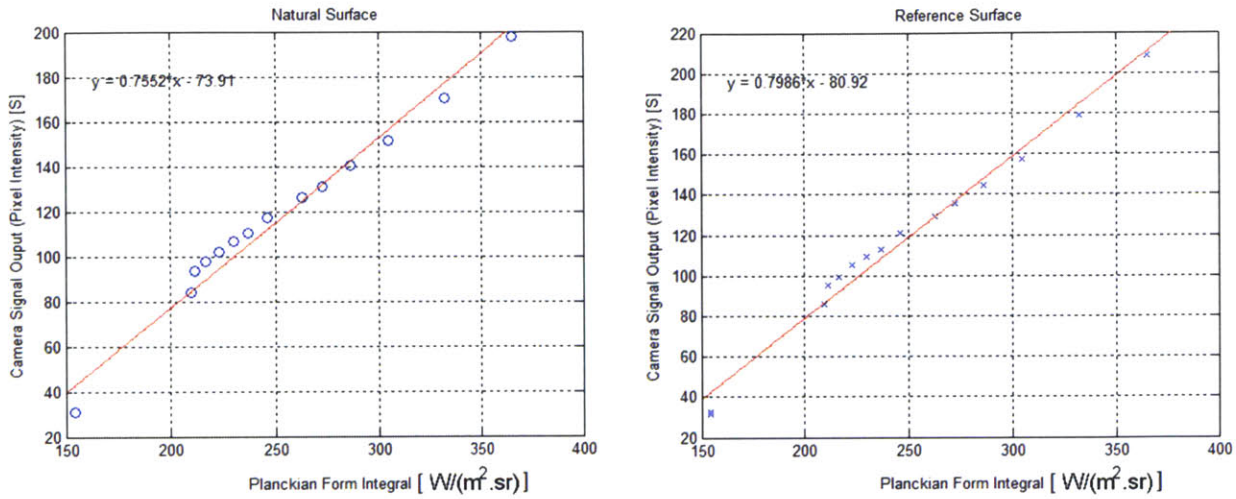

Figure 86: Camera Signal Output (Pixel Intensity) [S] vs LWIR Planckian Integral for (8-14 μm) for Natural Surface(Left) and Reference Surface (Right) with ε_r=0.95

The radiance emitted from the object's surface can be modeled according to Minkina (2009) [35], Rogalski 2009 [37], and Fehlman and Hinders 2009 [43] as:

$$S_o(T_o) = \tau\varepsilon_o\tilde{S}(T_o) + \tau(1-\varepsilon_o)\tilde{S}(T_b) + (1-\tau)\tilde{L}(T_a) \quad (76)$$

Where S_o is the observed radiance detected by the infrared camera, $\tilde{S}$ is the radiance from the Planckian form integral (8-14 μm) of a black body, T_o is the surface temperature of the object, T_b is the background temperature, T_a is the ambient temperature, τ is the transmission coefficient of the atmosphere, and ε_o is the emissivity of the object. Since the object is close to the camera, we can neglect the effects of due to the atmosphere and set τ =1. Therefore, the observed radiance becomes:

$$S_o(T_o) = \varepsilon_o\tilde{S}(T_o) + (1-\varepsilon_o)\tilde{S}(T_b) \quad (77)$$

Next, if we assume that the object is a diffuse surface where $(1-\varepsilon_o)\tilde{S}(T_b)$ is independent of the reflection angle such that

$$(1-\varepsilon_o)\tilde{S}(T_b) \approx \frac{(1-\varepsilon_o)}{\pi}E \quad (78)$$

Where E is the total irradiance energy from the target surface to the surrounding background environment. The total irradiance from the background can be estimated to be:

$$S_b(T_b) = \frac{E}{\pi} \quad (79)$$

Therefore, the observed signal detected becomes:

$$S_o(T_o) = \varepsilon_o \tilde{S}(T_o) + (1 - \varepsilon_o) S_b(T_b) \quad (80)$$

To estimate the emissivity of an object, ε_o, we use a reference emitter object such with known emissivity ε_r such as the black-tape. In our experiments described in the last section, we observed a linear relationship between camera signal output (pixel intensity) and the corresponding observed radiance from the Planckian form integral (8-14 μm) of the temperature of the reference surface:

$$y_{48\ in-black\ tape} = 0.383x + 7.8\,,\ R^2 = 0.9922$$

We choose the object surface such that both surfaces ε_o and ε_r are known to be at the same reference temperature and experiencing the same background irradiance. Fehlman and Hinders 2009 [43] shows a similar method for determining emissivity using a reference material. Madding [88] reports on emissivity estimation using either a reference material, a reference temperature, or a two temperature method. The radiance from the object's reference emitter surface is:

$$S_r(T_o) = \varepsilon_r \tilde{S}(T_o) + (1 - \varepsilon_r) S_b(T_b) \quad (81)$$

We solve for the theoretical black body radiance $\tilde{S}$ for the object:

$$\tilde{S}(T_o) = \frac{S_o(T_o) - (1 - \varepsilon_o) S_b(T_b)}{\varepsilon_o} \quad (82)$$

We solve for the total radiance of the black body $\tilde{S}$ for the reference emitter:

$$\tilde{S}(T_o) = \frac{S_r(T_o) - (1 - \varepsilon_r) S_b(T_b)}{\varepsilon_r} \quad (83)$$

Since the black body radiance $\tilde{S}$ of both surfaces are the same, we equate the two equations:

$$\frac{S_o(T_o) - (1-\varepsilon_o)S_b(T_b)}{\varepsilon_o} = \frac{S_r(T_o) - (1-\varepsilon_r)S_b(T_b)}{\varepsilon_r} \quad (84)$$

Solving for the emissivity of an object, ε_o, yields:

$$\varepsilon_o = \frac{S_o(T_o) - S_b(T_b)}{S_r(T_o) - S_b(T_b)} \cdot \varepsilon_r \quad (85)$$

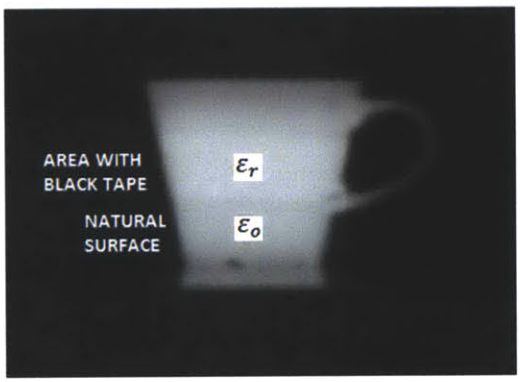

Figure 87: Close-up of object, ε_o used for experimental calibration

To solve for ε_o, we utilize a reference emitter surface of a black electric tape with a calculated emissivity of $\varepsilon_r = 0.95$ from the initial experiment. From the chart, we determine that $S_b(T_b = 20°C) \approx 32$. Solving for $S_o(T_o)$ and $S_r(T_o)$ based on the linear regression of the experiment for T_o= 80° C yields:

$$S_b(T_b) = 32 \text{ Lum}$$

$$S_o(T_o) = 181.64 \text{ Lum}$$

$$S_r(T_o) = 188.51 \text{ Lum}$$

$$\varepsilon_r = 0.95$$

Finally, solving for ε_o, the emissivity of the object, yields a mean $\varepsilon_o = 0.920$ with a standard deviation of $\varepsilon_{stdev} = 0.010$ over 13 sampled data points.

To use the calibration techniques presented in this section in the field for an unknown surface temperature and emissivity, we present the following procedure:

1. Perform on-field infrared camera autogain (AGC) lock using two reference objects with high emissivity values representing two temperature extremes (i.e. a warm hand and a bag of ice). The temperature extremes will seek to maximize the dynamic range of the system between two those reference temperatures.
2. Measure the temperature of the two reference objects using a portable thermistor.
3. From the infrared image for max and min temperature references estimate the corresponding grey-scale pixel intensity values.
4. Derive a Planckian form integral (8-14 μm) or use an existing look-up table of radiance values between the max and min temperatures.
5. Map the corresponding grey-scale values with the radiance values (similar to Figure 84 - Figure 86).
6. Correct those values accordingly for emissivity, which should be a linear relationship.

4.4.2 Observing Directional Emissions

In Chapter 2 we discussed the concept of directional emissivity. In the experiment described below, we confirm through the following, the dependency on viewing angle and camera signal output (pixel intensity). In the experiment, the temperature profile is mapped along the center of the cup area where the $T_{black\text{-}tape}$ is measured using a thermistor and camera signal output (pixel intensity) is calculated based on a scale of 1 through 256 using 8 bits. As one can see, observed radiance and emissivity is invariant for a fixed temperature for viewing angle between 0° and 60°. However, as the viewing angle on the cup goes beyond 60°, the observed radiance begins to drop off for the same isothermal temperature line. The experiment indicates that radiance and emissions are not independent of angle. This further implies that the Lambertian surface approximation is not verified by our experimental data and hence is not application. A similar observation has been shown by Schmidt & Eckert 1935 [42]. However, we note that the subsequent researchers have sometimes

been careless in applying Lambertian approximation without paying attention to the angle dependence. This experiment was conducted along the surface of the cup with black electrical tape where previously, we estimated $\varepsilon_r = 0.95$.

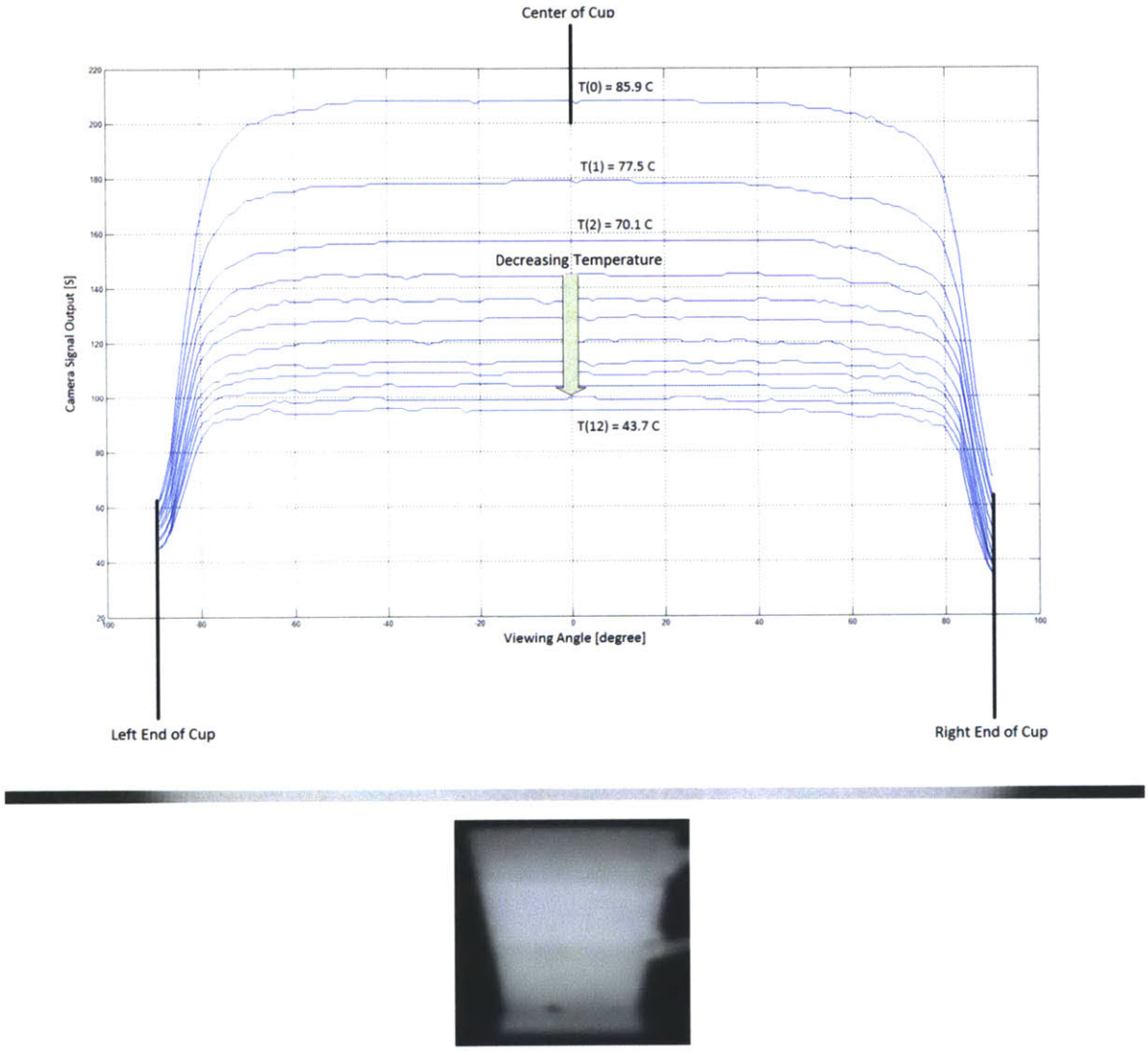

Figure 88: Experimental results for camera signal output (pixel intensity)[S] vs viewing angle θ for varying temperatures.

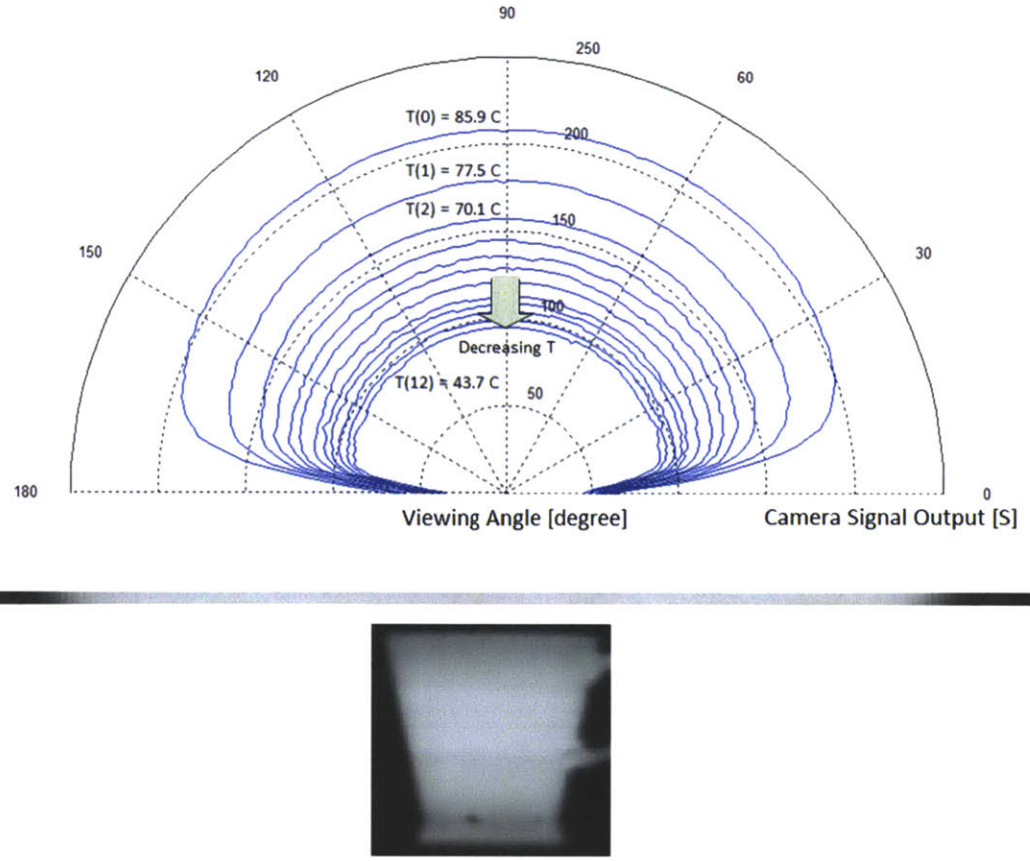

Figure 89: Experimental results for camera signal output (pixel intensity) [S] vs angle θ for varying temperatures in polar plot.

In Chapter 2, we discussed the limits to a Lambertian surface approximation. When viewed from any angle, a Lambertian surface will exhibit the same observed radiance. This is based on the assumption that that object's surface is a perfect diffuser and a perfect grey body. In practice, most surfaces are neither ideal specular or diffuse emitters, and will exhibit fractional amounts of both. Further, we note that radiant emissions depend on viewing angle, therefore, the surface can not be perfectly Lambertian.

We discussed at the beginning of the Chapter the heat transfer between two bodies, where the view factor between surface 1 and 2 is:

$$F_{1\to 2} = \frac{\cos\theta_1 \cdot \cos\theta_2}{\pi S^2} dA_2 \qquad (86)$$

Here, as θ_1 and θ_2 becomes large, the product $(\cos\theta_1 \cdot \cos\theta_2)$ becomes very small. Additionally, $\varepsilon_o(\theta)$ changes which would affect the overall heat transfer $\dot{Q}$ accordingly.

Using ARTIST as an experimental platform, we can perform further experiments under different conditions for mapping the relationship between observed radiance received by the camera to viewing angle θ.

4.4.3 Understanding Situations where Emissivity Matters

Currently, there is no scientific method for directly measuring emissivity on the fly. Consider some situations in which misunderstanding of emissivity really matters as it relates to incorrect surface temperature estimation and subsequently incorrect radiant emission estimate.

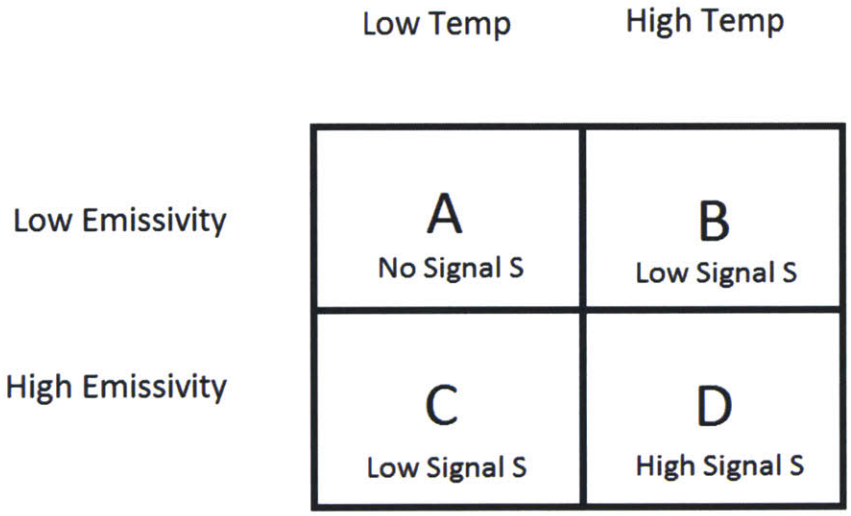

Figure 90: Emissivity possibility matrix diagram

In this exercise, we limit the discussion to street level thermography where the observed temperatures are in the range of 0°C - 40°C. The scenarios A, B, C, and Dare representative of varying signals S observed by the infrared cameras.

Scenario A: The observable signal S is nearly zero. This is due to very low emissivity combined with low temperature, producing little to no observable signal.

Scenario B: The observable signal S is low or weak. This is due to the object having a high temperature surface, with low emissivity. Objects such as polished steel, polished aluminum, or shiny metallic surfaces which are hot, can be in state B.

Scenario C: The observable signal S is low or weak. The object has high emissivity, and low temperature. A majority of surfaces will exhibit this in many cases where the temperature is low. Wood, painted walls, single pane glass, and most building surface materials have relatively high emissivity.

Scenario D: the observable signal S is high or strong. The object has high emissivity and a high surface temperature. In these cases, observed surface is clearly "hot" relative to the surrounding surfaces. These are the cases where the energy leak is high, due to poor insulation, a thermal bridge, or major air leaks.

In terms of energy leak detection, we are primarily concerned with the scenarios B & D, where the surface temperature is high and with associated radiant energy loss. A & C are not of concern because in these cases, the energy loss is low or nearly zero. We focus the rest of the discussion on scenarios B & D.

Scenario D is clearly observable and detectable in nearly all cases because a situation where high temperature with high emissivity surface will certainty lead to a high signal S with no false positive readings. However, scenario B is different. The low signal S can lead to a false negative reading and be possibly mistaken for scenario C, exhibiting low signal S.

We propose 2 methods to help identify or narrow the selection between scenarios A or B:

1. Introduce object detection algorithms to determine the likelihood of specific material possibilities based on the morphology or visual clues from the object in the infrared band. This process uses a pre-defined heuristic database to limit the search possibilities and reduce the uncertainty surrounding material properties estimate
2. Extend Process (1) to include multi-spectral (multi-band) information similar to Figure 41, from EO/NIR and introduce alternative sources of information (such as GIS mapping) to

search for color, shape, transparency, or texture based visual clues from the other wavelengths. This assumes that object surface pixel location can be accurately mapped between imaging modalities. In this case, multi-spectral imaging capability of ARTIST plays an important role in provide information from different imaging wavelengths.

4.4.4 Directional Correction to Lambert's cosine law

In this section, I would like to introduce the concept of a directional correction factor for non-Lambertian surfaces. Assuming ARTIST can be used as a reliable platform to gather and interpret observable radiance for a 3D environment, we further develop ARTIST to correct for situations where observed emissions is non-uniform. From what we observed from our experiments and from our understanding of Schmidt & Eckert 1935 [42], directional emissions are dependent on the viewing angle for metal (low-emissivity) and non-metals (high-emissivity). However, this contrary to Lambert's cosine law, which states that when viewed from any angle, the observed radiance is uniform.

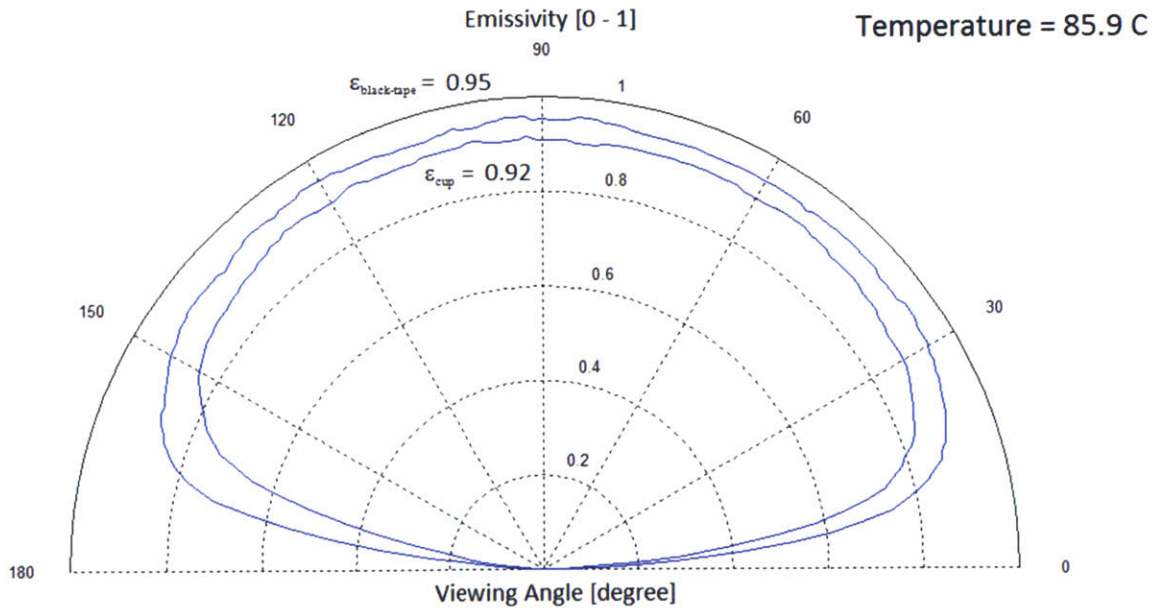

Figure 91: Directional emissivity for two surfaces ($\varepsilon_{black\text{-}tape}$ = 0.95 and ε_{cup} = 0.92) with constant temperature (85.9°C) in polar plot

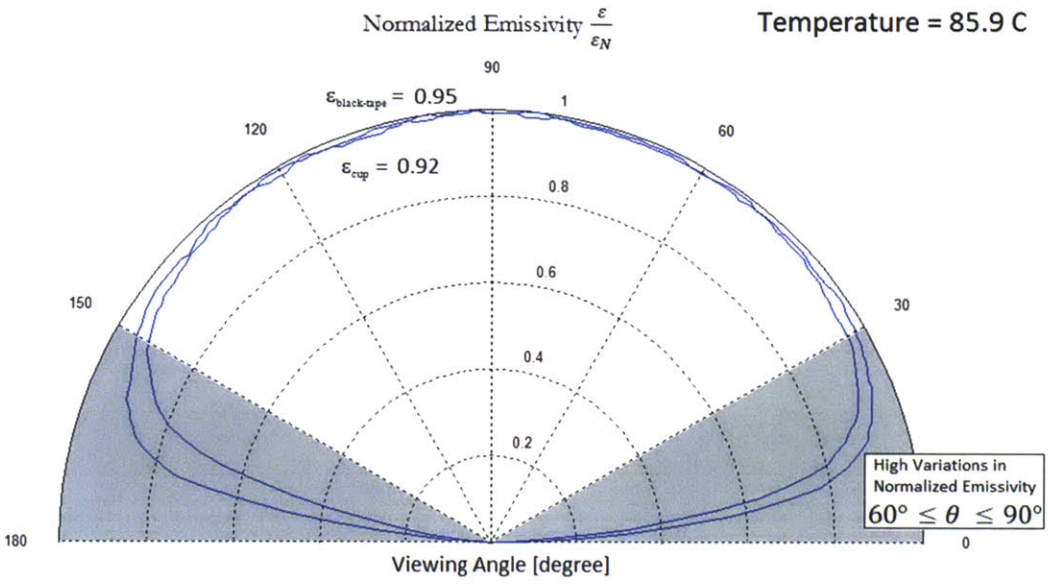

Figure 92: Normalized directional emissivity ($\frac{\varepsilon}{\varepsilon_N}$) for two surfaces ($\varepsilon_{black-tape}$ = 0.95 and ε_{cup} = 0.916) with constant temperature (85.9°C)

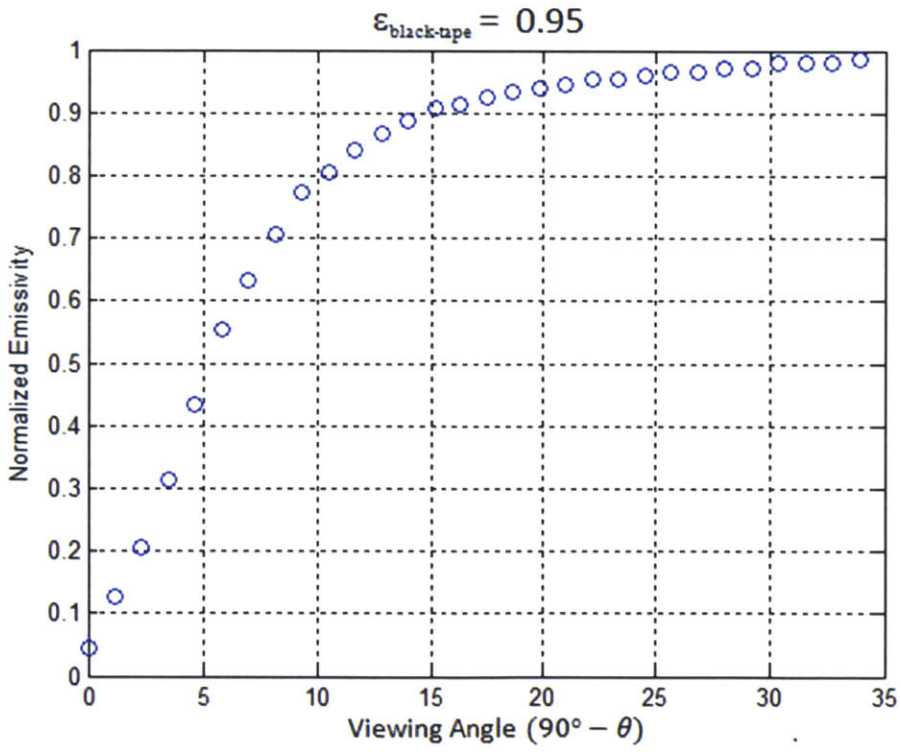

Figure 93: Normalized directional emissivity ($\frac{\varepsilon}{\varepsilon_N}$) for $\varepsilon_{black-tape}$ = 0.95, 0< θ<30°, (T=85.9°C)

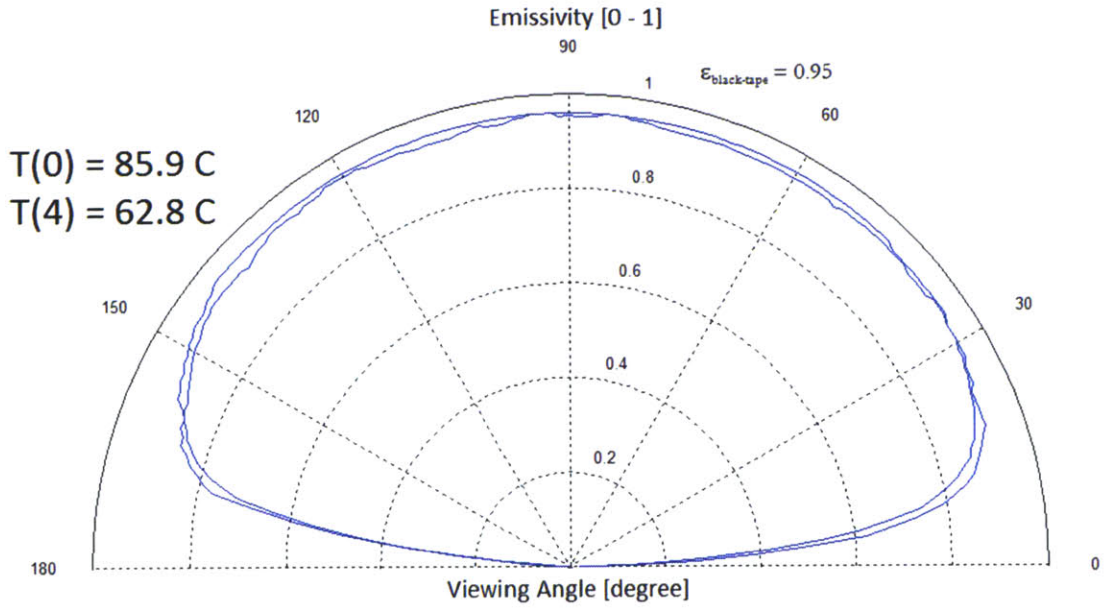

Figure 94: Directional emissivity for a single surface ($\varepsilon_{black-tape}$ = 0.95) with multiple temperature (T_0= 85.9°C and T_4= 62.8°C)

For non-metals surfaces, we introduce the concept of directional correction for normal emissivity that captures the angular variation in emissivity as a function of θ:

$$\varepsilon_{obs} = \varepsilon_N \cdot g(\theta) \quad (87)$$

$$g(\theta) = \text{directional correction factor} \quad (88)$$

4.4.5 Metallic Surfaces – an Exception

Metallic surfaces with low normal emissivity values behave differently than non-metallic surfaces as discussed earlier in Chapter 2. Normalized emissivity, $\frac{\varepsilon}{\varepsilon_N}$, can vary as much as 30% for metals versus 6% for non-metals according to Schmidt & Eckert 1935 [42]. Additionally, directional emissivity seems to increase for metals as a function of viewing angle θ for metals and decrease for higher angles in non-metals. In this thesis, no experimental calibration of emissions variation with angle was done for metals because of the following:

a. Metals are infrequently used in buildings because of poor thermal management (thermal bridge)
b. Metals (low emissivity) materials represent only 20% of the possible choices of building materials.
c. For signals from the IR cameras, the contributions from ε and temperature are equal. Given $\varepsilon_{metal} \sim 0.1 - 0.2$, the signal strength from metal in the region on the scene is highly attenuated and hard to calibrated on top of the ambient signal of the environment.

Therefore, for the purpose of this thesis, we will not focus on metallic building materials.

4.4.6 Conservation of Radiance & Etendue

To verify that the signal *s* [observed radiance] is the same regardless of distance, we conduct a separate experiment where 3 identically filled cups are filled with hot water and placed in the microwave until boil. They are taken out and placed at distance (a) = 38 inch, distance (b) = 140 inch, and distance (c) = 480 inch from the camera. The temperature is the same for all three cups T_o (cup) = 160° F [344°K].

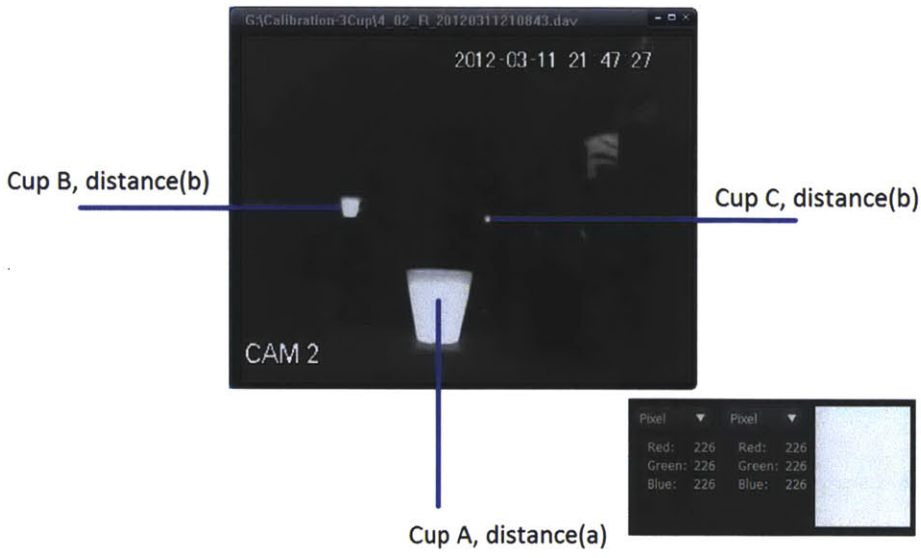

Figure 95: 3 Cup experiment to demonstrate conservation of radiance principle for fixed temperature at varying distances

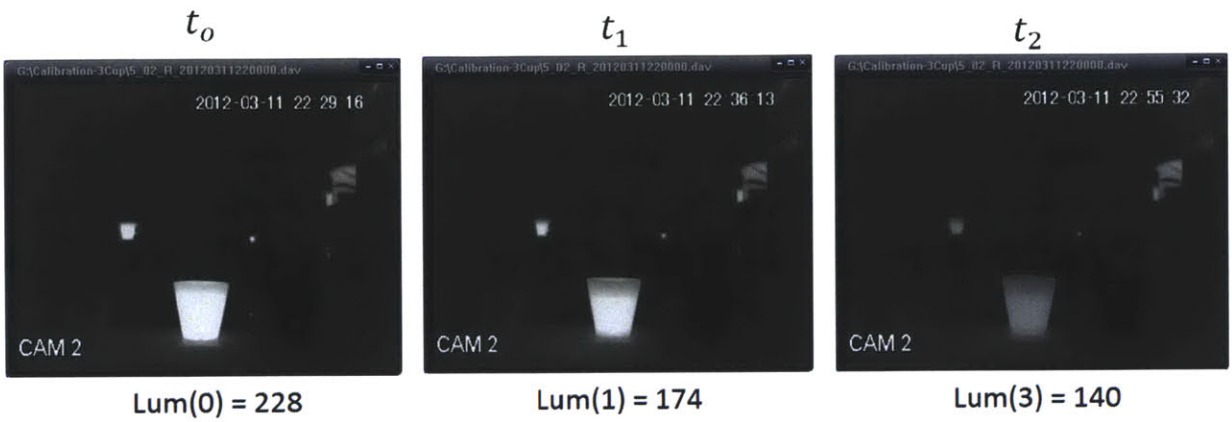

Figure 96: Experiment demonstrating the conservation of radiance using 3 Cup at t_o, t_1, t_3 with identical temperature in all cups

4.4.7 Conclusion and Insights

In this Chapter, we have explained the need for 3D radiometry. Based on the limits of a Lambertian surface approximation, the angular dependency of emissivity, and the 3D nature of the real world, we present the concept of 3D radiometry and specifically, the concept of a directional correction factor to account for directional emissions from a source and normalize the value relative to normal emissivity calculations for accurate temperature estimation. To develop a better understanding of the 3D world, I created a 3D model of the scene. In this Chapter, I presented a polynomial based optical flow method and showed how it can be used to create a depth map and a corresponding mesh map to generate a solid model of the building surfaces. From the solid surface, we can estimate distance and viewing angle to the camera. As it turns out, this information is critical to help us understand directional emissivity and its estimation and use within ARTIST. Additionally, I have shown a method to calibrate non-radiometric cameras to derive a calibration function for camera signal output (pixel intensity) vs observed radiance corresponding to a temperature. Additional experiments were conducted to show camera signal output (pixel intensity) as a function of angle for varying temperatures. The results confirm the theory from Schmidt & Eckert 1935 [42], that there is an angular variation in emissivity. I conclude from this Chapter that additional research should be emphasized on understanding emissivity as a function of angle, material properties, surface finish, and potentially many others.

Chapter 5: Image Processing

5.0 Introduction

In Chapter 4, I presented a case for 3D radiometry and why factoring in angular information is important to correct for direction emissivity. The emission variation, when viewed at an angle, can be corrected using we concept around direction corrections. In this Chapter, we will focus on image processing in thermography. As we concluded in Chapter 3, improving imaging resolution is critical to understanding the nature and characterization of small leaks. We also discussed in Section 3.2 that there were three forms of resolutions: spatial, spectral, and temporal resolution. In previous Chapters, I show how ARTIST increases resolution from a hardware implementation. We will focus on software approaches to improving resolution in Chapter 5.

I will present jointly developed research in software approaches to improving imaging resolution for infrared cameras based on super resolution techniques. Together with Dr. Jonathan Jesneck, Professor Sanjay Sarma, Dr. Hui Kong, and other members of the Field Intelligence Laboratory, our research team has made research progress in the areas of image processing for resolution enhancement. My responsibilities included developing the experimental procedures, contributions to its theories, and thinking of potential extended applications. A majority of the technical image processing implementation was the result of Dr. Jesneck's contributions due to his background in medical imaging.

5.1 Quantifying the Cost per Pixel of IR

One of the motivations of my thesis research has been to reduce the dependence on very expensive LWIR equipment. For the EO and NIR bands, the cameras are relatively inexpensive ($10,000-$40,000) and the cost per pixel is very low. However, when considering the various LWIR technologies that were available, the cost per pixel in the LWIR band were over 2 orders of magnitude more compared to the EO band. This is a likely limitation for broader deployment of LWIR instrumentation in thermography at an urban scale. LWIR technology is manufactured from materials such germanium and zinc selenide, making it very prohibitively costly. Unfortunately,

LWIR has not benefited from the mass production and competitive nature of modern digital camera technology. For example:

- FLIR Photon 320, 320x240 = 76,800 Pixels
  - Estimated Cost $10,000
  - Cost/Pixel = $0.13 /pixel
- Canon Powershot S500 5MP Camera = 5,000,000 Pixels
  - Estimated Cost $100
  - Cost/Pixel = $0.00002 / pixel

The cost calculation above shows 4 orders of magnitude difference in cost/pixel between LWIR and EO technology.

Thermal imaging hardware solutions are expensive, mainly driven by several major factors: (a) small production quantities relative to more common electro optical systems found on digital cameras and cell phones (b) use of expensive materials for the production of the *focal plane array* (FPA) and optics (typically germanium which is a versatile infrared material commonly used in imaging systems and instruments in the 2 to 12 microns spectral region) that allow transmission of thermal radiation through the lens.

In a limitation to widespread adption and use, LWIR technology is tightly controlled by the US State Department for export and heavily regulated under International Traffic in Arms Regulations (ITAR) as explained by Root, *United States export controls* [89]. These rules limit the export us of LWIR technology outside the United States and non-US citizens.

In summary, there are three basis methods to increase LWIR resolution and field of view (FOV):

a. FPA Hardware (high spatial pixel density per square area)
b. Optics
c. Arraying (multi-camera configuration)
d. Software (resolution enhancement algorithms)

Spectral bands	Range [μm]	Detector materials	Applications
NIR	0.74 – 1	SiO_2	Telecommunications
SWIR	1 – 3	InGaAs, PbS	Remote sensing
MWIR	3 – 5	InSb, PbSe, PtSi, HgCdTe	High temperature inspections
LWIR	8 – 14	HgCdTe	Ambient temperature inspection
VLWIR	14 - 1000		Spectrometry, astronomy
Si: silicon ; SiO_2: silica ; In: Indium ; Ga: galthum ; As: arsenic ; Pb: lead ; S: sulfu r; Sb: antimony ; Se:selenium ; Pt: platinum; Hg: mercury; Cd:cadmium; Te:tellurium			

Table 5: Detector material vs spectral wavelength table

The FLIR Model P-660 thermal imager (640x480 pixels) used in our initial research retailed for approximately $35,000 without any accessories as of January, 2010. Today, similar imagers can be purchased for around $30,000 from the manufacturer FLIR. FLIR holds a virtual monopoly in the infrared camera market, which, according to their own documentation holds approximately 61% of the global market share for thermal imaging equipment. Part of the reason why FLIR thermographic infrared cameras costs more than non-FLIR cameras is due to their unique radiometry feature, the ability to interpret thermal temperature from the images.

A 640x480 infrared image has the equivalent resolution of an old computer webcam, representing 307,000 pixels. This is considered 'state of the art' for small commercial off-the-shelf thermography. For large commercial applications such as satellite imaging or military related applications, significantly larger focal plane arrays with high pixel density must be specially manufactured. This increases the total development costs significantly.

Reducing cost of the equipment is a research objective both for practical reasons and for helping broader adoption. We have focused on using off-the-shelf components, specifically long wave infrared camera systems. Finding ways to improve resolution for LWIR systems became an

important topic of this thesis. Without shifting focus to hardware improvements, which is costly, a principal area of research involved improving resolution through software algorithms.

5.2 Super Resolution Imaging

Super resolution is a class of imaging techniques used to enhance the resolution of an imaging system beyond its native limit [90-93]. There are single frame and multi-frame variants to super resolution. Several well cited references on super resolution imaging includes Park [94], Farsui [95], Baker [96], and Freeman [97] from MIT.

5.2.1 Single-Frame Super Resolution

Single frame super resolution methods attempts to increase resolution be removing motion or camera blur. Examples of single frame super resolution is shown and discussed by Freeman [97] and Elad [98].

5.2.2 Multi-Frame Super Resolution

Multi-frame super resolution methods attempts to increase resolution through the use of sub-pixel shifts from the low resolution images to solve the inverse problem of resolving the high resolution pixels. Examples and discussion of multi-frame super resolution approaches is discussed by Farsui [99], Borman [100, 101]. For the purposes of this thesis, we will focus on multi-frame super resolution. ARTIST is a multi-frame capable system. Therefore, we will aim to maximize the use of our multi-frame information.

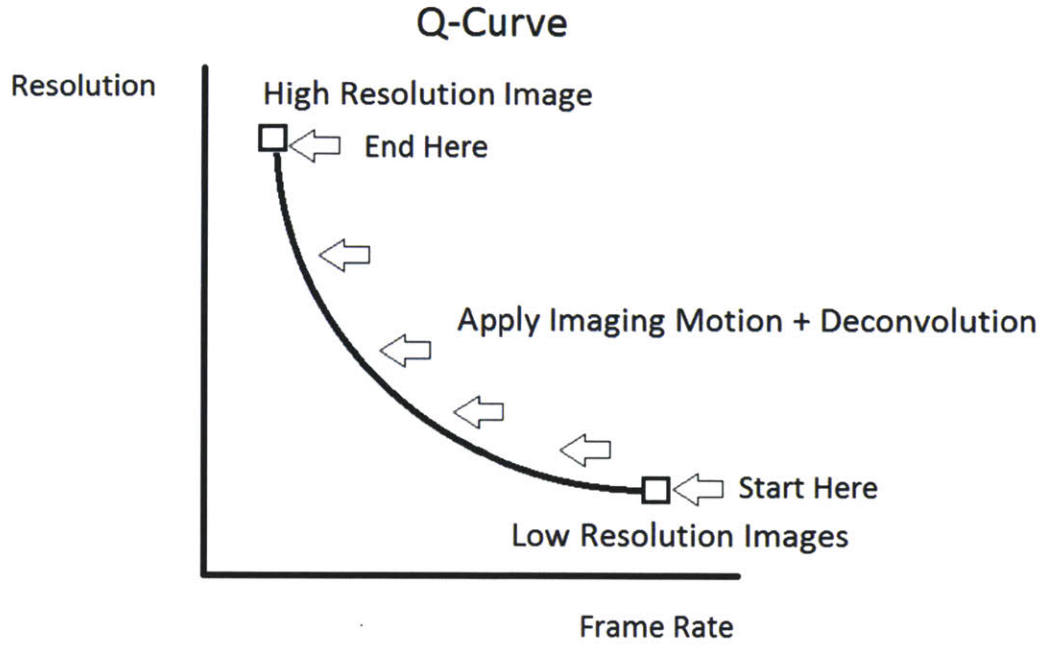

Figure 97: Multi-Frame super resolution conceptual diagram

In Figure 97, we show the multi-frame super resolution concept for a single camera. For a single imaging camera detector, we can describe its characteristic with using the following known convention:

a. Resolution (pixels), spatial
b. Color depth (bits), wavelength
c. Framerate (FPS), temporal

Together with other attributes (lens aperture, sensors, etc), these three primary specifications are used to help determine the overall system performance and information bandwidth.

$$\text{Bandwidth} = \text{Resolution} \cdot \text{Color Depth} \cdot \text{FPS} \quad (89)$$

For any imaging system, there is a maximum bandwidth (I define this as the 'Q') associated with the system. For example, an infrared camera with 640x480 resolution, 14-bit color depth, and 30 fps has a fixed bandwidth Q.

$$Q_{IR\text{-}camera} = (640x480)\cdot(14\ Bit)\cdot(30\ fps) \quad (90)$$

Without any additional hardware or software improvement, Q is typically fixed for any imaging system. However, using multi-frame super resolution, which is a motion based super resolution algorithm, one can combine multiple low resolution imaging frames from a single camera, and use the sub-pixel shift information to infer the high resolution pixel. This inverse problem is solved by making a very critical tradeoff, temporal versus spatial resolution. By combining multiple frames (temporal) and using the information to gain resolution (spatial), this method has been shown to improve overall resolution. The reverse can also occur, spatial versus temporal tradeoff. In this case, a high resolution frame can be down-sampled, or shifted to produce multi-frame low resolution images. Multi-frame super resolution is a process created to produce this effect, trading temporal resolution for an increase spatial resolution. Multi-frame super resolution algorithms can be used to help produce manipulate spatial vs temporal information in a way that allows us to control where we are on the Q-curve. This sub-class of software resolution improvement can be useful in ARTIST due to the imposed natural motion of the imaging system and needs for higher resolution.

We considered many super resolution methods to enhance imaging system resolution, specifically in the LWIR band where the cost per pixel is highest. Methods we considered included those by Farsui [99, 102, 103], Irani [91], Sroubek [104], Schultz [105], and Caron [106]. For infrared detectors and equipment an order of magnitude increase in resolution will result in at least am order of magnitude increase in cost. The marginal cost per pixel for LWIR in our estimate is non-linear. The cost-benefit analysis of super resolution imaging in long wave infrared applications will show that it is advantageous to focus on improving resolution through software versus a hardware approach.

5.3 Hyper Resolution Multi-Frame Imaging[5]

Operationally, ARTIST is capable of multi-spectral imaging and has the ability to image in EO, NIR, and LWIR wavelength bands. Such a capability led to the question of whether information can be used across different modalities to improve resolution, while viewing the same scene. As discussed in the last Section 5.2, multi-frame super resolution refers to the improvements using temporal versus spatial tradeoff in resolution. We extended this concept into temporal vs spatial vs spectral resolution and hence, the concept of hyper-resolution was created.

Hyper resolution refers to the process of combining two or more spatially, temporally, or spectrally (resolution) varying imaging system across multiple resolution modalities to achieve super resolution. Each imaging camera will have its own unique Q-curve and when multiple Q-curves are combined, the idea that that more information will be available to help solve the problem of improving the resolution of a pixel. For example, there are several combinations of cameras that would be highly beneficial to apply hyper resolution. I present two examples below:

1. Combination A: LWIR (640x480 Resolution, 14 bit, 30 fps) & EO (1920x1080,24 bit, 60 fps)
2. Combination B: LWIR (640x480 Resolution, 14 bit, 30 fps) & EO (640x480,16 bit, 500 fps)

Several methods have been introduced similar to this (1) "Image/Video Deblurring using a Hybrid Camera" by Tai, Du, Brown, and Lin [107, 108] and (2) A Hybrid Camera for Motion Deblurring and Depth Map Super-Resolution by Li, Yu, and Chai [109]. Both of these methods introduce the concept of a hybrid camera system to improve the resolution of a target imaging system. These methods are focused on addressing the problems of image deblurring by introducing the hybrid camera system to estimate global and spatially varying motion blur. Though unique, we would like to address the issues of resolution enhancement more specifically.

---

[5] "Hyper Resolution Multi-Frame Imaging" (MIT TLO No. 14572) L. Phan, J. Jesneck, S. Sarma

The proposed method for the Hyper Resolution methodology has the potential to yield significant resolution enhancement by one to two orders of magnitude. We have not fully characterized the potential of hyper resolution across the spatial, temporal, and spectral domain. I will demonstrate a limited use-case of hyper resolution and discussed the potential theoretical implications and use cases.

The basis for Hyper Resolution lies in a tightly coupled multi-camera setup where the motion of both imaging systems is well understood and can be mapped precisely. The coupling effect of cross-registering information from two different camera systems has the following potential beneficial effects:

1. Increased motion tracking resolution for spatial and temporal domains.
2. Reduced motion tracking errors
3. Imaging with multi-modality, across a broader combination of frequency spectrum
4. Enhanced single frame motion deblurring

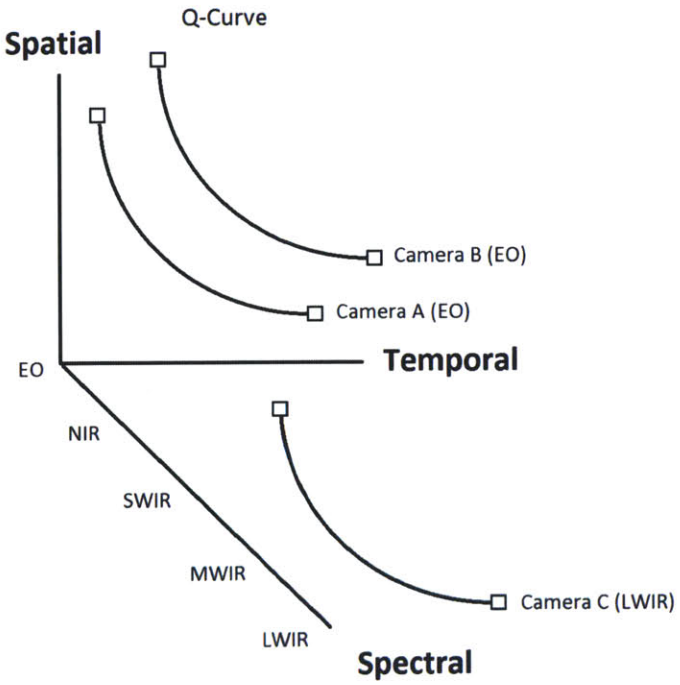

Figure 98: Q-Curve for 2 camera systems, Camera A with a fixed spatial and temporal characteristics and Camera B with superior spatial and temporal characteristics relative to Camera A, conceptual diagram

5.4 Modeling of a Scene within a Camera Image

Camera images are typically modeled as an output of an approximation, using a down-sampling process, for an unknown high-resolution image. A series of Y(k) of k=1,2, …K low-resolution camera images may be represented using the following model:

$$Y(k) = D(k)H(k)F(k)X + V(k), k = 1,2, \dots, K \quad (91)$$

where Y(k) is an observed sequence of K low-resolution images from a camera, D(k) is a down-sampling operator, which is also known as the "decimation operator", H(k) is a blurring kernel, $F(k)$encodes the motion information of the kth frame, X is the unknown high-resolution image, and $V(k)$ is additive system noise. A high-resolution scaled image X is down-sampled to match the low-resolution scale associated with the series of low-resolution images.

5.4.1 Passive Image Co-Registration

Image registration is the process of transforming different sets of data into one coordinate system [110]. In image processing, image registration may be performed using different strategies. Two such strategies include:

1. Feature identification and tracking
2. Spatial similarity metrics

In this thesis, the preferred image registration technique is performed on the basis of spatial similarity. For image registration, we consider horizontal, vertical, and rotational translation motion. We model the total camera motion F represented as a product of its translational and rotational motion operators:

$$F = S_x^l S_y^m R \quad (92)$$

where S_x^l and S_y^m are the operators corresponding to shifted the image by l pixels in the horizontal direction and m pixels in the vertical direction, and R represents the rotation matrix:

$$R = \begin{bmatrix} \cos(\theta) & -\sin(\theta) \\ \sin(\theta) & \cos(\theta) \end{bmatrix} \quad (93)$$

R is defined by a rotational angle θ. F(k) may also include a focus factor accounting for camera motion along the line-of-sight to the imaged object. Most generally, F(k) accounts for orientation, scaling and tilting of respective images relative to a reference image. The image offset between a reference image and a test image may be calculated by defining a loss function L, where:

$$L(x, y, \theta; Y_0, Y_k) = \left| Y_0(x, y, \theta) - Y_k(x - x_k, y - y_k, \theta - \theta_k) \right| \quad (94)$$

and the optimal solution to the loss function L is defined by:

$$(l', m', \theta') = \underset{x,y,\theta}{\operatorname{argmin}} \| Y_0 - FY \|_1 \quad (95)$$

where x_k is the row offset, y_k is the column offset, and θ_k is the angle offset for image Y_k compared to reference image Y_0.

Minimizing the loss function is one method for obtaining a reference image Y_0 with respect to its offsets. There is also the potential to use a reference image in a different modality (hyper-resolution). In that case, offsets (x_k, y_k, θ_k) are determined by linear transformation through matching the location of each low-resolution image to a corresponding location in an alternate modality's image. This will allow us to determine the phase shift of each low-resolution image inside using the registration information from an alternate mode's image. For example, we can couple two camera systems, EO (350-700 nm) with an LWIR system (8000-14000nm) and cross register the motion information from LWIR to help locate shifts in the low-lighting EO band.

Multi-frame super-resolution is highly dependent on accurate and precise image registration. The method introduced here uses only a sequence of images. This process uses a gradient that defines the steepness of the error surface during image registration may be represented as

$$G = \sum_{k=1}^{K} F^T(k) D^T \operatorname{sign}(DF(k)HX - Y(k)) \quad (96)$$

where G is the gradient vector and the remaining variables were previously defined. Minimization of the loss function L to yield (x_k, y_k, θ_k) for each image Y_k of the image sequence resulted in an accurate representation of camera movement F(k), which is used to extract the sub-pixel resolution information. This gradient descent approach helps identify the relative positions of all images in an image sequence and defines the camera's movement. The movement information is represented using a motion kernel intended for deconvolution to improve image resolution [104, 111]. The intuition behind this kernel formulation is that a high-resolution blur pattern of a single low-resolution pixel can be represented as a blurring kernel for a sequence of sub-pixel movements.

5.5 Kinetic Super Resolution

Together with my research colleagues, Dr. Jonathan Jesneck and Professor Sanjay Sarma, we developed a novel super resolution algorithm called Kinetic Super Resolution[6](KSR). KSR is based on a multi-frame approach to generating a motion kernel used to deconvolve a super positioned image representing the low-resolution images. Dr. Jesneck and I collaborated extensively to develop this algorithm. While I contributed to the conceptual ideas behind KSR, Dr. Jesneck worked on the technical implementation of KSR. KSR is currently patent pending through MIT's Technology Licensing Office.

KSR starts with the process of generating a motion based kernel representing the sub-pixel motions of the imaging system associated with K number of low resolution frames. The camera movement F(k), discussed previously, is modeled as an intrinsic quality of the imaging system. Using a kernel based description; a defined motion kernel can be used for deconvolution to improve image resolution. To begin, a two-dimensional impulse function is defined for a matrix with all zeros except for a single one in the center.

$$I = \text{diag}[0, \ldots, 0, 1, 0, \ldots, 0] \tag{97}$$

where I is defined in the low-resolution scale. In the high-resolution scale:

---

[6] "Kinetic Super Resolution" (MIT TLO No. 14538)

$$I = \begin{bmatrix} 0 & & & & & & 0 \\ & \ddots & & & & \iddots & \\ & & 0 & 0 & 0 & 0 & 0 \\ & & 0 & 1 & 1 & 1 & 0 \\ & & 0 & 1 & 1 & 1 & 0 \\ & & 0 & 1 & 1 & 1 & 0 \\ & & 0 & 0 & 0 & 0 & 0 \\ & \iddots & & & & \ddots & \\ 0 & & & & & & 0 \end{bmatrix} \quad (98)$$

I is represented by a single block of ones. This motion-based kernel may be easily combined with the traditional optical-blur kernel representation by replacing the block of ones with a blurring matrix, such as a 2D Gaussian kernel.

As an example, a 3×3 = 9× resolution increase can been projected from using the low-resolution image and projecting to a high-resolution scale. The motion-based point spread function may then be obtained by integration of that impulse function across the camera movements:

$$PSF_{camera} = \sum_{k=1}^{K} F(k)I \quad (99)$$

Where PSF_{camera} is a motion point spread function that we defined as the "kinetic point spread function" or a "kinetic PSF", $F(k)$ represents the camera movement, and I is the two-dimensional impulse function. The kinetic PSF is advantageously employed to remove the blurring effect of the kernel of the lower resolution super positioned image by applying standard deconvolution techniques, using regularization such as Tikhonov regularization [112, 113]. Accordingly, the following cost function is applied:

$$C = \sum_{k=1}^{K} \|DF(k)HX - Y\|_1^1 + \alpha\lambda(x) \quad (100)$$

Where C is the cost function and the remaining variables are previously defined. The cost function is minimized, where $\lambda(x) = \|Qx\|_2^2$ is a penalty term in which the matrix Q represents a high-pass filter so that the regularization represents a general smoothness constraint. In our case, minimizing C provides the sought-after high-resolution image.

5.5.1 KSR Example

We demonstrate KSR using a test setup that consisted of a US dollar bill taped onto a whiteboard pointed at distance of 10 feet from the camera. The camera is a USB based Microsoft Lifecam VX2000. Holding the camera with our hand and pointing the camera at the whiteboard, towards the dollar bill, we were able to record a 10 second sequence of video frames. The video frames were spliced into individual frames and the individual low-resolution 320x240 frames were used to demonstrate KSR. The following process was implemented as explained:

1. Capture video file using Microsoft Lifecam device
2. Hold camera at target object, a US dollar bill in this example, and apply a very small amount of hand motion during the video capture.
3. Split the video sequence into individual imaging frames.
4. Pick a sequence of frames (~20 frames)
5. Determine sub-pixel motion shifts between subsequent frames
6. Generate Kinetic PSF from the sub-pixel motion
7. Generate super position image by super imposing the low-resolution images
8. Deconvolve super position image with kinetic PSF using Tikhonov regularization

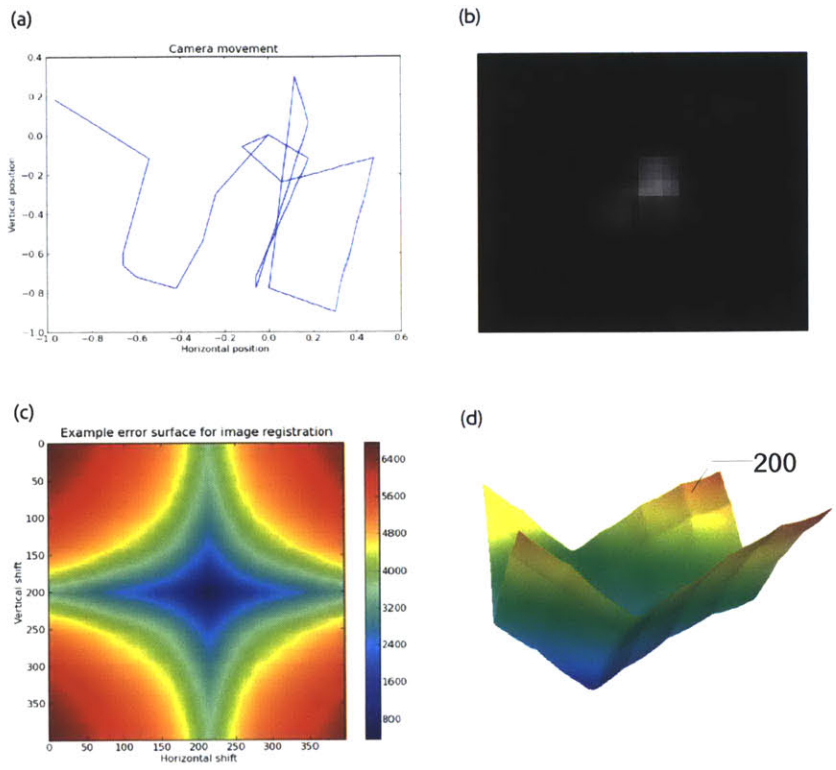

Figure 99: (a) Representative motion of camera (b) Motion PSF (c) 2d representation of gradient descent (d) 3d representation gradient descent used for image registration. (Implemented and tested by Dr. Jonathan Jesneck)

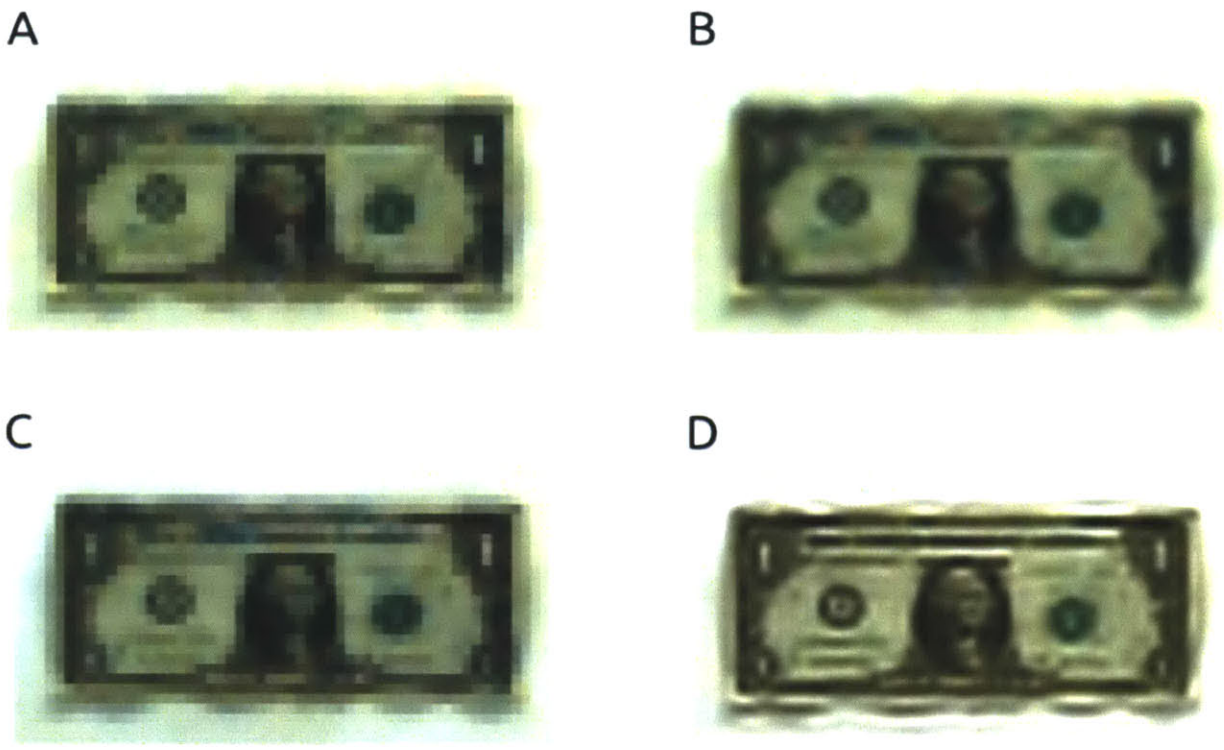

Figure 100: Demonstration of KSR with dollar bill taped on a wall 3 meters away from the camera. (Implemented and tested by Dr. Jonathan Jesneck)

A. Original video frame
B. Original video frame with bicubic interpolation
C. KSR with no motion
D. KSR with camera motion, natural hand motion

5.5.2 Testing of KSR algorithm based on Known Metrics

We demonstrate examples of KSR applied to greyscale, color, and infrared images. KSR demonstrated robust performance over a dataset of 25,000 images, outperforming nearest-neighbor interpolation, bilinear interpolation, and bicubic interpolation ($p < 1e\text{-}16$). In all cases, KSR was stably implemented and tested. This means KSR can potentially be adapted to many practical applications; including enhanced digital zoom for mobile phone cameras and increased signal-to-noise ratio for low lighting situations. KSR can be coupled with more traditional super-resolution techniques to further increase image resolution.

For quantitative and comprehensive performance comparison, we tested the KSR algorithm over a set of 25,000 non-simulated images, the MIRFLICKR data set [114]. From these images we simulated low-resolution, noisy video data, which we then subjected to the KSR algorithm in order to reconstruct images for comparison to the original high-resolution images. Each image we down-sampled five-fold (2.5 magnitude decrease), corrupted with Gaussian N(0,30) white noise, and shifted by randomly chosen sub-pixel amounts to produce a set of 40 low-resolution images. For each input image's low-resolution image set, we benchmarked the super-resolution performance by quantifying similarity to the original, unaltered image by two mechanical image similarity metrics: peak signal-to-noise ratio [115], cross-correlation, and by two metrics that better mimic the human visual system's perception: Q [116, 117]and structural similarity [116]. We compared the performance of the KSR method to that of nearest-neighbor, bilinear, and bicubic interpolation. *In all cases, the KSR method significantly outperformed each of the interpolation methods ($p < 1e\text{-}16$ by paired, two-sided Wilcoxon test).* Fully implementation of this testing procedure was carried out by Dr. Jonathan Jesneck. With permission from my collaborators, Dr. Jesneck and Professor Sarma, I have included the discussion on the KSR algorithm in this thesis for the sake of completeness.

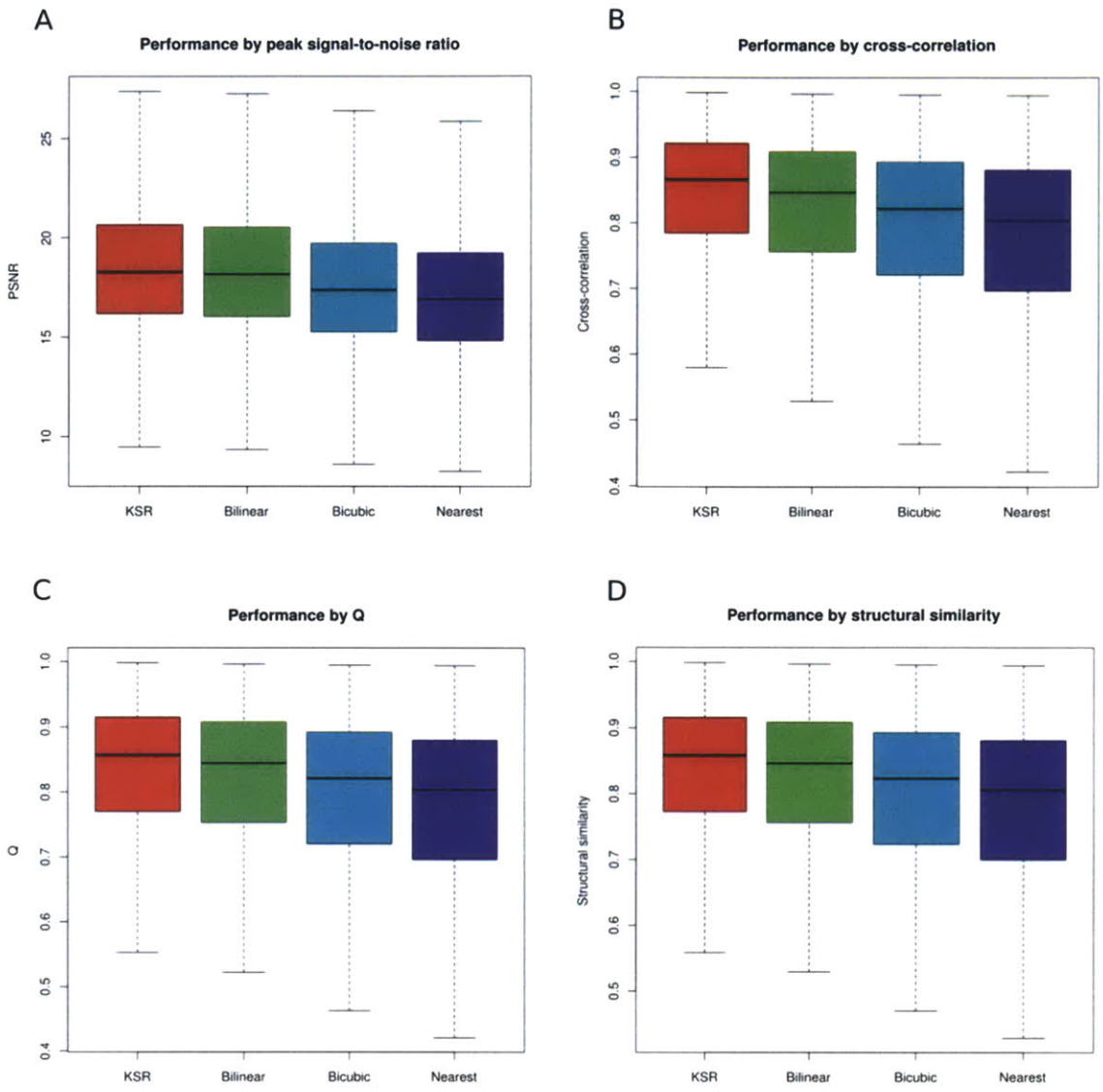

Figure 101: KSR performance across the MIRFLICKR image set.

The original images were down-sampled 5x and combined with Gaussian noise into sets of 40 images. The low-resolution images were transformed to higher resolution images by the kinetic super-resolution (KSR) algorithm, bilinear interpolation, bicubic interpolation, and nearest-neighbor interpolation. Super-resolution performance was measured by similarity with the original full-resolution image by several similarity metrics: (A) Peak signal-to-noise ratio, (B) Cross-correlation, (C) Q image quality metric, (D) Structural similarity.

5.5.3 Applying KSR to LWIR Imaging of an Urban Scene

For this demonstration, we used a drive-by scan of Burnside Avenue in Somerville, MA and focused on one particular home. In post processing, we focused on zooming into two particular areas of that home: (A) the upper right corner of the second floor window and (B) the front door on the first floor. In both cases, KSR was successful in improving image resolution overall. This approach can be utilized to improve image resolution overall, when condition demand the same, e.g. if on-site equipment, costs, LWIR resolutions are prohibitive. We demonstrate the image resolution improvement by applying KSR, which should improve pattern recognition detection rate in other applications require specific identification of thermal leakage type.

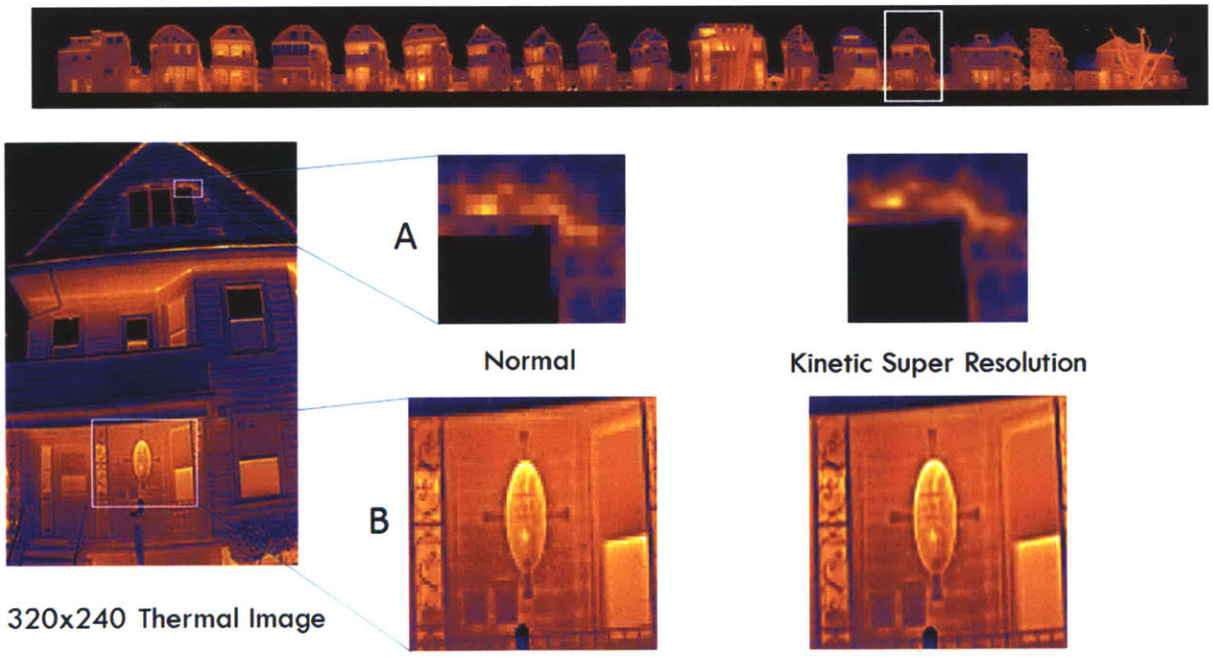

Figure 102: KSR example of home in Somerville, MA. (KSR, implemented and tested by Dr. Jonathan Jesneck)

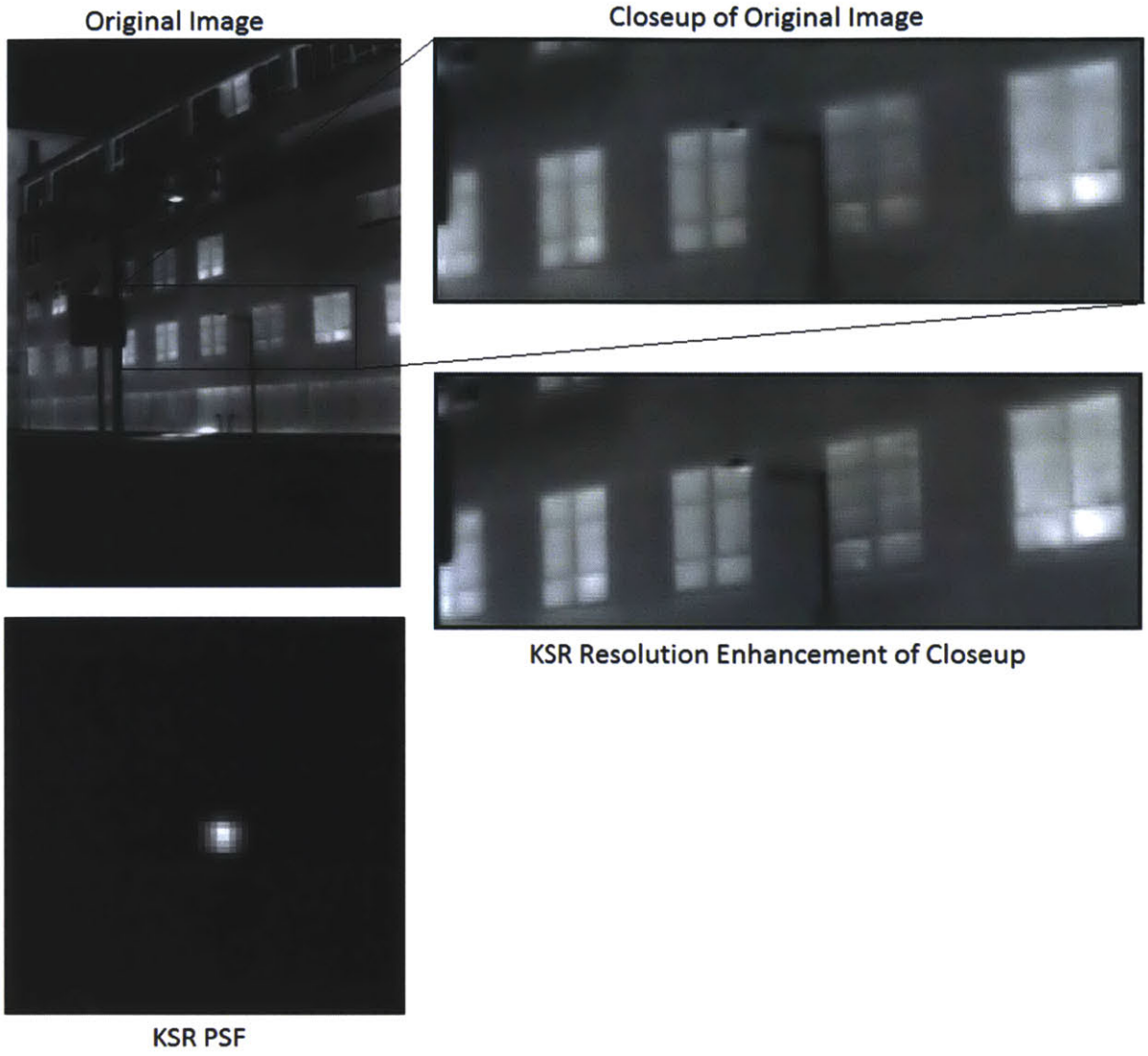

Figure 103: KSR of Building 35 at MIT, Cambridge, MA. (KSR, implemented and tested by Dr. Hui Kong)

5.6 Hyper Resolution in Single-Band `EO Imaging

Hyper-resolution is highly dependent on accurate and precise image co-registration. A simple spatial-to-spatial domain method is demonstrated. The sub-pixel image registration is introduced from the high resolution camera and transformed into motion information for low-resolution camera. We use a passive registration method to co-register the motion. By tightly fixturing two camera systems together, one may use the higher resolution/high/alternate modality of one system, to help co-register in a second imaging system.

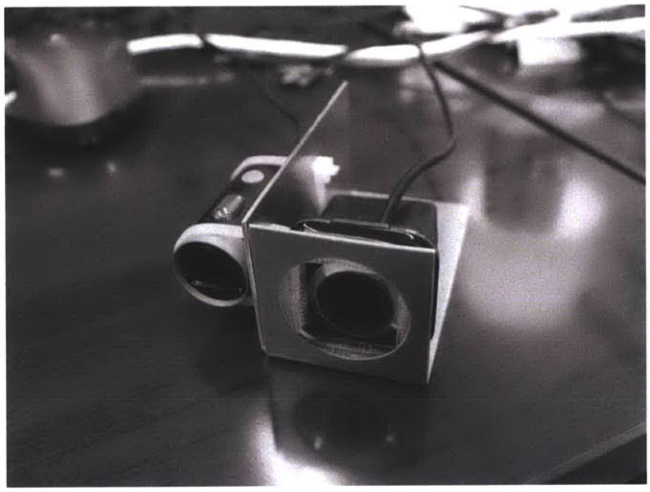

Figure 104: Couple imaging devices. Left Microsoft Lifecam Cinema-1280x720 pixel camera, Right Microsoft Lifecam VX-2000-320x240 pixel camera

In the following example we show imaging with have 2 devices, a high resolution camera and a low resolution camera. The high resolution camera has 1280x720 resolution and the low resolution camera is 320x240. We couple the devices as shown in Figure 104. We apply slight hand motion to coupled device, co-register the image, and apply our Kinetic Super Resolution methodology to generate a high resolution image with precise sub-pixel registration. Samples images from the two camera systems are shown in Figure 106. The two cameras are looking at the same scene, focusing specifically on the US dollar bill on the white board.

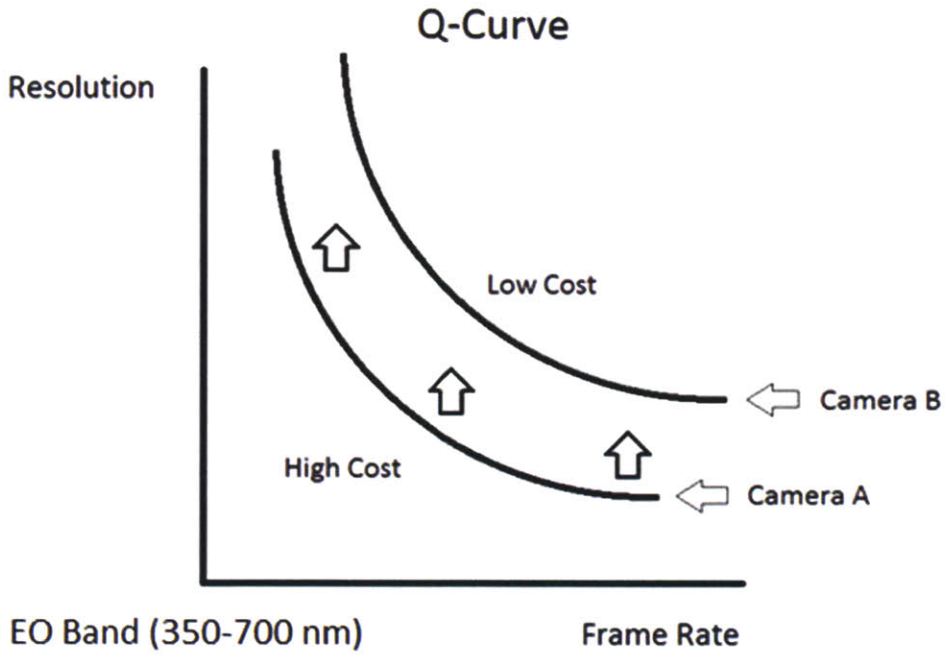

Figure 105: Single-modality, dual imaging system model for hyper resolution. Conceptual Diagram.

Camera A & B have unique Q-curves individually. Hyper resolution allows the lower Q-curve from Camera A to use information from Camera A to help make a unique bridge between the two curves that is advantageous to high resolution information reconstruction.

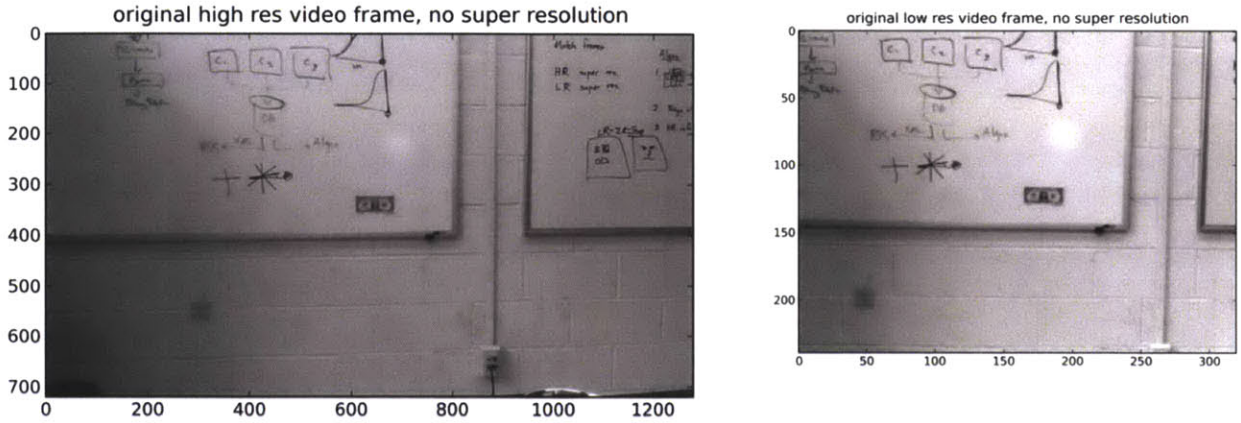

Figure 106: (Left) High Resolution 1280x720 pixel image from Microsoft Lifecam Cinema camera (Right) Low Resolution 320x240 pixel image from Microsoft Lifecam VX-2000 camera. Both cameras are tightly fixture to one another. The motion of left camera will be equally applied to the motion on the right.

5.6.1 Hyper Resolution Example

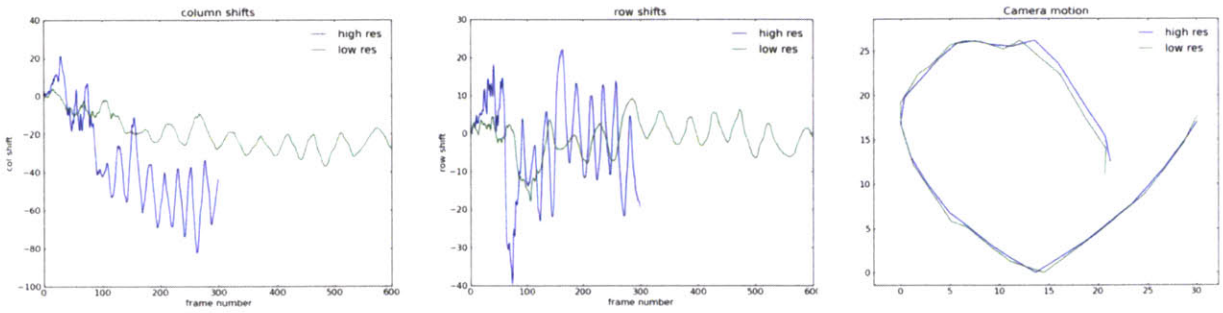

Figure 107: Motion tracking through coupling (Left) Column Shifts (Middle) Row Shifts (Right) Motion co-registration. With both cameras tightly coupled, the motion of both cameras are captured in the X and Y coordinates and normalized in the final image.

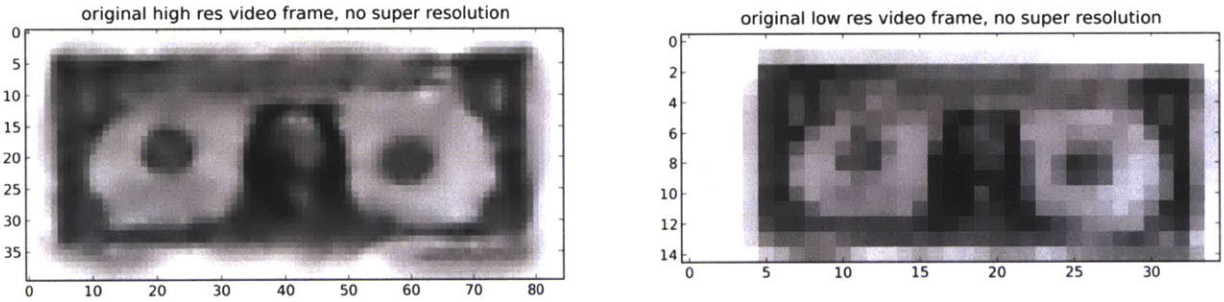

Figure 108: (Left) Zoomed in original high resolution image (Right) zoomed in original low resolution

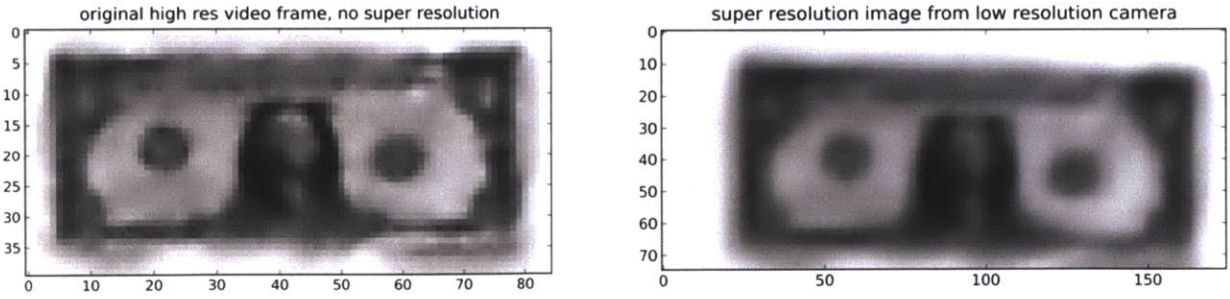

Figure 109: Left) Zoomed in original high resolution image (Right) Zoomed in hyper resolved image of low resolution camera using high resolution motion information only

(Implemented and tested by Dr. Jonathan Jesneck)

This is a simple example of hyper resolution across a single modality. Specifically, you can see immediately the advantages of hyper resolution. The original high resolution frame is 1280x720 while the original low resolution frame is 320x240, a ratio of 12:1. The low resolution hyper resolution result is equal (or better in some cases) than the original high resolution frame. Thus, hyper resolution is able to demonstrate approximately a 1200% improvement in resolution. This is significant.

The combinatory potential for hyper resolution to extend into image enhancement in multi-modality, temporal and spatial realm is limitless. For example, the sub-class of problems in "blind deconvolution" will be solved by coupling a fixed frame rate camera (camA) with one that is perhaps an order of magnitude higher in frame rate (camB). In this case, for every single frame of camA, that image is co-registered with potentially 10 frames of camB. camB will generate a motion based kinetic PSF that can be used to deconvolve the single image from camA. This single frame deconvolution will allow certain motion deblurring of frame A where it was not to practically possible before. Specific example of this combination is shown to work by Li (2008) [109] and Tai [107]. The examples shown in the papers and here are of single band hyper resolution. I propose to extend it to multi-band (spectral) resolution domain. If such a solution is employed, it will be possible to remove motion blur for low frame rate cameras such as long wave infrared using high frame rate cameras such as EO.

5.6.2 Future Works in Hyper Resolution

Perhaps one of the biggest advantages behind the concept of hyper resolution is the ability to couple information across vastly differing spatial and temporal performance and price performance. Inexpensive technology found in everyday digital cameras (300-1200 nm) that have high resolutions and high frame rates, can be used in conjunction with very expensive long wave infrared (8000-14000 nm) imaging systems. There is also the cost difference of cooled vs uncooled LWIR. In either case, LWIR has very high cost per pixel relative to its counterpart in the visible spectrum where the cost difference is very high specific and specific to the camera type. This cost difference can be of the order of several orders of magnitude depending on which system one is considering.

The potential of hyper-resolution will be further explored for research through the Field Intelligence Laboratory at MIT.

5.6.3 Key Findings of Hyper Resolution

I present some of key findings from our research into the concept of hyper resolution.

- The most important aspect of this method is the ability to co-register motion with very low motion registration errors. The motion based registration error of the low resolution imager is a direct function of the error of the high resolution device (which is typically much less).
- Though this specific example shows two imaging devices in the EO (Electro Optical) range, a more useful approach for this device is to couple two devices that have significantly cost/resolution differentials like an EO/Far IR combination where the high resolution, low cost functionality of the high resolution device and be used to significantly improve the imaging capabilities of the more expensive Far IR device.
- Multi-Band Imaging and information transfer. By coupling two or more devices in different bands, like EO, Near IR, Far IR, Millimeter Waves, and others, we can co-register many types of information beyond just shift information that will be useful in the reconstruction of high resolution information. Depth, angle, and texture information are potentially usefully information that can be transferred.

5.7 Multi-Frame Low-light Signal-to-Noise Enhancement and Super-Resolution[7]

We have developed an image processing algorithm that recovers information from extremely noisy, low-light video and creates a super-resolution image. This technology has many useful applications. Creating high-quality images in dim environments is a very challenging problem. Low-signal images typically appear grainy and ill-defined. In low-light conditions, the number of photons arriving at a detector is small enough to be modeled as a stochastic event. Compounding this problem are other stochastic processes, such as salt-and-pepper noise (aberrant pixel values caused by nonuniformly sensitive detector elements) and quantization noise (systematic bias in binning photon signals into discrete pixel values).

To correct for these low-light problems, there are three basic, but limited, solutions:

- Use a bigger aperture lens. Unfortunately, large lenses are quite expensive and are not always physically suitable for imaging devices, such as small portable cameras and medical imaging probes.
- Use a bigger detector. As one of the most expensive camera components, detectors drive camera cost. Larger detectors are often prohibitively expensive for many imaging systems.
- Use longer exposure times. Increasing exposure time allows more light to arrive at the detector, increasing the image signal strength. However, this greatly increases the susceptibility to motion blur. Unfortunately, many practical low-light imaging tasks have significant motion components, severely degrading the image quality.

We propose a new solution: aggregate multiple frames from a low-light video in order to produce a higher-quality, super-resolution image. Here we demonstrate our technique through a very low-light video taken in a dark lecture hall. We used a hand-held Olumpus E-P1 camera and panned it in the direction of a dollar bill that we had taped onto the blackboard. The camera was pointed at the

---

[7] "Multi-Frame Low-Light Signal-to-Noise Enhancement & Super Resolution" (MIT TLO No. 14596). J. Jesneck, L. Phan, S. Sarma

blackboard and recording a video sequence in real-time. There were no additional lighting sources in the room besides the source through a diffused glass window to the right of the blackboard. The ambient lighting conditions in the room was not enough see the dollar bill for a person (with myself and Dr. Jesneck present). The video display on the camera was also dark and not visibly clear that there was a signal in the scene.

5.7.1 Preprocessing low-signal, highly variant images

The first step in reconstructing a high resolution image is to increase the image contrast of the original image in order to identify image features that may be used for image position registration. We enhance the contrast using histogram equalization, which rescales the pixel values to a range that shows more detail.

$$p_x(i) = \frac{n_i}{n}, \qquad 0 \leq i < L \tag{101}$$

where $p_x(i)$is the probability of an occurrence of pixel value i of a discrete image $[x]$, n_i is the number of pixels with value i, n is the total number of pixels in the image, and L is the total number of pixel levels in the image. We then map the range of observed pixel values onto a wider range by

$$y' = y(\max(\{x\}) - \min(\{x\})) + \min(\{x\}) \tag{102}$$

where $y = \mathrm{cdf}_x(x)$ is the cumulative distribution function of the probability distribution of the pixel values.

5.7.2 Aggregating low-signal images to increase signal strength

By modeling the shot noise component in the video frames, we identify stable image features that can be used to determine a fixed position or feature of the images. Then we register the images with a search over the error surface defined by the difference between the two images with given offset:

$$E(x_l, y_l) = \sum_{x,y} | I_0(x, y) - I(x - x_l, y - y_l) | \tag{103}$$

where x_l and y_l are the row and column offsets for image I compared to reference image I_0.

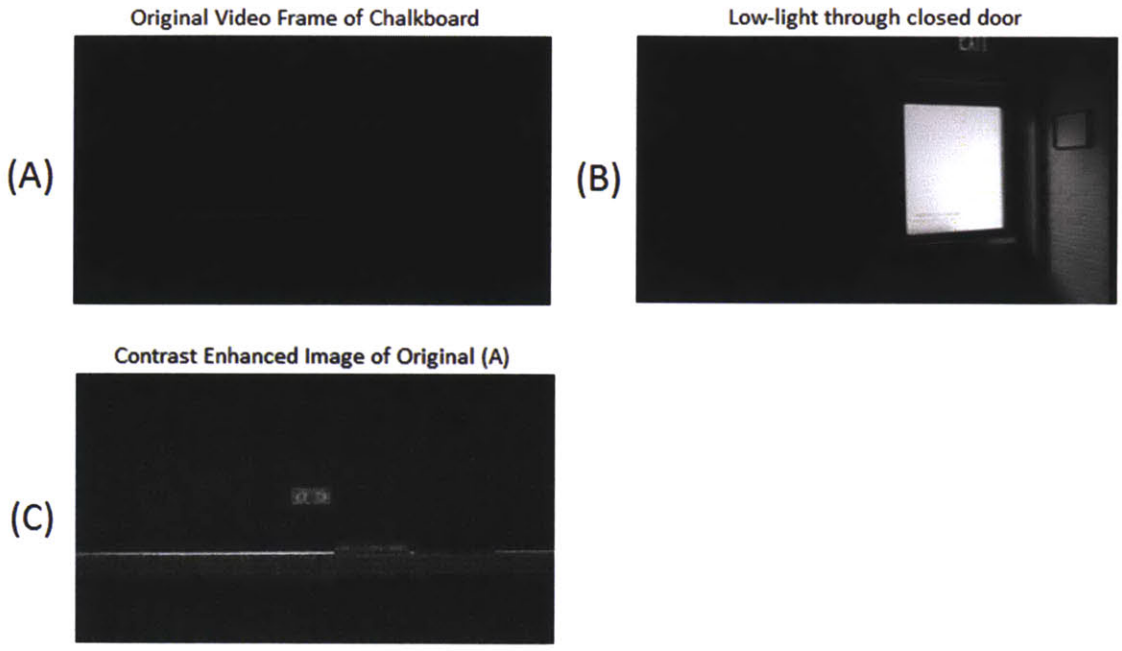

Figure 110: (A) Original Video Frame of Chalkboard from Olympus E-P1 Camera, 17mm F2.8 Lens, (B) Low-light Image through door to the right of (A), (C) Contrast Enhanced

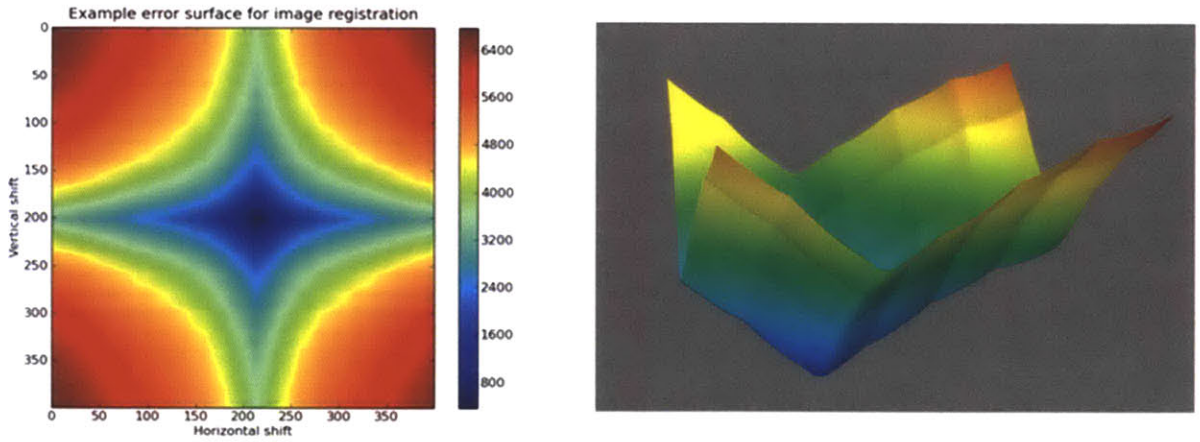

Figure 111: (Left) Apply 2D Error Surface Registration (Right) Generate 3D Error Surface Registration to find minimum displacement error. (Implemented and tested by Dr. Jonathan Jesneck)

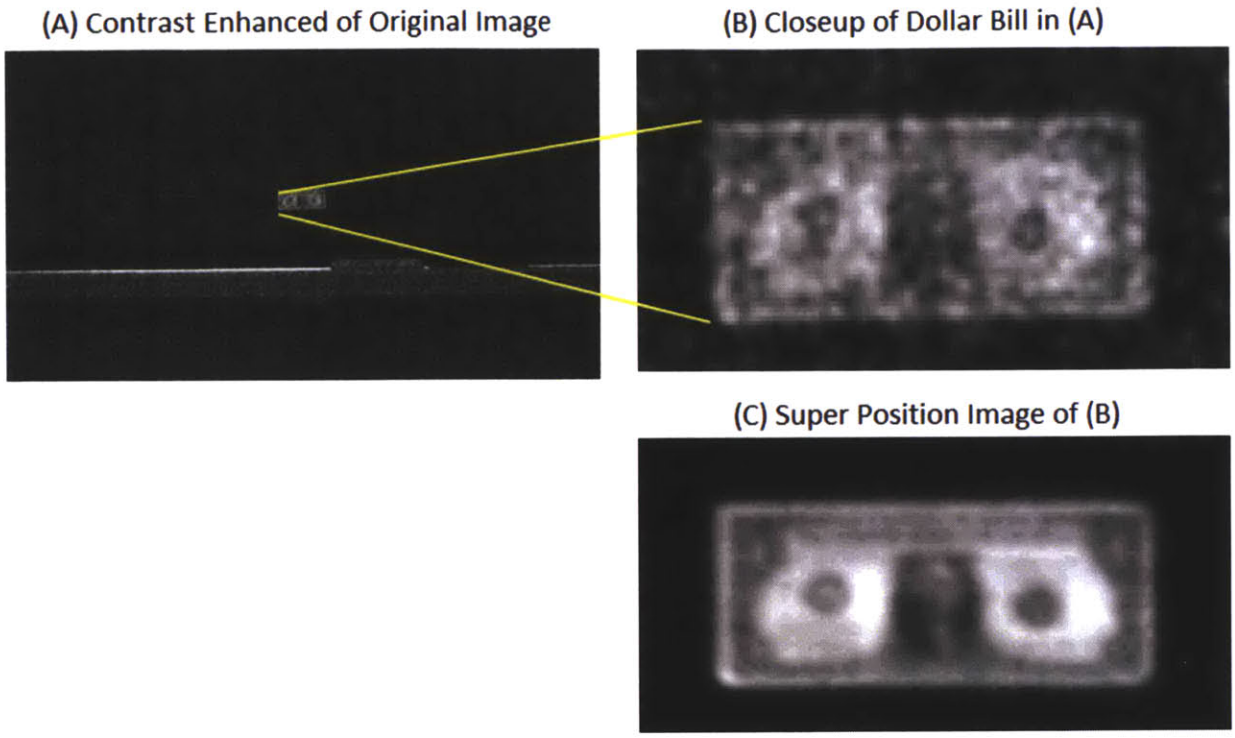

Figure 112: (A) A Contrast Enhanced Original Image, (B) A Closeup of Dollar Bill in (A), (C) Super Position Image of Dollar Bill in (B). (Implemented and tested by Dr. Jonathan Jesneck)

Once we have determined the video frames' registration offsets, we average each pixel value over the stack of collocated pixels. This averaging operation reduces the noise of the composite image while avoiding motion blur.

$$I_{super} = \sum_{n=1}^{N} I_n \sim \text{Poisson}(\sum \lambda) \quad (104)$$

Where I_{super} is the super positioned image, which has the same expected value $\text{E}(I_{super}) = \lambda$, but a greatly decreased variance $\text{var}(I_{super}) = \lambda/N$.

5.7.3 Increasing Image Resolution with KSR

Once we have the super-position image, we can apply our previously described Kinetic Super-Resolution algorithm to deconvolve against the KSR motion kernel(MIT TLO #14538).

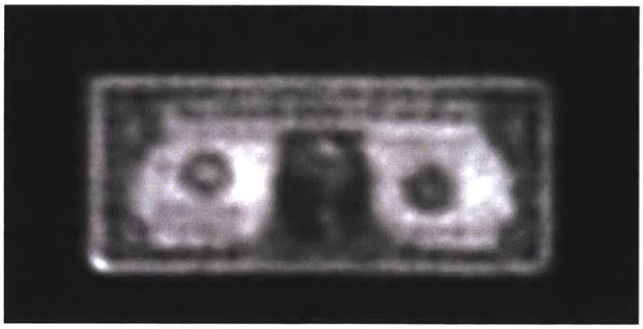

Figure 113: KSR Improvement on low-light image. (Implemented and tested by Dr. Jonathan Jesneck)

5.7.4 Applications for Low-Light Signal-to-Noise Enhancement using KSR

Improving the signal strength and resolution of very low-light images has several commercial opportunities.

Low-cost, portable cameras:

Cell phone cameras notoriously produce low-quality images in low-light conditions. They cannot have large lenses and detectors for space and cost reasons. Additionally, they cannot depend on long exposure times, since hand-held cameras would introduce significant motion blur. Therefore cell phone cameras would benefit greatly from our algorithm.

Night-time surveillance systems for high-speed targets:

Security and defense organizations could greatly benefit from higher-quality scans of moving vehicles and people, with greater image detail allowing for better object tracking and automated person identification.

Night vision systems:

Portable, hand-held and helmet-mounted night vision systems can greatly increase night-time visibility by applying a video version of this algorithm, thus avoiding the bulk of heavy lenses.

Passive low-signal imaging systems:

For many surveillance applications, it is imperative that the surveillance operation be undetected, which precludes the use of illuminators. Thus imaging is limited to passive systems. These systems would especially benefit from our algorithm.

5.8 Thermal Signature Identification[8]

We have developed a unique technique that can be used to extrapolate and infer the thermal properties of an object through naturally occurring or induced thermal cycling. By observing the temperature variations of such processes, it is possible to infer the object's thermal properties by mapping the transient time constant to pixel location. That information can be fused within a spatial and temporal domain as a unique identifier/marker for identification purposes. We name this method "thermal fingerprinting." Similar methods have been presented Szekely [118, 119], Murphy [120], and others for specific applications and methods.

5.8.1 Thermal Transients

Thermal Transients: Through the use of accurate thermal instrumentation device such as long wave infrared (IR) imager, we record the temperature changes of the object as it goes through a naturally occurring or induced thermal cycling in a time period sufficient to record noticeable changes. Assuming the object does not go through a phase change or vary significantly in thermal properties during the observed period, one can plot the temperature profile vs. time. In the case of IR imaging (2 dimensional surface), one simply superimposes the thermal information over a known 3D surface texture to plot the spatial temperature profile vs. time. A thermal transient response can be used to infer the thermal properties of object through thermal balancing of conduction, convection, and radiation effects. One can model and extrapolate one or more unique time constant(s) throughout

[8] "Thermal Signature Identification" (MIT TLO No. 14146) L. Phan, J. Jesneck, S. Sarma

the spatial domain. The superimposed spatial information can be fused along with unique thermal property identifiers to increase the spatial resolution of the object.

According to transient heat transfer:

$$\dot{Q}_{in} = \rho V c \frac{dT}{dt} \quad (105)$$

$$\frac{T - T_\infty}{T_i - T_\infty} = a e^{-hAt/\rho Vc} \quad (106)$$

$$\tau = \rho VC/hA \quad (107)$$

where τ is there thermal time constant of the observed temperature change per pixel which directly relates to the thermal properties of the object.

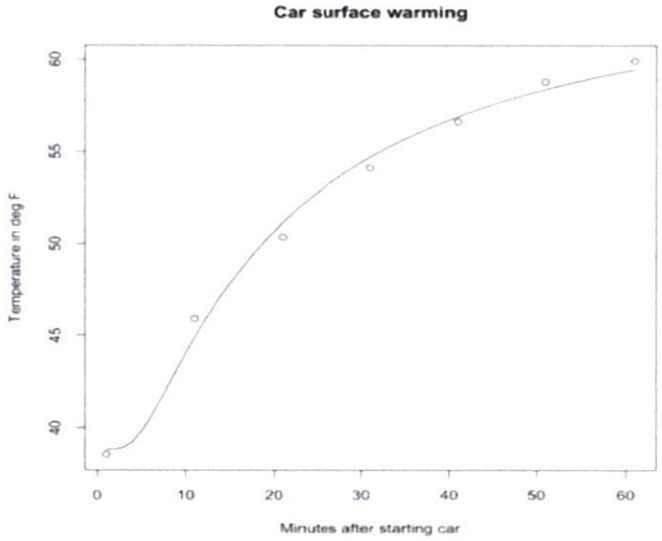

Figure 114: Temperature vs time map of a single pixel

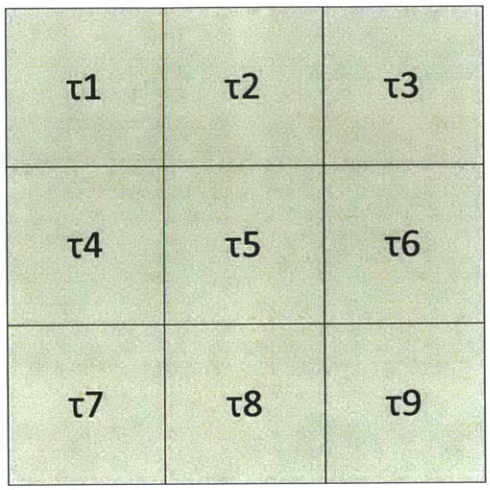

Figure 115: Up close 3x3 pixel example of a thermal signature

When viewed up close, each pixel represents a unique thermal signature, which in this refers to the thermal time constant τ_N mapped to the transient effects of an exponential function for that pixel. However, this need not be the case. The symbol τ may be replaced for by any pattern, linear, exponential, logarithmic, quadratic, or any function that be used as a unique identifier for that specific pixel. This concept is useful for applications beyond ARTIST.

Figure 116: The experiment was to show sequenced thermal images of observed vehicle (2009 Honda Civic) during heating cycle where car heating was turned to the max setting internally, while the external environment was approximately 30 degrees F

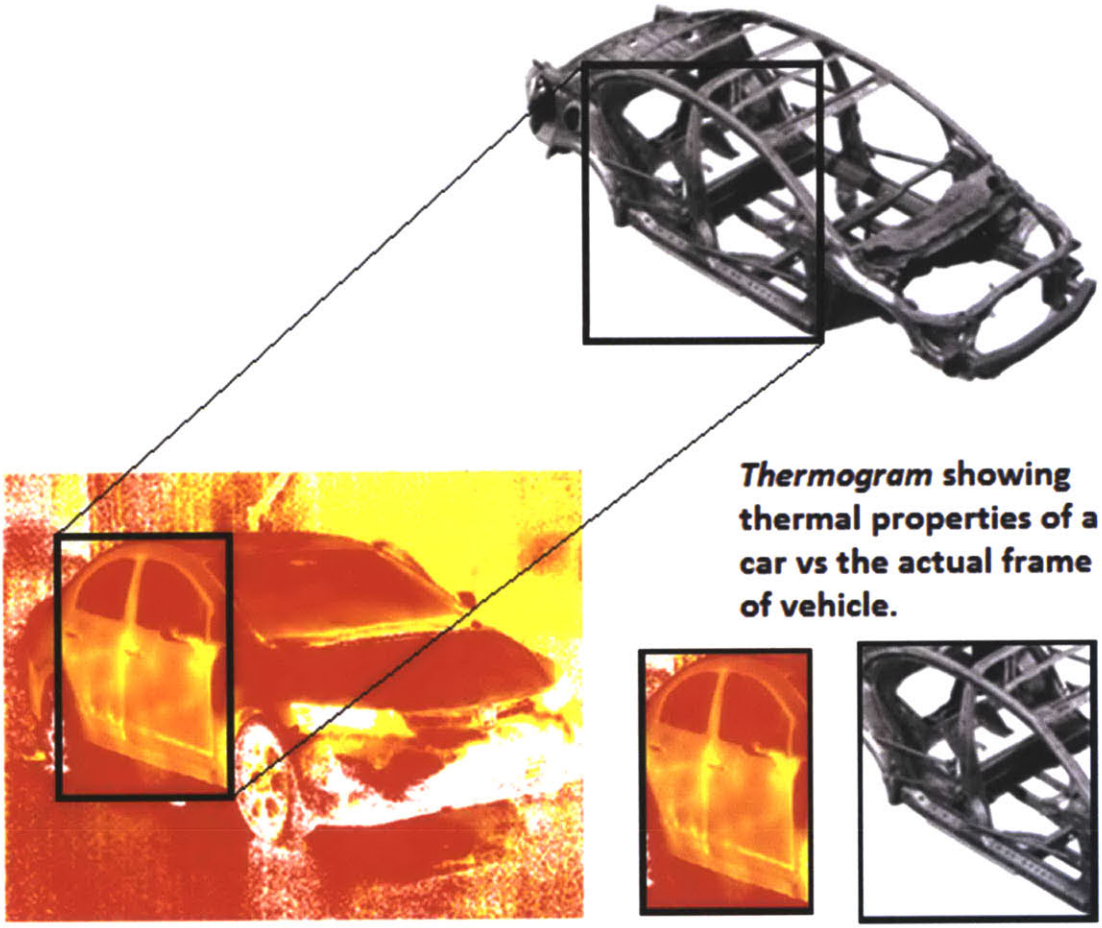

Figure 117: Spatial mapping of time constant onto image. (Implemented and tested by Dr. Jonathan Jesneck)

Notice that by mapping the time constant over the entire image, one is able to observe the thermal properties of the object below the surface of the exterior shell. This information is not directly observable directly from the thermal images. Only by mapping the transient time constant during the thermal cycling was this unique information visible.

5.8.2 Applications of Thermal Signature Identification

Medical Imaging – Thermal fingerprinting has several potential uses in cancer or medical research by using the process to identify unique thermal properties that are informative for phenotype or disease diagnosis. One can analyze the thermal signature on many spatial scales, such as within cells, tissues, organs, or whole organisms by identifying thermal spatial markers and then comparing the changes

of those markers through different observed time periods. For example, if a specific thermal marker has significant changes in thermal properties observed, one can attempt to explain what may be causing those changes, potentially cancerous or degrading conditions.

Intelligence – Potential uses in mapping or location based identification. In the case of using visual image recognition for location based terrain mapping and position identification, one can use the thermal signature identification process as additional markers. Combining the marker information will increase the accuracy of location identification through pattern recognition of visual markers with thermal markers.

Energy Efficiency – Potential uses in structural mapping and using the thermal signature identification process to find leaks. Thermal signature profiling along with pattern recognition can be used to identify thermally problematic areas of a structure.

Manufacturing – Potential uses in refining product design to optimize heat transfer. Thermal signatures can help identify regions with large risk for thermal damage, such as in a microchip. Thermal mapping information will facilitate design to account for heat flow and to protect thermally sensitive components.

Geology – Potential uses in structural mapping and risk prediction in thermally unstable locations. Thermal signatures can help identify changes in geographic hot spots around thermal vents and volcanoes. The thermal characteristics can help to improve risk prediction models for human and wildlife populations that live around hot spots.

Astronomy – Potential uses in mapping astronomical bodies. Thermal signatures can help identify thermally interesting regions of an astronomical body, such as thermal vents in a planet that may provide access for the heat harvesting for energy production. Thermal mapping may also find structurally weak parts in a frozen crust that would be more efficient for mining.

5.9 Conclusion

In this chapter, we have introduced several novel concepts highly applicable to ARTIST:

- Kinetic Super Resolution – a multi-frame super resolution algorithm based on generating a KSR motion kernel and deconvolving the super positioned low-resolution images using a single camera used to construct a high resolution image.
- Hyper Resolution – The use of spatial, temporal, and spectral resolution across different imaging modalities to reconstruct a high resolution image in a low resolution modality. The combinatory approach is advantageous to translating motion, depth, angle, texture, and other useful information that can be useful.
- Thermal Signature Identification – The mapping of the thermal transient response of each individual pixel to derive an accompanying time constant based expression that is unique to each pixel. By doing so, we can infer sub-surface information such as structure and thermal resistance at the surface.
- Low-Light Signal-to-Noise Enhancement using KSR – An algorithm used for low-signal and noisy environments where images are degraded reaching the noise level of the imaging system. In such situations, it is shown that it is possible to reconstruct a high resolution image using this technique combined with KSR.

Hyper resolution will further increase our ability to extract useful information from multiple modalities including significant resolution enhancements. KSR is a fundamentally important concept that is limited to single modality, but when applied can help improve both resolution and boost signal-to-noise ratios in very poor operating conditions such as low light applications. Thermal signature identification allows one to capture the thermal transient profile and use that profile as location based markers. Useful applications in thermal signature identification includes material property analysis, diagnostics level comparisons in different systems, and potentially navigation related purposes.

Chapter 6: Uncertainty Analysis

6.0 Introduction

We have developed and presented the ARTIST system in the first five Chapters of this thesis covering the three modules: hardware, 3D radiometry, and image processing. In this Chapter, I will discuss how each module contributes to the total uncertainty in the system. For each, we will develop a system model, perform sensitivity analysis, and develop design insights to reduce error. By understanding how uncertainty affects system performance for the individual components, we can determine where to focus on risk mitigation efforts.

6.1 Uncertainties in the ARTIST

ARTIST is designed as a multi-component engineering system meant for use in a large scale urban environment. Within the many components, numerous potential sources of uncertainty can exist. In ARTIST system, I defined three principle areas of uncertainty which can affect system performance and contribute to overall uncertainty:

1. 3D Radiometry: Scene Uncertainty in 3D
    a. Emissivity Variation
        i. Material variation: $\varepsilon = 0.7 - 1.0$ for common building materials
        ii. Angle Dependent
    b. Background Radiation & Reflection Effects from Nearby Objects
2. Hardware: Sensor Measurement Uncertainty – LWIR
    a. Noise limits to sensor performance
    b. Calibration based uncertainty in current IR cameras
3. Image Processing: Motion Based Uncertainty
    a. Limits to steady vehicle motion based on optical flow
    b. Vibration induced uncertainty in the imaging systems

Scene uncertainty in 3D refers to the uncertainty involved in the multi-step process of reconstructing a solid wireframe model of the scene based on camera motion and image displacement, and the resulting dependency of that information on inferring accurate temperatures. Here, the system is highly dependent on the performance of the 3D reconstruction method and effects of background radiation and reflections. From our discussions, we know there is variations in emissivity values for different materials. In my research, most common building materials have emissivity values between $\varepsilon = 0.7$ to 1.0. We also know there is an angle dependency for emissivity which can be quantified. Thus, the effects of emissivity uncertainty can be quantified. Scene uncertainty is also affected by background temperature and reflections from nearby objects. This will be discussed in detail in the following sections.

Sensor uncertainty in the hardware refers to the potential measurement errors that can arise from sampling and interpreting the measured radiance from the infrared camera system. Here, sensor noise and calibration errors can lead to uncertainty when inferring temperature. From references and camera spec sheets, we see that most cameras have a plus or minus 50 mK or better for most standard long wave camera.

For motion based uncertainty we have motion uncertainty which is related to two types of vehicle motion. First is steady state vehicle motion and second is vibration induced motion due to bumps and random excitation on the road. For steady state motion, I analyzed the limits of steady motion based on the limits of the optical flow algorithm to determine pixel displacement based on pixel velocities. By placing limits on velocity of pixel for stable optical flow operation, I am able to determine reasonable speed limits for the vehicle to be approximately 1. At distances of 10 m away from the vehicle, we can drive at up to 1.7 m/s or 4 miles per hour. For vehicle induced vibrations, we have observed stable operation of the system on the road for most bumps and conditions at speeds of up to 10 miles per hour. Most vibrations are attenuated by the vehicle's damping system.

In the following sections, I will discuss and present models for each of these three areas of uncertainties, show how the uncertainty will introduce errors in system performance, and present methods and ideas to help mitigate errors.

6.1.1 Defining Measurement Uncertainty

In a measurement environment, a sampling of the measured values helps us understand the dispersion of values - known as a distribution. Two of the most common measures of a distribution is the mean and standard deviation. The mean, m, is defined as:

$$m = \frac{1}{N}\sum_{i=1}^{N} X_i \quad (108)$$

Where N is the total number of measurements, X_i is the value of measured component. The mean is used as a measured estimate of the center of the distribution. The standard deviation, s, is calculated according to the following:

$$s = \sqrt{\frac{\sum_{i=1}^{N}(X_i - m)^2}{N-1}} \quad (109)$$

Where the standard deviation, s, measure the dispersion about the mean and direction proportion to the width of the distribution. Mean and standard deviation are general parameters used to quantify uncertainty in measurements [61, 62].

6.1.2 Total Uncertainty Approximation

For multiple independent variables influencing uncertainty, the combined uncertainty distribution must reflect the combination of the individual distributions. The combined distribution, the total variance, is the sum of the sum of the individual variances [61, 62]:

$$s_{total}^2 = s_1^2 + s_2^2 + s_3^2 + \cdots + s_k^2 \quad (110)$$

Where s_{total} is the total standard deviation, $s_1, \ldots, s_k$ is the standard deviation from each independent contributing variable. A similar approximation approach, called a quadrature, to combining uncertainty can be represented as the following:

$$U_{total}^2 = U_1^2 + U_2^2 + U_3^2 + \cdots + U_k^2 \quad (111)$$

Where U_{total} is the total uncertainty in the system.

6.2 Scene Uncertainty – 3D

In modeling the 3D environment presented in Chapter 4, ARTIST has the ability to account for the effects of directional emissivity variation as a function of the viewing angle and also consider the effects of background radiation.

To recap from the introduction of this Chapter, scene uncertainty has the following components:

1. Emissivity Variation
    i. Material variation: $\varepsilon = 0.7 - 1.0$ for common building materials
    ii. Angle Dependent – Limited to the performance limits of Optical Flow Algorithms
2. Background Radiation & Reflection Effects from Nearby Objects

6.2.1 Emissivity Uncertainty for Common Building Materials

I propose an approach for how material variations affect emissivity measurements. According to Saunders [34] and Minkina [35], with access to detailed information about a material, emissivity can usually be estimated to within ± 0.05. For any given material, the emissivity depends on the nature of the surface, the wavelength of the thermal sensor, the viewing angle to the surface, and on the temperature of the surface. With no apriori knowledge of an environment, estimating remote surface temperature can be challenging. Next, I show how I estimate material-based uncertainty in emissivity for building materials.

As we are most interested in scanning of an urban environment, we should consider a set of building materials presented in Appendix A (Normalized Emissivity Values for Common Building Materials). Of this subset of building materials, we have metal and non-metal materials. As explained in Chapter 4, metal materials on the surface of buildings do not constitute as good building material because of the potential thermal flaws it would cause in energy efficiency. Therefore, we will make

the general assumption of focusing on non-metal materials, which typically exhibit values of emissivity $\varepsilon > 0.70$. In this range, common materials make over 80% of the possible types of materials on the surface of building. Of the 126 building materials listed in Appendix A (Table of Normalized Emissivity Values), 105 of the materials have emissivity values > 0.70. Taking this specific subgroup of materials ($\varepsilon > 0.70$), we find the mean emissivity is 0.901 with a standard deviation of 0.067. We base the remainder of the discussion on emissivity uncertainty using this set of non-metallic materials. From Figure 14, we see the histogram of emissivity values is clustered at $\varepsilon \sim 0.90$.

Without a-priori knowledge of building materials, our average value of emissivity is 0.901 with a standard deviation of 0.067 and represent an element of uncertainty in the system, defined as $U_{\varepsilon,mat}$, the uncertainty related to estimating the accurate emissivity for common building materials.

The second element of uncertainty comes from our estimate of the normal angle of the object, which is propagated through angular error estimates based on optical flow reconstruction. In this case, we need to consider the additional uncertainty related to estimating the remote surface's angle with respect to the camera. This analysis was performed in the last section on 3D modeling uncertainty. We will integrate the results of that analysis to determine the combined effects.

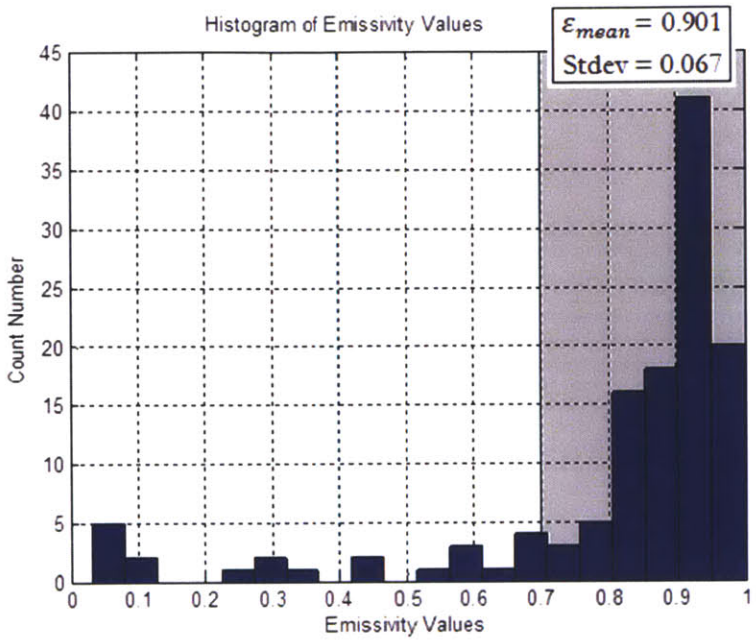

Figure 118: Histogram of Normalized Emissivity Values for common building materials

6.2.2 Angle Dependency and Angular Errors in Optical Flow Techniques

In this section, we will discuss the angular dependency of the ARTIST system. In Chapter 4 on 3D Radiometry, I used an optical-flow algorithm method based on Farneback [85] to generate a 3D model of the environment based on the following steps:

1. Generate optical flow diagram of the images of a scene based on the lateral displacement between frames.
2. Use optical flow diagram to generate a depth map by integrating navigational information from the vehicle blackbox system.
3. Use depth map to create a wireframe of the 3D surfaces. The wireframe model can used to provide distance and viewing angle information of a target object's surface, with respect to the camera.

Although this method was observed to perform satisfactorily in ARTIST, the absolute performance of the method was not fully characterized and tested against a reference to analyze for errors. Other models are presented by Micusik, B. [121], L Dreschler [55], D Anguelov, C Dulong, D Filip, C

Frueh [122], and others. ARTIST system allows for plug and play of many of these optical flow techniques. The polynomial approach that I have currently deployed offers a good performance as reported in the paper by Farneback[85].

In ARTIST, the 3D reconstruction is based on an optical flow method to create the depth map. Next, we will focus on modeling the errors associated with creation of the optical flow depth map proces. In this analysis, we will follow Fleet and Jepson 1990 [83] convention for the angular measure of error for optical flow methods, where they describe angular error as:

$$\psi_E = arccos(\vec{v}_c \cdot \vec{v}_e) \quad (112)$$

Where ψ_E is the angular error,$v = (u, v)$ is the velocity in displace per time unit in units of pixel/frame, $\vec{v}_c$ is the correct velocity vectors in 3D, $\vec{v}_e$is the estimated velocity vector in 3D. According to Fleet (1992) the directional errors at small speeds do not have as large an angular error compared to directional errors at higher speeds. The error measure for component velocities is the angle between the measured component velocity and actual component velocity such that:

$$\psi_E = arccos(\vec{v}_c \cdot \vec{v}_n) \quad (113)$$

where $\vec{v}_n \equiv \frac{1}{\sqrt{1+s^2}}(n, -s)$, v_n is the normal velocity, and v_c is the 2-D velocity. According to Barron, Fleet, and Beauchemin [1994] [86], relative errors of 10% correspond to angular errors of approximately 2.5° at pixel velocities near 1 pixel/frame.

6.2.2.1 Analysis of Different Optical Flow Models

The ARTIST system can use any optical flow algorithm and hence, the 3D model generation and associated errors are dependent on the choice of algorithm. We summarize below a comparison of various optical flow methods in the literature. Although there are multiple ways to describe optical flow based errors, I will focus on a study by Barron, Fleet, and Beauchemin [1994] [86] which simulated a number of different optical flow methods including those of Horn and Schunck [75], Lucas and Kanade [76], Uras [77], Nagel [123], Anandan [79], Singh [80], Heeger [81], Waxman [82], and Fleet and Jepson [83], which is described in detail in the published paper. In the paper, Barron,

Fleet, and Beauchemin [1994] [86] conducted simulated studies on a number of datasets including the Yosemite Sequence, SRI Sequence, NASA Sequence, Rotating Rubik Cube, and the Hamburg Taxi Sequence. Of these different datasets, the simulation dataset most relevant and similar to our analysis is the Yosemite Sequence (Synthetic sequence with ground truth)[9]. The Yosemite Sequence is the most challenging dataset in the group where a range of velocities (between 2-5 pixels/frame) and occluding edges between the mountains and horizon creates a challenging environment and produces poor velocity measurements in optical flow techniques. We will look at the results obtains by Barron, Fleet, and Beauchemin [1994] [86] and corresponding projected optical flow error estimate to determine an error budget for our own optical flow error equivalent in ARTIST.

By analyzing the Barron, Fleet, and Beauchemin [1994] [86] results, we hope to use the insights provided by the paper to:

1. Compare the performance of different optical flow algorithms.
2. Compare the performance of those algorithms through a range of test sequences, and find the test sequence most similar to the type of situation ARTIST is more likely to encounter. In our case, we think the Yosemite Sequence is most similar.
3. Use the results to infer potential performance limits on ARTIST if ARTIST used existing off-the-shelf optical flow algorithms in a plug-n-play manner.

The Barron, Fleet, and Beauchemin [1994] [86] paper is a very well cited and insightful publication regarding performance limits of well-known optical flow algorithms. Although the paper is a little dated, the optical flow methods presented, particularly the Lucas and Kanade [76], are well known and commonly used in many existing applications.

[9] http://www.cs.brown.edu/~black/images.html

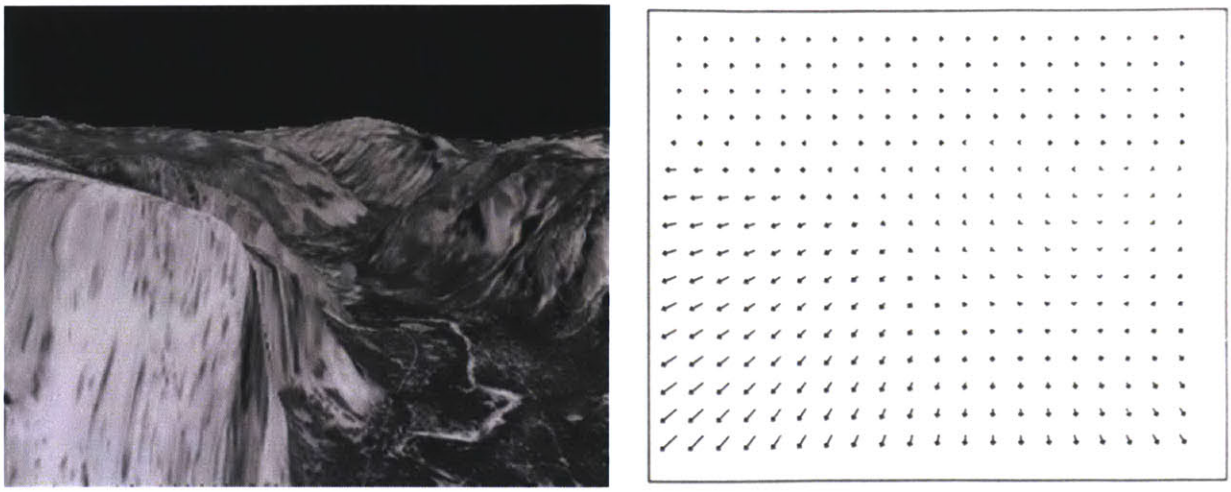

Figure 119: (Left) Yosemite Sequence Image (Right) Optical Flow from Yosemite Sequence Image with velocities as high as 2-5 pixel/frame. Barron, Fleet, and Beauchemin [1994] [83] (With permission from Publisher)

The results of the Barron, Fleet, and Beauchemin [1994] [86] simulation experiments shows the challenges associated with estimating the normal surface for 3D environments using optical flow algorithms for all the techniques presented. This is shown in Table 6(with permission from Publisher). Although other datasets showed significantly lower angular error results, the challenges presented from the Yosemite Sequence dataset helps us develop an upper bound error estimate for the ARTIST system in understanding angular errors based on optical flow based 3d reconstruction. The angular error, ψ_E, in the Yosemite Sequence were significantly higher than the SRI Sequence, NASA Sequence, Rotating Rubik Cube, and the Hamburg Taxi Sequence in some cases by over an order of magnitude both for the average angular error and standard deviation. Even within the Yosemite Sequence dataset, the performance range for angular error can be significant, ranging from the best performing method, based on the Lucas and Kanade ($\lambda_2 \geq 1.0$, where λ_2 is a parameter) with 3.22° average error, 8.92° standard deviation to the worst performing method based on the Horn and Schunck (original) with an average error of 31.69°, standard deviation 31.18°.

Technique	Average Error	Standard Deviation	Density
Horn and Schunck (original)	31.69°	31.18°	100%
Horn and Schunck (original) $\|\nabla I\| \geq 5.0$	25.33°	28.51°	59.6%
Horn and Schunck (modified)	9.78°	16.19°	100%
Horn and Schunck (modified) $\|\nabla I\| \geq 5.0$	5.59°	11.52°	32.9%
Lucas and Kanade ($\lambda_2 \geq 1.0$)	4.28°	11.41°	35.1%
Lucas and Kanade ($\lambda_2 \geq 5.0$)	3.22°	8.92°	8.7%
Uras et al. (unthresholded)	8.94°	15.61°	100%
Uras et al. (det (H) ≥ 1.0)	7.55°	19.64°	14.7%
Nagel	10.22°	16.51°	100%
Nagel $\|\nabla I\|_2 \geq 5.0$	6.06°	12.02°	32.9%
Anandan	13.36°	15.64°	100%
Singh (step 1, $n = 2$, $w = 2$)	15.28°	19.61°	100%
Singh (step 1, $n = 2$, $w = 2$, $\lambda_1 \leq 6.5$)	12.01°	21.43°	11.3%
Singh (step 2, $n = 2$, $w = 2$)	10.44°	13.94°	100%
Singh (step 2, $n = 2$, $w = 2$, $\lambda_1 \leq 0.1$)	10.03°	13.13°	97.7%
Heeger (combined)	15.93°	23.16°	44.8%
Heeger (level 0)	22.82°	35.28°	64.2%
Heeger (level 1)	9.87°	14.74°	15.2%
Heeger (level 2)	12.93°	15.36°	2.4%
Waxman et al. $\sigma_f = 2.0$	20.05°	23.23°	7.4%
Fleet and Jepson ($\tau = 1.25$)	5.28°	14.34°	30.6%
Fleet and Jepson ($\tau = 2.5$)	4.63°	13.42°	34.1%

Table 6: Yosemite Sequence angular error simulation results for different well-known optical flow techniques from the Barron, Fleet, and Beauchemin (1994) [86] (with permissions from Publisher)

Dataset	Best	Worst
Sinusoidal	Fleet & Jepson (mean=0.03, stdev=0.01)	Singh (mean=64.26, stdev=26.14)
Square2	Fleet & Jepson (mean=0.07, stdev=0.02)	Horn and Schunck (mean=47.21, stdev=14.60)
Translating Tree	Fleet & Jepson (mean=0.23, stdev=0.19)	Horn and Schunck (mean=38.27, stdev=27.67)
Diverging Tree	Fleet & Jepson (mean=0.73,stdev=0.46)	Singh (mean=17.66, stdev=14.25)
Yosemite	Lucas and Kanade (mean=3.22,stdev=8.92)	Horn and Schunck (mean=31.69,stdev=31.18)

Table 7: Summary of angular error simulation results for different datasets from Barron, Fleet, and Beauchemin (1994) [86]

6.2.2.2 Estimating Effects of Angular Error on Emissivity for 3D Radiometry

To create the 3D model in ARTIST we used a polynomial based optical flow method (detailed in Chapter 4). This method was applied to drive-by imaging of the scene in the LWIR band. In Chapter 4, 3D Radiometry, we explained angle dependency in radiance and the role of directional emissivity. In Chapter 2, directional emissivity is uniform for non-metal surfaces up to 60° viewing angle and drops for angles greater than 60°. For example, at angle $\theta = 85°$, the mean normalized emissivity $(\frac{\varepsilon}{\varepsilon_N})$ can drop significantly to 0.433 and have variations for $\varepsilon_{min} = 0.127$ and a $\varepsilon_{max} = 0.706$. We construct the uncertainty bars for $\theta = 85°$ and $\theta = 80°$ below.

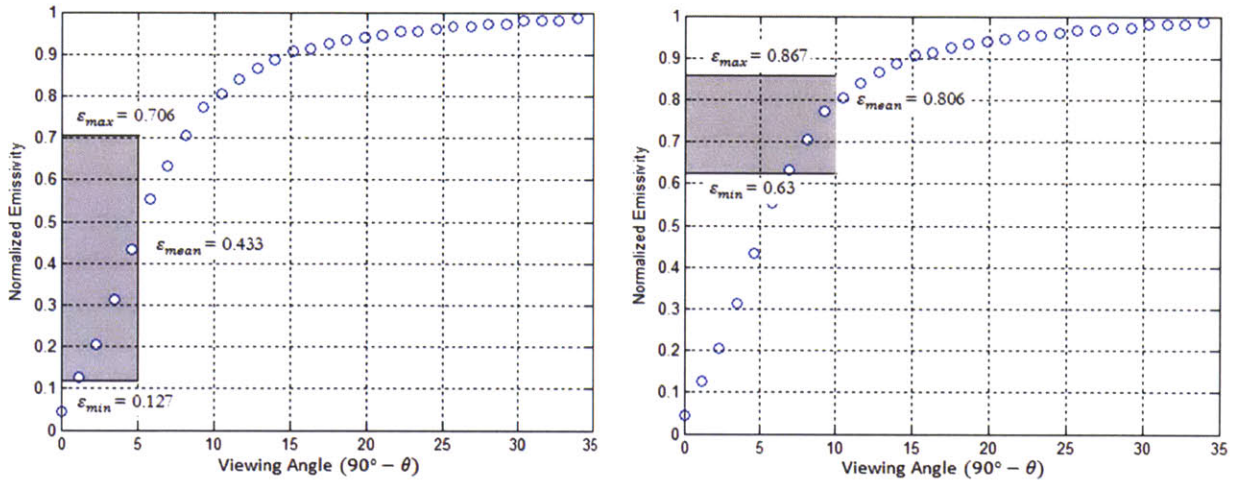

Figure 120: Emissivity Error Estimation for θ=85° (Left) and θ=80° (Right)

We will focus on the 60° - 90° viewing angle region where the directional emissivity has the greatest variation. For this analysis, we will use our own experimental data presented in Chapter 4, which presents normalized emissivity vs viewing angle for the reference material (ε_{tape}=0.95) shown in Figure 92. We will use the implied angular error estimate in the Yosemite Sequence from Barron, Fleet, and Beauchemin [1994] [86] as a proxy to develop the error in direction emissary estimate. We will use the results from Barron, Fleet, and Beauchemin [1994] [86] to project the average error to derive the following chart in the 60° - 90° region.

$$\theta_{actual}(\max) = \theta_{projected} + \psi_E \quad (114)$$

$$\theta_{actual}(\min) = \theta_{projected} - \psi_E \quad (115)$$

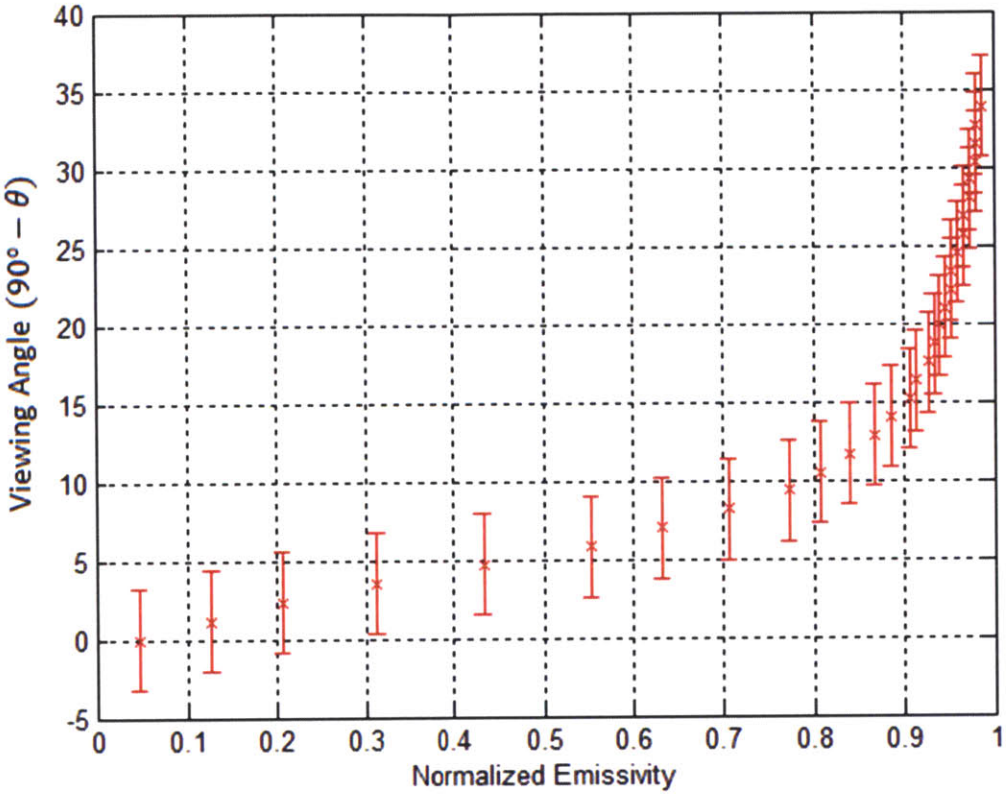

Figure 121: Projected error based on the Lucas and Kanade algorithm for normalized emissivity in 3D radiometry based on the reference material (ε_{tape}=0.95). Error bars indicate the angular error at each viewing angle.

Viewing Angle (90° - θ)	$\frac{\varepsilon}{\varepsilon_N}$	$\alpha + \psi_E$	$\alpha + \psi_E$	$\frac{\varepsilon}{\varepsilon_N}(\alpha + \psi_E)$	$\frac{\varepsilon}{\varepsilon_N}(\alpha - \psi_E)$	$\Delta\varepsilon$
10	0.806	6.78	13.22	0.63	0.867	0.237
20	0.94	16.78	23.22	0.913	0.953	0.04
30	0.98	26.78	33.22	0.967	0.98	0.013
40	0.98	36.78	43.22	0.986	0.987	0.001
50	0.99	46.78	53.22	0.987	0.99	0.003
60	0.99	56.78	63.22	0.987	0.987	0
70	0.99	66.78	73.22	0.987	0.987	0
80	0.99	76.78	83.22	0.987	1	0.013
90	1	86.78	93.22	0.993	1	0.007

Table 8: Projected Angular Error for normalized emissivity based on the Lucas and Kanade error projection ($\psi_E$mean=3.22,stdev=8.92) based on the Yosemite Sequence

6.2.2.3 Summary of Angular Error Effects on Emissivity

The ARTIST system is capable of utilizing any of the well-known optical flow techniques and one must be careful to understand their particular performance limits and how they affect the 3D radiometry computations. By comparing alternative optical flow methodologies on a challenging dataset like the Yosemite Sequence, we are able to use the projected angular errors presented by Barron, Fleet, and Beauchemin [1994] [86] as a proxy to develop an upper bound error projection for ARTIST. Looking closer at the results tested by Barron, Fleet, and Beauchemin (1994) [86], there are two potential optical flow algorithms that show similar performance:

1. Lucas and Kanade (mean angular error ψ_E = 3.22°, stdev = 8.92°)
2. Fleet & Jepson (τ = 2.5) (mean angular error ψ_E = 4.63°, stdev = 13.42°)

The Lucas and Kanade [76] method was tested to have a lower mean angular error and standard deviation than the Fleet and Jepson [83] method. Alternatively, we can consider the use of either of these algorithms as a preferred optical flow methodology for ARTIST due to the similar performance of both methods.

Looking closer at the uncertainty analysis results from Table 8, we can see that the optical flow algorithm's projected angular error effect is most prominent for $70° \leq \theta \leq 90°$. At $\theta \leq 70°$, the net effect on $\Delta\varepsilon = (\varepsilon_{max} - \varepsilon_{min})$ ranges between 0.04-0.237 in potential emissivity error based the Lucas and Kanade optical flow algorithm. Also from Table 8, at angles between $60° \leq \theta \leq 70°$, the net effect on angular error $\Delta\varepsilon$ is less than 0.10. At angles between $0° \leq \theta \leq 60°$, the effects of angular error has almost no net effect on $\Delta\varepsilon$. We show that the ARTIST system is robust to angular errors in the range of $0° \leq \theta \leq 60°$, but is severely affected elsewhere. In our case, the ARTIST system's optical flow further compounds the uncertainty on directional emissivity. Variations in emissivity are directly related to our ability to estimate temperature. Thus, $\Delta\varepsilon$ is directly related to T_{est} which is summarized as follows regarding angular uncertainty:

θ Range	$\Delta\varepsilon$
$70° \leq \theta \leq 90°$	0.237
$60° \leq \theta \leq 70°$	≤ 0.100
$0° \leq \theta \leq 60°$	≤ 0.013

Table 9: Angular errors effect on emissivity

6.2.3 The Effects of Background Radiation and Reflections

In a 3D scene, the effects of background radiation and reflections from nearby objects should also be included. From Chapter 4 on 3D Radiometry, we model the observed radiance from the object's reference emitter surface as the following:

$$S_r(T_o) = \varepsilon_r \tilde{S}(T_o) + (1 - \varepsilon_r)\tilde{S}(T_b) \quad (116)$$

Observed Radiance Source Signal Background/Reflections

Where $S_r(T_o)$ is the observed radiance, ε_r is the emissivity of the surface, $\tilde{S}$ is total radiance of the black body, T_o is the surface temperature of the object, $T_b$is the background temperature. The observed radiance measured by the detector can be decomposed into a source signal due to the

emittance by the source and component representing the reflections due to background radiation and represented by the following:

1. Source Signal
2. Background/Reflections

These two components (1) Source Signal and (2) are highly dependent on the weighted emissivity and reflection relationship established in Chapter 2:

$$\varepsilon + r = 1 \tag{117}$$

Where ε is the emissivity and r is the reflectivity of the signal. From the expression, what you can expect to see that at low emissivity values, observed radiance due to reflections from background radiation would dominate the signal source.

It is possible to evaluate for $\tilde{S}$ using the Planckian form integral that was shown earlier in Chapter 2 when we integrate for wavelengths between 8000 nm and 14000 nm. :

$$M_b(T,\lambda) = \frac{c_1}{\lambda^5 \cdot \left[e^{\frac{c_2}{\lambda \cdot T}} - 1\right]} \tag{118}$$

$$\tilde{S} = \int_{\lambda_1}^{\lambda_2} R(\lambda) \cdot M_b(T,\lambda) d\lambda \tag{119}$$

We can numerically solve for $\tilde{S}$ to determine the solution and expected signal. From this, we can evaluate the effects of background radiation component$(1 - \varepsilon_r)\tilde{S}(T_b)$ which is the reflection from the target to the detection. In Figure 122 plot the Planckian form integral to show blackbody spectral radiance as a function of wavelength. In Figure 123, we evaluate the integral of the Planckian form from 8000nm to 14000nm using Mathematica and plot the integral of Equation (119) vs Temperature.

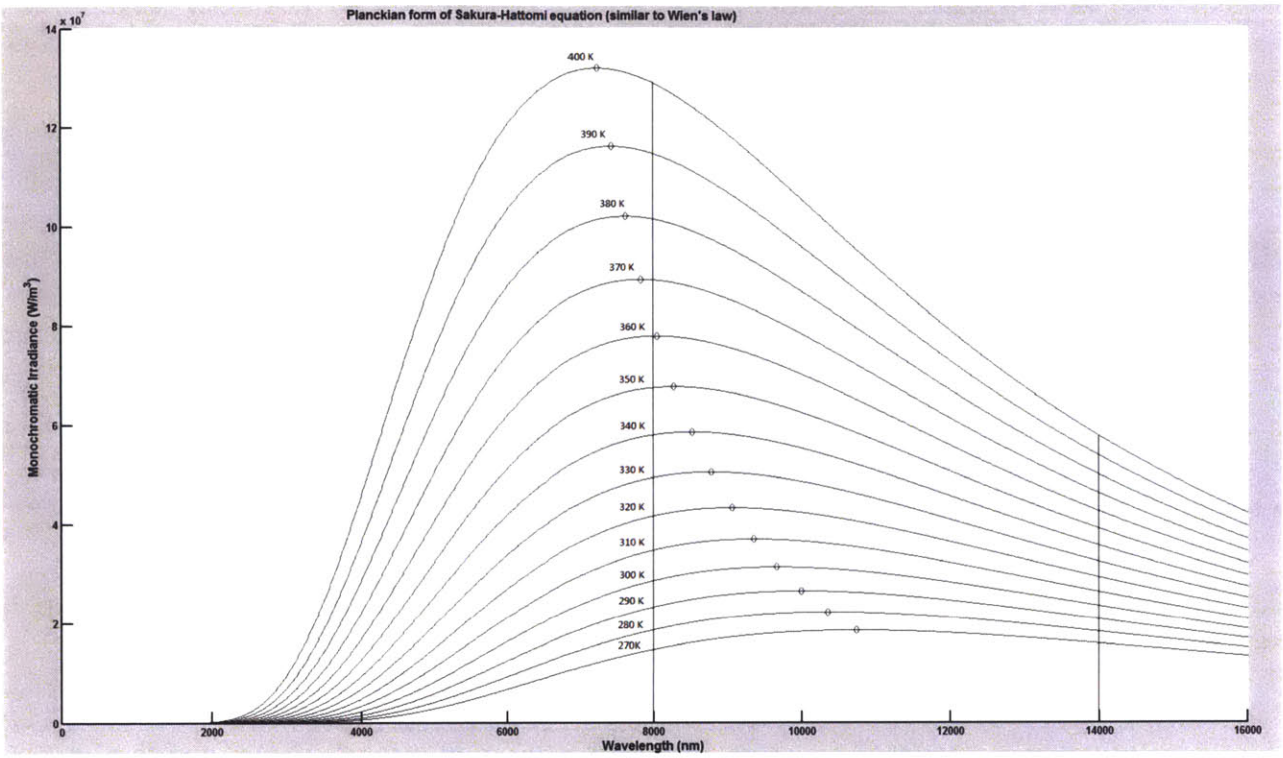

Figure 122: Plackian form Monochromatic Irradiance for Temperature Range [270°K-400°K]

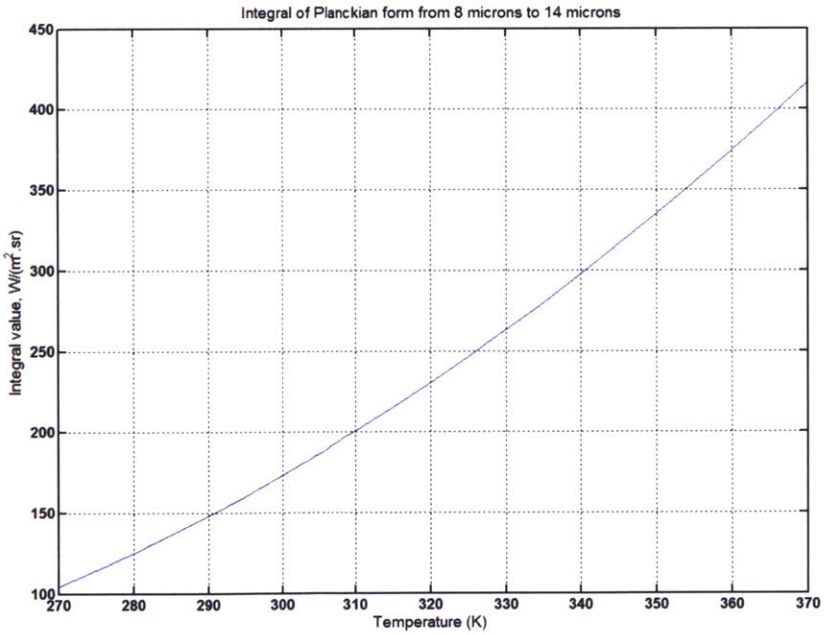

Figure 123: Integral of the Planckian form from 8 μm to 14 μm

Simulation of Background Radiation Effects: $\varepsilon_r = 0.9$

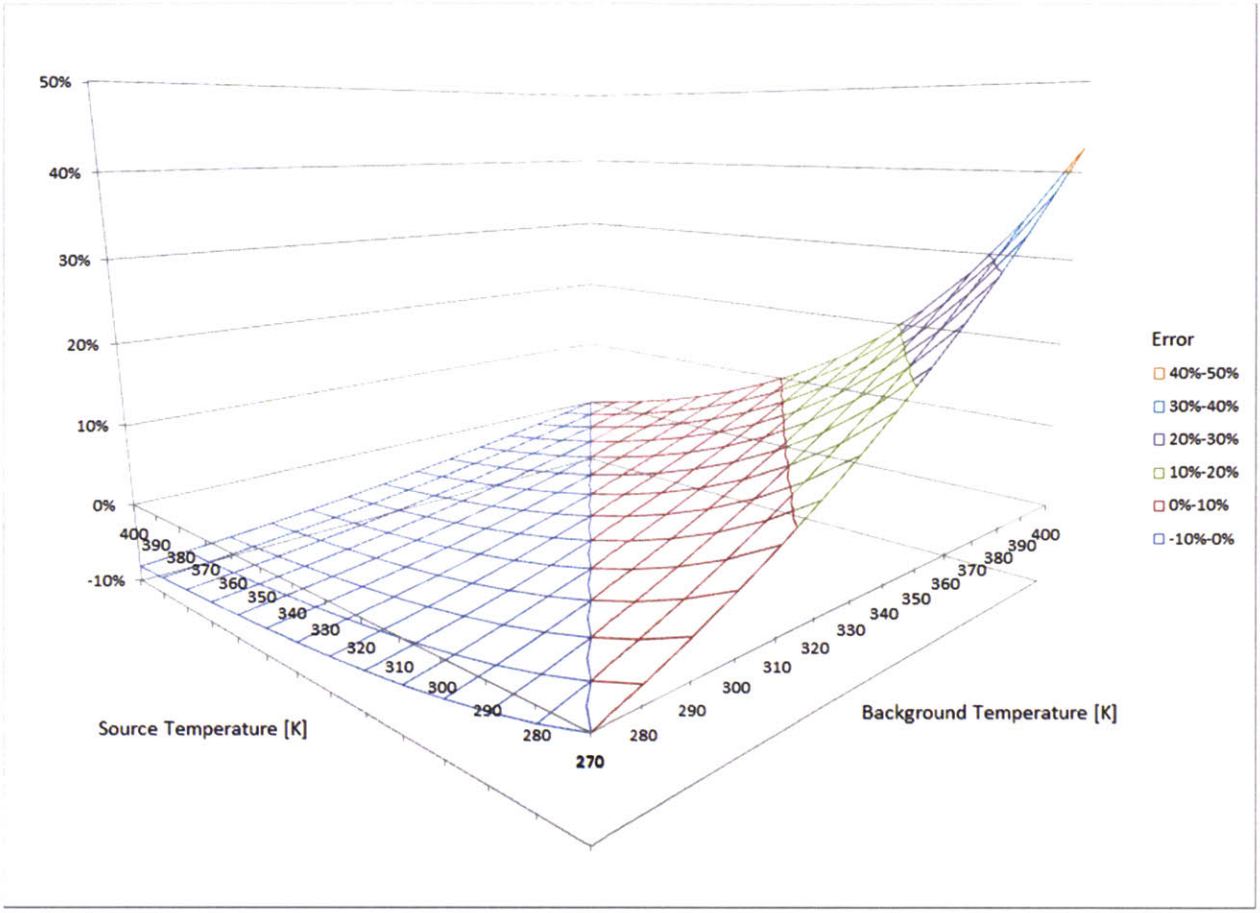

Figure 124: 3D Error Estimate of Background Radiation Effect for $\varepsilon_r = 0.9$

Source Temperature [K] \ Background Temperature [K]	270	280	290	300	310	320	330	340	350	360	370	380	390	400
270	0%	2%	4%	6%	9%	12%	15%	18%	22%	25%	29%	34%	38%	43%
280	-2%	0%	2%	4%	6%	8%	11%	14%	17%	20%	23%	27%	30%	34%
290	-3%	-2%	0%	2%	4%	6%	8%	10%	13%	15%	18%	21%	24%	28%
300	-4%	-3%	-1%	0%	2%	3%	5%	7%	9%	12%	14%	17%	19%	22%
310	-5%	-4%	-3%	-1%	0%	1%	3%	5%	7%	9%	11%	13%	15%	18%
320	-5%	-5%	-4%	-2%	-1%	0%	1%	3%	5%	6%	8%	10%	12%	14%
330	-6%	-5%	-4%	-3%	-2%	-1%	0%	1%	3%	4%	6%	8%	9%	11%
340	-6%	-6%	-5%	-4%	-3%	-2%	-1%	0%	1%	3%	4%	6%	7%	9%
350	-7%	-6%	-6%	-5%	-4%	-3%	-2%	-1%	0%	1%	2%	4%	5%	7%
360	-7%	-7%	-6%	-5%	-5%	-4%	-3%	-2%	-1%	0%	1%	2%	4%	5%
370	-7%	-7%	-6%	-6%	-5%	-4%	-4%	-3%	-2%	-1%	0%	1%	2%	3%
380	-8%	-7%	-7%	-6%	-6%	-5%	-4%	-4%	-3%	-2%	-1%	0%	1%	2%
390	-8%	-8%	-7%	-7%	-6%	-5%	-5%	-4%	-3%	-3%	-2%	-1%	0%	1%
400	-8%	-8%	-7%	-7%	-6%	-6%	-5%	-5%	-4%	-3%	-3%	-2%	-1%	0%

Table 10: Error Table of Estimate of Background Radiation Effect for $\varepsilon_r = 0.9$

Simulation of Background Radiation Effects: $\varepsilon_r = 0.8$

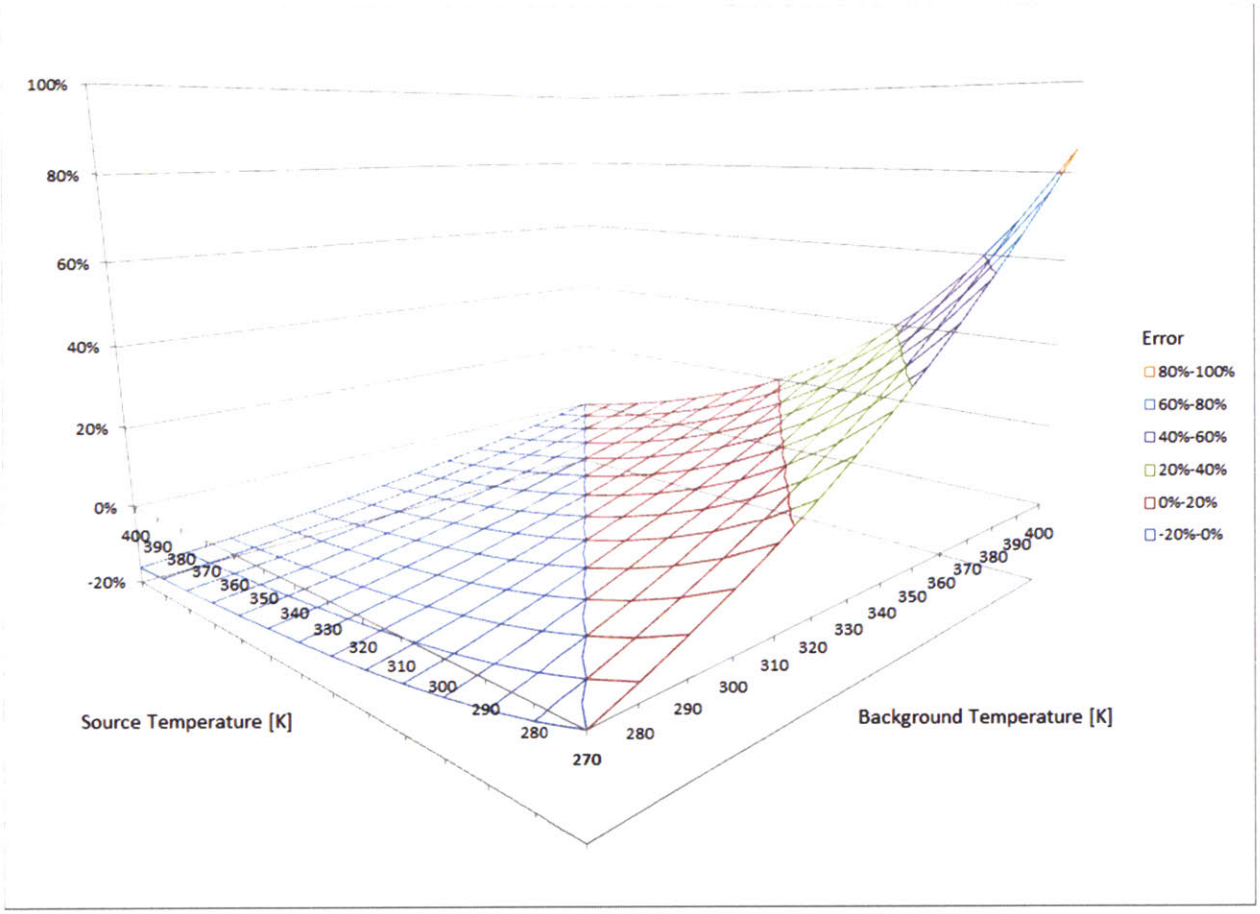

Figure 125: 3D Error Estimate of Background Radiation Effect for $\varepsilon_r = 0.8$

Source Temperature [K] \ Background Temperature [K]	270	280	290	300	310	320	330	340	350	360	370	380	390	400
270	0%	4%	8%	13%	18%	24%	30%	36%	43%	51%	59%	67%	76%	85%
280	-3%	0%	4%	8%	12%	17%	22%	27%	33%	39%	46%	53%	61%	69%
290	-6%	-3%	0%	3%	7%	11%	15%	20%	25%	30%	36%	42%	49%	55%
300	-8%	-5%	-3%	0%	3%	7%	10%	14%	19%	23%	28%	33%	39%	44%
310	-9%	-7%	-5%	-3%	0%	3%	6%	10%	13%	17%	22%	26%	31%	36%
320	-11%	-9%	-7%	-5%	-3%	0%	3%	6%	9%	13%	16%	20%	24%	28%
330	-12%	-10%	-9%	-7%	-5%	-2%	0%	3%	5%	9%	12%	15%	19%	22%
340	-13%	-12%	-10%	-8%	-7%	-5%	-2%	0%	3%	5%	8%	11%	14%	18%
350	-14%	-12%	-11%	-10%	-8%	-6%	-4%	-2%	0%	2%	5%	8%	10%	13%
360	-14%	-13%	-12%	-11%	-9%	-8%	-6%	-4%	-2%	0%	2%	5%	7%	10%
370	-15%	-14%	-13%	-12%	-10%	-9%	-7%	-6%	-4%	-2%	0%	2%	4%	7%
380	-15%	-15%	-14%	-12%	-11%	-10%	-9%	-7%	-5%	-4%	-2%	0%	2%	4%
390	-16%	-15%	-14%	-13%	-12%	-11%	-10%	-8%	-7%	-5%	-4%	-2%	0%	2%
400	-16%	-15%	-15%	-14%	-13%	-12%	-11%	-9%	-8%	-7%	-5%	-3%	-2%	0%

Table 11: Error Table of Estimate of Background Radiation Effect for $\varepsilon_r = 0.8$

Simulation of Background Radiation Effects: $\varepsilon_r = 0.2$

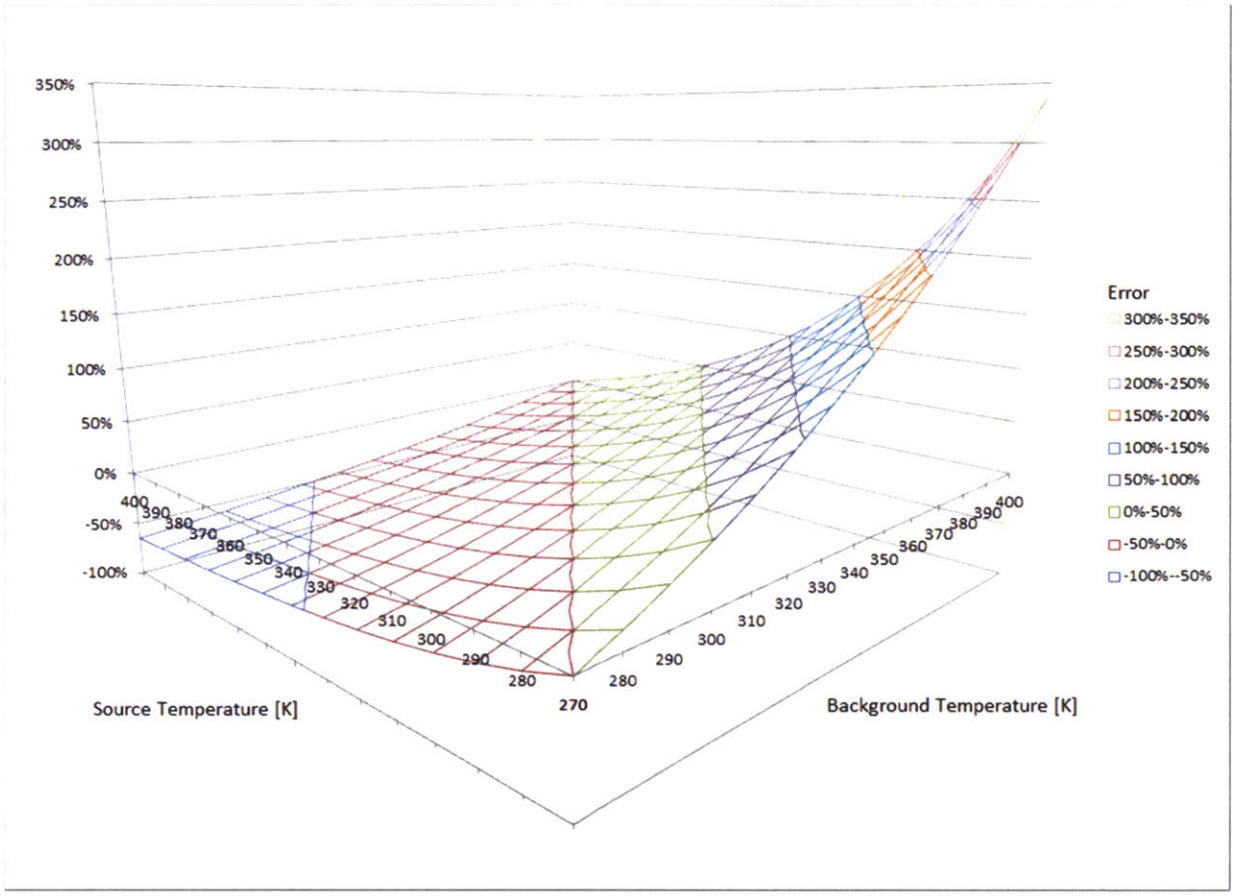

Figure 126: 3D Error Estimate of Background Radiation Effect for $\varepsilon_r = 0.2$

Source Temperature [K] \ Background Temperature [K]	270	280	290	300	310	320	330	340	350	360	370	380	390	400
270	0%	15%	32%	51%	71%	94%	118%	145%	173%	203%	235%	269%	304%	342%
280	-13%	0%	14%	30%	47%	66%	87%	109%	133%	158%	185%	213%	243%	275%
290	-23%	-12%	0%	13%	28%	44%	62%	80%	101%	122%	145%	169%	194%	221%
300	-31%	-22%	-11%	0%	13%	26%	41%	57%	75%	93%	113%	133%	155%	178%
310	-38%	-30%	-21%	-11%	0%	12%	25%	39%	54%	69%	86%	104%	123%	143%
320	-43%	-36%	-28%	-20%	-10%	0%	11%	23%	36%	50%	65%	80%	97%	114%
330	-48%	-42%	-35%	-27%	-19%	-10%	0%	11%	22%	34%	47%	61%	75%	90%
340	-52%	-46%	-40%	-33%	-26%	-18%	-9%	0%	10%	21%	32%	44%	57%	70%
350	-55%	-50%	-45%	-39%	-32%	-25%	-17%	-9%	0%	10%	20%	30%	42%	53%
360	-57%	-53%	-48%	-43%	-37%	-31%	-24%	-16%	-8%	0%	9%	19%	29%	39%
370	-60%	-56%	-52%	-47%	-42%	-36%	-30%	-23%	-16%	-8%	0%	9%	18%	27%
380	-62%	-58%	-54%	-50%	-45%	-40%	-34%	-28%	-22%	-15%	-8%	0%	8%	17%
390	-63%	-60%	-57%	-53%	-48%	-44%	-39%	-33%	-27%	-21%	-14%	-7%	0%	8%
400	-65%	-62%	-59%	-55%	-51%	-47%	-42%	-37%	-32%	-26%	-20%	-14%	-7%	0%

Table 12: Error Table of Estimate of Background Radiation Effect for $\varepsilon_r = 0.2$

Simulation of Background Radiation Effects: $\varepsilon_r = 0.1$

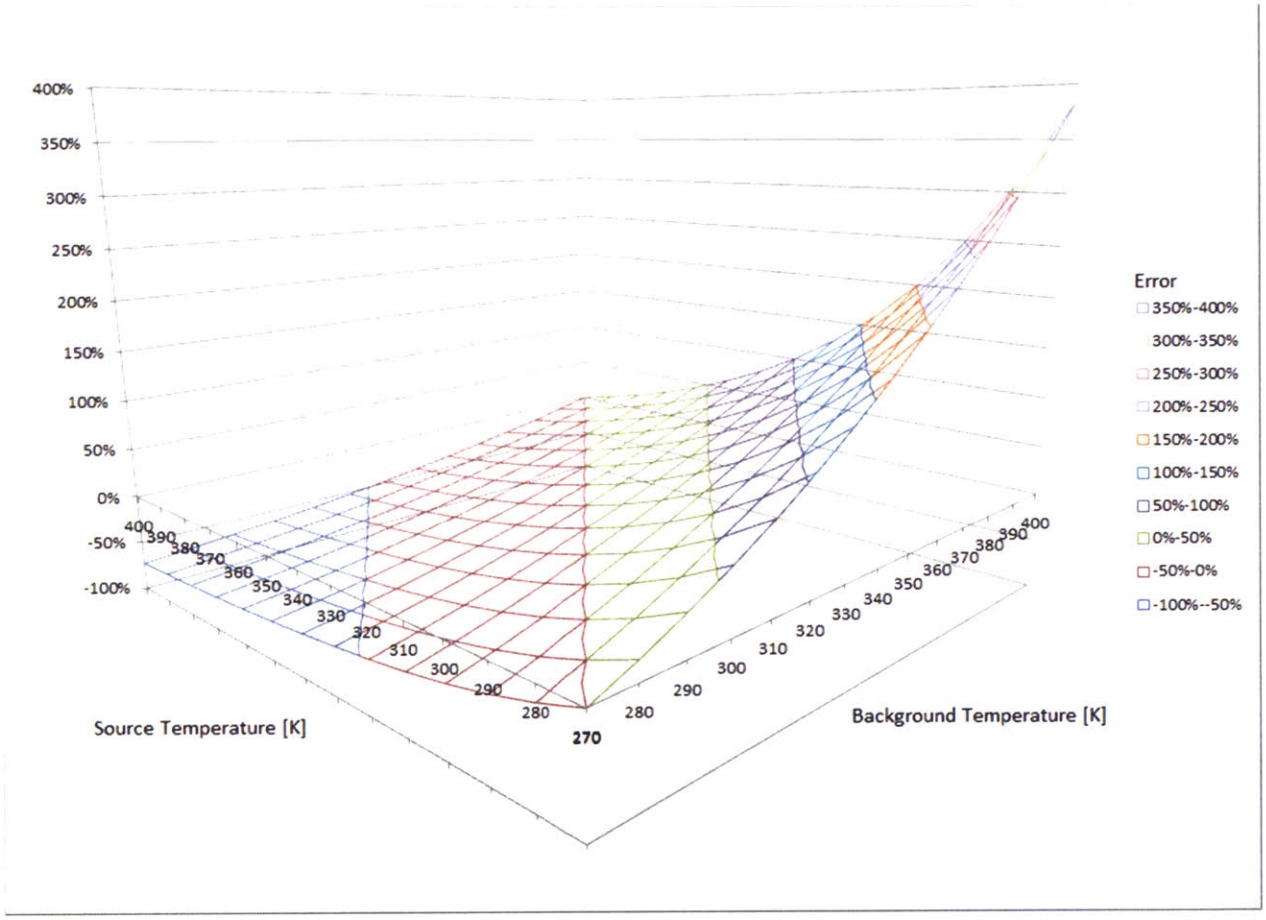

Figure 127: 3D Error Estimate of Background Radiation Effect for $\varepsilon_r = 0.1$

Source Temperature [K] \ Background Temperature [K]	270	280	290	300	310	320	330	340	350	360	370	380	390	400
270	0%	17%	36%	57%	80%	106%	133%	163%	195%	228%	264%	302%	342%	384%
280	-14%	0%	16%	34%	53%	75%	98%	123%	149%	178%	208%	240%	274%	309%
290	-26%	-14%	0%	15%	32%	50%	69%	90%	113%	137%	163%	190%	219%	249%
300	-35%	-25%	-13%	0%	14%	30%	46%	65%	84%	105%	127%	150%	174%	200%
310	-42%	-33%	-23%	-12%	0%	13%	28%	44%	60%	78%	97%	117%	138%	160%
320	-49%	-41%	-32%	-22%	-12%	0%	13%	26%	41%	56%	73%	90%	109%	128%
330	-54%	-47%	-39%	-31%	-21%	-11%	0%	12%	25%	38%	53%	68%	84%	101%
340	-58%	-52%	-45%	-38%	-29%	-20%	-11%	0%	11%	23%	36%	50%	64%	79%
350	-62%	-56%	-50%	-43%	-36%	-28%	-19%	-10%	0%	11%	22%	34%	47%	60%
360	-65%	-60%	-54%	-48%	-42%	-35%	-27%	-19%	-10%	0%	10%	21%	32%	44%
370	-67%	-63%	-58%	-53%	-47%	-40%	-33%	-26%	-18%	-9%	0%	10%	20%	30%
380	-69%	-65%	-61%	-56%	-51%	-45%	-39%	-32%	-25%	-17%	-9%	0%	9%	19%
390	-71%	-68%	-64%	-59%	-55%	-49%	-44%	-37%	-31%	-24%	-16%	-8%	0%	9%
400	-73%	-70%	-66%	-62%	-58%	-53%	-48%	-42%	-36%	-30%	-23%	-16%	-8%	0%

Table 13: Error Table of Estimate of Background Radiation Effect for $\varepsilon_r = 0.1$

Figure 124 through Figure 127 shows a simulation of the measurement error due to background radiation for varying emissivity values of ε_r = 0.9, 0.8, 0.2, 0.1. We vary the source vs mean background temperature between 270K and 400K we plot the error on the measured signal of the LWIR camera. Negative error denotes that the signal will be underestimated and positive error denotes the signal will be overestimated by the percentage amounts. In the horizontal axes, the source temperature variation is represented on the left and background temperature on the right.

The insight(s) from simulating the effects of background/reflective radiation is the following:

1. If the source and background temperature are equivalent, the error is very low and variation in emissivity has minimal effect in temperature estimate.
2. If the source temperature is higher than the background temperature, the weighted effect of reflectance with a lower background temperature component will cause the observed radiance to underestimate the actual temperature. The greater the temperature difference, the greater the effect of background temperature in causing this underestimate.
3. If the background temperature is higher than the source temperature, the weighted effect of reflectance with a higher background temperature component will cause the observed radiance to overestimate the actual temperature. Here, the influence from the background is much greater as shown by the steep slope on the right in Figure 124 to Figure 127. An example where this effect prevalent is LWIR imaging during the day, where solar radiation dominates the background radiation. Such an example is indicated in Figure 128.
4. When considering the effects of directional emissivity, one should consider the resulting background/reflective component of (1 - ε_r), which can dominate the signal if ε_r values are low. In the case of non-metal materials, at oblique viewing angles of $\theta > 60°$, the effect of directional emissivity can drop rather significantly, especially as viewing angles gets closer to 90°. In those cases, we expect the (1 - ε_r)·background/reflection's term to become a critical factor in determining the observed signal at the detector.

Here, we show that sources of uncertainty due to background radiation is unavoidable, but that the error can be quantifiable if we have an idea of the background radiation environment.

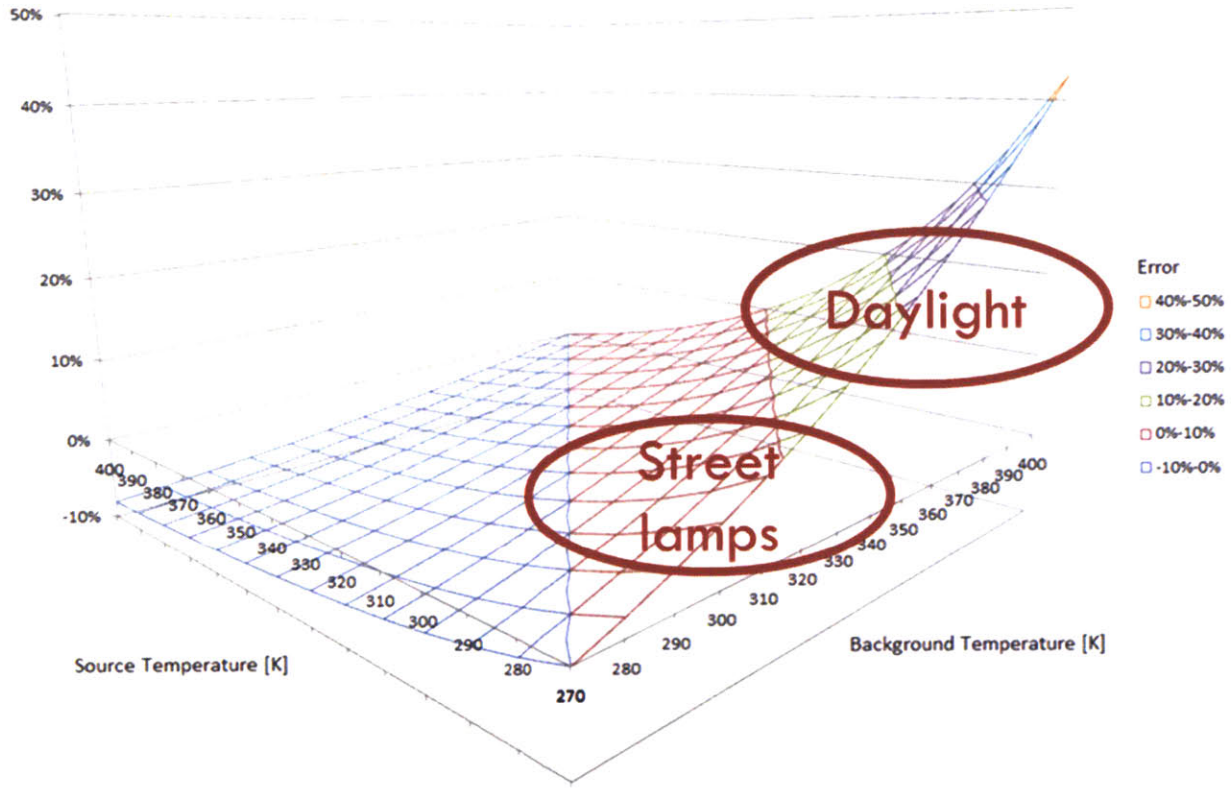

Figure 128: The effect of solar radiation and other background radiation sources such as street lamps.

6.2.4 Mitigating uncertainty associated with 3D modeling

In our analysis of scene uncertainty in ARTIST, we have identified three areas that will affect overall performance when it comes to accurately inferring temperature in the scene:

1. Emissivity Variation of Different Building Materials
2. Performance Limits of Optical Flow Algorithms
3. Background Radiation & Reflection Effects from Nearby Objects

The emissivity variation of different building materials is an uncertainty that can be quantified and shown. The performance limits of off-the-shelf optical flow algorithms were used to infer angular error, which affects our ability to resolve accurate viewing angles from the wireframe models.

Angular errors relate directly to directional emissivity in the ARTIST system. Finally, the effects of background radiation and reflection effects from nearby objects were analyzed. To minimize errors relating to scene uncertainty, it is critical to develop an accurate model of the 3D environment for which we are inferring temperature. In doing so, we can improve ARTIST through the following:

1. Correct for emissivity variation in materials and viewing angle
2. Develop more accurate 3D model of the scene
3. Correct for background radiation & reflection effects from nearby objects
4. Increase sampling measurements with slower moton

In the past, I have developed sensing systems for autonomous UAVs. This includes my MIT Masters Thesis in 1999, Collision Avoidance via Laser Range Finding [124], which was one the earliest miniature LIDAR systems developed for UAVs. For ARTIST, I propose the following methodologies to reduce scene uncertainty, thereby improving the performance of the 3D Radiometry by reducing 3D modeling uncertainties:

1. Introduce 3D LIDAR scanning
2. Introduce GIS modeling from existing GIS database
3. Fusion of 3D Reconstruction techniques using aerial imagery from satellite data
4. Introduce light field technology for active 3D
5. Multi-spectral image fusion through Hyper Resolution, using alternative spatial, temporal, and spectral resolution to generate accurate 3D modeling
6. Super Resolution using KSR to increase imaging resolution
7. Off-the-shelf systems for stereo vision or use existing commercial technologies for 3D mapping.

These methods will help ARTIST create more accurate 3D modeling of the environment, reduce angular errors, and thus, allow the directional correction factor to more accurately be applied to correct for directional emissivity in non-Lambertian surfaces.

6.3 Sensor Measurement Uncertainty for our Experiment and LWIR Imaging

In this section, we will describe the sensor measurement uncertainty for our experimental setup based on the cup, as shown in Chapter 4: 3D Radiometry. By examining the uncertainties related to the experimental setup, we infer a similar procedure for understanding how the uncertainties shown here relate to a real drive-by imaging environment. For infrared cameras, most modern uncooled microbolometer LWIR imagers have specifications of 50 mK or better [23, 24, 27, 59, 125]. Appendix B discusses noises induced limits. In IR thermography, the effects of measurement uncertainty can be quantified using the Sakuma-Hattori equations. In this section, we will see how measurement uncertainty is affected when combined with scene and material uncertainty.

We describe the signal error model as a function of the following variables:

$$s_{error} = f(\lambda, \varepsilon_{source}, T_{source}, T_{ambient}) \quad (120)$$

Where λ is the wavelength, ε_{source} is the emissivity of the source, T_{source} is the temperature of the source, and $T_{ambient}$ is the ambient temperature surrounding the object. From this, we can develop an uncertainty analysis of the signal based on the following form:

$$\Delta s^2 = \left(\frac{\partial s}{\partial \lambda} \cdot \Delta\lambda\right)^2 + \left(\frac{\partial s}{\partial \varepsilon} \cdot \Delta\varepsilon\right)^2 + \left(\frac{\partial s}{\partial T_{source}} \cdot \Delta T_{source}\right)^2 + \left(\frac{\partial s}{\partial T_{ambient}} \cdot \Delta T_{ambient}\right)^2 \quad (121)$$

Where Δs^2 is the total variance of the system. Since λ is the wavelength and is fixed for a detector, we will remove its effects on our uncertainty analysis and focus instead on the remaining three variables, $\varepsilon_{source}, T_{source}, T_{ambient}$.

6.3.1 Total Uncertainty Components

We will now translate uncertainties in our experiment to the following form:

$$U_{T_s,total}{}^2 = \left(\frac{\partial T}{\partial \mathcal{E}} \cdot U_\varepsilon\right)^2 + \left(\frac{\partial T}{\partial T_m} \cdot U_{T_m}\right)^2 + \left(\frac{\partial T}{\partial T_{amb}} \cdot U_{T_{amb}}\right)^2 \quad (122)$$

Where $U^2_{T_s,total}$ is the total temperature variance uncertainty of the system, $U^2_{T_s,T_m}$ is the variance uncertainty related to the radiance temperature (T_{source}), $U^2_{T_s,T_\varepsilon}$ is the variance uncertainty related to the emissivity (ε_{source}), and $U^2_{T_s,T_w}$ is the variance uncertainty related to the effective background temperature ($T_{ambient}$).

6.3.2 Temperature Measurement Uncertainty

To estimate the temperature using camera signal output (pixel intensity) from the camera, we sample the center area of the experimental surface using the reference material (ε=0.95) and at normal incidence θ=0 as shown in Figure 129.

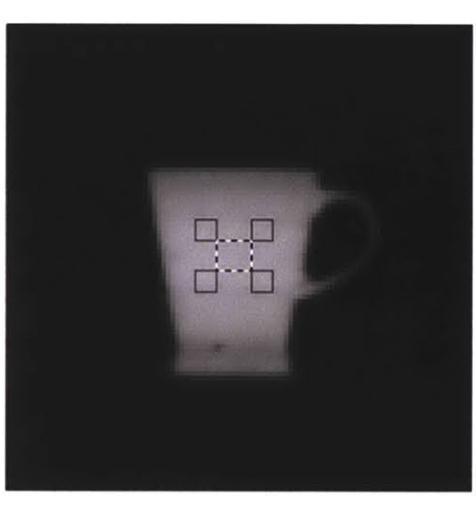

Sample	Mean	Stdev	T(Degree C)
1	193.7	1.4	81.9871
2	193.6	1.2	81.9488
3	193.7	1.1	81.9871
4	193.5	0.9	81.9105
5	193.4	0.9	81.8722
6	193.7	1.1	81.9871
7	193.9	1.3	82.0637
8	193.5	1.1	81.9105
9	193.3	1	81.8339
10	193.3	1	81.8339

Figure 129: Experimental setup for sampling T_m

By sampling 10 different frames and taking a sample measurement of the center area (as indicated above), we determine that the mean of the readings is 193.56 and the standard deviation is 0.195. Using the calibration settings we derived in Chapter 4, we apply the calibration T(°C) = 0.383x +7.8°C to yield mean temperature 81.93°C and standard deviation 0.075°C. We assign an approximate 95% confidence internal as twice the value of the standard deviation: U_{fluc}=0.15°C. Therefore, we yield the uncertainty in radiance temperature measurement to be:

$$U_{T_m} = \left(U_{fluc}{}^2\right)^{½} = (0.15^2)^{½} = 0.15°C \quad (123)$$

6.3.3 Combined Material and Directional Emissivity Uncertainty

First, we will model the combined effects of these two elements of emissivity uncertainty:

$$U_\varepsilon = \left(U_{\varepsilon,mat}{}^2 + U_{\varepsilon,\alpha}{}^2\right)^{½} \quad (124)$$

Where U_ε is the total emissivity uncertainty, $U_{\varepsilon,mat}$ is the uncertainty in estimating an object's normal emissivity without a priori knowledge, and $U_{\varepsilon,\alpha}$ is uncertainty in emissivity related to angular dependencies. If we assign an approximate 95% confidence internal as twice the value of the standard deviation for estimating emissivity our boundary continue for common building materials for $\varepsilon > 0.70$, we will yield the following:

$$U_\varepsilon = \left((2 \cdot \sigma_\varepsilon)^2 + U_\alpha{}^2\right)^{½} = \left((2 \cdot 0.067)^2 + U_\alpha{}^2\right)^{½} = \left(0.1314^2 + U_\alpha{}^2\right)^{½} \quad (125)$$

Our emissivity uncertainty $U_{\varepsilon,mat} = 0.1314$ for a majority of a common building materials. Next, we will integrate the results from our 3D modeling uncertainty and its effect on emissivity as a function of angle. In the last section, we discussed 3D modeling uncertainty, specifically, angular errors based on optical flow 3D mapping and variations in directional emissivity. The result of analysis showed the following:

θ Range	$\Delta\varepsilon$
$70° \leq \theta \leq 90°$	0.237
$60° \leq \theta \leq 70°$	≤ 0.100
$0° \leq \theta \leq 60°$	≤ 0.013

Table 14: Angular errors effect on emissivity

Where θ is normal minus viewing angle, $\Delta\varepsilon$ is expected normal emissivity uncertainty conditional on θ. Combining the effects of an unknown building material's normal emissivity with the uncertainty created by angular effects on normal emissivity yields the following results:

θ Range	$\Delta\varepsilon$	$\Delta\varepsilon^2$	$U_{\varepsilon,mat}{}^2$	$U_\varepsilon(\varepsilon)$
$70° \leq \theta \leq 90°$	0.237	0.056	0.014568	0.266
$60° \leq \theta \leq 70°$	≤ 0.100	0.010	0.014568	0.157
$0° \leq \theta \leq 60°$	≤ 0.013	0.000169	0.014568	0.121

Table 15: Extended Emissivity Uncertainty conditional on Directional Angle θ

Where θ is normal minus viewing angle, $\Delta\varepsilon$ is expected normal emissivity uncertainty conditional on θ, $\Delta\varepsilon^2$ is the variance, $U_{\varepsilon,mat}$ is the net variance of uncertainty related to estimating normal emissivity for building materials, and U_ε is the net uncertainty of both of $U_{\varepsilon,mat}$ and $U_{\varepsilon,\alpha}$. The results show that U_ε is conditional on the directional angle θ as indicated in the table above.

6.3.4 Effective Background Temperature Uncertainty from Experiment

We sample 3 different contribution areas on the image to determine the contributing variance from the background. This includes the left of the cup (the table), the right of the cup (the table), and the top of the cup (the background wall behind the cup) to determine the contributions from the surrounding background.

Left	Stdev	Right	Stdev	Top	Stdev
19.4432	0.1915	18.9453	0.6128	17.1069	0.3447
19.3283	0.2681	18.9836	0.6128	16.992	0.383
19.29	0.2298	18.9453	0.6511	17.1069	0.383
19.4049	0.1915	18.9836	0.6894	17.1835	0.383
19.3283	0.2298	18.9453	0.6511	17.0303	0.3064
19.29	0.1915	18.8304	0.6894	16.8388	0.3064
19.2517	0.1915	18.9453	0.6511	16.9154	0.2298
19.4815	0.3064	19.0985	0.4979	16.992	0.2681
19.3666	0.2298	18.9836	0.6511	16.992	0.2681
19.4049	0.2681	19.0219	0.6128	16.9537	0.3064
Mean	Stdev	Mean	Stdev	Mean	Stdev
19.35894	0.074003	18.96828	0.068036	17.01115	0.100929

Figure 130: Effective Background Temperature in three locations

From the data, we fine the estimate the effective background temperature uncertainty to be the following:

$$U_{T_w}{}^2 = U_{left}{}^2 + U_{right}{}^2 + U_{top}{}^2 \quad (126)$$

We assign an approximate 95% confidence interval as twice the value of the standard deviation of each of the left, right, and top standard deviation values:

$$U_{T_w}{}^2 = (0.074 \cdot 2)^2 + (0.0.68 \cdot 2)^2 + (0.101 \cdot 2)^2$$

$$U_{T_w} = 0.143°C$$

Where the net effect of uncertainty on the background temperature U_{T_w} is 0.143°C

6.3.5 Total Measurement Uncertainty for Experiment

.The signal measured by the detector is given by the Planckian form integral below and is approximated using the Saunders model we discussed earlier in this thesis, where A and B are fixed camera calibration constants.

$$S(T_{meas}) = \varepsilon S(T) + (1 - \varepsilon) S(T_{amb}) \quad (127)$$

$$\frac{1}{e^{\frac{c_2}{AT_{meas}+B}} - 1} = \frac{\varepsilon}{e^{\frac{c_2}{AT+B}} - 1} + \frac{(1-\varepsilon)}{e^{\frac{c_2}{AT_{amb}+B}} - 1} \quad (128)$$

The total uncertainty in the temperature measurement is given by:

$$U_{T_s,total}{}^2 = \left(\frac{\partial T}{\partial \mathcal{E}} \cdot U_\varepsilon\right)^2 + \left(\frac{\partial T}{\partial T_m} \cdot U_{T_m}\right)^2 + \left(\frac{\partial T}{\partial T_{amb}} \cdot U_{T_{amb}}\right)^2 \quad (129)$$

Differentiate the signal equation implicitly:

$$\frac{-1}{\left[e^{\frac{c_2}{AT_{meas}+B}}-1\right]^2}\cdot e^{\frac{c_2}{AT_{meas}+B}}\cdot\frac{-c_2A\partial T_m}{(AT_{meas}+B)^2}=\frac{-\varepsilon}{\left[e^{\frac{c_2}{AT+B}}-1\right]^2}\cdot e^{\frac{c_2}{AT+B}}\cdot\frac{-c_2A\partial T}{(AT+B)^2}+ \quad (130)$$

$$\frac{\partial\varepsilon}{e^{\frac{c_2}{AT+B}}-1}-\frac{\partial\varepsilon}{e^{\frac{c_2}{AT_{amb}+B}}-1}+(1-\varepsilon)\cdot\frac{1}{\left[e^{\frac{c_2}{AT_{amb}+B}}-1\right]^2}\cdot e^{\frac{c_2}{AT_{amb}+B}}\cdot\frac{c_2A\partial T_{amb}}{(AT_{amb}+B)^2}$$

Using this equation, one will be able to compute the sensitivity parameters $\frac{\partial T}{\partial T_{meas}}$, $\frac{\partial T}{\partial \varepsilon}$, and $\frac{\partial T}{\partial T_{amb}}$. These sensitivity parameters will enable a user to develop parametric charts to plot temperature uncertainty for variations in ambient temperature and emissivity. A and B are constants related to the shape of the spectral responsivity function of the detector. Below, we show an illustrative calculation of uncertainty when the measured signal is 350°K, source emissivity ε = 0.8, and the ambient temperature is 280°K. For a uniform responsivity function centered at λ_o, we compute:

$$A=\lambda_o(1-6r^2) \quad (131)$$

$$B=\frac{c_2}{2}r^2 \quad (132)$$

Where r = $\frac{\sigma}{\lambda_o}$ is the ratio of standard deviation to the central wavelength of the spectral responsivity function. For a LWIR at 8-14 μm, A ≈ 9.3632 μm, B ≈ 178.25 μmK. We solve for the source temperature, using Equation (128), to be 363.09 K. We compute $\frac{\partial T}{\partial T_{meas}}$ = 1.15628 , $\frac{\partial T}{\partial \varepsilon}$ = -15.795 K, and $\frac{\partial T}{\partial T_{amb}}$ = -0.13039. We then use relation:

$$U_{T_s,total}{}^2=\left(\frac{\partial T}{\partial \mathcal{E}}\cdot U_\varepsilon\right)^2+\left(\frac{\partial T}{\partial T_m}\cdot U_{T_m}\right)^2+\left(\frac{\partial T}{\partial T_{amb}}\cdot U_{T_{amb}}\right)^2$$

to obtain total uncertainty. Previously we have shown U_{T_m} = 0.15°C, $U_{T_{amb}}$ = 0.143°C, and $U_\varepsilon$varies according to angle according to Table 16.

With $U^2_{T_s,\varepsilon}$ is conditional on the following:

θ Range	U_ε (ε)
$70° \leq \theta \leq 90°$	0.266
$60° \leq \theta \leq 70°$	0.157
$0° \leq \theta \leq 60°$	0.121

Table 16: Conditional Uncertainty Contribution in emissivity

We compute the total uncertainty under two conditions, one where the viewing angle is less than 45° and the other at highly oblique viewing angles. U_ε in 0.121 and 0.266 corresponding to these two scenarios. Plugging these values, we estimate total uncertainty to be 1.92°C and 4.21°C for the two viewing angles scenarios.

What this means is that uncertainty in estimating the target object's true temperature is largely a direct result of emissivity uncertainties. The greater the temperature of the object, the greater the absolute effect on observed radiance which translate directly to temperature.

6.4 Motion Based Uncertainty

The ARTIST imaging system is vehicle-mounted and depends primarily on the vehicle motion to gather the thermal imaging data from different fields of view relative to the target object. As a result, we have to consider the effect of vehicle motion and disturbances on the efficacy of the imaging system. In the literature, there are many examples of 'egomotion'—solving for the motion trajectory of a camera from images of the scene [65, 68, 84]. The effect of motion induced uncertainty on the ARTIST system can be better understood based on the concept of egomotion. At the same time, the error budget estimates we develop in this section are specific to ARTIST and are not commonly done in typical egomotion analysis of unexplored scenes.

The effect of vehicle motion on the ARTIST system can be analyzed in two main categories:

3. Steady vehicle motion and its effect on the optical flow algorithm and on motion blur
4. Vibration induced uncertainty on the imaging system overall.

In both cases for motion, the relative changes of scene motion will cause changes in the optical scenery. These changes are what the optical flow algorithms use to help estimate motion flow information. By estimating the displacement of pixels between two scenes, the optical flow motion algorithms are used to characterize velocity vectors, which are then used to infer depth of the scene. In an earlier section in Chapter 6 regarding scene uncertainty for 3d modeling, we summarized a review article [86] regarding optical flow performance through a synthetic testing environment. In many these image datasets including the Yosemite Sequence, the maximum pixel displace/frame or pixel velocity ranges anywhere from 3-5 pixel/frame.

6.4.1 Limits of Steady Vehicle Motion

In this section, I show how vehicle motion causes pixel displacement and how that may affect our ability to estimate motion.

First, we will model vehicle motion based the forward motion of the vehicle, lateral to the scene that the camera is pointed at. We will assume that vehicle motion is steady and develop a model that translates the vehicle motion into intra-frame pixel displacement.

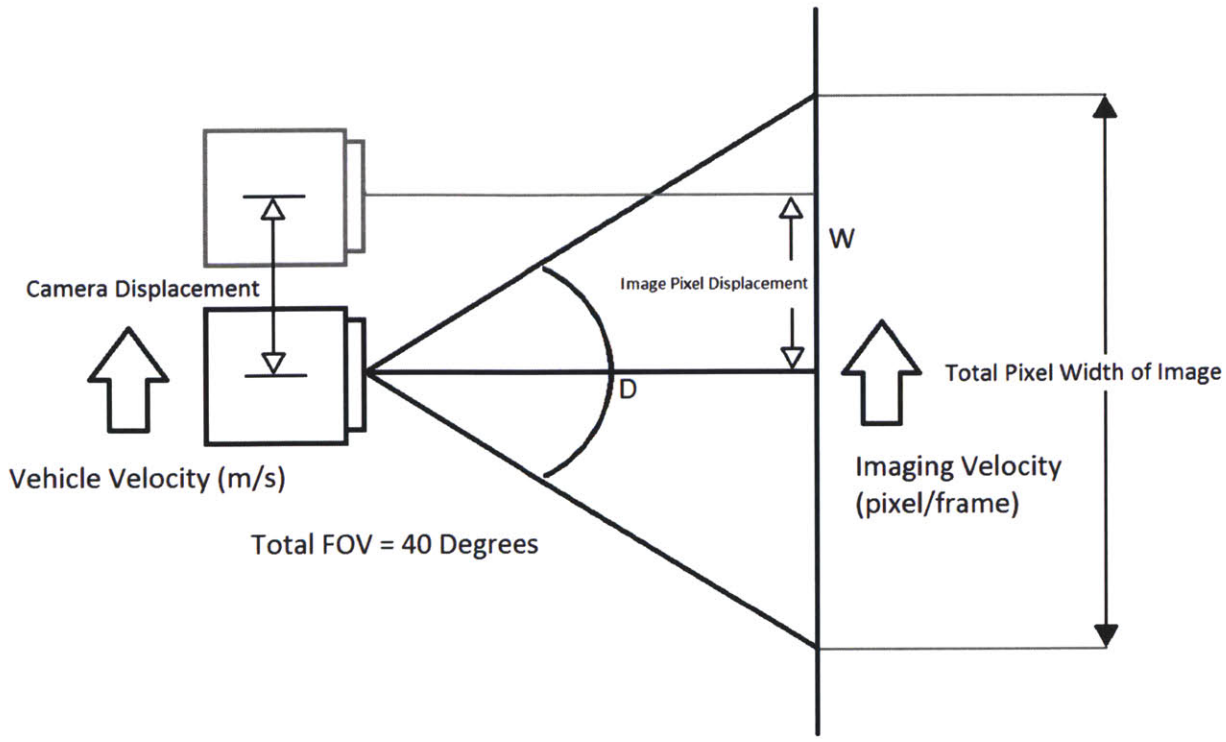

Figure 131: Steady Lateral Vehicle Motion

In Figure 131, we show the camera moving forward with velocity v (m/s), pointed at a scene with distance D (m), having a total horizontal field of view of 40°, and half-width length W (m), and projected pixel displacement v_{pixel} (pixel/frame). In our case, the infrared imaging camera has a resolution of 640x480, with 640 pixels in the horizontal direction and a frame rate of 30 frames per second. At an estimated distance D of 10 m to the target surface, which is a reasonable distance to target building, W = 3.6m. The following relationships are formed:

$$Camera\ Displacement = \frac{v_{max}}{FrameRate} \quad (133)$$

Where camera displacement is the physical displacement of the camera between each frame (m/frame), v_{max} is the vehicle's speed (m/s), and frame rate is the camera's frame rate (frames/s).

$$Image\ Pixel\ Diplacement\ = v_{pixel} \cdot \left[\frac{W}{Pixel\ Width}\right] \quad (134)$$

$$W(m) = 2D \cdot \tan\theta \quad (135)$$

Where the image pixel displacement (m/frame) is the absolute displacement of the imaging frame movement between frames, v_{pixel} (pixel/frame) is the pixel displacement velocity, W (m) is the absolute width of the imaging frame, D (m) is the distance to the target surface, and θ (degree) is half of the total horizontal field of view (FOV) of the imaging camera, and pixel width (pixels) is the number of pixels corresponding to the width W. In steady state, the camera displacement must equal to the image pixel displacement to derive the following:

$$\frac{v_{max}}{FrameRate} = \left[\frac{2D \cdot \tan\theta}{(Pixel\ Width)}\right] v_{pixel} \quad (136)$$

Which can be rewritten as the following:

$$v_{max} = FrameRate \left[\frac{2 \cdot \tan\theta}{Pixel\ Width}\right] \cdot D \cdot v_{pixel} \quad (137)$$

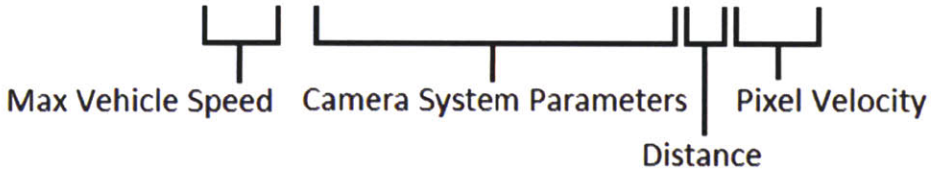

Intuitively, the vehicle's speed combined with the camera system performance parameter, and distance to the target object will determine the translated relative pixel velocity of the system. At a distance D = 10m, W=3.6m, based on the DRS 640 Camera parameters, θ = 40°, Pixel Width = 640 Pixels, FrameRate = 30 frames/sec, we derive the following relationship for velocity v_{max} vs v_{pixel}:

$$v_{max} = 30\left(\frac{frame}{s}\right)\left[\frac{7.2m}{640\ Pixels}\right] v_{pixel} \quad (138)$$

It can be seen from Equation (137) that we if we hold the vehicle velocity constant, with all else being the same, and we adjust the distance of the vehicle from the scene, we can reduce pixel velocity. The same relationship holds in reverse, the less the distance to the target, the greater the

pixel velocity, hence, the lower the performance of the optical flow algorithm and the greater the error.

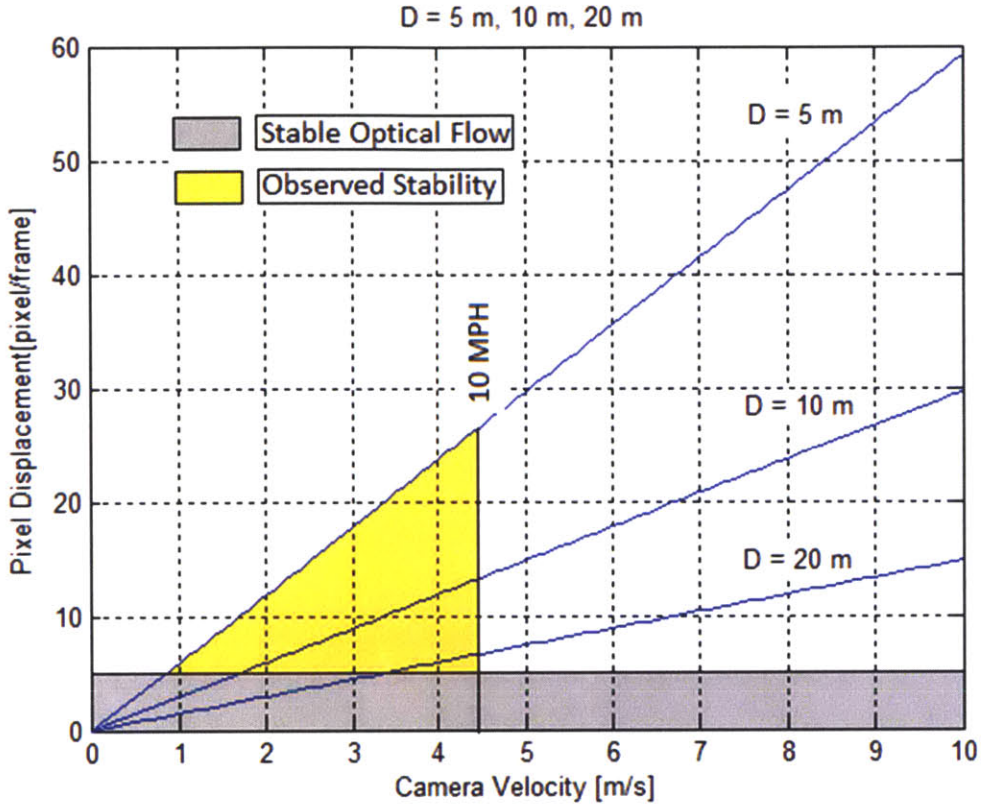

Figure 132: Camera velocity v_{max} (m/s) vs pixel displacement v_{pixel} (pixel/frame)

Figure 132 shows the projected pixel displacement velocity vs camera velocity of three different distances (5m,10m,20m) from the camera system. The greater the velocity of the camera system, the greater the pixel displacement velocity per frame. The grey area of the chart projects a stable region of pixel displacement velocity using techniques such as Lucas and Kanade [76] optical flow method presented in Section 6.2. However, using the polynomial optical flow method by Farneback [85] applied to ARTIST, we have observed stable optical flow reconstruction for vehicle velocities up to 10 mph ~ 4.46 m/s. Therefore, although we have not characterized the performance of the Farneback [85] method, our applied observations based on the data suggests stable operations of the algorithm at speeds up to 10 mph.

To increase the performance of the system and reduce angular errors, which are critical to 3D radiometry, we must look closely at the relationship between vehicle velocity and pixel displacement velocity. Stable optical flow methods presented by Barron, Fleet, and Beauchemin [1994] [86] using various video sequence was shown to be stable at pixel displacement velocities of up to 5 pixels/frame, as seen in the Yosemite Sequence. If the same pixel displacement velocity limits were placed on ARTIST, it would suggest that the maximum vehicle velocity is limited to 1.69 m/s which is 3.8 mph to achieve the same performance.

To reduce uncertainty due to vehicle motion, we suggest the following::

1. Increasing the FrameRate of the imaging system
2. Increasing the spatial resolution of the imaging system by maximizing (θ/pixel width) relationship.
3. Decrease vehicle speed
4. Maximize distance to object

We seek to minimize the pixel displacement velocity by optimizing the above. For solution (2) above, the use of increased resolution will add increased hardware cost and complexity in the image processing algorithms. Therefore, although beneficial on a net basis, there are tradeoffs involved in the solution. In implementing these suggestions, we help to minimize optical flow errors that will lead to reduced angular errors and improved performance for 3D radiometry.

6.4.2 Vehicle Vibration Induced Uncertainty

As the vehicle with the roof-mounted ARTIST system is driven around, the uneven road surface, e.g. bump, and traffic conditions, e.g. sudden braking may induce vibrations in the vehicle. The ARTIST hardware is capable of being rigidly mounted to the roof of a typical sedan. The particular vehicle used in our data collection was an Acura RDX. To the first order, the fixturing that holds the camera hardware is assumed to have very high stiffness and hence, the ARTIST system and the vehicle cabin is assumed to move as one unit.

Dynamic analysis of typical automobiles, such as a car, would suggest that the vertical bounce, roll, and pitch are the three main degrees of freedom for the vehicle cabin. We also learn from [63] and other well published results that the natural frequencies of these three modes are on the order of ~ 1 Hz for most sedans.

The response of a vehicle to road disturbances is highly specific to the vehicle under study and the particular road conditions that are encountered. When the vehicle carrying the roof-mounted ARTIST system encounters a bump, the resulting displacement (linear and rotary) causes a displacement of the features in the field of view, as recorded by the cameras. This necessitates image registration and correction of images before performing the optical flow calculations for 3D modeling. Extreme displacements may cause some features to go outside the field of view. The multi-camera synthetic aperture used in ARTIST has a vertical FOV of 90° and a horizontal FOV of 30°.

With a natural frequency of ~ 1 Hz, the resulting natural frequency of the system will limit the camera velocity and impact from the induced motion of the system. In this case, refer to Figure 122 relating the camera velocity to pixel displacement. By analyzing the response due to vibration induced motion, we will see that the induced velocity in the vehicle is limited by the attenuation of the damper system in the vehicle. The attenuation of vehicle motion limits the maximum induced velocity in the system in a regime that where pixel displacement/frame is relatively low and can be managed by the performance of the optical flow motion estimation.

6.4.3 Mitigation approaches of Motion Based Uncertainty

From a theoretical viewpoint, the uncertainty in the vertical positioning of the imaging system under the effect of road conditions can be inferred from the 2-norm of the transfer function of the automobile's suspension system assuming a typical road profile as a forcing function. From a practical standpoint, once the ARTIST system is rigidly roof-mounted, the effects of vibrations are dependent upon the vehicle's suspension design. One could improve the position accuracy of the imaging systems by using vibration isolation gyroscopic mounts or active vibration isolation mounts. Alternatively, the artist system could be appended with accelerometers so that the image frame are time and location stamped, allow for post-processing and re-centering/registration correction.

To improve imaging quality and increase system resolution, I propose applying the following:

1. Motion blur removal in image processing.
2. Hyper resolution – applying a hybrid camera system of higher frame rate to infer integration motion of the slower camera and using projected motion kernel to remove blur.
3. Use of higher frame rate cameras and systems.
4. Isolate physical motion of imaging system from potential disturbance motions.

6.5 Conclusion

In this Chapter, we have discussed three principle areas of uncertainty in the ARTIST that will affect the overall performance to the system:

1. 3D Radiometry: Scene Uncertainty in 3D
    a. Emissivity Variation
    b. Background Radiation & Reflection Effects from Nearby Objects
2. Hardware: Sensor Uncertainty – LWIR
3. Image Processing: Motion Based Uncertainty

We have presented the potential errors caused by each situation, quantified the impact of such errors on the ARTIST system, and presented methods to help mitigate the risks. Based on Chapter 6, I will list and rank the top tree sources of errors by greatest impact:

1. Emissivity Uncertainty
    i. Unknown Building Materials
    ii. Effects of Directional Emissivity
    iii. Performance of Optical Flow Model
2. Background Radiation and Reflections
    i. For Non-Metal
        1. Lower Mean Background Temperature will cause underestimated temperature inference from lower observed radiance.

2. Higher Mean Background Temperature will cause an overestimated temperature inference from higher observed radiance.

3. Motion Uncertainty
    i. The maximum vehicle speed is determined by camera system parameters, distance to the object, and inter-frame pixel velocity limits based on stable optical flow model operation.

Chapter 7: Conclusion

In Chapter 1 through 6 of this thesis, I have presented the problem, developed the ARTIST framework, and showed how ARTIST can be used to pursue urban scale temperature mapping. Over time, I hope the ARTIST system will evolve with new components, algorithms, and methods but the fundamentals will remain the same. Much of the theory will be equally applicable for future generations to apply.

7.1 Fundamental Contributions of Thesis

The fundamental contributions of this thesis relate to the Automated Rapid Thermal Imaging Systems Technology (ARTIST) includes the following individual contributions:

- Multi-camera synthetic aperture imaging system
- 3D Radiometry – justification and implementation
- Non-radiometric infrared camera calibration techniques
- Image enhancement algorithms – justification and implementation covering:
    - Hyper Resolution
    - Kinetic Super Resolution
    - Thermal Signature Identification
    - Low-Light Signal-to-Noise Enhancement using KSR

In summary, in my thesis, I have tried to do for IR thermography what Google Streetview did for visual imaging.

7.2 Future Works

I suggest the following areas as topics for future work:

1. Improving the ARTIST system from the current state:
    a. Hardware – the integration of new technology; camera, storage, geo-location, light field, LIDAR, and other performance enhancing components.

b. 3D Radiometry
    i. Measuring temperatures of surfaces at oblique angles
    ii. Thermography of metallic surfaces (e.g. in industrial applications)
c. Image Processing – to continue the development of an urban scale hyper resolution technique to maximize imaging resolution(s) by combining spatial, spectral, and temporal resolution modalities.

2. Scalability challenges for urban scale deployment of ARTIST – the mass deployment of the ARTIST system in a global scale to gather useful information for residential, commercial, and industrial applications.
3. New research areas in IR thermography using Thermal Signature Identification – the expansion of the thermal signature identification concept to be used as a diagnostics process, with possible applications in technology, medical, and other scientific fields.
4. Use of ARTIST hardware as a characterization tool for 3D radiometry – the ARTIST framework can be applied for other infrared (long-wave, mid-wave, short-wave) applications including other remote sensing and interplanetary studies.
5. Application of ARTIST to further heat transfer studies related to energy loss analysis – for energy loss analysis for residential, commercial, and industrial sectors, accurate temperature information should be used in conjunction with conduction, convection, and radiation heat transfer models to improve the reliability of those models.

7.3 Long Term Vision

My vision of the future is for ARTIST system to be developed into a globally scalable technology that can be deployed on-demand for high throughput thermography applications in energy efficiency analysis of residential, commercial, and industrial applications. Although ARTIST focuses on enhancing the performance of the long wave infrared band, the information from the other spectrum is also valuable and important. In the future, newer applications may include disaster recovery, automated remote sensing, industrial monitoring, and in any application where thermal, multi-spectral, high resolution imaging is useful. As an on-demand technology, I hope that this system can put into practical use to further help solve scientific and practical needs for mankind.

7.4 Gaps in this thesis

The following topics are not covered in this thesis and are potential opportunities for future research:

1. Heat Transfer analysis of energy loss – the translation of an accurate temperature map into R-values for building materials, identifying and quantifying air leakage energy loss on the envelope, studies correlating problem identification into an assessment of energy saved, etc.
2. The performance of the polynomial based optical flow algorithm by Farneback [85] and our specific implementation of the algorithm of drive-by imaging has not been fully tested for performance. I refer the Farneback [85] paper for analyzing the performance of the algorithm.
3. Multi-spectral hyper resolution has only been presented as a concept with a single-band multi-camera example shown. It has not been extended in practice to multi-band super resolution. This area of research will be continued at the MIT Field Intelligence Laboratory with applications and publications to follow.
4. Motion based uncertainty has not been quantified or corroborated with experimentation. A more precise model would account for motion induced blur and its corresponding translational effects in the images. Once such a process is well understood, we can reverse the process and enhance imaging performance through image deblurring processing. By doing so, we can potentially increase the speed of the vehicle beyond the current limits.

The End

Appendix

Appendix A: Normalized Emissivity Values of Common Building Materials

The following table has normal emissivity numbers for common materials.

Material	Normalized Emissivity Value
Aluminum: anodized	0.77
Aluminum: polished	0.05
Asbestos: board	0.96
Asbestos: fabric	0.78
Asbestos: paper	0.93
Asbestos: slate	0.96
Brass: highly polished	0.03
Brass: oxidized	0.61
Brick: common	0.83
Brick: common, red	0.93
Brick: facing, red	0.92
Brick: fireclay	0.75
Brick: masonry	0.94
Brick: red	0.9
Carbon: candle soot	0.95
Carbon: graphite, filed surface	0.98
Carbon: purified	0.8
Cement:	0.54
Charcoal: powder	0.96
Chipboard: untreated	0.9
Chromium: polished	0.1
Clay: fired	0.91
Concrete	0.92
Concrete: dry	0.95
Concrete: rough	0.95
Copper: polished	0.05
Copper: oxidized	0.65
Enamel: lacquer	0.9
Fabric: Hessian, green	0.88
Fabric: Hessian, uncolored	0.87
Fiberglass	0.75
Fiber board: porous, untreated	0.85

Fiber board: hard, untreated	0.85
Filler: white	0.88
Firebrick	0.68
Formica	0.94
Galvanized Pipe	0.46
Glass	0.92
Glass: chemical ware (partly transparent)	0.97
Glass: frosted	0.96
Glass: frosted	0.7
Glass: polished plate	0.94
Granite: natural surface	0.96
Graphite: powder	0.97
Gravel	0.28
Gypsum	0.08
Hardwood: across grain	0.82
Hardwood: along grain	0.7
Ice	0.97
Iron: heavily rusted	0.94
Lacquer: bakelite	0.93
Lacquer: dull black	0.97
Lampblack	0.96
Limestone: natural surface	0.96
Mortar	0.87
Mortar: dry	0.94
P.V.C.	0.92
Paint: 3M, black velvet coating	1
Paint: aluminum	0.45
Paint, oil: average of 16 colors	0.94
Paint: oil, black, flat	0.94
Paint: oil, black, gloss	0.92
Paint: oil, grey, flat	0.97
Paint: oil, grey, gloss	0.94
Paint: oil, various colors	0.94
Paint: plastic, black	0.95
Paint: plastic, white	0.84
Paper: black	0.9
Paper: black, dull	0.94
Paper: black, shiny	0.9
Paper: cardboard box	0.81
Paper: green	0.85

Paper: red	0.76
Paper: white	0.68
Paper: white bond	0.93
Paper: yellow	0.72
Paper: tar	0.92
Pipes: glazed	0.83
Plaster	0.88
Plaster: rough coat	0.91
Plasterboard: untreated	0.9
Plastic: acrylic, clear	0.94
Plastic: black	0.95
Plastic: white	0.84
Plastic paper: red	0.94
Plastic paper: white	0.84
Plexiglas: Perpex	0.86
Plywood	0.9
Plywood: commercial, smooth finish, dry	0.82
Plywood: untreated	0.83
Polypropylene	0.97
Porcelain: glazed	0.92
Quartz	0.93
Redwood: wrought, untreated	0.83
Redwood: unwrought, untreated	0.84
Rubber	0.95
Rubber: stopper, black	0.97
Sand	0.9
Skin, human	0.98
Snow	0.8
Soil: dry	0.92
Soil: frozen	0.93
Soil: saturated with water	0.95
Stainless Steel	0.59
Stainless Plate	0.34
Steel: galvanized	0.28
Steel: rolled freshly	0.24
Styrofoam: insulation	0.6
Tape: electrical, insulating, black	0.97
Tape: masking	0.92
Tile: floor, asbestos	0.94
Tile: glazed	0.94

Tin: burnished	0.05
Tin: commercial tin-plated sheet iron	0.06
Varnish: flat	0.93
Wallpaper: slight pattern, light grey	0.85
Wallpaper: slight pattern, red	0.9
Water:	0.95
Water: distilled	0.95
Water: ice, smooth	0.96
Water: frost crystals	0.98
Water: snow	0.85
Wood: planed	0.9
Wood: paneling, light finish	0.87
Wood: spruce, polished, dry	0.86

Table 17: Emissivity values of common materials

Appendix B: Noise Equivalent Temperature Difference - NETD

The NETD is the difference between the temperature of an observed object and the ambient temperature which generates a signal level at the detector equal to the noise level. This is also known as the temperature resolution of the system. Infrared camera manufacturers often use NETD as an important camera specification for differentiating the quality of their camera to their competitor's. The differences in value for an infrared camera can range from 10 mK to 100 mK, an order of magnitude difference. NETD [K] is technically defined as the ratio of the RMS noise voltage U_n to the voltage increment ΔU_s which is generated by the differences in temperature between the measurement area of a black body T_{ob} and the background temperature T_o:

$$NETD = \frac{U_n}{\frac{\Delta U_s}{T_{ob} - T_o}} = \frac{T_{ob} - T_o}{\frac{\Delta U_s}{U_n}} \quad (139)$$

According to Niklaus, Decharat, Jansson, and Stemme [29] the model for NETD for a conventional uncooled infrared bolometer array using a column based readout design and integrated analog-to-digital conversion can be expressed as:

$$NETD^2 = NETD^2_{\frac{1}{f}} + NETD^2_{Johnson} + NETD^2_{thermal} + NETD^2_{ROIC} \quad (140)$$

Where the $NETD_{\frac{1}{f}}$ is the 1/f-noise of the bolometer, the $NETD_{Johnson}$ is the Johnson noise of the bolometer, the $NETD_{thermal}$ is the thermal fluctuation noise of the bolometer, and the $NETD_{ROIC}$ is the readout integrated circuit (ROIC) related noise.

$$NETD_{\frac{1}{f}} = \left[4 \cdot \frac{F^2}{\phi_{\lambda 1-\lambda 2} \cdot \left(\frac{\Delta P}{\Delta T}\right)_{\lambda 1-\lambda 2}}\right] \cdot \frac{G \cdot \sqrt{\frac{K}{v}} \cdot \sqrt{ln\left(\frac{f_r}{f_s}\right)} \cdot \sqrt{1 + \omega^2 \cdot \left(\frac{C}{G}\right)^2}}{TCR \cdot \beta \cdot A \cdot \varepsilon_{\lambda 1-\lambda 2}} \quad (141)$$

$$NETD_{Johnson} = \left[4 \cdot \frac{F^2}{\phi_{\lambda 1-\lambda 2} \cdot \left(\frac{\Delta P}{\Delta T}\right)_{\lambda 1-\lambda 2}}\right] \cdot 2 \cdot \sqrt{k} \cdot \frac{G \cdot \sqrt{R_{bol}} \cdot \sqrt{f_r} \cdot \sqrt{T_1} \cdot \sqrt{1 + \omega^2 \cdot \left(\frac{C}{G}\right)^2}}{U_{bias} \cdot TCR \cdot \beta \cdot A \cdot \varepsilon_{\lambda 1-\lambda 2}} \quad (142)$$

$$NETD_{thermal} = \left[4 \cdot \frac{F^2}{\phi_{\lambda 1-\lambda 2} \cdot \left(\frac{\Delta P}{\Delta T}\right)_{\lambda 1-\lambda 2}}\right] \cdot 4 \cdot \sqrt{k} \cdot \frac{f_{eff} \cdot T_1 \cdot \sqrt{C}}{\beta \cdot A \cdot \varepsilon_{\lambda 1-\lambda 2}} \quad (143)$$

$$NETD_{ROIC} = \left[4 \cdot \frac{F^2}{\phi_{\lambda 1-\lambda 2} \cdot \left(\frac{\Delta P}{\Delta T}\right)_{\lambda 1-\lambda 2}}\right] \cdot \frac{(R_{ROIC} + R_{bol}) \cdot G \cdot \sqrt{1 + \omega^2 \cdot \left(\frac{C}{G}\right)^2}}{R_{ROIC} \cdot U_{bias} \cdot TCR \cdot \beta \cdot A \cdot \varepsilon_{\lambda 1-\lambda 2}} \cdot V_{ROIC} \quad (144)$$

$$V_{ROIC} = \sqrt{V_{amp}(f_r)^2 + \frac{V_Q^2}{12} + \left(\frac{R_{ROIC} \cdot R_{bol}}{R_{ROIC} + R_{bol}}\right)^2 \cdot I_{ROIC} \cdot (f_r)^2} \quad (145)$$

$$f_r = x_l \cdot f_i \quad (146)$$

$$f_{eff} = min|f_r, f_{bol}| \quad (147)$$

$$f_{bol} = \frac{1}{4\tau} \quad (148)$$

$$\tau = \frac{C}{G} \quad (149)$$

Where F is the F-number of the infrared optics, $\phi_{\lambda 1-\lambda 2}$ is the transmission of the infrared optics in the wavelength interval from λ_1 to λ_2, G is the total thermal conduction between the bolometer and its surrounding, C is the thermal capacity of the bolometer pixel, TCR is the temperature coefficient of resistance of the thermistor material, K is the 1/f noise constant of the thermistor material, υ is the volume of the thermistor material, R_{bol} is the resistance of the bolometer thermistor, β is the bolometer fill factor, A is the bolometer pixel area, $\varepsilon_{\lambda 1-\lambda 2}$ is the infrared absorption rate of the bolometer membrane in the wavelength internal from λ_1 to λ_2, f_s is the shutter uniformity correction frequency for the bolometer array, f_r is the read-out frequency of the bolometer, x_l is the amount of bolometer pixels per column, f_i is the image readout frequency, f_{eff} is the effective integration

frequency of the bolometer, f_{bol} is the thermal integration frequency of the bolometer, τ is the thermal time constant of the bolometer pixel, U_{bias} is the bolometer bias voltage, R_{ROIC} is the input impedance of the ROIC, V_{ROIC} is the total noise voltage of the ROIC, V_{amp} is the input reference noise voltage of the ROIC, V_Q is the input reference analog to digital quantization interval, I_{ROIC} is the current noise from the ROIC input including the bolometer bias current source, $\left(\frac{\Delta P}{\Delta T}\right)_{\lambda 1-\lambda 2}$ is the temperature contrast in the wavelength interval from λ_1 to λ_2, T_1 is the bolometer membrane temperature, ω is the modulation frequency of the infrared signal (embedded in the electronics) from the image scene, and k is the Boltzmann constant.

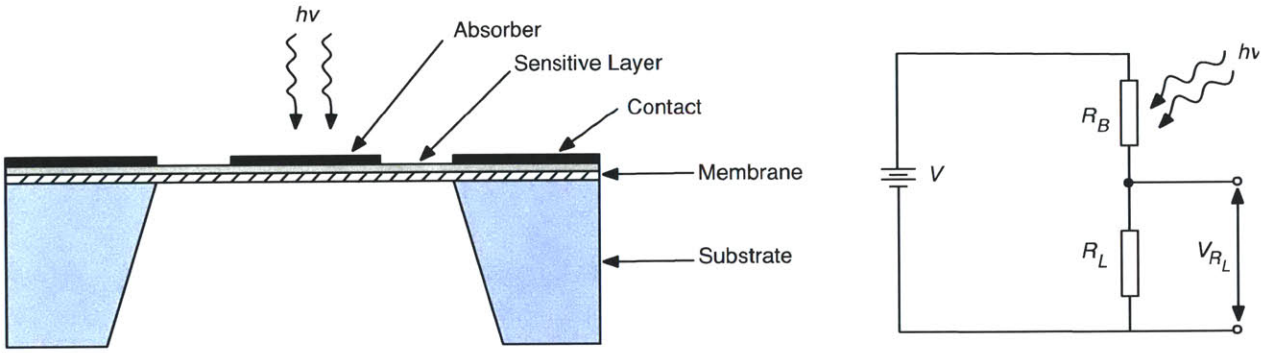

Figure 133: Schematic Cross section of a thin film bolometer (left) Bolometer circuit (right)

Appendix C: References & Bibliography

1. Council, U.S.G.B., *LEED certification process*, 2004, Retrieved March.

2. Balaras, C. and A. Argiriou, *Infrared thermography for building diagnostics.* Energy and Buildings, 2002. **34**(2): p. 171-183.

3. Snell, J., *RESNET & Infrared Thermography.* Home Energy, 2010: p. 48-52.

4. Outlook, A.E., *Energy Information Administration.* US Department of Energy, Januar, 2010.

5. Sakuma F, K.M., *"Interpolation equations of scales of radiation thermometers"*, . Proceedings of TEMPMEKO 1996,, (1996): p. pp. 305–310.

6. A Greening, L., D.L. Greene, and C. Difiglio, *Energy efficiency and consumption—the rebound effect—a survey.* Energy Policy, 2000. **28**(6): p. 389-401.

7. Clinch, J.P. and J.D. Healy, *Cost-benefit analysis of domestic energy efficiency.* Energy Policy, 2000. **29**(2): p. 113-124.

8. Clinch, J.P. and J.D. Healy, *Valuing improvements in comfort from domestic energy-efficiency retrofits using a trade-off simulation model.* Energy economics, 2003. **25**(5): p. 565-583.

9. Farrell, D., S.S. Nyquist, and M.C. Rogers, *Curbing the growth of global energy demand.* The McKinsey Quarterly, 2007.

10. Granade, H.C., McKinsey, and Company, *Unlocking energy efficiency in the US economy.* 2009.

11. Granade, H., et al., *Unlocking Energy Efficiency in the US Economy. McKinsey & Company, July*, 2009.

12. Thumann, A. and W.J. Younger, *Handbook of energy audits*2008: The Fairmont Press, Inc.

13. Krarti, M., *Energy audit of building systems: an engineering approach.* Vol. 47. 2010: CRC Press.

14. Hendron, R. and C. Engebrecht, *Building America Research Benchmark Definition: Updated December 2009.* 2010.

15. Patel, T., et al. *Comparison of Blower Door and Tracer Gas Testing Methods for Determination of Air Infiltration Rates Through Building Envelopes at Normal Operating Conditions.* 2011. ASME.

16. Council, U.S.G.B., *Leadership in energy and environmental design (LEED).* webpage http://www. usgbc. org, 2007.

17. Sarma, S. and E.C. Shao, *Detecting sources of heat loss in residential buildings from infrared imaging*, 2011, Massachusetts Institute of Technology.

18. Sherman, M.H. and D.J. Dickerhoff, *Airtightness of US dwellings.* TRANSACTIONS-AMERICAN SOCIETY OF HEATING REFRIGERATING AND AIR CONDITIONING ENGINEERS, 1998. **104**: p. 1359-1367.

19. Erinjeri, J.J., et al., *Empirical Modeling of Air Tightness in Residential Homes in North Louisiana.* Louisiana Tech University, 2009.

20. Hay, G.J., et al., *Geospatial technologies to improve urban energy efficiency.* Remote Sensing, 2011. **3**(7): p. 1380-1405.

21. Sakuma, F. and S. Hattori, *Establishing a practical temperature standard by using a narrow-band radiation thermometer with a silicon detector.* Temperature: Its Measurement and Control in Science and Industry, 1982. **5**: p. 421-427.

22. Liebman, J.R. and K.J. Lombardo, *Guide to Export Controls for the Non-Specialist, A.* Loy. LA Int'l & Comp. L. Rev., 2006. **28**: p. 497.

23. Li, C., et al. *DRS uncooled VOx infrared detector development and production status.* 2010.

24. Radford, W.A., et al. *320 x 240 microbolometer focal plane array for uncooled applications.* 1996.

25. Tissot, J., *IR detection with uncooled focal plane arrays. State-of-the art and trends.* Opto-electronics review, 2004. **12**(1): p. 105-109.

26. Wood, R., *Uncooled microbolometer infrared sensor arrays.* Infrared detectors and emitters: materials and devices, 2001: p. 149-175.

27. Chen, C., et al., *Characterizations of VO< sub> 2</ sub>-based uncooled microbolometer linear array.* Sensors and Actuators A: Physical, 2001. **90**(3): p. 212-214.

28. Niklaus, F., et al., *Performance model for uncooled infrared bolometer arrays and performance predictions of bolometers operating at atmospheric pressure.* Infrared Physics & Technology, 2008. **51**(3): p. 168-177.

29. Niklaus, F., et al. *Uncooled infrared bolometer arrays operating in a low to medium vacuum atmosphere: performance model and tradeoffs.* 2007.

30. Dewitt, D.P. and F.P. Incropera, *Fundamentals of heat and mass transfer.* John Wiley & Sons: New York, 1996.

31. Eckert, E.R.G., *Introduction to the Transfer of Heat and Mass*1950: McGraw-Hill.

32. Incropera, F.P., et al., *Fundamentals of heat and mass transfer*2011: Wiley.

33. Lienhard IV, J.H., *JH Lienhard V, A heat transfer textbook*, 2006, Cambridge, MA, Phlogiston Press.

34. Saunders, P., *Calibration and use of low-temperature direct-reading radiation thermometers.* Measurement Science and Technology, 2009. **20**(2): p. 025104.

35. Minkina, W. and S. Dudzik, *Errors of Measurements in Infrared Thermography*, in *Infrared Thermography*2009, John Wiley & Sons, Ltd. p. 61-80.

36. Rogalski, A., *Infrared detectors: an overview.* Infrared Physics & Technology, 2002. **43**(3–5): p. 187-210.

37. Rogalski, A., *Fundamentals of infrared detector technologies*2009: CRC.

38. Minano, J.C., *Application of the conservation of etendue theorem for 2-D subdomains of the phase space in nonimaging concentrators.* Applied optics, 1984. **23**(12): p. 2021-2025.

39. Vollmer, M. and K.P. Möllmann, *Infrared thermal imaging: fundamentals, research and applications*2010: Wiley-VCH.

40. Budzier, H. and G. Gerlach, *Thermal Infrared Sensors: Theory, Optimisation and Practice*2011: Wiley.

41. Wolfe, W.L. *Introduction to infrared system design.* 1996. SPIE-International Society for Optical Engineering.

42. Schmidt, E. and E. Eckert, *Über die Richtungsverteilung der Wärmestrahlung von Oberflächen.* Forschung auf dem Gebiet des Ingenieurwesens A, 1935. **6**(4): p. 175-183.

43. Fehlman, W.L. and M.K. Hinders, *Mobile robot navigation with intelligent infrared image interpretation*2009: Springer Verlag.

44. Cardone, G., et al., *Temperature maps measurements on 3D surfaces with infrared thermography.* Experiments in Fluids, 2012. **52**(2): p. 375-385.

45. Fronapfel, E., M. Bradley, and J. Stolz, *Emissivity measurements of common construction materials.* InfraMation 2006, 2006.

46. Siegel, R. and J.R. Howell, *Thermal radiation heat transfer.* Vol. 1. 2002: Taylor & Francis.

47. DeWitt, D.P. and G.D. Nutter, *Theory and practice of radiation thermometry*1988: Wiley Online Library.

48. Vellvehi, M., et al., *Irradiance-based emissivity correction in infrared thermography for electronic applications.* Review of Scientific Instruments, 2011. **82**(11): p. 114901-114901-9.

49. Liebmann, F.E., et al., *Radiometic Comparison Between a National Laboratory and an Industrial Laboratory.* International Journal of Thermophysics, 2011: p. 1-11.

50. Rigolini, J., et al., *2D-Infrared Thermography Monitoring of Ultrasound-Assisted Polymerization of Water-Soluble Monomer in a Gel Process.* Macromolecules, 2011.

51. Carr, G., *Resolution limits for infrared microspectroscopy explored with synchrotron radiation.* Review of Scientific Instruments, 2001. **72**: p. 1613.

52. Slocum, A.H., *Precision machine design*1992: Society of Manufacturing.

53. Slocum, A., *FUNdaMENTALS of Design*, 2005, Alexander Slocum.

54. Segall, J.E., *Google Street View: Walking the Line of Privacy-Intrusion upon Seclusion and Publicity Given to Private Facts in the Digital Age.* University of Pittsburgh Journal of Technology Law & Policy, 10 (1), 1, 2010. **32**.

55. Andersen, E.R., *Multibody dynamics modeling and system identification for a quarter-car test rig with McPherson strut suspension*, 2007, Virginia Polytechnic Institute and State University.

56. Levitt, J. and N. Zorka, *The influence of tire damping in quarter car active suspension models.* Journal of dynamic systems, measurement, and control, 1991. **113**: p. 134.

57. Türkay, S. and H. Akçay, *A study of random vibration characteristics of the quarter-car model.* Journal of sound and vibration, 2005. **282**(1): p. 111-124.

58. Hildebrandt, C., C. Raschner, and K. Ammer, *An overview of recent application of medical infrared thermography in sports medicine in Austria.* Sensors, 2010. **10**(5): p. 4700-4715.

59. Howard, P.E., et al. *DRS U6000 640x480 VO uncooled IR focal plane.* 2002.

60. Gaussorgues, G., *La Thermographie infrarouge : principes, technologie, applications*1984, Paris: Lavoisier.

61. Dieck, R.H. and I.S.o. America, *Measurement uncertainty: methods and applications*1997: Instrument Society of America.

62. Ramsey, M.H., *Sampling as a source of measurement uncertainty: techniques for quantification and comparison with analytical sources.* J. Anal. At. Spectrom., 1998. **13**(2): p. 97-104.

63. Brincker, R., L. Zhang, and P. Andersen. *Modal Identification from Ambient Responses using Frequency Domain Decomposition.* 2000.

64. Caron, F., et al., *GPS/IMU data fusion using multisensor Kalman filtering: introduction of contextual aspects.* Information Fusion, 2006. **7**(2): p. 221-230.

65. Gluckman, J. and S.K. Nayar. *Ego-motion and omnidirectional cameras.* 1998. IEEE.

66. Lin, X., J. Xu, and M. Zhou, *Integrated navigation system and experiment of a low-cost and low-accuracy SINS/GPS.* Geo-Spatial Information Science, 2007. **10**(3): p. 177-180.

67. Clipp, B., et al. *Robust 6dof motion estimation for non-overlapping, multi-camera systems.* 2008. IEEE.

68. Tian, T.Y., C. Tomasi, and D.J. Heeger. *Comparison of approaches to egomotion computation.* 1996. IEEE.

69. Avdelidis, N. and A. Moropoulou, *Emissivity considerations in building thermography.* Energy and Buildings, 2003. **35**(7): p. 663-667.

70. Cuenca, J. and J.A. Sobrino, *Experimental measurements for studying angular and spectral variation of thermal infrared emissivity.* Applied optics, 2004. **43**(23): p. 4598-4602.

71. Labed, J. and M. Stoll, *Angular variation of land surface spectral emissivity in the thermal infrared: laboratory investigations on bare soils.* Remote Sensing, 1991. **12**(11): p. 2299-2310.

72. Sobrino, J.A. and J. Cuenca, *Angular variation of thermal infrared emissivity for some natural surfaces from experimental measurements.* Applied optics, 1999. **38**(18): p. 3931-3936.

73. Cramer, K.E. and W.P. Winfree, *Method and apparatus for the portable identification of material thickness and defects using spatially controlled heat application*, 1999, Google Patents.

74. Memarian, N., A.N. Venetsanopoulos, and T. Chau, *Infrared thermography as an access pathway for individuals with severe motor impairments.* Journal of NeuroEngineering and Rehabilitation, 2009. **6**(1): p. 11.

75. Horn, B.K.P. and B.G. Schunck, *Determining optical flow.* Artificial intelligence, 1981. **17**(1-3): p. 185-203.

76. Lucas, B.D. and T. Kanade. *An iterative image registration technique with an application to stereo vision.* 1981.

77. Uras, S., et al., *A computational approach to motion perception.* Biological cybernetics, 1988. **60**(2): p. 79-87.

78. Nagel, H.H., *Displacement vectors derived from second-order intensity variations in image sequences.* Computer Vision, Graphics, and Image Processing, 1983. **21**(1): p. 85-117.

79. Anandan, P., *A computational framework and an algorithm for the measurement of visual motion.* International journal of computer vision, 1989. **2**(3): p. 283-310.

80. Singh, A. *An estimation-theoretic framework for image-flow computation.* 1990. IEEE.

81. Heeger, D.J., *Model for the extraction of image flow.* JOSA A, 1987. **4**(8): p. 1455-1471.

82. Waxman, A.M. and K. Wohn, *Contour evolution, neighborhood deformation, and global image flow: Planar surfaces in motion.* The International journal of robotics research, 1985. **4**(3): p. 95.

83. Fleet, D.J. and A.D. Jepson, *Computation of component image velocity from local phase information.* International journal of computer vision, 1990. **5**(1): p. 77-104.

84. Prazdny, K., *Egomotion and relative depth map from optical flow.* Biological cybernetics, 1980. **36**(2): p. 87-102.

85. Farnebäck, G., *Two-frame motion estimation based on polynomial expansion.* Image Analysis, 2003: p. 363-370.

86. Barron, J.L., D.J. Fleet, and S. Beauchemin, *Performance of optical flow techniques.* International journal of computer vision, 1994. **12**(1): p. 43-77.

87. Liebmann, F. and M.A.C. Carrasco. *Infrared Calibration Development at Fluke Corporation Hart Scientific Division.* 2008. Society of Photo-Optical Instrumentation Engineers.

88. Madding, R.P. *Emissivity measurement and temperature correction accuracy considerations.* 1999.

89. Root, W.A., J.R. Liebman, and R.C. Thomsen, *United States export controls*2006: Aspen Publishers.

90. Bertero, M. and P. Boccacci, *Super-resolution in computational imaging.* Micron, 2003. **34**(6-7): p. 265-273.

91. Irani, M. and S. Peleg. *Super resolution from image sequences.* 1990. IEEE.

92. Irani, M. and S. Peleg, *Improving resolution by image registration.* CVGIP: Graphical models and image processing, 1991. **53**(3): p. 231-239.

93. Zalevsky, Z. and D. Mendlovic, *Optical superresolution.* Vol. 91. 2004: Springer Verlag.

94. Park, S.C., M.K. Park, and M.G. Kang, *Super-resolution image reconstruction: a technical overview.* Signal Processing Magazine, IEEE, 2003. **20**(3): p. 21-36.

95. Farsiu, S., et al., *Advances and challenges in super-resolution.* International Journal of Imaging Systems and Technology, 2004. **14**(2): p. 47-57.

96. Baker, S. and T. Kanade, *Limits on super-resolution and how to break them.* Pattern Analysis and Machine Intelligence, IEEE Transactions on, 2002. **24**(9): p. 1167-1183.

97. Freeman, W.T., T.R. Jones, and E.C. Pasztor, *Example-based super-resolution.* Computer Graphics and Applications, IEEE, 2002. **22**(2): p. 56-65.

98. Elad, M. and Y. Hel-Or, *A fast super-resolution reconstruction algorithm for pure translational motion and common space-invariant blur.* Image Processing, IEEE Transactions on, 2001. **10**(8): p. 1187-1193.

99. Farsiu, S., et al. *Robust shift and add approach to super-resolution.* 2003.

100. Borman, S. and R.L. Stevenson. *Super-resolution from image sequences-a review.* 1998. IEEE.

101. Borman, S. and R. Stevenson, *Spatial resolution enhancement of low-resolution image sequences-a comprehensive review with directions for future research.* Lab. Image and Signal Analysis, University of Notre Dame, Tech. Rep, 1998.

102. Farsiu, S., M. Elad, and P. Milanfar, *Multiframe demosaicing and super-resolution of color images.* Image Processing, IEEE Transactions on, 2006. **15**(1): p. 141-159.

103. Farsiu, S., et al., *Fast and robust multiframe super resolution.* Image Processing, IEEE Transactions on, 2004. **13**(10): p. 1327-1344.

104. Sroubek, F., G. Cristobál, and J. Flusser. *Simultaneous super-resolution and blind deconvolution.* 2008. IOP Publishing.

105. Schultz, R.R., L. Meng, and R.L. Stevenson, *Subpixel motion estimation for super-resolution image sequence enhancement.* Journal of visual communication and image representation, 1998. **9**(1): p. 38-50.

106. Caron, J.N., *Rapid supersampling of multiframe sequences by use of blind deconvolution.* Optics letters, 2004. **29**(17): p. 1986-1988.

107. Tai, Y.W., et al. *Image/video deblurring using a hybrid camera.* 2008. Ieee.

108. Tai, Y.W., et al., *Correction of spatially varying image and video motion blur using a hybrid camera.* Pattern Analysis and Machine Intelligence, IEEE Transactions on, 2010. **32**(6): p. 1012-1028.

109. Li, F., J. Yu, and J. Chai. *A hybrid camera for motion deblurring and depth map super-resolution.* 2008. Ieee.

110. Robinson, D. and P. Milanfar, *Fundamental performance limits in image registration.* Image Processing, IEEE Transactions on, 2004. **13**(9): p. 1185-1199.

111. Šroubek, F. and J. Flusser, *Resolution enhancement via probabilistic deconvolution of multiple degraded images.* Pattern Recognition Letters, 2006. **27**(4): p. 287-293.

112. Groetsch, C.W., *The theory of Tikhonov regularization for Fredholm equations of the first kind.* Vol. 105. 1984: Pitman Boston.

113. Hansen, P.C. and D.P. O'Leary, *The use of the L-curve in the regularization of discrete ill-posed problems.* SIAM Journal on Scientific Computing, 1993. **14**: p. 1487.

114. Huiskes, M.J. and M.S. Lew. *The MIR flickr retrieval evaluation.* 2008. ACM.

115. Huynh-Thu, Q. and M. Ghanbari, *Scope of validity of PSNR in image/video quality assessment.* Electronics letters, 2008. **44**(13): p. 800-801.

116. Wang, Z., et al., *Image quality assessment: From error visibility to structural similarity.* Image Processing, IEEE Transactions on, 2004. **13**(4): p. 600-612.

117. Zhu, X. and P. Milanfar, *Automatic parameter selection for denoising algorithms using a no-reference measure of image content.* Image Processing, IEEE Transactions on, 2010. **19**(12): p. 3116-3132.

118. Székely, V., *A new evaluation method of thermal transient measurement results.* Microelectronics Journal, 1997. **28**(3): p. 277-292.

119. Szekely, V., et al., *A thermal benchmark chip: Design and applications.* Components, Packaging, and Manufacturing Technology, Part A, IEEE Transactions on, 1998. **21**(3): p. 399-405.

120. Murphy, J., *Transient response of the Hadley Centre coupled ocean-atmosphere model to increasing carbon dioxide. Part 3: Analysis of global-mean response using simple models.* Journal of Climate, 1995. **8**(3).

121. Micusik, B. and J. Kosecka. *Piecewise planar city 3D modeling from street view panoramic sequences.* 2009. IEEE.

122. Anguelov, D., et al., *Google street view: Capturing the world at street level.* Computer, 2010. **43**(6): p. 32-38.

123. Nagel, H.H., *On the estimation of optical flow: Relations between different approaches and some new results.* Artificial intelligence, 1987. **33**(3): p. 299-324.

124. Phan, L.N., *Collision avoidance via laser rangefinding*, 1999, Massachusetts Institute of Technology, Department of Mechanical Engineering; and,(SM)--Massachusetts Institute of Technology, Department of Electrical Engineering.

125. Radford, W.A., et al. *Microbolometer uncooled infrared camera with 20-mK NETD.* 1998.

126. Al-Rabghi, O.M. and D.C. Hittle, *Energy simulation in buildings: overview and BLAST example.* Energy conversion and Management, 2001. **42**(13): p. 1623-1635.

127. Cardone, G., et al., *Temperature maps measurements on 3D surfaces with infrared thermography.* Experiments in Fluids, 2012: p. 1-11.

128. Crawley, D.B., et al., *Contrasting the capabilities of building energy performance simulation programs.* Building and environment, 2008. **43**(4): p. 661-673.

129. Crawley, D.B., et al., *EnergyPlus: creating a new-generation building energy simulation program.* Energy and Buildings, 2001. **33**(4): p. 319-331.

130. Fleet, D.J., *Measurement of image velocity.* 1992.

131. Hand, J.W., et al., *Improving non-geometric data available to simulation programs.* Building and environment, 2008. **43**(4): p. 674-685.

132. Harley, B., *Insulate and weatherize: expert advice from start to finish*2002: Taunton Pr.

133. Herman, G.T., *Fundamentals of Computerized Tomography: Image Reconstruction from Projections*2009: Springer Verlag.

134. Jensen, S.Ø., *Validation of building energy simulation programs: a methodology.* Energy and Buildings, 1995. **22**(2): p. 133-144.

135. Klein, Y.L., *Residential energy conservation choices of poor households during a period of rising fuel prices.* Resources and Energy, 1987. **9**(4): p. 363-378.

136. Kośny, J. and E. Kossecka, *Multi-dimensional heat transfer through complex building envelope assemblies in hourly energy simulation programs.* Energy and Buildings, 2002. **34**(5): p. 445-454.

137. Lam, J.C., et al., *Principal component analysis and long-term building energy simulation correlation.* Energy conversion and Management, 2010. **51**(1): p. 135-139.

138. Laouadi, A., *Development of a radiant heating and cooling model for building energy simulation software.* Building and environment, 2004. **39**(4): p. 421-431.

139. Lomas, K., et al., *Empirical validation of building energy simulation programs.* Energy and Buildings, 1997. **26**(3): p. 253-275.

140. Maruyama, Y. and F. Yamazaki, *Seismic response analysis on the stability of running vehicles.* Earthquake engineering & structural dynamics, 2002. **31**(11): p. 1915-1932.

141. Maruyama, Y. and F. Yamazaki, *Fundamental study on the response characteristics of drivers during an earthquake based on driving simulator experiments.* Earthquake engineering & structural dynamics, 2004. **33**(6): p. 775-792.

142. Min, J., Z. Hausfather, and Q.F. Lin, *A High-Resolution Statistical Model of Residential Energy End Use Characteristics for the United States.* Journal of Industrial Ecology, 2010. **14**(5): p. 791-807.

143. Moropoulou, A. and N.P. Avdelidis. *Emissivity measurements on historic building materials using dual-wavelength infrared thermography.* 2001.

144. Nicodemus, F.E., *Reflectance nomenclature and directional reflectance and emissivity.* Applied optics, 1970. **9**(6): p. 1474-1475.

145. Pasqualetto, L., R. Zmeureanu, and P. Fazio, *A case study of validation of an energy analysis program: MICRO-DOE2. 1E.* Building and environment, 1998. **33**(1): p. 21-41.

146. Pesterev, A., L. Bergman, and C. Tan, *Pothole-induced contact forces in a simple vehicle model.* Journal of sound and vibration, 2002. **256**(3): p. 565-572.

147. Pesterev, A.V., L.A. Bergman, and C.A. Tan, *POTHOLE-INDUCED CONTACT FORCES IN A SIMPLE VEHICLE MODEL.* Journal of Sound and Vibration, 2002. **256**(3): p. 565-572.

148. Pesterev, A.V., L.A. Bergman, and C.A. Tan, *A novel approach to the calculation of pothole-induced contact forces in MDOF vehicle models.* Journal of Sound and Vibration, 2004. **275**(1–2): p. 127-149.

149. Polly, B., *A Method for Determining Optimal Residential Energy Efficiency Retrofit Packages*2011: National Renewable Energy Laboratory.

150. Schott, J.R. *Incorporation of angular emissivity effects in long wave infrared image models.* 1986.

151. Noda, I., *Two-dimensional infrared spectroscopy.* Journal of the American Chemical Society, 1989. **111**(21): p. 8116-8118.

152. Slavin, G.S. and D.A. Bluemke, *Spatial and Temporal Resolution in Cardiovascular MR Imaging: Review and Recommendations1.* Radiology, 2005. **234**(2): p. 330-338.

153. Stein, J.R. and A. Meier, *Accuracy of home energy rating systems.* Energy, 2000. **25**(4): p. 339-354.

154. Vosselman, G., *3d reconstruction of roads and trees for city modelling.* International Archives of Photogrammetry, Remote Sensing and Spatial Information Sciences, 2003. **34**(3/W13): p. 231-236.

155. Wetter, M., *BuildOpt—a new building energy simulation program that is built on smooth models.* Building and environment, 2005. **40**(8): p. 1085-1092.

156. Zhai, Z.J. and Q.Y. Chen, *Performance of coupled building energy and CFD simulations.* Energy and Buildings, 2005. **37**(4): p. 333-344.

157. Zhu, L., et al., *Detailed energy saving performance analyses on thermal mass walls demonstrated in a zero energy house.* Energy and Buildings, 2009. **41**(3): p. 303-310.